E-ISSN: 2687-6167
NUMBER 53
JUNE 2023

JSR A

JOURNAL OF SCIENTIFIC REPORTS A

Kutahya Dumlupinar University Journal of Reports A
Evliya Celebi Campus Tavsanli Road 10 KM. 43270 Kutahya
Phone : (0274) 443 11 42
E-mail : journsra@gmail.com
gpjsra.com

Dumlupinar University Press

gate of science

Kütahya Dumlupınar University
Institute of Graduate Studies

Journal of Scientific
Reports-A
E-ISSN: 2687-6167
Number 53, June 2023

Journal of Scientific Reports-A started its publication life in 2000 as name of Journal of Science and Technology of Dumlupınar University and is a national peer-reviewed journal published regularly twice a year in June and December. The language of the journal is English. Articles submitted to the journal are evaluated by at least two referees who are experts in the subject and selected by the editorial board. All articles submitted to the journal are evaluated by the double-blind method. Articles submitted to our journal for review should not be previously published, accepted for publication and in the process of being evaluated for publication in another journal. All responsibility for the articles published in the journal belongs to the author(s).

The journal aims to share scientific studies carried out in the fields of science and engineering at national and international level with scientists and the public. Original research articles, review articles and short notes in science and engineering disciplines are accepted for the journal. Original research articles are expected to contain theoretical and experimental results and should not be published in other journals. In the review articles, it is expected that scientific, technological and current developments on a specific subject are reflected by using an extensive bibliography and made a satisfying evaluation of these. Short notes should be brief writings prepared to announce the first findings of an original study.

Editorial Policy

The journal is open access and the article evaluation period is between 1-2 months.

Correspondence Address: Kütahya Dumlupınar Üniversitesi Evliya Çelebi Yerleşkesi Fen Bilimleri Enstitüsü 43270 KÜTAHYA
E-mail: joursra@gmail.com
Webpage: gsjsra.com
Phone: 0 274 443 19 42
Fax: 0 274 265 20 60

JSR A
Journal of Scientific Reports

JSR A
Journal of Scientific Reports

JSR A
Journal of Scientific Reports

JOURNAL OF SCIENTIFIC REPORTS-A
E-ISSN: 2687-6167

CONTENTS

RESEARCH ARTICLES

JSR A
Journal of Scientific Reports

Kütahya Dumlupınar University
Institute of Graduate Studies

Journal of Scientific
Reports-A
E-ISSN: 2687-6167
Number 53, June 2023

RESEARCH ARTICLE

PERFORMANCE ASSESSMENT OF LANDSAT 8 AND SENTINEL-2 SATELLITE IMAGES FOR THE PRODUCTION OF TIME SERIES LAND USE/LAND COVER (LULC) MAPS

Recep Ugur ACAR[1*], Enes ZENGIN[2]

[1*] Kutahya Dumlupinar University, Geological Engineering, Kütahya, Türkiye,
ugur.acar@dpu.edu.tr, ORCID: 0000-0002-0420-6263
[2] Kutahya Dumlupinar University, Urban and Regional Planning, Kutahya, Türkiye
enes.zengin@dpu.edu.tr, ORCID: 0000-0002-5740-7763

Receive Date:02.12.2022 *Accepted Date: 06.04.2023*

ABSTRACT

Land use/Land cover (LULC) maps are essential tools used in various disciplines, including geosciences, urban and regional planning, climate, and agriculture. LULC maps provide a visual representation of the Earth's surface, depicting the different types of land use and land cover in a given area. Land use refers to the human activities that take place on the land, such as agriculture, urban development, and mining, while land cover refers to the physical characteristics of the land, such as forests, grasslands, and wetlands. Researchers can gain insights into environmental trends and patterns, such as deforestation, urbanization, and climate change by analysing changes in LULC over time. While Landsat 8 images have been used to create LULC maps for years, the high-resolution images provided by Sentinel-2 since 2017 have allowed for the creation of highly detailed LULC maps. However, it is still necessary to use Landsat 8 images to produce LULC maps for time-series analyses and future predictions. Unsupervised classification is a method used to create LULC maps using Landsat 8 images, but this study found that the resulting maps differed from those created using Sentinel-2 images, with up to a two-fold difference in the classification of classes such as "Bare Ground," "Built Area," "Crops," and "Trees". Especially when using Landsat data, it is suggested that it would be useful to make evaluations for wider areas/regions as the resolution of Landsat 8 satellite images is limited to 30 meters.

Keywords: *Landsat 8, Land use map, Land cover map, Sentinel-2, Unsupervised classification*

1. INTRODUCTION

The enactment of global endeavours towards climate change mitigation, sustainable development, and preserving ecosystem and biodiversity functions directly in association with the U.N. Sustainable Development Goals in relation with the production of land use/land cover (LULC) change maps on global, national, and regional scales. The need for globally reliable LULC maps has long been a focus, with the promise of improved quantification made possible using remote sensing data from various

sources like Landsat and Sentinel satellites [1–4]. To meet the need in this regard, the maps have been published in recent years with different spatial resolutions for both global or regional use by Esri Land Cover and European Space Agency World Cover [5,6]. These new and up to date LULC maps provide unprecedentedly heightened spatial and accurate mapping details [7]. However, they lack typology customization or monitoring capabilities required for earth science and urban and regional planning applications. The Landsat program, which is another source which can be used to produce LULC maps operated by the United States Geological Survey (USGS) and the National Aeronautics and Space Administration (NASA), provides satellite data with a medium spatial resolution which is 30 meters [8]. Although satellites such as Sentinel-2 are used widely for LULC today, Landsat is also a significant source for monitoring historical changes, especially since it provides publicly available data from 1972. Since the resolution of Landsat is 30 meters, it provides data with lower resolution than satellites such as Sentinel-2. Despite its limitations, Landsat is used by many researchers for different thematic studies like forest monitoring, structure mapping, vegetation health assessment, flood, and drought analysis, as it can be used for preliminary and fast assessments [9–14].

In addition to the maps provided by various organizations, it is also possible to produce LULC maps with unsupervised learning algorithms by using geographic information systems software like ArcGIS or QGIS [15]. The Iterative Self-Organizing (ISO) Cluster classifier is one of the featured algorithms for unsupervised classification applications with its capability to handle very large images. ISO clustering does not require prior knowledge of the classes present in the satellite image. This makes it a useful tool for exploratory analysis and for identifying patterns and structures in the data. It can identify complex structures in the data, such as irregular shapes and clusters of different densities. This makes it useful for satellite image classification, where objects of interest can have varying shapes and sizes. ISO clustering is computationally efficient and can handle large datasets with many variables, making it suitable for analyzing high-resolution satellite imagery. It is also flexible and can be used with different distance metrics and linkage methods, depending on the characteristics of the data being analyzed. Overall, ISO clustering is a powerful tool for satellite image classification that can identify complex structures and patterns in the data, without requiring prior knowledge of the classes present [4,16]. Furthermore, the ISO cluster classifier can take a segmented RGB raster from a third-party application. ISO cluster classifier can both work with Esri-supported raster files and other segmented raster datasets. The multidimensional attribute space is used by the ISO Cluster algorithm to perform an unsupervised classification to identify the properties of the naturally occurring cell/pixel groupings. In this study, LULC maps for 2017 and 2021were produced using Landsat data with 30 meters spatial resolution for Kütahya located in the western part of the Türkiye which was chosen as the study area, by using the unsupervised learning algorithm. ArcGIS Pro software was used to production LULC maps using an unsupervised learning algorithm. In order to assess unsupervised classification algorithm performance of the LULC maps produced for 2017 and 2021, the LULC maps provided by Sentinel-2 with a resolution of 10 meters were used for each time-series. The relevant satellite images were taken from the June data sets of 2017 and 2021 to reach the lowest cloud density values.

JSR A
Journal of Scientific Reports

2. MATERIALS and METHODS

2.1. Study Area

Kütahya is a major settlement, with a population of 578,640 and a surface area of 11,632 km^2, located in the Aegean Region of Türkiye, was chosen as the study area (Figure 1). Kütahya, which is adjacent to Eskişehir, Afyonkarahisar, Uşak, Manisa, Balıkesir, Bursa and Bilecik, is located on 39°16′10.2″N and 29°33′10.8″E central coordinates. Forests, rangelands and crops are the predominant LULC classes in the study area. Forest areas within the study area are in the mountain regions on the Gediz-Altıntaş and Domaniç-Simav lines. Rangelands are spread in regions where forest areas exist throughout the study area. Agricultural areas are mainly concentrated in the Çavdarhisar-Aslanapa-Altıntaş region.

2.2. Sentinel-2 Collection

The LULC maps have been distributed as open sources since 2017 with 10 meters of high spatial resolution using satellite images from Sentinel-2 by the Environmental Systems Research Institute (ESRI). The dataset was classified by applying a high-level of deep learning algorithm that classifies surface reflectance data on Sentinel-2 satellite images [5]. The Sentinel-2 satellite has a multispectral imager that captures images in 13 spectral bands, which are divided into four groups. Among these, six bands are particularly important for monitoring and assessing vegetation health, water quality, and land use/land cover changes. The first band is the coastal aerosol band, which has a wavelength range of 443 nanometers and is used to study the concentration of aerosols and chlorophyll-a in coastal waters. The blue band, with a wavelength range of 490 nanometers, is used to monitor water quality and vegetation health. The green band, with a wavelength range of 560 nanometers, is used to study vegetation health and growth. The red band, with a wavelength range of 665 nanometers, is used to assess vegetation health, identify different crop types, and monitor forest cover. The vegetation red edge band, with a wavelength range of 705 to 745 nanometers, is used to study vegetation health and growth. Finally, the near-infrared band, with a wavelength range of 785 nanometers, is used to monitor vegetation density, water content, and soil moisture. In addition to these six bands, the Sentinel-2 satellite also captures images in the high-resolution visible (HRV) band and six shortwave infrared (SWIR) bands, which are used to study mineral content, soil moisture, and land use/land cover changes. As a result of using different bands with various wavelengths, final LULC maps were produced with nine different classes; water (rivers, ponds, lakes), trees (dense/tall vegetation), flooded vegetation (irrigated and inundated agriculture), crops (corn, wheat, soy), built area (houses, dense villages, cities), bare ground (rocks, soils, mines), snow/ice (glaciers), clouds and rangeland (bushes, shrubs, grass). 10-meter resolution GeoTIFF scenes from 2017 and 2021 were downloaded to create LULC maps for the study area based on Sentinel-2 data which was used to assess the unsupervised classification performance of Landsat 8 data.

JSR A
Journal of Scientific Reports

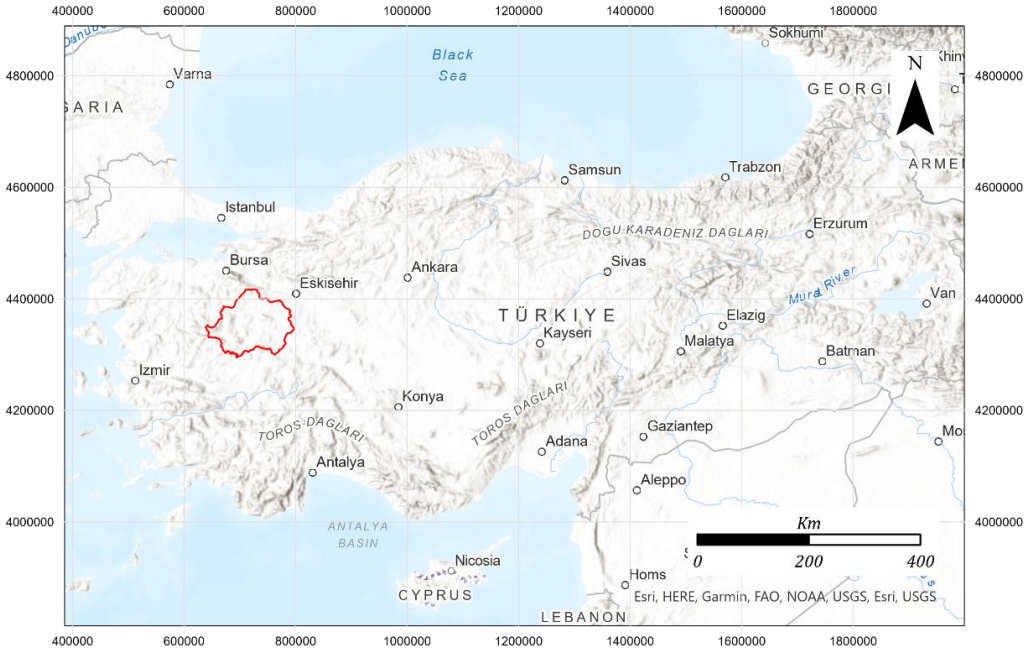

Figure 1. Study area.

2.3. Landsat 8 OLI/TIRS Collection

Traditional digital cameras are designed to imitate as the human eye sees, for this they capture light only in the red, green and blue wavelengths. Then those cameras apply red, green and blue filters to these wavelengths to create a natural RGB image. There will be a lot of information to work on a multispectral image from a complex sensor system like Landsat 8. Different wavelengths would be useful for researchers to discern some features more and better than others or even help to see through features such as clouds or smoke using various bands. Near Infrared (NIR) wavelength is one of the most typically used wavelengths on multispectral sensors because vegetation reflects intensely in this part of the electromagnetic spectrum. In this way, this information provides a handy method for vegetation analysis. The Shortwave Infrared (SWIR) bands on Landsat 8 are very useful for discerning disparities in bare earth and describing what is wet and dry in a study area. There are many other benefits of the available bands in Landsat 8 images that can be used for different purposes. Landsat 8 has two primary sensors, which are the Operational Land Imager (OLI) and Thermal Infrared (TIRS). OLI produces nine spectral bands varying from Band 1 to Band 9 with 15, 30 and 60-meter resolution. Using the OLIs 9 spectral band to discriminate vegetation, biomass, vigour and similar focuses is possible. TIRS of Landsat 8 consists of 2 thermal bands with a spatial resolution of 100 meters and can be used for tracking land and water usage by measuring the Earth's thermal energy. Bandwidths and resolutions of OLI and TIRS sensors of Landsat 8 are given in Table 1 [17]. In order to assess the unsupervised classification performance, Landsat 8 OLI/TIRS Collection 2 Level-2 science product with 30-meter multispectral data belong paths and rows covering (179-32,

179-33, 180-33) the study area were used. The summer periods of 2017 and 2021 were chosen as the acquisition dates to have the least cloud density and more high-quality outputs in classification. For this reason, attention was paid to ensuring that the cloud cover was less than 5% while accessing the Landsat 8 images.

Table 1. Landsat 8 OLI and TIRS bandwidth and resolutions [17].

Band Name	Bandwidth (µm)	Resolution (m)
Band-1: Coastal	0.43 – 0.45	30
Band-2: Blue	0.45 – 0.51	30
Band-3: Green	0.53 – 0.59	30
Band-4: Red	0.64 – 0.67	30
Band-5: NIR	0.85 – 0.88	30
Band-6: SWIR 1	1.57 – 1.65	30
Band-7: SWIR 2	2.11 – 2.29	30
Band-8: Pan	0.50 – 0.68	15
Band-9: Cirrus	1.36 – 1.38	30
Band-10: TIRS 1	10.6 – 11.19	100
Band-11: TIRS 2	11.5 – 12.51	100

The most common band combinations used in this study were summarized to provide helpful information for researchers. The natural colour composite uses a band combination of red (4), green (3), and blue (2), which can be used to detect urban features. These composite replicates what human eyes can see very similarly. Urban features appear white and grey, while water is dark blue or black. It is also possible to distinguish healthy vegetation with green and unhealthy flora with brown colour. The colour-infrared combination is also called the near-infrared (NIR) composite. It uses near-infrared (5), red (4), and green (3). As chlorophyll reflects near-infrared light, NIR band composition is proper for investigating vegetation. In particular, areas in red have better vegetation health, while dark areas are urban areas and water zones. SWIR-1 (6), near-infrared (5), and blue (2) band combination is instrumental in detecting agriculture zones and crop monitoring as this combination uses short-wave and near-infrared, which provide reliable results for vegetation. This band combination shows healthy vegetation with darker shades of green, while the bare surface has a magenta hue. Another band combination that efficiently determines geological elements, lithological features, and faults uses SWIR-2 (7), SWIR-1 (6), and blue (2). Furthermore, other band combinations are needed for extensive geological features like rock types and ore deposit exploration. The bathymetric band combination uses the red (4), green (3), and coastal bands to penetrate the water. The coastal band is good in coastal, bathymetric, and aerosol analyses because it reflects blues and violets. This band combination is good for assessing and evaluating sedimentation in water. The Landsat 8 band combinations and RGB codes used are given in Table 2.[17].

Table 2. Landsat 8 band combinations for different applications [17].

Band Combinations	Red	Green	Blue
Natural Colour	4	3	2
False Colour (Urban)	7	6	4

Colour Infrared (Vegetation)	5	4	3
Agriculture	6	5	2
Atmospheric Penetration	7	6	5
Healthy Vegetation	5	6	2
Land/Water	5	6	4
Shortwave Infrared	7	5	4
Vegetation Analysis	6	5	4

2.4. Processing Flow

The flow given in Figure 2 was applied to create LULC maps using Landsat 8 data with unsupervised classification and to assess the unsupervised classification performance using Sentinel-2 LULC. The study can be divided into three sub-groups data preparation, pre-processing, and evaluation. As a part of the data preparation, Landsat 8 and Sentinel-2 images were combined and cropped into a single mosaic raster covering the study area. To slightly increase the resolution of Landsat 8 images, pixels with a resolution of 30 meters were resampled to 10 meters. The same processes were applied to Sentinel-2 images, except for resampling.

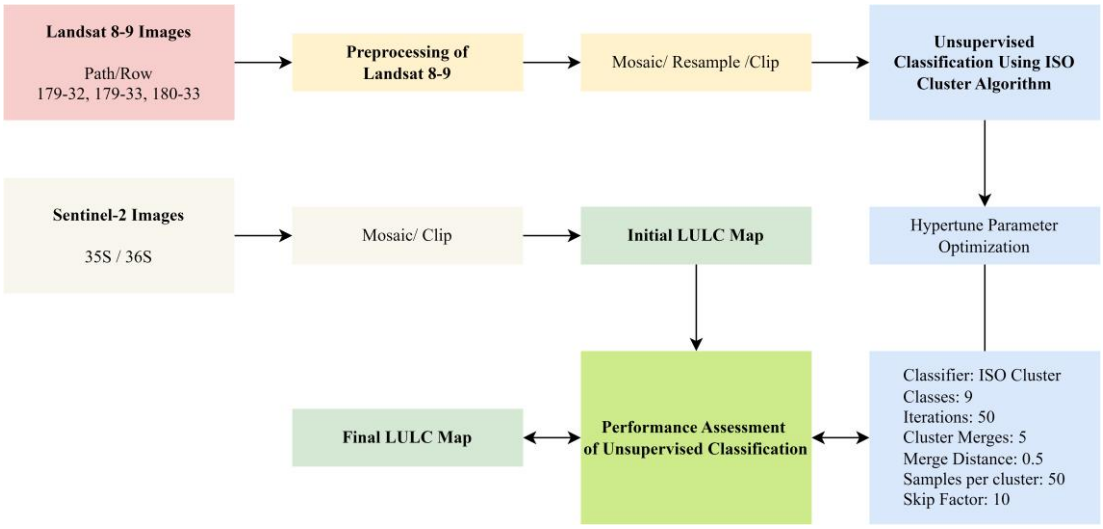

Figure 2. Flowchart for assessing unsupervised classification algorithm performance.

3. UNSUPERVISED CLASSIFICATION PROCESS

Pixel-based classification method was used during the production of the maps with the unsupervised learning algorithm [18]. This classification approach performs on a per-pixel base, where the spectral attributes of the individual pixel determine the class to which it is assigned. Characteristics of adjacent pixels are not considered in the pixel-based technique. Pixel-based classification can be described as a more traditional method and may result in speckled outcomes in the classified image. Another critical

stage of unsupervised learning is to decide the classification schema, which determines the total number of classes in the final raster. Sentinel-2 LULC map classes were used to classify the Landsat 8-based rasters. Several crucial variables impact the outcome images in the categorization procedure using the unsupervised learning algorithm. The ISO Cluster classifier performs an unsupervised classification using the K-means approach [19]. The K-Nearest Neighbour classifier performs a K-nearest neighbour classification, classifying a pixel by a plurality voting of its neighbours. The training process assigns the training samples to their individual classes. K is the defined number of neighbours used in voting. In order to achieve a statistically meaningful signature file generation process for the forthcoming classification, each individual cell should have appropriate cells that represent related clusters accurately. In this study, it was determined the minimum class size is ten times bigger than the number of layers in the input raster bands. The value chosen for the selection interval implies one cell out of every n-by-n block of cells is used in the cluster calculations [19]. Commonly, the additional cells included in the extent of the intersection of the input bands, the more heightened the values for minimum class size should be specified along with the sample interval. However, the sample interval value should be small enough to represent the most diminutive categories in the rasters or input data. It is always possible to achieve better results as long as all input bands have the same data ranges. The data ranges can be transformed to the same range using Map Algebra to perform the equation, as the band have broadly different data ranges [16,20]. The map algebra formula that applied is given in Equation 1 below;

$$Z = \frac{(X - oldmin)\ x\ (newmax - newmin)}{(oldmax - oldmin)} + newmin \tag{1}$$

where;

- *Z:* output raster with new data ranges,
- *X:* input raster, *oldmin* is the minimum value of the input raster,
- *oldmax:* maximum value of the input raster,
- *newmin*: desired minimum value for the output raster,
- *newmax:* desired maximum value for the output raster.

Furthermore, the maximum number of classes must be defined in the output raster. The number of classes in the Sentinel-2 maps used in the analysis of unsupervised classification performance was chosen as the maximum number of classes which is 9. The maximum number of iterations during unsupervised classification is an important parameter. This number defines the maximum number of iterations the clustering process will run. In order to achieve the optimum number of iterations during the processing, 50, 100 and 250 iterations were chosen. As a result of the hyper-tuning parameter technique, 50 was chosen the maximum number of iterations. However, a number between 10 and 20 is suggested to keep the processing time acceptable. All of the hyperparameters preferred during the creation of LULC maps using Landsat 8 images are given in Figure 2.

JSR A
Journal of Scientific Reports

4. RESULTS

LULC maps created for 2017 and 2021 using images provided by Sentinel-2 and available as open source by ESRI are given in Figure 3 and Figure 4. It was decided to assess the unsupervised classification performance based on the LULC maps produced using the satellite images provided by Sentinel-2 as they have 10 meters spatial resolution. Therefore, field classes were separately calculated for the years 2017 and 2021. Class details and the percentage of all individual classes are given in Table 3. According to the LULC maps produced for 2017 and 2021 using Sentinel-2 satellite images, the highest increase was seen in "Crops" at 2.3%, "Trees" at 0.9% and "Built Area" at 0.5%. The change in these classes are 264.2 km^2, 102.2 km^2 and 60.3 km^2, respectively. These three classes constitute 96.3% of the study area. All nine classes in the LULC maps produced by ESRI can be seen in the study area. These data were used to analyze the performance of the unsupervised classification using Landsat 8 images. LULC maps created for 2017 and 2021 by unsupervised learning using Landsat 8 images are given in Figure 5 and Figure 6. All nine classes in Sentinel-2 do not appear on the generated LULC maps. Accurately classifying areas with flooded vegetation, snow/ice, water and clouds was not possible. The main reason for the low performance of unsupervised classification of some field types is that the resolution of Landsat 8 data is limited to 30 meters.

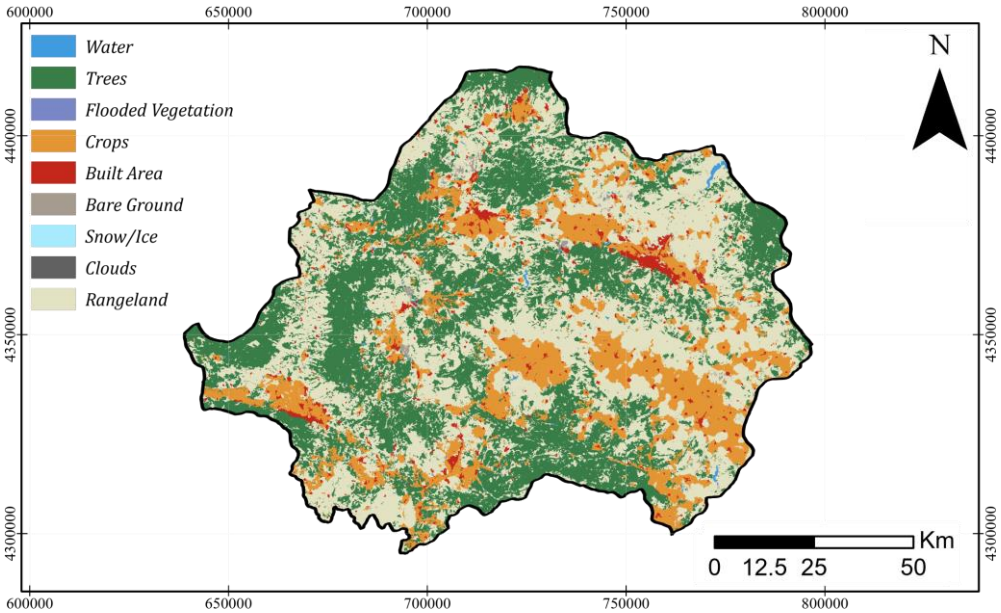

Figure 3. 2021 LULC map produced by using Sentinel-2 satellite images.

JSR A
Journal of Scientific Reports

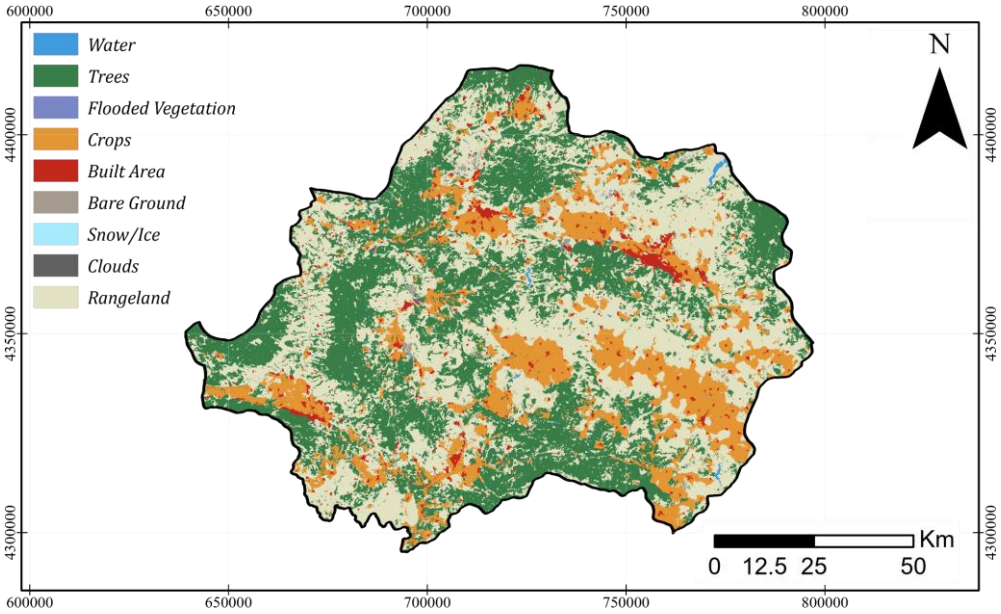

Figure 4. 2017 LULC map produced by using Sentinel-2 satellite images.

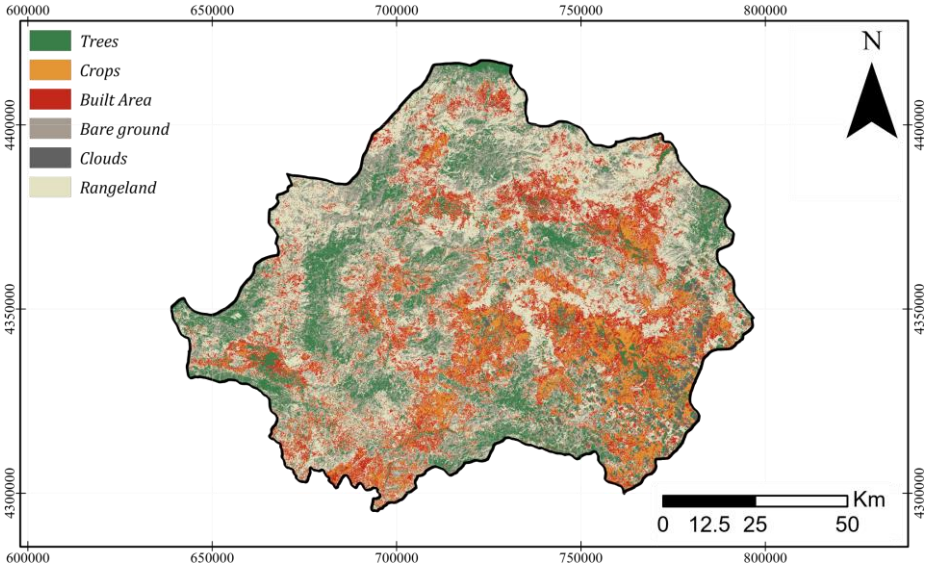

Figure 5. 2021 LULC map produced with unsupervised learning algorithms by using Landsat 8 satellite images.

JSR A
Journal of Scientific Reports

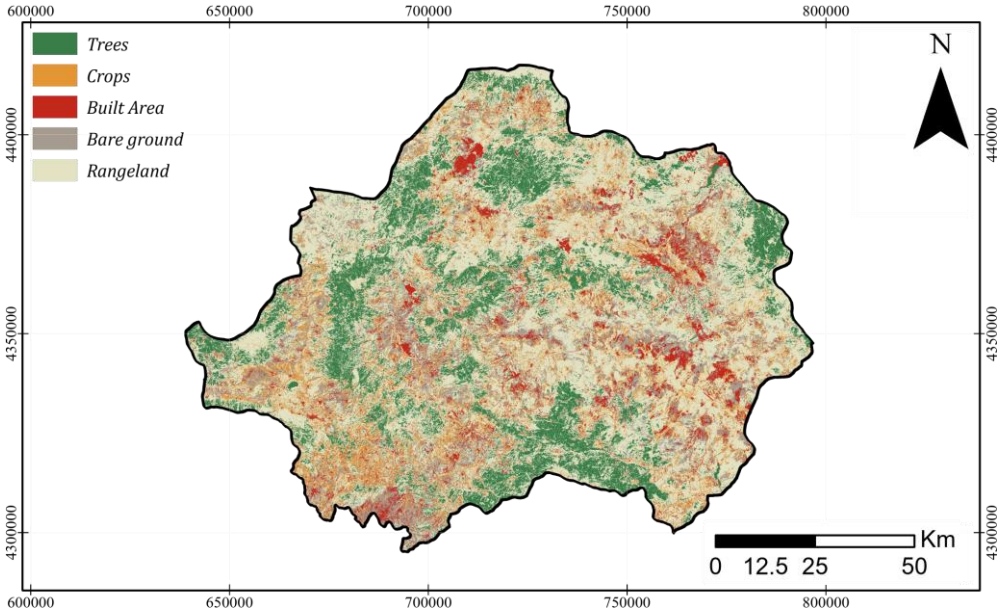

Figure 6. 2017 LULC map produced with unsupervised learning algorithms by using Landsat 8 satellite images.

In addition, the fact that these field classes cover very few surfaces in the study area is another reason. Although Landsat 8 images were resampled with a resolution of 10 meters in the pre-processing data stage, this process did not significantly improve the images' resolution. The other classes were successfully determined by unsupervised classification. Class details and the percentage of all individual classes are given in Table 4. Considering the LULC maps created for 2021 and 2017 using Landsat 8, the highest increase was seen in "Built Area" at %11.9 and "Bare Ground" at %3.2". The change in these classes are 1383.2 km2 and 376.0 km2, respectively. In addition to these, 13.9% and 2.3% decreases were calculated in "Rangeland" and "Crops" areas. The area classes and areas calculated on the LULC maps created for the years 2021 and 2017 using Sentinel-2 and Landsat 8 are given in Figure 7. "Cloud", "Flooded Vegetation", "Snow/Ice", and "Water" classes were ignored during the performance analysis of the unsupervised classifications as they cover a small area in the study area.

Table 3. 2021 and 2017 Sentinel-2 LULC maps classes.

Class	2017 (km^2)	Ratio (%)	2021 (km^2)	Ratio (%)
Bare Ground	74.2	0.6	62.3	0.5
Built Area	326.6	2.8	266.3	2.3
Crops	2005.7	17.2	1741.5	15
Flooded veg.	0.2	0	0.3	0

Rangeland	5027.5	43.2	5464	46.9
Snow/Ice	0.2	0	0.1	0
Trees	4171.2	35.8	4069	35
Water	33.8	0.3	35.8	0.3

Table 4. 2021 and 2017 Landsat 8 LULC maps classes.

Class	2021 (km^2)	Ratio (%)	2017 (km^2)	Ratio (%)
Bare Ground	2084.4	17.9	1708.4	14.7
Built Area	2078.0	17.9	694.8	6.0
Clouds	225.6	1.9	0.0	0.0
Crops	1106.8	9.5	1380.0	11.9
Flooded veg.	0.0	0.0	0.0	0.0
Rangeland	4123.9	35.4	5744.2	49.4
Snow/Ice	0.0	0.0	0.0	0.0
Trees	2019.6	17.4	2112.1	18.1
Water	0.0	0.0	0.0	0.0

5. DISCUSSIONS and CONCLUSIONS

It is shown that the unsupervised classification was insufficient to distinguish "Clouds", "Flooded Vegetation", "Snow/Ice" and "Water" classes. The main reason for this problem is that the resolution of Landsat 8 images is smaller than the size of the areas they cover in classes where unsupervised classification is inadequate. Therefore, "Bare Ground", "Built Area", "Crops", "Rangeland" and "Trees" classes were taken into account in evaluating the performance of unsupervised classification. A similar study on the subject indicated that the Sentinel-2 may have some misleading information in water extraction, while Landsat-8 could not accurately classify urban and agricultural areas [21]. However, it is also stated that the choice of hyperparameter directly affects the output in the analyses performed with the unsupervised algorithm [22]. Considering the data obtained from the LULC maps produced for the years 2017 and 2021 unsupervised classification was insufficient to differentiate the "Bare Ground", "Built Area", "Crops" and "Trees" areas (Table 4). It is seen that unsupervised classification error in LULC maps created using Landsat 8 images, especially in the "Bare Ground", "Built Area", "Crops" and "Trees" classes, more than 2 times compared to LULC maps created using Sentinel-2 images. However, the unsupervised classification successfully defined "Rangeland" class from Landsat 8 images. Considering these reasons put forward, it is evident that maximum attention should be paid to the creation of time-series LULC maps with unsupervised classification and the analysis of land cover/land use. The use of unsupervised classification on a local scale will be inefficient due to the low resolution of Landsat 8 images, and its use in production LULC maps for larger regions will be more beneficial. At the time that unsupervised classification is preferred during the creation of LULC maps at a local scale, it is recommended to verify with high-resolution images such as Sentinel-2 and to perform class-based controls to increase the quality of final outputs.

JSR A
Journal of Scientific Reports

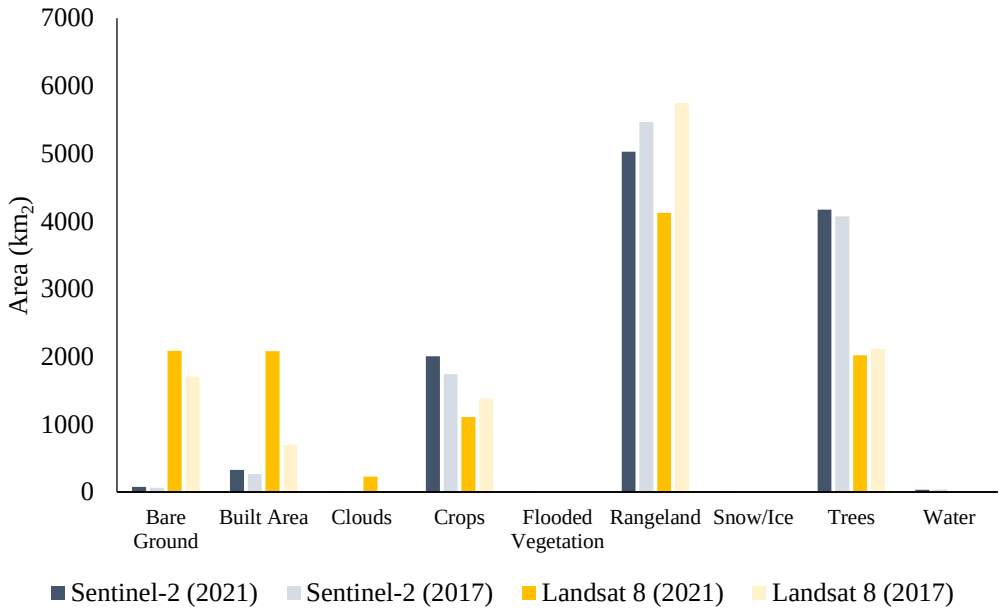

Figure 7. Distribution of Sentinel-2 and Landsat 8 based LULC maps classes.

Table 5. Distribution of cover area (km^2) Sentinel-2 and Landsat 8 based LULC maps classes.

Class	Sentinel-2 (2021)	Landsat 8 (2021)	Sentinel-2 (2017)	Landsat 8 (2017)
Bare Ground	74	2084	62	1708
Built Area	327	2078	266	695
Crops	2006	1107	1741	1380
Rangeland	5027	4124	5464	5744
Trees	4171	2020	4069	2112

This study conducted to assess the performance of unsupervised classification through high-resolution LULC maps prepared using Sentinel-2 during the production of LULC maps using Landsat 8 data. The following findings were obtained in this study;

i. Low-resolution (30 meters) LULC maps can be created by utilizing an unsupervised learning method using Landsat 8 data for large regional focus.

ii. The maximum iteration number were chosen as 50, 100 and 250 during unsupervised classification hyper-tuning processes. However, the obtained results do not reveal a significant difference when

compared with the recommended maximum number of iterations, 10-20. Therefore, the recommended values as the maximum number of iterations can be used to save computational time.
iii. The unsupervised classification algorithm was insufficient for the separation of *"Bare Ground"*, *"Built Area"*, *"Crops"* and *"Trees"* for LULC maps created by using Landsat 8 satellite.

iv. The unsupervised classification algorithm has successfully parsed fields belonging to the "Rangeland" class in both the 2017 and 2021 LULC maps.

v. It is expected that the use of supervised classification techniques to produce LULC maps by using Sentinel-2 images to compare their results with the unsupervised classification would be beneficial for future studies.

ACKNOWLEDGEMENT

The authors express their gratitude to the Kütahya Dumlupınar University for providing licensed access to ArcGIS Pro software developed by ESRI.

REFERENCES

[1] Townshend, J.R.G., (1992), Improved global data for land applications. A proposal for a new high resolution data set. Report of the Land Cover Working Group of IGBP-DIS, Global Change Report (Sweden).

[2] Duku, E., Mattah, P.A.D., and Angnuureng D.B., (2021), Assessment of land use/land cover change and morphometric parameters in the keta lagoon complex ramsar site, ghana, Water (Switzerland). 13 2537.

[3] Ekumah B., Armah, F.A., Afrifa, E.K.A., Aheto, D.W., Odoi, J.O. and Afitiri,A., (2020) Assessing land use and land cover change in coastal urban wetlands of international importance in Ghana using Intensity Analysis, Wetl Ecol Manag. 28, 271-284.

[4] Ma, Z., Liu, Z., Zhao, Y., Zhang, L., Liu, D., Ren, T., Zhang, X., and Shaoming, Li,(2020), An unsupervised crop classification method based on principal components isometric binning, ISPRS Int J Geoinf. 9(11, 648).

[5] Karra, K., Kontgis, C., Statman-Weil, Z., Mazzariello, J.C., Mathis, M., Brumby, S.P., (2021), Global land use / land cover with Sentinel 2 and deep learning, in: 2021 IEEE International Geoscience and Remote Sensing Symposium IGARSS, 4704–4707.

[6] Zanaga, D., van de Kerchove, R., de Keersmaecker, W., Souverijns, N., Brockmann, C., Quast, R., Wevers, J., Grosu, A., Paccini, A., Vergnaud, S., Cartus, O., Santoro, M., Fritz, S., Georgieva, I., Lesiv, M., Carter, S., Herold, M., Li, L., Tsendbazar, N.E., Ramoino, F., Arino, O., (2021), ESA World Cover 10 m 2020 v100.

[7] Enderle, D.I.M., Weih R.C. (2005), Integrating Supervised and Unsupervised Classification Methods to Develop a More Accurate Land Cover Classification, J Ark Acad Sci. 59, 10.

[8] Olofsson, P., Foody, G.M., Herold, M., Stehman, S.V., Woodcock, C.E., Wulder, M.A., (2014), Good practices for estimating area and assessing accuracy of land change, Remote Sens Environ. 148, 42–57.

[9] Khan, A., Hansen, M.C., Potapov, P., Adusei, B., Stehman, S.V., Steininger, M.K., (2021), An operational automated mapping algorithm for in-season estimation of wheat area for Punjab, Pakistan, 42, 3833–3849.

[10] Pickens, A.H., Hansen, M.C., Hancher, M., Stehman, S.V., Tyukavina, A., Potapov, P., Marroquin, B., Sherani, Z., (2020), Mapping and sampling to characterize global inland water dynamics from 1999 to 2018 with full Landsat time-series, Remote Sens Environ. 243, 111792.

[11] Ying, Q., Hansen, M.C., Potapov, P.V., Tyukavina, A., Wang, L., Stehman, S.V., Moore, R., Hancher, M., (2021), Global bare ground gain from 2000 to 2012 using Landsat imagery, Remote Sens Environ. 194, 161–176.

[12] Potapov, P., Li, X., Hernandez-Serna, A., Tyukavina, A., Hansen, M.C., Kommareddy, A., Pickens, A., Turubanova, S., Tang, H., Silva, C.E., Armston, J., Dubayah, R., Blair, J.B., Hofton, M., (2021), Mapping global forest canopy height through integration of GEDI and Landsat data, Remote Sens Environ. 253, 112165.

[13] Hansen, M.C., Potapov, P.V., Moore, R., Hancher, M., Turubanova, S.A., Tyukavina, A., Thau, D., Stehman, S.V., Goetz, S.J., Loveland, T.R., Kommareddy, A., Egorov, A.V., Chini, L., Justice, C.O., Townshend, J.R.G., (2013), High-resolution global maps of 21st-century forest cover change, Science. 342 (6160), 850-853.

[14] Zengin, E., A Combined Assessment of Sea Level Rise (SLR) Effect on Antalya Gulf (Türkiye) and Future Predictions on Land Loss, (2023), Journal of the Indian Society of Remote Sensing.

[15] Paris, C., Bruzzone, L., Fernandez-Prieto, D., (2019), A Novel Approach to the Unsupervised Update of Land-Cover Maps by Classification of Time Series of Multispectral Images, IEEE Transactions on Geoscience and Remote Sensing. 57, 4259–4277.

[16] Lemenkova, P., (2021), ISO Cluster classifier by ArcGIS for unsupervised classification of the Landsat TM image of Reykjavík, Bulletin of Natural Sciences Research. 11 29–37.

[17] U.S. Geological Survey 2018 Landsat collections: U.S. Geological Survey Fact Sheet, (2018), 3049.

[18] Lemenkova, P., (2021), ISO Cluster Classifier by ArcGIS for Unsupervised Classification of the Landsat TM Image of Reykjavik Iso Cluster Classifier By Arcgis For Unsupervised

Classification Of The Landsat Tm Image Of Reykjavík, Bulletin of Natural Sciences Research, 11, 29–37.

[19] Altman, N.S., (1992), An introduction to kernel and nearest-neighbor nonparametric regression, American Statistician. 46 175–185.

[20] Abburu, S., Babu Golla, S., (2015), Satellite Image Classification Methods and Techniques: A Review, Int J Comput Appl. 119 20–25.

[21] Ahady, A.B., Kaplan, G., (2022), International Journal of Engineering and Geosciences Classification comparison of Landsat-8 and Sentinel-2 data in Google Earth Engine, study case of the city of Kabul, International Journal of Engineering and Geosciences. 7, 24–31.

[22] Ghayour, L., Neshat, A., Paryani, S., Shahabi, H., Shirzadi, A., Chen, W., Al-Ansari, N., Geertsema, M., Amiri, M.P., Gholamnia, M., Dou, J., Ahmad, A., (2021), Performance evaluation of sentinel-2 and landsat 8 OLI data for land cover/use classification using a comparison between machine learning algorithms, Remote Sens (Basel), 13, 1349.

Kütahya Dumlupınar University
Institute of Graduate Studies

Journal of Scientific
Reports-A
E-ISSN: 2687-6167
Number 53, June 2023

RESEARCH ARTICLE

A NEW FORCE MEASUREMENT MECHANISM IN WIND TUNNEL: CFD AND EXPERIMENTAL VALIDATION ON A CYLINDER

Seda KIRMACI ARABACI[1*], Emre KİRAZ[2]

[1] Manisa Celal Bayar University, Mechanical Engineering Department, Manisa, seda.kirmaci@cbu.edu.tr, ORCID: 0000-0001-8903-5952
[2] Manisa Celal Bayar University, Mechanical Engineering Department, Manisa, emre.kiraaz@gmail.com, ORCID: 0000-0003-1524-2865

Receive Date:08.02.2023 *Accepted Date: 06.03.2023*

ABSTRACT

Wind tunnel tests are experiments carried out in private and state-supported institutions, which are of great importance for studies in aerodynamics. Wind tunnels are essential in the defense industry, the automotive industry, and even the construction industry. In this study, a force sensor holder (FSH), in the open subsonic wind tunnel test room is designed, and it is made to measure angled structures, angled prototypes, and especially for wings. The critical angles of wings and the angles of attack are necessary, especially regarding aerodynamic performance. This force sensor holder can be adjusted at 0-90 degree angles and used experimentally. After holder manufacturing, experiments and CFD analysis are carried out at a 0 degree angle on the cylinder body. This study conducts a Computational Fluid Dynamics (CFD) analysis using Realizable k-ε, and SST k-ω turbulence models. In this study, the accuracy of the CFD analysis of the drag coefficient on a cylinder is evaluated through a comparison with both experimental and literature data. The results revealed that the CFD analysis has a deviation of 5,11% (using the Realizable k-ε model) and 5,22% (using the SST k- ω model) from the literature data. On the other hand, the experimental results show a discrepancy of 3,77% compared to the literature data. These findings demonstrate the effectiveness of the CFD analysis in predicting drag coefficients and highlight the importance of validating such simulations with experimental data.

Keywords: *Wind tunnel, Force sensor holder, Drag coefficient, Angle of attacks.*

1. INTRODUCTION

Aerodynamic forces can be calculated with wind tunnels used in academic and sectoral studies. The Aerodynamic forces that depend on speed and exterior body design can be calculated in computational fluid analysis programs and wind tunnels in inland vehicles. By examining the aerodynamic properties of aircraft such as airplanes, unmanned aerial vehicles, helicopters, balloons, parachutes, and land vehicles such as cars, trucks, buses, and motorcycles, fuel savings, and forces can be examined. In buildings such as high buildings, towers, and bridges, the wind tunnel's airflow effects, the strengths

of the storm, and their results can be investigated. In addition, wind turbine blades, jet blades, and speedboat forces can be calculated in wind tunnels. Ariyani et al. designed a model holder system in an open subsonic wind tunnel, and this holder is aimed to be dynamic, with three angular motions containing target seeking and wobbling [1]. Behavior tests of external objects can be performed more reliably as the aircraft model must be simulated based on the force and angular measurement between the external object [2]. A wind tunnel's force sensor and sensor holding are crucial measurement tools [3]. A balance rig is an instrument that measures the needed moment and forces of the prototype in the wind tunnel. Balance is divided into two; external and internal [4]. Computational Fluid Dynamics (CFD) is used as a verification method in wind tunnel applications. It is influential in creating suitable parameters for wind tunnels in CFD [5]. Gebel et al. conducted on the vehicles, and it was found that the datas in the wind tunnel and CFD were close and consistent between 0,75% and 7,40% [6]. Five different turbulence models are studied to find the most suitable model [7].

The force balance provided by internal and external balancing systems and load balancing systems made with complex and expensive components makes wind tunnel force measurement expensive and complicated. In addition, due to the non-standardization of materials, in case of any deformation, all production processes, from design to analysis, from production to quality control, require the production of parts by repeating, creating great difficulties in terms of time, operation, and finance. In addition, no force measurement mechanism in the domestic/foreign market can take measurements at different angles of attack/different angles while the prototype is positioned in a fixed position.

Experiments with force measurement mechanisms of wind tunnels will be more straightforward and give reliable results with this force sensor holder (FSH). This mechanism, which is durable and does not require constant adjustment, will be preferred over competitors. This invention's use of the wind tunnel will be made easier and more accessible with all these advantages provided. The invention aims to present a force measurement mechanism in which force measurement can be achieved by holding the test prototype at different angles to the airflow and the floor of the test chamber. The acceptability of the results are confirmed with experimental and CFD analyses on a cylinder body with L(length)/D(diameter)=2 (the literature supports) at 0 degrees. The aim of this study is to design a holder for a force sensor that can measure drag force at various angles for use in wind tunnels. Using this holder, a study was conducted on a cylinder at a 0-degree angle to measure drag force at different angles.

2. MATERIALS AND METHODS

In this part, a new Force Sensor Holder used in the wind tunnel mechanism is investigated. This force sensor holder can be adjusted at 0-90 degrees angles and used experimentally.

2.1. The Mechanism of FSH

The force sensor holder mechanism is adapted for the Wind Tunnel test room of Manisa Celal Bayar University, and this mechanism has been made available for all wind tunnels. Instead of preparing a separate experimental setup for each prototype, the mechanism is designed to apply to all prototypes. The primary condition for obtaining efficient and accurate data in wind tunnel tests is to develop the experimental setup so that it is not affected by the forces of the mechanism or other external factors.

The designed force sensor holder can measure the holding force without loss. It is to enable the experiments of prototypes at all desired angles and positions in the investigations of the Defense Industry, Automotive Industry, Civil Aviation, and Wind Energy and to provide the opportunity to find the desired aerodynamic forces. Moreover, this design is aimed to reduce costs compared to mechanisms that take measurements with other holders. A restrained force measurement mechanism that can move at different angles, which is the subject of the invention, is the essential component of the wind tunnel in terms of the accuracy and reliability of the data to be obtained from the wind tunnel. It moves at different angles, especially unmanned aerial vehicle wing structures. It is a great privilege to be used in models where the angle of attack is essential. As a result of the wind tunnel experiment calculations, the drag (C_D) and the lift (C_L) coefficients can be calculated. Defining the values of aerodynamic performance (C_L / C_D) at different angles will provide a tremendous advantage for experimental calculations.

Moreover, the fact that it can be done at a low cost will enable much better than other holders. The C_L/C_D values obtained by experimental studies with this holder will be able to analyze the changes with the angle of attack and free flow velocity. The FSH is located in the center of the Wind Tunnel test chamber and positioned to be mounted from the prototype's center of gravity.

It has been designed by mounting on the prototype to avoid creating any rolling moment, pitching moment, or yaw moment that will occur, especially in the axis. By opening two channels on the prototype, the assembly process will be ensured and connected to all kinds of prototypes with the help of bolts through these channels. The invention is a force measurement mechanism for holding the test component inside the wind tunnel for aerodynamic tests by exposing it to airflow in a wind tunnel where airflow is provided. The holder (Figure 1), which provides the fixation of the test piece, can ensure that the two extensions are connected from a support point and that the test component is held at different angles according to the airflow. Moreover, it has freedom of rotation about the support point. (Figure 1(a)-number 2 and detail figure in Figure 1(b)). It includes at least one fixing element to ensure the extensions are fixed after adjusting the angle between them. In addition, this mechanism consists of a sensor to measure force. (Figure 1(a)-number 4). A force measuring mechanism includes a sensor holder with a sensor slot for holding the sensor and connecting it to the test part. Moreover, a cable channel is configured so the cable providing power transmission to the sensor can be positioned. (Figure 1(a)-number 3). The sensor holder; includes a cable channel cover (Figure 1(a)-number 5) that enables the sensor slot to form an isolated volume from the external environment. The others parts in Figure 1(a) are the bolts and the screw pins.

JSR A
Journal of Scientific Reports

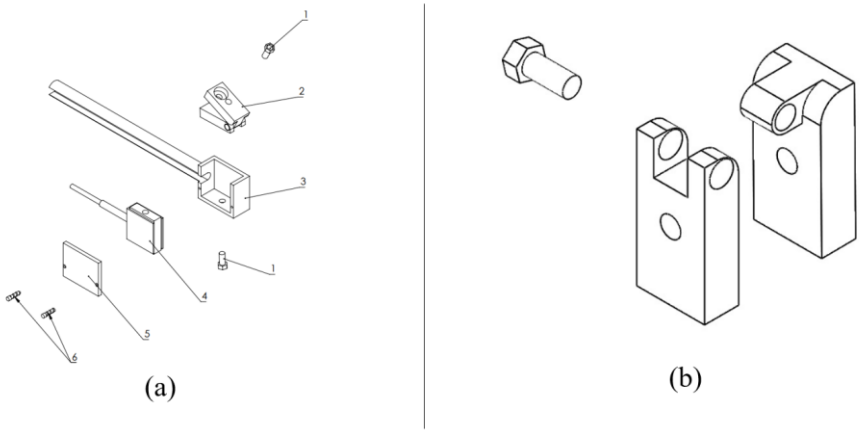

Figure 1. The force sensor holder (a) the Mechanism of FSH (b) number 2 detail of FSH in 'Figure 1.a'.

Depending on the direction, the prototype can yield results for both vertical and horizontal forces when the force sensor is mounted onto the mechanism. Force measurement mechanisms created with complex balancing systems are expensive and difficult to use. The first condition to get correct results in a wind tunnel is to neutralize internal and external loads. While testing the aerodynamic forces of the test prototype, it is of great importance that the test system does not affect these loads and that the weights of the prototype and the test mechanisms are balanced. The wind tunnel's work area needs three degrees of kinematic rotational motion. The planned angular motion is 00-900 for the pitch link. The yaw, pitch, and roll rotations are shown in Figure 2. In the study, the angle of pitch rotation is designed for wings.

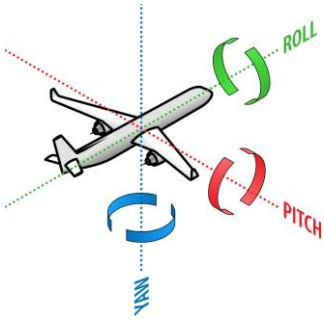

Figure 2. Yaw, pitch, and roll rotations of a plane.

In this study, a holder that can change the pitch rotation angle and take a smooth and accurate measurement in the x-axis direction is designed. It is planned that the place of use will be mainly the wings.

JSR A
Journal of Scientific Reports

2.2. Calculating Drag and Lift

The effect that the force applied to an object in a fluid will create in the opposite direction is called the drag force. The drag coefficient, the essential property among the parameters in the drag force, is a dimensionless number displayed as C_D (Eq. 1). ρ; is the density of the fluid, V; is the velocity of the fluid, and A; is the cross-sectional area perpendicular to flow.

$$C_D = \frac{F_d}{0.5\rho AV^2} \tag{1}$$

The value of the sensor on the axis of the wind speed vector in the experiment set will give the drag force. The measurement taken on the vertical axis will provide the lift force. Lift, for an airfoil, results from the surface forces generated by the fluid across the wing. When air flows around a wing at a specific velocity, a lower pressure is detected on the upper surface of the wing than on its lower surface.

The lift force is obtained if the pressure on the bottom surface is high. The lift force is denoted as F_L. The lift coefficient is one of the most critical parameters in the lift force. The lift coefficient is also dimensionless and defined as C_L (Eq. 2).

$$C_L = \frac{F_l}{0.5\rho AV^2} \tag{2}$$

The angle of attack is the angle between the relative motion vectors between the fluid and the reference line on the body. The angle of attack affects the lift coefficient of the airplane. The plane is observed at critical angles in a stalled state. The plane's stall depends on the air speed, the plane's weight, and the plane's center of gravity. Critical angles of attack are 15-18 degrees on most wings [8]. The newly invented force sensor holder will enable measurements to be taken up to 90 degrees. (Figure 1).

3. CFD METHOLOGY

Fluent software is used for the CFD solution and the boundary conditions used in the experiment are adapted to the CFD.

3.1. Governing Equations

The Navier-Stokes is utilized to model the flow of fluids. These equations include momentum equations and continuity, which are necessary for describing the movement of fluids. The three-dimensional, compressible, unsteady flow is represented by Eq. (3) and (4) derived from the Navier-Stokes equations. The continuity equation is written as follows:

$$\frac{\partial \rho}{\partial t} + \vec{\nabla}(\rho\vec{V}) = 0 \tag{3}$$

The Navier-Stokes equations is written as in x direction:

JSR A
Journal of Scientific Reports

$$\frac{\partial(\rho u)}{\partial t} + \nabla(\rho u V) = -\frac{\partial \rho}{\partial x} + \frac{\partial \tau_{xx}}{\partial x} + \frac{\partial \tau_{yy}}{\partial y} + \frac{\partial \tau_{zz}}{\partial z} + \rho f_x \quad (4)$$

3.2. Turbulence Model

3.2.1. SST k-ω turbulence model:

The shear stress transport (SST) k-ω turbulence model is a two-equation that combines the Standard k-ω model and the Standard k-ω model [9]. The model is well-suited for simulating complex turbulent flow fields that involve separation. However, achieving convergence in the analysis can be challenging and a proper mesh resolution near the wall is necessary, which can result in increased computational effort and power consumption. The SST k-ω turbulence model is calculated by (5) and (6) Eq.

$$\frac{\partial(\rho k)}{\partial t} + \frac{\partial(\rho u_j k)}{\partial x_j} = \tau_{ij}\frac{\partial U_i}{\partial x_j} - \beta^* \rho \omega k + \frac{\partial}{\partial x_j}\left[(\mu + \sigma_k \mu_t)\frac{\partial k}{\partial x_j}\right] \quad (5)$$

$$\frac{\partial(\rho \omega)}{\partial t} + \frac{\partial(\rho u_j \omega)}{\partial x_j} = \frac{\gamma}{v_t}\tau_{ij}\frac{\partial U_i}{\partial x_j} - \beta \rho \omega^2 + \frac{\partial}{\partial x_j}\left[(\mu + \sigma_k \mu_t)\frac{\partial \omega}{\partial x_j}\right] + 2(1 - \tanh(arg_1{}^4))\frac{\rho \sigma \omega_2}{\omega}\frac{\partial k}{\partial x_i}\frac{\partial \omega}{\partial x_j} \quad (6)$$

3.2.2. Realizable k-ε turbulence model:

The Realizable k-ε model is known for its performance in simulating boundary layers with rotation, adverse pressure gradients and recirculation. Additionally, it can accurately capture the flow of complex structures. The turbulence model is represented by Eq. (7) and (8) [10,11].

$$\frac{\partial(\rho k)}{\partial t} + \frac{\partial(\rho u_j k)}{\partial x_i} = \frac{\partial}{\partial x_j}\left[\left(\mu + \frac{\mu_t}{\sigma_k}\right)\frac{\partial k}{\partial x_j}\right] + P_k + P_b - \rho \varepsilon - Y_M + S_k \quad (7)$$

$$\frac{\partial(\rho \varepsilon)}{\partial t} + \frac{\partial(\rho u_j \varepsilon)}{\partial x_j} = \frac{\partial}{\partial x_j}\left[\left(\mu + \frac{\mu_t}{\sigma_\varepsilon}\right)\frac{\partial \varepsilon}{\partial x_j}\right] + \rho C_1 S_\varepsilon - \rho C_2 \frac{\varepsilon^2}{k + \sqrt{\vartheta \varepsilon}} + C_{1\varepsilon}\frac{\varepsilon}{k}C_{3\varepsilon}P_b + S_\varepsilon \quad (8)$$

P_k is the turbulence kinetic energy generation, P_b is the turbulence kinetic energy generation.

3.3. CFD Analysis

A cylinder body is designed with an aspect ratio of L/D=2 using NX. A rectangular control volume is created with a length ten times that of the body and a total height four times the body height. The mesh is generated four times starting from 82000 up to 330000. During the investigation of the drag coefficient, it was observed that the range at which the drag coefficient begins to remain constant starts from 300000 when examining the mesh values. Figure 3 shows the tetrahedral mesh.

JSR A
Journal of Scientific Reports

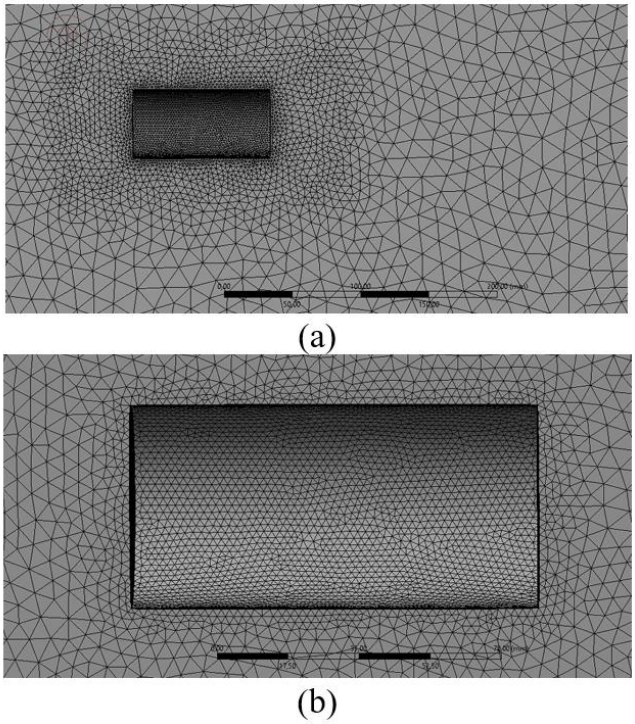

Figure 3. Tetrahedral Mesh of cylinder body a) around the body b) near the body wall.

The CFD solution is computed using Fluent software, with the solution method being chosen as second order upwind for the flow. The flow field is solved as a steady-state condition. The wall function is defined as enhancement wall treatment Realizable k-ε turbulences model. And the other turbulence model is selected SST k-ω model. First layer thickness also wall distance y is calculated as 1.8e-5 m when y^+=1; and Reynolds number of cylinder body is calculated as 1.3e+6.

4. EXPERIMENTAL METHODS

The wind tunnel test room at Manisa Celal Bayar University has a mechanism for measuring force. The dimensions of the test room are 1000 mm in length and 300 x 300 mm^2 in section. The wind tunnel (Figure 4) has a maximum flow velocity of 70 m/s and a distance of approximately 6400 mm. The weight of the wind tunnel is 400 kg, and it has a contraction ratio of 11.1 [12].

Figure 4. Manisa Celal Bayar University wind tunnel.

The cylinder's drag coefficient and drag force are calculated as in Figure 5 with the new force sensor holder for 0^0 at pitch rotation; this drag value is verified in the literature.

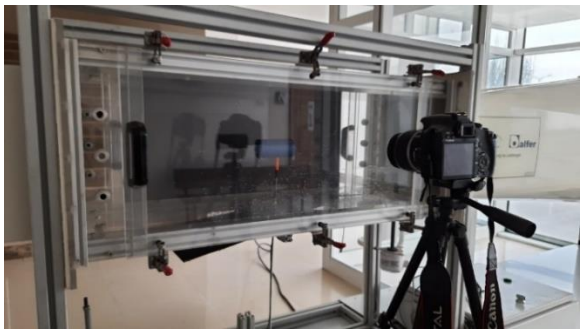

Figure 5. A cylinder body prototype (L/D=2).

5. RESULTS

This study presents a newly developed force sensor holder that is capable of moving at various angles, suitable for use in wind tunnel experiments. The cylinder body is tested using this newly developed force holder, and CFD analyses are conducted and compared with existing literature. The drag coefficient values obtained from the CFD solutions and experimental results are presented in Table 1 for each turbulence model. The differences between the results from the literature data and the experimental and CFD results are analyzed at a Reynolds Number of 94595. This paper calculates the drag coefficients at a speed of 28 m/s for both experimental and CFD results.

JSR A
Journal of Scientific Reports

Table 1. The results of drag coefficient for cylinder as L/D=2.

Results	**Drag coefficient** (C_d)	**Different (%)**
Experimental result	0,866	3,77%
k- ε Realizable (CFD)	0,854	5,11%
k-ω SST (CFD)	0,853	5,22 %
Çengel&Cimbala (2010) [9]	0,90	-

In the wind tunnel, the drag force is measured in the x direction at 0 degrees on the cylinder body. To validate the results, data from Çengel&Cimbala is taken into account. The drag coefficient values of the cylinder are determined when the drag force is calculated in the wind tunnel, and these values are attempted to be verified. The wind tunnel experimental results and literature results are presented in Table 1. The drag coefficient value of the cylinder is found to be 0,866 in the wind tunnel experiment, while it is 0,90 in the literature [13], 0,854 in the CFD analysis for the k-ε Realizable turbulence model, and 0,853 in the CFD analysis for the k-ω SST turbulence model.

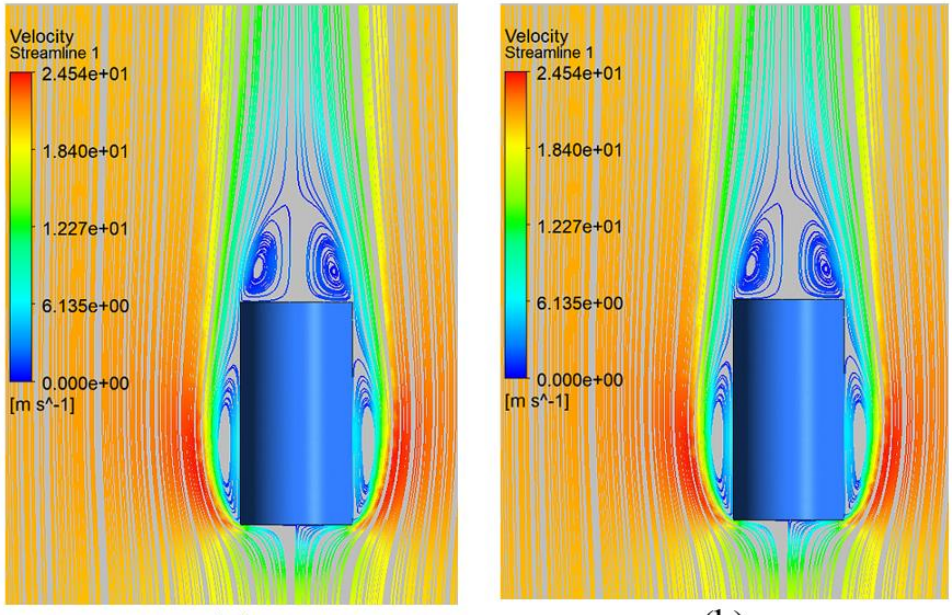

Figure 6. Velocity streamline on the cylinder body a) the realizable k- ε b) SST k-ω models.

Velocity streamlines are displayed in the rear of the cylinder model in Figure 6. It can be seen that a vortex forms in this area for both the Realizable k-ε and SST k-ω turbulence models.

JSR A
Journal of Scientific Reports

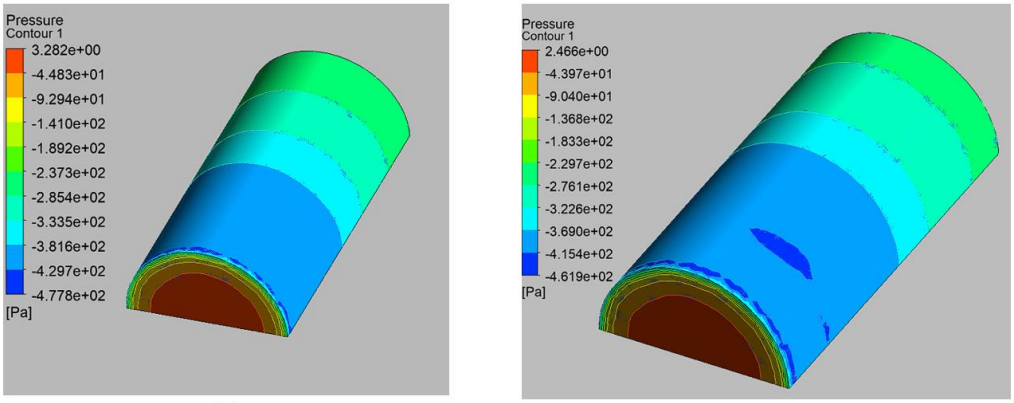

(a) (b)

Figure 7. Pressure contour of the cylinder body a) the realizable k- ε b) SST k-ω models.

Figure 7 presents the pressure contour of the cylinder body, which clearly shows a significant pressure difference between the front and rear regions for both turbulence models. The airflow behavior around a cylinder has been studied and observed to exhibit compression at the front of the cylinder, leading to a considerable increase in frontal pressure, as shown in Figure 7. The airflow moves smoothly along the body of the cylinder until it reaches the rear end, where it converges from various directions (top, bottom, and sides), creating a small vortex or flow recirculation at the rear end of the body. Due to the pressure difference, a considerable fraction of the overall drag force is experienced by the body.

The results of the study indicate that there is a deviation of 5,11% between the CFD analysis using the Realizable k-ε model and the literature data, and a deviation of 5,22% for the SST k-ω model, whereas the experimental results have a discrepancy of 3,77% when compared to the literature data. These results were calculated at a Reynolds number of 94595.

6. DISCUSSION AND CONCLUSION

This article presents the design and application of a new force sensor holder (FSH) for use in wind tunnel experiments. The FSH is designed to be frictionless, lossless, and innovative, allowing for stable and accurate measurements without being affected by moment forces. Its versatility and adaptability enable it to be mounted on various prototypes, measuring force at different angles.

An experimental study is conducted on a cylinder body (for L/D=2) at a 0 degree angle using the FSH. The results of the study matched the theoretical data, indicating that the FSH provided reliable data. The study is also compared with CFD analyses.

The findings indicated that the deviation of drag coefficient between the CFD analysis and literature data is 5,11% for the Realizable k-ε model and 5,22% for the SST k-ω model, while the experimental result has a discrepancy of 3,77% compared to the Çengel & Cimbala [13]. The differences between

the results in the literature data and the experimental and CFD results are given at 94595 Reynolds Number. The drag coefficients are calculated at 28 m/s in experimental and CFD results.

The FSH is intended for use mainly on wings in future studies, and it is planned to study wings from different angles. Overall, this new force sensor holder shows promise for providing accurate and reliable data in wind tunnel testing. Its frictionless and lossless design offers significant advantages over previous technologies, enabling accurate measurements of forces at different angles.

ACKNOWLEDGEMENT

The support of Manisa Celal Bayar University is highly appreciated. Funding Information: Manisa Celal Bayar University under project numbers BAP 2013-037.

REFERENCES

[1] Ariyani, N. R. and Nugroho, L., (2019). Conceptual design methodology of a 3-DOF Dynamic model holder system for open subsonic wind tunnel. IEEE International Conference on Aerospace Electronics and Remote Sensing Technology, ICARES, 1-7.

[2] Ulusal, N., (2005). Conceptual design of a model support system and its controller for Ankara wind tunnel, phD Thesis, Mechanical Engineering. Middle East Technical University, Ankara, Turkey, 1-119.

[3] Ahangar, M.R.H., Kangavari, M.R., and Vahedi, K. (2011). Reliability model of a wind tunnel balance system, Turkısh Journal of Engıneerıng and Envıronmental Scıences, 35, 21 – 30.

[4] Ahangar, M.R.H., Kangavari, M.R. and Berangi, R. (2006). Investigation of error sources on the balance and the standard dynamic model in the wind tunnel, ICAS Conference, Hamburg, Germany,1-9.

[5] Gonzalez, M., Ezquerro, J. M., Lapuerta, V., Laverón, A., and Rodríguez, J. (2011). Components of a wind tunnel balance: Design and calibration. Wind Tunnels and Experimental Fluid Dynamics Research, 1-20.

[6] Gebel, M. E., Önaldi, S., Korkmaz, S., Osmanoğlu, S., Özçelik, B., Ermurat, M. and İmal, M. (2018). Bir elektrikli aracin aerodinamik özelliklerinin deneysel ve sayisal olarak incelenmesi, 9th International Automotive Technologies Congress, Otekon, Bursa, Turkey, 850-858.

[7] Şumnu, A. (2021). Shape modification of Ahmed body to reduce drag coefficient and determination of turbulence model. Niğde Ömer Halisdemir University Journal of Engineering Sciences, 10(2), 824-832.

[8] https://fly8ma.com/topic/angle-of-attack-2/ (accessed date: 11.12.2022)

[9] Menter, F. R. (1994). Two-Equation Eddy-Viscosity Turbulence Models for Engineering Applications., AIAA journal., 32, 1598-1605.

[10] Wilcox, D.C. (1998). Turbulence modeling for CFD., La Canada, 2, 103-217.

[11] Fluent. (2009). ANSYS Fluent 12.0. Theory Guide. ANSYS Inc., Canonsburg, PA.

[12] Kırmacı Arabacı, S. and Pakdemirli, M., (2016). Improvement of aerodynamic design of vehicles with inspiration from creatures, PhD Thesis, Manisa Celal Bayar University, Manisa, 135s.

[13] Cengel, Y. and Cimbala, J., (2010). Fundamentals and Applications, McGraw-Hill (2nd Edition), 1006s.

Kütahya Dumlupınar University
Institute of Graduate Studies

Journal of Scientific
Reports-A
E-ISSN: 2687-6167
Number 53, June 2023

RESEARCH ARTICLE

ITERATION SCHEME FOR APPROXIMATING FIXED POINTS OF G −NONEXPANSIVE MAPS ON BANACH SPACES VIA A DIGRAPH

Esra YOLAÇAN[1,*]

[1] Cappadocia University, School of Applied Sciences, Department of Airframe and Powerplant Maintenence, Mustafapasa Campus, Ürgüp, Nevşehir yolacanesra@gmail.com , ORCID: 0000-0002-1655-0993

Receive Date:30.01.2023 *Accepted Date: 23.03.2023*

ABSTRACT

In this writing, an influential modified multistep iterative process for finding a common fixed point of G −nonexpansive maps is presented. Some convergence theorems are constructed by *Property P* for the recommended schema on Banach spaces by which digraph. Two numerical examples are given to illustrate the convergence behavior and the validity of the process. The achieved conclusions enlarge, generalise and complement some well-known fixed point results from the literature.

Keywords: *Digraph,G −nonexpansiveness, Property P, Fixed Point*

1. INTRODUCTION and PRELIMINARIES

Khan et al. [1] expressed the nouvelle iterative schema contains the modified Mann and Ishikawa, Noor iteration algorithm for a finite family. Yıldırım and Ozdemir [2] considered multi-step iteration schema for a finite family of non-self asymptotically nonexpansive maps on a uniformly convex Banach space (shortly, UCBS). Kettapun et al. [3] inspired and motivated by [1], and thus they acquainted a novel iteration technic for solving a common fixed point. Gürsoy et al. [18] modified a multistep iterative procees presented by [2]. They also testified several convergence results of this iterative procees and S −iteration for contractive-like operators. Ahmad et al. [31] presented some convergence results on Picard-Krasnoselskii hybrid iterative process in CAT(0) spaces. More recently, El Kouch and Mouline [32] studied convergence of Mann and Ishikawa iterative processes for some contractions in convex generalized metric space.

Jachymski [4] established the conception of G −contraction, and unified two notions of graph and fixed point theories. Since then, varied authors have widely probed fixed point theorems in metric space, Banach and Hilbert via graph (see [6], [19-25]). Aleomraninejad et al. [5] achieved several iterative method consequences for G −nonexpansiveness and G −contractive maps on graphs. Tripak [7] studied two-step iteration method to approach common fixed point of G −nonexpansiveness. Suparatulatorn et al. [8] evidenced some convergence theorems for the modified S −iterative method

JSR A
Journal of Scientific Reports

of G −nonexpansiveness in UCBS with a directed graph. Subsequently Hunde et al. [9] studied an explicit iterative algorithm for various common fixed point of a family of G −nonexpansiveness, further gave some convergence results without supposing the Opial's condition. Recently, Sridarat et al. [12] considered SP −iterative schema for common fixed point of G −nonexpansiveness. They further parallel the rate of convergence between Noor and SP −iteration.
Motivated by [3], [8] and [9], we present a novel iteration technic for solving a common fixed point of a finite family of G −nonexpansiveness as noted below:
For $x_0 \in C$ and $k \geq 2$, let the sequence $\{x_n\}$ identified as

$$\begin{aligned} x_{n+1} &= (1-\mu_n^k)y_n^{k-1} + \mu_n^k g_k y_n^{k-1}, \\ y_n^{k-1} &= (1-\mu_n^{k-1})y_n^{k-2} + \mu_n^{k-1} g_{k-1} y_n^{k-2}, \\ y_n^{k-2} &= (1-\mu_n^{k-2})y_n^{k-3} + \mu_n^{k-2} g_{k-2} y_n^{k-3}, \\ &\vdots \\ y_n^2 &= (1-\mu_n^2)y_n^1 + \mu_n^2 g_2 y_n^1, \\ y_n^1 &= (1-\mu_n^1)x_n + \mu_n^1 g_1 x_n, \end{aligned} \tag{1}$$

where for $n \geq 1$ and $i = \overline{1,k}$, $x_n = y_n^0$, $\{\mu_n^i\} \in [0,1]$.

Goal of the present writing is to attain some convergence deductions for the iteration algorithms Eq. 1 of a finite family of G −nonexpansiveness on UCBS through a digraph.

Next, we present some lemmas, definitions and remark which are favourable to the main results in the manuscript.

Let $G = (V(G), E(G))$ be digraph, where $V(G)$ is the set of vertices of graph, $E(G)$ is the set of its edges which covers versal loops, i.e. $(x,x) \in E(G)$ for $\forall x \in V(G)$. G is mentioned to be transitive if, $x, y, z \in V(G)$; $(x,y), (y,z) \in E(G) \Longrightarrow (x,z) \in E(G)$.

Fixed point set of g is indicated by $g_{fix} = \{x \in C : gx = x\}$. If $g_{fix} \neq \emptyset$, then g is said

(I) G −nonexpansive [6] if it provides (i) $(x,y) \in E(G) \Rightarrow (gx, gy) \in E(G)$ (g preserves edges of G), (ii) $(x,y) \in E(G) \Rightarrow \|gx - gy\| \leq \|x - y\|$;
(II) G −continuous [4] if for any given $\omega \in X, \{\omega_n\} \subseteq X$, $\omega_n \longrightarrow \omega$ and $(\omega_n, \omega_{n+1}) \in E(G)$ imply $g\omega_n \to g\omega$;
(III) $semicompact$ [17] if for $\{x_n\} \subseteq C$ with $\|x_n - gx_n\| \to 0$ as $n \to \infty$, there exists a subsequence $\{x_{n_i}\}$ of $\{x_n\}$ such that $x_{n_i} \to s_* \in C$.

Let $X \supseteq C \neq \emptyset$, $\{g_i\}_{i=1}^k : C \to C$ supply $Condition\ (A'')$ [3] if there is a nondecreasing function $f : [0,\infty) \to [0,\infty)$ with $f(t) > 0$ for $\forall t \in (0,\infty)$, $f(0) = 0$ such that $\|x - g_l x\| \geq f\left(d\left(x, g_{fix}\right)\right)$ for $\forall x \in C$ and $1 \leq l \leq k$, here $d\left(x, g_{fix}\right) = inf\{\|x - s_*\| : s_* \in g_{fix} := \cap_{i=1}^k g_{fix}(g_i) \neq \emptyset\}$.

JSR A
Journal of Scientific Reports

Definition 1. [8] Let $x_0 \in V(G)$ and $V(G) \supseteq \Theta$. We call that (i) Θ is dominated by x_0 if $(x_0, x) \in E(G)$ for $\forall x \in \Theta$, (ii) Θ dominates x_0 if for each $x \in \Theta$, $(x_0, x) \in E(G)$.

Definition 2. [8] Let $C \neq \emptyset \subseteq X$, $g: C \longrightarrow X$ be a map. Then is called to be $G - demiclosed$ at $y \in X$ if, for any $\{x_n\} \subseteq C$ such that $\{x_n\} \rightharpoonup x \in C$, $\{gx_n\} \to y$ and $(x_n, x_{n+1}) \in E(G)$ imply $gx = y$.

Definition 3. [13] Let $C \neq \emptyset \subseteq X$, $G = (V(G), E(G))$ be digraph such that $V(G) = C$. Then C is called to own *Property P* if for each $\{x_n\} \subseteq C$ such that $\{x_n\} \rightharpoonup x \in C$, $(x_n, x_{n+1}) \in E(G)$, there is a subsequence $\{x_{n_l}\}$ of $\{x_n\}$ such that $(x_{n_l}, x) \in E(G)$ for $\forall l \in N$.

Remark 1. [9] If G is transitive, then *Property P* is equal to the feature: If $\{x_n\} \subseteq C$ with $(x_n, x_{n+1}) \in E(G)$ such that for any subsequence $\{x_{n_l}\}$ of $\{x_n\}$ converging weakly to x in X, then $(x_n, x) \in E(G)$ for $\forall n \in N$.

Lemma 1. [14] Let X be $UCBS$. Supposing that $n \geq 1$, $1 > c \geq t_n \geq b > 0$. Let $\{u_n\}, \{w_n\} \subseteq X$ be such that $limsup_{n\to\infty}\|u_n\| \leq a$, $limsup_{n\to\infty}\|w_n\| \leq a$, $\|(1-t_n)w_n + t_n u_n\| \to a \geq 0$ as $n \to \infty$. Then $\|u_n - w_n\| \to 0$ as $n \to \infty$.

Lemma 2. [9] Let $C \neq \emptyset$ be a closed convex subset of UCBS X. Assume that C own *Property P*. Let $\{g_i\}_{i=1}^k$ be G −nonexpansive maps in C. Then $I - g_i$ are $G - demiclosed$ at 0.

Lemma 3. [12] Let $C \neq \emptyset$ be a closed convex subset of a normed space, and let $G = (V(G), E(G))$ be digraph which is transitive with $V(G) = C$. Let $g: C \to C$ be G −nonexpansive map. If C own the *Property P*, then g is G −continuous.

2. MAIN RESULTS

Henceforward, $C \neq \emptyset$ express a subset of UCBS X involving $G = (V(G), E(G))$ such that convexness of $E(G)$, $V(G) = C$ and transitive of G. The maps $\{g_i\}_{i=1}^k: C \to C$ are G −nonexpansiveness with $g_{fix} := \cap_{i=1}^k g_{fix}(g_i) \neq \emptyset$. For $x_0 \in C$, let the sequence $\{x_n\}$ identified by Eq. 1.

Proposition 1. Let $c_0 \in g_{fix}$ be such that $(x_0, c_0), (c_0, x_0) \in E(G)$. Then (x_n, c_0), (c_0, x_n), $(x_n, y_n^i), (y_n^i, x_n)$, (c_0, y_n^i), (y_n^i, c_0), $(x_n, x_{n+1}) \in E(G)$ for $i = \overline{1, k-1}$.

Proof. Using mathematical inductive, we shall show our results. Let $(x_0, c_0) \in E(G)$. Due to edge-preserving of g_1, $(g_1 x_0, c_0) \in E(G)$. Due to convexness of $E(G)$, we own $(y_0^1, c_0) \in E(G)$. From edge-preserving of g_2, $(g_2 y_0^1, c_0) \in E(G)$, by virtue of convexness to $E(G)$, we get $(1-\mu_0^2)(y_0^1, c_0) + \mu_0^2(g_2 y_0^1, c_0) = \left((1-\mu_0^2)y_0^1 + \mu_0^2 g_2 y_0^1, c_0\right) = (y_0^2, c_0) \in E(G)$. Suppose that $\left(y_0^j, c_0\right) \in E(G)$ for $j = \overline{1, k-2}$. Due to edge-preserving of g_{j+1}, $\left(g_{j+1} y_0^j, c_0\right) \in E(G)$, by virtue of convexness to $E(G)$, we furnish $\left(y_0^{j+1}, c_0\right) \in E(G)$. Consequently for $i = \overline{1, k-1}$; $\left(y_0^i, c_0\right) \in E(G)$. We enjoy $(y_0^{k-1}, c_0) \in E(G)$. Owing to edge-preserving of g_k, $(g_k y_0^{k-1}, c_0) \in E(G)$. Because $E(G)$ is

JSR A
Journal of Scientific Reports

convexness, we possess $(1-\mu_0^k)(y_0^{k-1},c_0)+\mu_0^k(g_k y_0^{k-1},c_0)=\left((1-\mu_0^k)y_0^{k-1}+\mu_0^k g_k y_0^{k-1},c_0\right)=(x_1,c_0)\in E(G)$. Renewing prior procedure for (x_1,c_0) instead of (x_0,c_0), we acquire $\left(y_1^i,c_0\right)\in E(G)$ and $(x_2,c_0)\in E(G)$. Assume that $(x_l,c_0)\in E(G)$ for $l\geq 1$. Due to edge-preserving of g_1, $(g_1x_l,c_0)\in E(G)$. Since $E(G)$ is convexness, we possess $(y_l^1,c_0)\in E(G)$. From edge-preserving of g_2, $(g_2y_l^1,c_0)\in E(G)$, as $E(G)$ is convexness, we belong $(y_l^2,c_0)\in E(G)$. Repeating the algorithm, we conclude that $\left(y_l^i,c_0\right)\in E(G)$ and $(x_{l+1},c_0)\in E(G)$. Prolong the argument againward for $(x_{l+1},c_0)\in E(G)$, we attain $\left(y_{l+1}^i,c_0\right)\in E(G)$. From induction, we deduce that $(x_n,c_0)\in E(G)$, we gain $(y_n^i,c_0)\in E(G)$ for $n\geq 1$ and $i=\overline{1,k-1}$. Using an analog argument, we can indicate (c_0,x_n), $(c_0,y_n^i)\in E(G)$ for $n\geq 1$ and $i=\overline{1,k-1}$, under the hypothesis that $(c_0,x_0)\in E(G)$. As the graph G is transitive, we hold (x_n,y_n^i), (y_n^i,x_n), $(x_n,x_{n+1})\in E(G)$ for $n\geq 1$ and $i=\overline{1,k-1}$.

Lemma 4. If $C\neq\emptyset$ is a closed convex subset of UCBS X, $\{\mu_n^i\}_{i=1}^k\subset[\varrho,\varsigma]$, where $0<\varrho<\varsigma<1$ and $(x_0,c_0),(c_0,x_0)\in E(G)$ for $x_0\in C$ and $c_0\in g_{fix}$, then for $n\geq 1$ and $i=\overline{1,k}$;

(i) $\|x_{n+1}-c_0\|\leq\|x_n-c_0\|$, and hence $\lim_{n\to\infty}\|x_n-c_0\|$ exists;
(ii) $\lim_{n\to\infty}\left\|x_n-g_i y_n^{i-1}\right\|=0$;
(iii) $\lim_{n\to\infty}\|x_n-g_i x_n\|=0$.

Proof. (i) Let $c_0\in g_{fix}$. It follows from Eq. 1, Proposition 1 and G −nonexpansiveness of g_1, we have

$$\begin{aligned}\|y_n^1-c_0\|&=\|(1-\mu_n^1)x_n+\mu_n^1 g_1x_n-c_0\|\\&\leq(-\mu_n^1+1)\|-c_0+x_n\|+\mu_n^1\|-c_0+g_1x_n\|\\&\leq(1-\mu_n^1)\|-c_0+x_n\|+\mu_n^1\|-c_0+x_n\|\\&=\|x_n-c_0\|.\end{aligned}\tag{2}$$

Using an analogue way, allied to Eq. 2, we have

$$\begin{aligned}\|y_n^2-c_0\|&=\|(1-\mu_n^2)y_n^1+\mu_n^2 g_2y_n^1-c_0\|\\&\leq(-\mu_n^2+1)\|-c_0+y_n^1\|+\mu_n^2\|-c_0+g_2y_n^1\|\\&\leq(1-\mu_n^2)\|-c_0+y_n^1\|+\mu_n^2\|-c_0+y_n^1\|\\&=\|y_n^1-c_0\|\leq\|x_n-c_0\|.\end{aligned}\tag{3}$$

By induction, it follows from Eq. 1 and G −nonexpansiveness of $\{g_i\}_{i=1}^{k-1}$, we have

$$\left\|y_n^j-c_0\right\|\leq\|x_n-c_0\|\tag{4}$$

for $j=1,2,\cdots,k-1$. Hence, it follows from Eq. 1, Eq. 4 and G −nonexpansiveness of g_k, we have

$$\begin{aligned}\|x_{n+1}-c_0\|&=\|(1-\mu_n^k)y_n^{k-1}+\mu_n^k g_k y_n^{k-1}-c_0\|\\&\leq(1-\mu_n^k)\|y_n^{k-1}-c_0\|+\mu_n^k\|g_k y_n^{k-1}-c_0\|\\&\leq(1-\mu_n^k)\|y_n^{k-1}-c_0\|+\mu_n^k\|y_n^{k-1}-c_0\|\end{aligned}\tag{5}$$

JSR A
Journal of Scientific Reports

$$= \|y_n^{k-1} - c_0\| \leq \|x_n - c_0\|.$$

Hence, $\lim_{n\to\infty}\|x_n - c_0\|$ exists.

(ii) From hypothesis (i), we get that $\{x_n\}$ is bounded. In turn there is a real numbers $\gamma \geq 0$ such that

$$\|x_n - c_0\| \to \gamma \ \ as\ n \to \infty. \tag{6}$$

By Eq. 4, we have $\left\|y_n^j - c_0\right\| \leq \|x_n - c_0\|, for\ i = \overline{1, k-1}$.
Getting $lim\ sup$ on both aspects of the hereinabove inequality, we have $j = \overline{1, k-1}$;

$$limsup_{\,n\to\infty}\left\|y_n^j - c_0\right\| \leq \gamma. \tag{7}$$

We further write down that

$$\begin{aligned}
&\|x_{n+1} - c_0\| = \|(1-\mu_n^k)(y_n^{k-1} - c_0) + \mu_n^k(g_k y_n^{k-1} - c_0)\| \\
&\leq (1-\mu_n^k)\|y_n^{k-1} - c_0\| + \mu_n^k\|y_n^{k-1} - c_0\| \\
&\leq \|y_n^{k-1} - c_0\| \\
&\vdots \\
&\leq \left\|y_n^j - c_0\right\|, for\ j = \overline{1, k-1}. \\
&\Longrightarrow \\
&liminf_{n\to\infty}\left\|y_n^j - c_0\right\| \geq \gamma, for\ j = \overline{1, k-1}.
\end{aligned} \tag{8}$$

By Eq. 7 and Eq. 8, we get $lim_{n\to\infty}\left\|y_n^j - c_0\right\| = \gamma, for\ j = \overline{1, k-1}$.

In other words, $\lim_{n\to\infty}\left\|\left(1-\mu_n^j\right)(y_n^{j-1} - c_0) + \mu_n^j(g_j y_n^{j-1} - c_0)\right\| = \gamma, for\ j = \overline{1, k-1}$.

Owing to G −nonexpansiveness of $\{g_i\}_{i=1}^{k-1}$, from Eq. 7, we possess $limsup_{n\to\infty}\left\|g_j y_n^{j-1} - c_0\right\| \leq \gamma, for\ j = \overline{1, k-1}$.

By Lemma 1, we have $for\ j = \overline{1, k-1}$

$$\lim_{n\to\infty}\left\|g_j y_n^{j-1} - y_n^{j-1}\right\| = 0. \tag{9}$$

For $j = k$, by Eq. 4 and G −nonexpansiveness of g_k, we own $\left\|g_j y_n^{j-1} - c_0\right\| \leq \left\|y_n^{j-1} - c_0\right\| \leq \|x_n - c_0\|$. Taking lim sup on both sides of the above term, we get $limsup_{n\to\infty}\|g_k y_n^{k-1} - c_0\| \leq \gamma$.
As $\lim_{n\to\infty}\|x_{n+1} - c_0\| = \gamma$, we have $\lim_{n\to\infty}\|(1-\mu_n^k)(y_n^{k-1} - c_0) + \mu_n^k(g_k y_n^{k-1} - c_0)\| = \gamma$.
By Eq. 7 and Lemma 1, we get

$$\lim_{n\to\infty}\|-g_k y_n^{k-1} + y_n^{k-1}\| = 0. \tag{10}$$

JSR A
Journal of Scientific Reports

Therefore, Eq. 9 and Eq. 10 we deduced that

$$\lim_{n\to\infty}\left\|g_j y_n^{j-1} - y_n^{j-1}\right\| = 0, j = \overline{1,k}. \tag{11}$$

By Eq. 1, we have for $i = \overline{1,k-1}$, $\left\|y_n^i - y_n^{i-1}\right\| = \mu_n^i\left\|g_i y_n^{i-1} - y_n^{i-1}\right\|$.

By Eq. 11, we own for $i = \overline{1,k-1}$

$$\lim_{n\to\infty}\left\|y_n^i - y_n^{i-1}\right\| = 0. \tag{12}$$

Using Eq. 12, we have for $i = \overline{1,k-1}$

$$\begin{aligned}\left\|y_n^i - x_n\right\| \le \|-x_n + y_n^1\| + \cdots + \left\|-y_n^{i-2} + y_n^{i-1}\right\| \\ +\left\|-y_n^{i-1} + y_n^i\right\| \to 0 \; as \; n \to \infty.\end{aligned} \tag{13}$$

It implies from Eq. 11 and Eq. 13 that for $i = \overline{1,k}$

$$\begin{aligned}\left\|-x_n + g_i y_n^{i-1}\right\| \le \left\|-y_n^{i-1} + g_i y_n^{i-1}\right\| + \left\|-x_n + y_n^{i-1}\right\| \\ \to 0 \; as \; n \to \infty.\end{aligned} \tag{14}$$

(iii) Due to the case $i = 1$, by (ii), we get

$$\|x_n - g_1 x_n\| \to 0 \; as \; n \to \infty. \tag{15}$$

It follows from Eq. 13 and Eq. 14, by G −nonexpansiveness of $\{g_i\}_{i=2}^k$, we get

$$\begin{aligned}\|g_i x_n - x_n\| \le \left\|g_i x_n - g_i y_n^{i-1}\right\| + \left\|g_i y_n^{i-1} - x_n\right\| \\ \le \left\|x_n - y_n^{i-1}\right\| + \left\|g_i y_n^{i-1} - x_n\right\| \\ \to 0 \; as \; n \to \infty, for \; i = 2,3,\cdots,k.\end{aligned} \tag{16}$$

Hence, from Eq. 15 and Eq. 16, for $i = \overline{1,k}$ we deduce that

$$\|x_n - g_i x_n\| \to 0 \; as \; n \to \infty. \tag{17}$$

Theorem 1. Let $C \neq \emptyset$ is a closed convex subset of UCBS X, $\{\mu_n^i\}_{i=1}^k \subset [\varrho, \varsigma]$, where $0 < \varrho < \varsigma < 1$. Let $c_0 \in g_{fix}$ such that $(x_0, c_0), (c_0, x_0) \in E(G)$ for $x_0 \in C$. Given that C hold the *Property P*, $\{g_i\}_{i=1}^k$ satisfy the $Condition\ (A'')$, g_{fix} is dominated by x_0 and g_{fix} dominates x_0, then $\{x_n\} \to w^* \in g_{fix}$.

Proof. Let $c_0 \in g_{fix}$ such that $(x_0, c_0), (c_0, x_0) \in E(G)$ for $x_0 \in C$. We know that $\|x_n - g_i x_n\| \to 0 \; as \; n \to \infty$, for $i = \overline{1,k}$ with Lemma 4 (iii). By $Condition\ (A'')$, we can write

JSR A
Journal of Scientific Reports

$$\|x_n - g_l x_n\| \geq f\left(d\left(x_n, g_{fix}\right)\right), for\ 1 \leq l \leq k. \tag{18}$$

Getting lim sup on both aspects of the hereinabove term, we hold

$$\lim_{n\to\infty} \|x_n - g_l x_n\| \geq \lim_{n\to\infty} f\left(d\left(x_n, g_{fix}\right)\right), for\ 1 \leq l \leq k. \tag{19}$$

Namely, $f\left(d\left(x_n, g_{fix}\right)\right) \to 0\ as\ n \to \infty$. Because of $Condition\ (A'')$, we get $d\left(x_n, g_{fix}\right) \to 0\ as\ n \to \infty$. Thus, we may receive a subsequence $\{x_{n_v}\}$ of $\{x_n\}$ and $\{w_v^*\} \subset g_{fix}$ such that $\|x_{n_v} - w_v^*\| < 2^{-v}$. For strong convergence implies weak convergence, by Remark 1, we get $(x_{n_v}, w_v^*) \in E(G)$. From the proof method of [15], we own $\|x_{n_{v+1}} - w_v^*\| \leq \|x_{n_v} - w_v^*\| < 2^{-v}$, thus

$$\|w_{v+1}^* - w_v^*\| \leq \|w_{v+1}^* - x_{n_{v+1}}\| + \|x_{n_{v+1}} - w_j^*\| \leq \frac{3}{2}2^{-v} \tag{20}$$

We conclude that $\{w_v^*\}$ is a Cauchy sequence, so $w_j^* \to w^*$. Due to closed of g_{fix}, $w^* \in g_{fix}$. Then $x_{n_v} \to w^*$. Thereof Lemma 4 (i), $x_n \to w^* \in g_{fix}$.
The following two example illustrate which is inspired by Example 2.2 and Example 3.2 in [16] for fulfilling of Theorem $1-2$ which the *Condition* (A'') and *semicompact* are used to verify the convergence of iterative algorithm Eq. 1, resp.

Example 1. Let $C = [0,2]$ and $G = (V(G), E(G))$ be digraph via $E(G) = \{(x,y): x \in [0,1], y \in [0,2]\ with\ 1 \geq |x-y|\}$ and $V(G) = C$. For every $i = \overline{1,k}$, let $\{g_i\}_{i=1}^k : [0,2] \to [0,2]$ be defined by

$$\{g_i\}_{i=1}^k = \begin{cases} [(1-x)/2^i] + 1 & if\ x \in [0,1], \\ 5/2 & if\ x \in (1,2]. \end{cases} \tag{21}$$

Let $\{\mu_n^i\} = [(4^i - 1)(5^i - 1)].\, 20^{-i}$ for $\forall i = \overline{1,k}$. Then $g_{fix} := \{1\}$ and $\{g_i\}_{i=1}^k : C \to C$ be $G-$nonexpansive maps for every $i = \overline{1,k}$.

Theorem 2. Let $C \neq \emptyset$ is a closed convex subset of UCBS X, $\{\mu_n^i\}_{i=1}^k \subset [\varrho, \varsigma]$, where $0 < \varrho < \varsigma < 1$. Let $c_0 \in g_{fix}$ such that $(x_0, c_0), (c_0, x_0) \in E(G)$ for $x_0 \in C$. Supposing that C has the *Property P* and one of $\{g_i\}_{i=1}^k$ is *semicompact*, g_{fix} is dominated by x_0 and g_{fix} dominates x_0, then $\{x_n\} \to \kappa \in g_{fix}$.

Proof. Let $c_0 \in g_{fix}$ such that $(x_0, c_0), (c_0, x_0) \in E(G)$ for $x_0 \in C$. Let g_l is semicompact for $1 \leq l \leq k$. We get $\|x_n - g_l x_n\| \to 0\ as\ n \to \infty$ by Lemma 4. On account of the fact that $\{x_n\}$ is bounded and g_l is semicompact, there exists a subsequence $\{x_{n_j}\}$ of $\{x_n\}$ such that $x_{n_j} \to \kappa \in C$ as $j \to \infty$. As strong convergence implies weak convergence, by Remark 1, we get $(x_{n_j}, \kappa) \in E(G)$ It is apparent that $\kappa \in g_{fix}$. By Lemma 3 and Lemma 4 (iii), we obtain that

JSR A
Journal of Scientific Reports

$$\| \kappa - g_l \kappa \| = \lim_{j \to \infty} \left\| x_{n_j} - g_l x_{n_j} \right\| = 0, \; for \; 1 \leq l \leq k. \tag{22}$$

Therefore $\kappa \in g_{fix}$ so that $\lim_{n\to\infty}\|x_n - \kappa\|$ exists. Hence, $x_n \to \kappa$ as $j \to \infty$.

Example 2. Let $G = (V(G), E(G))$ be digraph via

$$E(G) = \{(x, y): x \in [3,3.2], y \in [3,3.3] \; with \; |x - y| < 1\} \text{ and } V(G) = [3,3.3]. \tag{23}$$

For every $i = \overline{1,k}$, let $\{g_i\}_{i=1}^{k}: [3,3.3] \to [3,3.3]$ be defined by

$$\{g_i\}_{i=1}^{k} = \begin{cases} [x/2^i] + \left[\left((2^i - 1)/2^i\right)(22/7)\right] & if \; x \in [3,3.2], \\ 3 & if \; x \in (3.2,3.3]. \end{cases} \tag{24}$$

Let $\{\mu_n^i\} = (2^i - 1).6^{-i}$ for $\forall i = \overline{1,k}$. Then $g_{fix} \coloneqq \{22/7\}$ and $\{g_i\}_{i=1}^{k}$ be G −nonexpansive maps for every $i = \overline{1,k}$.

Table 1: The value of $\{x_n\}$ with initial value $x_0 = 3.0000$ and $n = 25$, resp.

n	$k = 5 \; in$ Eq. 1	$k = 3 \; in$ Eq. 1	$k = 2 \; in$ Eq. 1	$k = 1 \; in$ Eq. 1
1	3.0000	3.0000	3.0000	3.0000
2	3.0254	3.0236	3.0201	3.0119
3	3.0463	3.0432	3.0373	3.0228
4	3.0634	3.0596	3.0521	3.0328
5	3.0775	3.0733	3.0649	3.0420
6	3.0854	3.0848	3.0759	3.0504
7	3.0956	3.0943	3.0853	3.0581
8	3.1040	3.1023	3.0934	3.0652
9	3.1108	3.1090	3.1003	3.0717
10	3.1165	3.1145	3.1062	3.0776
11	3.1211	3.1192	3.1114	3.0830
12	3.1249	3.1232	3.1158	3.0880
13	3.1281	3.1264	3.1196	3.0926
14	3.1306	3.1291	3.1228	3.0968
15	3.1327	3.1313	3.1256	3.1006
16	3.1344	3.1333	3.1280	3.1041
17	3.1359	3.1348	3.1301	3.1073
18	3.1372	3.1362	3.1319	3.1103
19	3.1382	3.1374	3.1334	3.1130
20	3.1390	3.1383	3.1347	3.1155
21	3.1396	3.1391	3.1359	3.1178
22	3.1402	3.1397	3.1369	3.1199
23	3.1407	3.1403	3.1377	3.1218

JSR A
Journal of Scientific Reports

24	3.1411	3.1407	3.1384	3.1236
25	3.1413	3.1411	3.1391	3.1252

Theorem 3. Let $C \neq \emptyset$ is a closed convex subset of UCBS X, $\{\mu_n^i\}_{i=1}^k \subset [\varrho, \varsigma]$, where $0 < \varrho < \varsigma < 1$. Let $c_0 \in g_{fix}$ such that $(x_0, c_0), (c_0, x_0) \in E(G)$ for $x_0 \in C$. Supposing that C has the *Property P*, g_{fix} is dominated by x_0 and g_{fix} dominates x_0, then $\{x_n\} \rightharpoonup c_0 \in g_{fix}$.

Proof. Let $c_0 \in g_{fix}$ such that $(x_0, c_0), (c_0, x_0) \in E(G)$ for $x_0 \in C$. Owing to Lemma 4 (i) and weaakly compact, there exists a subsequnce $\{x_{n_v}\}$ of $\{x_n\}$ such that $x_{n_v} \to \kappa^* \in C \; as \; v \to \infty$. It follows by Lemma 4, $\lim_{n\to\infty}\|x_{n_v} - c_0\| = 0$, $\lim_{n\to\infty}\|x_{n_v} - g_i y_{n_v}^{i-1}\| = 0$ and $\lim_{n\to\infty}\|x_{n_v} - g_i x_{n_v}\| \to 0 \; as \; n \to \infty$ for $i = \overline{1,k}$. Using Lemma 2, $I - g_i$ are G −demiclosed at 0. Afterward the remainder of proving follows as in the proof of Theorem 3.4 in [9].

Remark 2.

(i) Taking $k = 3$ and $g_1 = g_2 = g_3 = g$ in Eq. 1, we acquire the generalized form of the SP −iteration scheme by Phuengrattana and Suantai [10].

(ii) Taking $k = 2$ in Eq. 1, we have the two-step iterative schema by Thianwan [11] for a self-map.

(iii) Taking $k = 1$ in Eq. 1, then we obtain some convergence theorems of Mann algorithm for G −nonexpansiveness in the frame of UCBS via graph.

(iv) Theorem $1 - 2$ widen and advance the concerning deductions of Khan et al. [1], Kettapun et al. [3] and Yildirim and Özdemir [2] for a self-map in a finite family of G −nonexpansiveness in UCBS via digraph.

(v)The iteration method (1.3) in [9] is replaced by the modified multistep iterative process of a finite family of G −nonexpansiveness, also additionally, we give strong convergence result under the Condition (A'').

(vi)Taking $k = 3$ in Eq. 1, then Theorem $2 - 3$ extend and improve the outcomes of Theorem 3.7-3.8 in [12] without supposing the Opial's condition, resp.

3. CONCLUSION

Withinside the forthcoming scope of the sight, reader may verify the convergence theorems of the following iteration processes to a common fixed point of nonexpansiveness identified on UCBS via digraph.

Let $C \neq \emptyset$ is a closed convex subset of UCBS X with a digraph $\big(V(G), E(G)\big) = G$ such that convexness of $E(G)$, $V(G) = C$ and transitive of G. Let $\{h_i\}_{i=1}^k, \{g_i\}_{i=1}^k : C \to C$ are G −nonexpansive

JSR A
Journal of Scientific Reports

maps; supposing the existence of common fixed points of these operators, our results and proof procedure go along to this class of maps by using the sequence $\{x_n\}$ generated by

$$\begin{aligned} x_{n+1} &= (1-\mu_n^k)h_k y_n^{k-1} + \mu_n^k g_k y_n^{k-1}, \\ y_n^{k-1} &= (1-\mu_n^{k-1})h_{k-1} y_n^{k-2} + \mu_n^{k-1} g_{k-1} y_n^{k-2}, \\ y_n^{k-2} &= (1-\mu_n^{k-2})h_{k-2} y_n^{k-3} + \mu_n^{k-2} g_{k-2} y_n^{k-3}, \\ &\vdots \\ y_n^2 &= (1-\mu_n^2)h_2 y_n^1 + \mu_n^2 g_2 y_n^1, \\ y_n^1 &= (1-\mu_n^1)h_1 x_n + \mu_n^1 g_1 x_n, \end{aligned} \tag{25}$$

or, in brief,

$$\begin{aligned} x_{n+1} &= (1-\mu_n^k)h_k y_n^{k-1} + \mu_n^k g_k y_n^{k-1}, \\ y_n^l &= (1-\mu_n^l)h_l y_n^{l-1} + \mu_n^l g_l y_n^{l-1}, for\ l = 2,3,\cdots,k-1 \\ y_n^1 &= (1-\mu_n^1)h_1 x_n + \mu_n^1 g_1 x_n, n \geq 1 \end{aligned} \tag{26}$$

where $x_n = y_n^0$, $\{\mu_n^i\} \in [0,1]$.

In image deblurring, many engineers seek to recover the original, sharp image by using a mathematical model of the blurring process [26]. Signal recovery presents potential problems for most researchers at one stage or another in an experiment. The most frequent problem here is either a very weak signal, or a very low signal to noise ratio [27]. Many mathematicians have been interested in simulated results for image deblurring and signal recovering problems in recent years, also see e.g. [28-30]. The reader on the other hand can apply our proposed method to solve image deblurring and signal recovering problems.

ACKNOWLEDGEMENT

This research received no specific grants from any funding agency in public, commercial or non-profit sectors.

REFERENCES

[1] Khan, A. R., Domlo, AA., and Fukhar-ud-din, H. (2008). Common fixed point noor iteration for a finite family of asymptotically quasi-nonexpansive mappings in banach spaces. The Journal of Mathematical Analysis and Applications, 341(1), 1-11.

[2] Yıldırım, İ., and Özdemir, M. (2009). A new iterative process for common fixed points of finite families of non-self-asymptotically non-expansive mappings. Nonlinear Analysis: Theory, Methods & Applications, 71 (3-4), 991-999.

[3] Kettapun, A., Kananthai, A., and Suantai, S. (2010). A new approximation method for common fixed points of a finite family of asymptotically quasi-nonexpansive mappings in Banach spaces. Computers and Mathematics with Applications, 60, 1430-1439.

[4] Jachymski, J. (2008). The contraction principle for mappings on a metric space with a graph. Proceedings of the American Mathematical Society, 136, 1359-1373.

[5] Aleomraninejad, S. M. A., Rezapour, S., and Shahzad, N. (2012). Some fixed point result on a metric space with a graph. Topology and its Applications, 159, 659-663.

[6] Alfuraidan, M. R., and Khamsi, M. A. (2015). Fixed points of monotone nonexpansive mappings on a hyperbolic metric space with a graph. Fixed Point Theory Applications, 44.

[7] Tripak, O. (2016). Common fixed points of G −nonexpansive mappings on Banach spaces with a graph. Fixed Point Theory Applications, 87.

[8] Suparatulatorn, R., Cholamjiak, W., and Suantai, S. (2018). A modified S −iteration process for G − nonexpansive mappings in Banach spaces with a graph. Numerical Algorithms, 77, 479-490.

[9] Hunde, T. W., Sangago, M. G., and Zegeye, H. (2017). Approximation of a common fixed point of a family of G −nonexpansive mappings in Banach spaces with a graph. International journal of Advances in Mathematics, 6, 137-152.

[10] Phuengrattana, W., and Suantai, S. (2011). On the rate of convergence of Mann, Ishikawa, Noor and SP-iterations for continuous functions on an arbitrary interval. Journal of Computational and Applied Mathematics, 235 (9), 3006-3014.

[11] Thianwan, S. (2009). Common fixed points of new iterations for two asymptotically nonexpansive nonself-mappings in a Banach space. Journal of Computational and Applied Mathematics, 224 (2), 688-695.

[12] Sridarat, P., Suparatulatorn, R., Suantai, S., and Cho, Y. J. (2018). Convergence analysis of SP −iteration for G −nonexpansive mappings with directed graphs. Bulletin of the Malaysian Mathematical Sciences Society, 42, 2361–2380.

[13] Alfuraidan, M. (2015). Fixed points of monotone nonexpansive mappings with a graph. Fixed Point Theory and Applications, 49.

[14] Sahu, J. (1991). Weak and strong convergence to fixed points of asymptotically nonexpansive mappings. Bulletin of the Australian Mathematical Society, 43, 153-159.

[15] Tan, K. K., and Xu, H. K. (1993). Approximating fixed points of nonexpansive mappings by the Ishikawa iteration process. Journal of Mathematical Analysis and Applications, 178, 301-308.

[16] Kangtunyakarn, A. (2018). Modified Halpern's iteration for fixed point theory of a finite family of $G-$nonexpansive mappings endowed with graph. Revista de la Real Academia de Ciencias Exactas, Físicas y Naturales. Serie A. Matemáticas, 112, 437-448.

[17] Shahzad, N., and Al-Dubiban, P. (2006). Approximating common fixed points of nonexpansive mappings in Banach spaces. Georgian Mathematical Journal, 13 (3), 529-537.

[18] Gürsoy, F., Karakaya, V., and Rhoades, B. E. (2013). Data dependence results of new multi-step and $S-$ iterative schemes for contractive-like operators. Fixed Point Theory and Applications, 76.

[19] Beg, I., Butt, A. R., and Radojevic, S. (2010). The contraction principle for set valued mappings on a metric space with a graph. Computers & Mathematics with Applications, 60, 1214-1219.

[20] Alfuraidan, M. (2015). Remark on monotone multivalued mappings on a metric space with a graph. Journal of Inequalities and Applications, 202.

[21] Kır, M., Yolacan, E., and Kızıltunc H. (2017). Coupled fixed point theorems in complete metric spaces endowed with a directed graph and application. Open Mathematics, 15, 734-744.

[22] Yolacan, E. (2017). A Brief note concerning non-self contractions in Banach Space endowed with a Graph. General Letters in Mathematics, 3 (1), 25-30.

[23] Yolacan, E., Kızıltunc, H., and Kır, M. (2016). Coincidence point theorems for $\varphi-\psi-$ contraction mappings in metric spaces involving a graph. Carpathian Mathematical Publications, 8 (2), 251-262.

[24] Yolacan, E., Debnath, P., and Aktürk, M. A. (2018). Common coupled fixed point theorems for generalized nonlinear contractions on metric spaces involving a graph. Sigma Journal of Engineering and Natural Sciences, 36 (2), 419-432.

[25] Suparatulatorn, R., Suantai, S., and Cholamjiak, W. (2017). Hybrid methods for a finite family of $G-$ nonexpansive mappings in Hilbert spaces endowed with graphs. AKCE International Journal of Graphs and Combinatorics, 14 (2), 101-111.

[26] Hansen, P. C., Nagy, J. G., and O'Learg, D. P. (2006). Deblurring Images Matrices, Spectra, and Filtering. (1st Edition). Philadelphia: Society for Industrial and Applied Mathematics, 16-22.

[27] Wilmshurst, T. H. (1990). Signal recovery from noise in electronic instrumentation. (2nd Edition). Florida: CRC Press**,** 7-10.

[28] Chairatsiripong, C., Yambangwai, D., and Thianwan, T. (2023). New iterative methods for nonlinear operators as concerns convex programming applicable in differential problems, image

deblurring, and signal recovering problems. Mathematical Methods in the Applied Sciences, 46(2), 3332–3355.

[29] Janngam, K., and Wattanataweekul, R. (2022). An accelerated fixed-point algorithm with an inertial technique for a countable family of G −nonexpansive mappings applied to image recovery. Symmetry, 14(4), 662.

[30] Yambangwai, D., and Thianwan, T. (2021). Convergence point of G-nonexpansive mappings in Banach spaces endowed with graphs applicable in image deblurring and signal recovering problems. Ricerche di Matematica.

[31] Ahmad, J., Ullah, K., Arshad, M., De la Sen, M., and Ma, Z. (2021). Convergence results on Picard-Krasnoselskii hybrid iterative process in CAT(0) spaces. Open Mathematics, 19, 1713–1720.

[32] El Kouch, Y., and Mouline, J. (2022). Convergence of mann and ishikawa iterative processes for some contractions in convex generalized metric space. Abstract and Applied Analysis, volume 2022, Article ID 3168414, 11 pages.

Kütahya Dumlupınar University
Institute of Graduate Studies

Journal of Scientific
Reports-A
E-ISSN: 2687-6167
Number 53, June 2023

RESEARCH ARTICLE

SIMULTANEOUS QUALITATIVE AND QUANTITATIVE ANALYSIS OF CERTAIN FLAVONOID GLYCOSIDES AND TERPENE LACTONES IN PHARMACEUTICAL PRODUCTS CONTAINING *GINKGO BILOBA L.* LEAF EXTRACT BY LC-TOF/MS

Selda DOĞAN ÇALHAN[1*], Hatice FİDAN[2], Nefise Özlen ŞAHİN[1]

[1] Mersin University Faculty of Pharmacy, Department of Pharmaceutical Biotechnology, Mersin, seldadgn@gmail.com, ORCID: 0000-0003-2589-8585
[2] Mersin University Faculty of Pharmacy, Department of Pharmaceutical Technology, Mersin, fidan_hatice21@hotmail.com, ORCID: 0000-0002-8590-2868
[1]Mersin University Faculty of Pharmacy, Department of Pharmaceutical Biotechnology, Mersin, nefisesahin@gmail.com ,ORCID:0000-0003-2357-8262

Receive Date:27.02.2023 *Accepted Date: 04.04.2023*

ABSTRACT

In this study, three drugs and three dietary supplements containing *G. biloba* leaf extract were obtained from pharmacies and two dietary supplements were obtained from herbalists. Certain flavonoid glycosides and ginkgolide A, B, C, and J amounts of these products were determined simultaneously using LC-TOF/MS. The total phenol and flavonoid content of these products were also determined with spectrophotometric technique.
Objective: We aimed to emphasize that adulteration is still a critical problem in herbal products frequently used during the Covid-19 pandemic and propose a fast, validated analytical method for detecting adulteration.
Conclusions: The qualitative and quantitative results of all drugs and dietary supplements obtained from the pharmacy were compatible with the information declared by the manufacturer. However, neither qualitative nor quantitative flavonoid glycosides or ginkgolides A, B, and C were detected, although the total phenolic and flavonoid values were very high in one of the dietary supplements taken by the herbalist. The study's data is considered significant, mainly due to the considerable increase in interest in herbal products during the Covid-19 pandemic.

Keywords: *G. Biloba, Drug, Dietary Supplement, Adulteration, Validation, LC-TOF/MS.*

1. INTRODUCTION

G. biloba is one of the most widely used natural medicinal plants, containing many bioactive components with therapeutic efficacy. Environmental factors have little effect on the survival of *G. biloba*, the only surviving species of the Ginkgoaceae family [1]. In fact, after the explosion of the atomic bomb in Hiroshima, Japan in 1946, the first plant to germinate was *G. biloba* [2]. G. biloba, a

tree native to China and used as a traditional medicinal plant for over 2,000 years [3] is now grown in Europe, Asia, Argentina, North America, and New Zealand [4].

With the discovery of the effectiveness of *G. biloba* leaf extract in peripheral blood circulation disorders and cerebral vascular diseases in the 1960s [5-8] it began to be used for different purposes. Pharmaceuticals containing *G. biloba* standardized leaf extract (EGb 761) are used in the treatment of tinnitus [9], cognitive impairment and Alzheimer's disease [10], retinal diseases [11], cardiovascular disease [12], cerebrovascular ischemia [13], peripheral vascular disease [14] and diabetic nephropathy [15]. Standardized *G. biloba* leaf extract is one of the most widely used herbal products and/or dietary supplements in the world [16-19] and it is possible to find different forms of pharmaceutical products such as tablets, capsules, solutions, etc. containing *G. biloba* approved by the Ministry of Health in Turkey [20].

Although there are many different bioactive compounds such as terpene lactones, flavonoids, fatty acids, proanthocyanidins, and polysaccharides in *G. biloba* leaf extract, [21,22] flavonoids and terpene lactones are considered to be the two main groups of biologically effective components [23-26]. Some studies performed on standardized *G. biloba* leaf extract show that it contains approximately 24% flavonol glycoside (22%- 27%) and 6% terpene lactone (2.6% - 3.2% bilobalide, 2.8% - 3.4% ginkgolide A (GA), ginkgolide B (GB), ginkgolide C (GC), and ginkgolide J (GJ)) [27-30]. Therefore, qualitative, and quantitative determination of flavonol glycosides and terpene lactones is one of the important parameters for evaluating the quality of products containing *G. biloba* [31]. *G. biloba* leaf extract contains more than 30 flavonol glycosides [16,25,29]. These flavonol glycosides are converted to three aglycones (Quercetin (QUE), Kaempferol (KAE), and Isorhamnetin (ISH)) by hydrolytic reactions. Therefore, the total amount of flavonoid aglycones is multiplied by 2.51 to calculate the total amount of flavonoid glycosides [16].

The mentioned values should be stated on the labels of products using standardized EGb 761 extract. However, studies carried out on the products containing *G. biloba* leaf extract in the world market reported varying concentrations of the contents [30, 31]. This situation reveals that the active ingredient can be mixed with cheaper and easily available botanical materials [32]. Unfortunately, due to some economic concerns, adulteration is still encountered in these products. This situation is a source of great danger to product reliability [33,34]. In the determination of adulteration, chromatographic and spectroscopic analytical methods are used to detect and characterize bioactive components. The most widely used techniques are thin-layer chromatography (TLC), inductively coupled plasma mass spectrometry (ICP-MS), high-performance liquid chromatography (HPLC), gas chromatography (GC), nuclear magnetic resonance spectroscopy (NMR), and near-infrared spectroscopy (NIR) [25,32,35-38]. In addition, tandem systems such as liquid chromatography/time-of-flight/mass spectrometry (LC-TOF/MS), which we used in our study, are an option.

In addition to the fact that pharmaceutical products prepared from *G. biloba* leaf extract and standardized extract have many useful applications, the efficacy and content controls of dietary supplements containing these herbal products and mainly supplied out of pharmacies should be evaluated scientifically. This is especially important when considering the frequency of people using herbal products due to the Covid 19 pandemic, which has been affecting the world for the last three

JSR A
Journal of Scientific Reports

years. Because anti-inflammatory and antioxidant agents have been claimed to be crucial in reducing COVID-19 patients' problems in the research [39].

For this purpose, it is aimed to control the content of selected pharmaceuticals and dietary supplements containing *G. biloba* leaf extract in the Turkish market with a fast, easy-to-apply and validated analytical method. In addition, the total phenol content of these products was determined using the Folin-Ciocalteu method, and the flavonoid content was determined using the aluminum chloride method. Thus, both content comparisons and phenolic capacities of pharmaceutical preparations containing *G. biloba* leaf extract were evaluated to determine possible adulteration.

2. MATERIAL and METHODS

2.1. Chemicals and Instruments

QUE, KAE, GA, GB, and GC were purchased from Sigma Aldrich (St. Louis, MO, USA). HPLC purity formic acid and methanol were provided from Merck (Darmstadt, Germany). Sodium carbonate, sodium nitrite, Folin reagent, gallic acid, and aluminum chloride were purchased from Sigma Aldrich (St. Louis, MO, USA). UV-1601 spectrophotometer (UV-1601, Shimadzu, Japan) and LC-TOF/MS (6545 Accurate-Mass, Agilent, USA) were used throughout this work.

2.2. Preparation of Samples and Standards

Stock solutions of QUE, KAE, GA, GB, and GC, used as standards in the analyses, were prepared with methanol. The extraction of drugs (D, E, F), dietary supplements (A, B, C, G, H) used in the study (Table 1) was carried out as described in sections 2.3 and 2.4. Before LC-TOF/MS analysis, all standards and samples were filtered through 0.45 µm membrane filters (Millipore).

Table 1. Information on drugs and dietary supplements.

Product Code	Form	Formulation	Standardized amount of extract	Purchased from
A	Dietary supplement	Capsule	*G. biloba* leaf extract 90 mg	Pharmacy
B	Dietary supplement	Capsule	*G. biloba* leaf extract 100 mg	Pharmacy
C	Dietary supplement	Capsule	*G. biloba* leaf extract 125 mg	Pharmacy
D	Drug	Tablet	*G. biloba* leaf extract 120 mg	Pharmacy
E	Drug	Tablet	*G. biloba* leaf extract 120 mg	Pharmacy
F	Drug	Tablet	*G. biloba* leaf extract 80 mg	Pharmacy

JSR A
Journal of Scientific Reports

G	Dietary supplement	Tablet	*G. biloba* leaf extract 60 mg	Herbalist
H	Dietary supplement	Powder	*G. biloba* leaf extract 100 mg	Herbalist

2.3. Acid Hydrolysis Extraction for Flavonoid Glycosides

Extraction was performed with some modifications to the method proposed by Czigle et al. [40] Ten tablets and 10 capsules were crushed separately in mortars and homogenized. An amount equivalent to 1 tablet or capsule was weighed and taken from the resulting homogeneous mixture. 45 mL of methanol (99%, Merck) was added to the weighed samples, and they were extracted ultrasonically. Then, 5 mL concentrated HCl (37%, Merck) and 9 mL ultrapure water were added. They were refluxed in the oil bath at 100-135 °C in the condenser. The obtained pink-red extracts were stored in the refrigerator at +4 °C for LC-TOF/MS analysis. The same procedures were repeated by taking 100 mg from the powder samples obtained from the herbalist.

2.4. Liquid-Liquid Extraction with Ethyl Acetate for Terpene Lactones

Extraction was performed with some modifications to the method proposed by Li et al. [28] Ten tablets and 10 capsules were crushed separately in mortars and homogenized. An amount equivalent to 1 tablet or capsule was weighed and taken from the resulting homogeneous mixture. 45 mL ultrapure water was added to the weighed samples and their extraction was done ultrasonically. After each extraction, the dissolved fractions were collected and filled to a final volume of 50 mL with distilled water. The extracts were taken into a separating funnel and liquid extraction was achieved three times with 20 mL of ethyl acetate. The ethyl acetate organic phases were combined and evaporated to dryness. The resulting residue was diluted with 10 mL analytical grade (99%) MeOH. It was stored in the refrigerator at +4 °C for LC-TOF/MS analysis. The same procedures were repeated by taking 100 mg of the powder samples obtained from the herbalist.

2.5. Equipment and Chromatographic Conditions

Qualitative and quantitative analysis of samples was performed with an Agilent LC-TOF/MS. The equipment and chromatographic are shown in Table 2.

Table 2. LC-TOF/MS conditions for analysis.

Equipment	Parameter	Conditions
LC-TOF/MS	Column	Agilent Poroshell 120 EC-C18 (3.0×50 mm, particle size 2.7 µm)
	Mobile phase	Gradient elutions of 0.1% formic acid (A) and 99% methanol (B) solutions 0 to 2 min, 0%B→5%B; 2 to 4 min, 5%B→95%B, 4 to 30 min, 95%B
	Analysis time	32 min
	Column temperature	30 °C
	Injection volume	10.0 µL
	Mobile phase	1.0 mL/min

JSR A
Journal of Scientific Reports

	flow rate	
	MS system and ion source	Agilent 6545 Accurate-Mass TOF/MS Negative ion mode Drying gas flow: 10.0 L/min, Nebulizer pressure: 35 psi Gas drying temperature: 325 °C Sheath gas temperature: 400 °C Sheath gas flow: nitrogen at 12 L/min Scan range: m/z 100 to 1400

2.6. Validation Parameters

Limit of Detection (LOD), Limit of Quantification (LOQ), measurement range and linearity, accuracy, and precision parameters were examined for the validation of the proposed method. In addition, the precision of the proposed method was evaluated intraday and between days. Recovery calculations were carried out to determine the accuracy of the proposed method. Therefore, LC-MS analyses were done by performing the extractions of the standards at known concentrations as in sections 2.3 and 2.4. The recovery values obtained were calculated using Eq. 1 [35].

$$\text{Recovery (\%)} = (\text{amount found} - \text{original amount})/\text{amount added} \times 100\% \quad (1)$$

2.7. Total Phenol Content

The total phenol content of the samples was determined spectrophotometrically using the Folin-Ciocalteu method [41]. First, 100 µL of each sample (A, B, C, D, E, F, G, and H) was prepared as in Section 2.3, then 7900 mL distilled water and 500 µL Folin-Ciocalteu reagent were added (10%, v/v in water). This mixture was vortexed and incubated for 2 min at room temperature in the dark. Immediately after, 1.5 mL 20% (w/v) Na_2CO_3 solution was added to the mixture and vortexed again. The resulting mixture was kept in the dark for 2 h at room temperature, and the absorbance of the blue solution formed was measured in a UV-Vis spectrophotometer at a wavelength of 765 nm against the blank. Gallic acid was used as standard. The results obtained were calculated as the mean of three measurements and expressed mg GAE/g.

2.8. Total Flavonoid Content

The total flavonoid amounts of the samples were measured spectrophotometrically according to the aluminum chloride/sodium nitrite method [42]. First, 500 µL of each sample (A, B, C, D, E, F, G, and H), was prepared as in section 2.3. It was transferred to a tube containing 3 mL distilled water and vortexed after adding 0.3 mL 5% aqueous $NaNO_2$ solution. After 5 min, 0.3 mL 10% aqueous AlCl3 solution was added to the mixture. After 1 min, 2 mL 1 M NaOH solution was added to the mixture, and the tube was filled to a total volume of 10 mL with distilled water. The final mixture was vortexed again and the absorbance was measured at 510 nm against water. The results obtained were calculated as the mean of three measurements and expressed mg Quercetin/g.

JSR A
Journal of Scientific Reports

3. RESULTS and DISCUSSION

3.1. Method Validation

Calibration lines with acceptable linearity were obtained for QUE, KAE, GA, GB, and GC. Correlation coefficients were obtained with r^2>0.98. LOD, LOQ, precision and recovery values were calculated as described in Section 2.6. The data obtained as a result of the validation studies were summarized in Table 3.

Table 3. Validation parameters of QUE, KAE, GA, GB, and GC.

	Calibration curve	**R^2**	**Linearity mg/L**	**LOD mg/L**	**LOQ mg/L**	**Repeatability**		**Recovery %**
						Intra Day RSD%	**Between Days RSD%**	
QUE	Y=4E+06x+2E+07	0.988	0.625-5	0.256	0.853	1.91	3.01	98.72 ± 0.04
KAE	Y=6E+06x+9E+06	0.998	0.625-10	0.391	1.304	1.95	3.90	98.25 ± 0.09
GA	Y=145657x+343882	0.995	2.5-20	0.263	0.878	1.72	2.64	97.32 ± 0.34
GB	Y=2E+06x+3E+06	0.990	1.25-10	0.086	0.287	1.13	2.44	96.33 ± 0.13
GC	Y=2E+06x+2E+06	0.992	1.25-10	0.136	0.453	1.31	2.40	96.84 ± 0.21

3.2. Retention Times of Standards and Samples for LC-TOF/MS Analysis

The analyses were performed under the conditions specified in Section 2.5 for the individually prepared solutions of all analyzed standard substances (QUE, KAE, GA, GB, and GC). Retention times were determined for each standard. Meanwhile, the analysis of the mixture containing all the standards was also performed. The chromatogram obtained for the standards was shown in Figure 1, and the retention time and molecular ion peaks of each standard were shown in Table 4.

JSR A
Journal of Scientific Reports

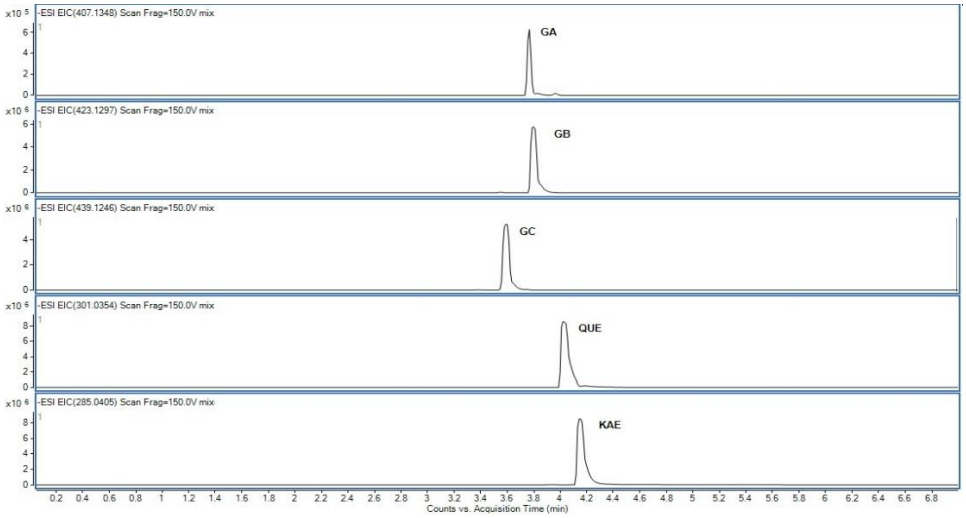

Figure 1. Chromatogram of standards.

Table 4. Molecular ion peaks and retention times of the standards.

Standards	**M^-**	**t_R (min)**
QUE	301.0379	4.03
KAE	285.0433	4.15
GA	443.1157	3.77
GB	423.1331	3.80
GC	439.1283	3.60

On the other hand, it is seen that there are studies carried out using HPLC-UV in the literature [43,44]. However, the reason for using LC-TOF/MS in this study is to avoid peak overlaps [45] since terpene lactones have low ε-values for maximum absorbance at about 219 nm. The chromatogram obtained for the samples was shown in Appendix A. Retention times of QUE, KAE, GA, GB, and GC present in the analyzed pharmaceutical samples were given in Table 5. The retention times of QUE, KAE, GA, GB, and GC in the samples were found to be compatible with the retention times of the standards. QUE, KAE, GA, GB, and GC were not found in the H sample obtained from herbalists.

Table 5. Retention times of the samples.

Samples	**t_R (min)**				
	QUE	**KAE**	**GA**	**GB**	**GC**
A	4.03	4.15	3.77	3.80	3.60
B	4.03	4.15	3.77	3.81	3.59

JSR A
Journal of Scientific Reports

C	4.03	4.15	3.76	3.81	3.59
D	4.03	4.15	3.77	3.81	3.59
E	4.04	4.15	3.77	3.81	3.59
F	4.03	4.14	3.76	3.80	3.59
G	4.03	4.14	3.76	3.80	3.60
H	-	-	-	-	-

3.3. Quantification of Total Flavonoids and GA, GB, GC, and GJ

The results of analyses showed that all the drugs and dietary supplements obtained from the pharmacy qualitatively contained QUE, KAE, GA, GB, and GC. The standard curve of GB for GJ and the calibration curve of QUE for ISH were used due to their similar structures and close molecular weights. The amounts of GJ and ISH were calculated using the molecular weight correction factor. As previously stated, this approach could be used [46]. The total flavonoid value was calculated by multiplying the amounts of QUE, BAE, and ISH with the appropriate conversion factors, and the results were compared with the declared values. The amount per tablet/capsule in all drugs and dietary supplements was detected within the declared limits. However, neither qualitative nor quantitative QUE, KAE, GA, GB or GC were present in the dietary supplement (H) obtained from the herbalist. The amounts found in the other dietary supplement (G) were detected as much lower than stated on the label (Table 6, 7).

Table 6. Total flavonoid glycosides content of 8 samples containing *G. biloba* leaf extracts (n=3, Mean ± SD).

Sample	**QUE (mg/tb or capsule)**	**KAE (mg/tb or capsule)**	**ISH (mg/tb or capsule)**	**Total (mg)**	**Total Flavonoid Glycosides Found (mg)**	**Total Flavonoid Glycosides Expected (mg)**
A	3.98 ± 0.02	3.59 ± 0.03	1.11 ± 0.02	8.68	21.79	19.8-24.30
B	4.36 ± 0.03	4.05 ± 0.04	1.35 ± 0.03	9.76	24.50	22-27
C	5.17 ± 0.01	5.11 ± 0.03	1.85 ± 0.04	12.13	30.44	27.5-33.75
D	5.02 ± 0.04	4.78 ± 0.05	1.58 ± 0.06	11.38	28.56	26.4-32.40
E	4.90 ± 0.06	4.79 ± 0.04	1.51 ± 0.05	11.20	28.11	26.4-32.40
F	3.11 ± 0.03	3.34 ± 0.02	0.93 ± 0.04	7.38	18.52	17.6-21.60
G	1.86 ± 0.02	1.52 ± 0.05	0.25 ± 0.03	3.63	9.11	13.2-16.20
H	-	-	-	-	-	22-27

JSR A
Journal of Scientific Reports

Table 7. GA, GB, GC, and GJ content of samples containing *G. biloba* leaf extracts (n=3, Mean ± SD).

Sample	GA (mg/tb or capsule)	GB (mg/tb or capsule)	GC (mg/tb or capsule)	GJ (mg/tb or capsule)	GA GB GC GJ Found (mg)	GA GB GC GJ Expected (mg)
A	0.90 ± 0.02	0.88 ± 0.03	0.62 ± 0.04	0.13 ± 0.02	2.53	2.52-3.06
B	1.04 ± 0.04	0.97 ± 0.05	0.63 ± 0.02	0.21 ± 0.03	2.85	2.8-3.40
C	1.54 ± 0.03	1.07 ± 0.02	0.71 ± 0.04	0.47 ± 0.03	3.79	3.5-4.25
D	1.46 ± 0.05	0.95 ± 0.04	0.69 ± 0.02	0.46 ± 0.03	3.56	3.36-4.08
E	1.38 ± 0.02	0.90 ± 0.03	0.67 ± 0.05	0.47 ± 0.04	3.42	3.36-4.08
F	0.52 ± 0.06	0.30 ± 0.02	0.22 ± 0.04	0.05 ± 0.03	1.09	2.24-2.72
G	0.31 ± 0.04	0.25 ± 0.05	0.20 ± 0.03	0.05 ± 0.02	0.81	1.68-2.04
H	-	-	-	-	-	2.8-3.40

The results obtained from our study show that adulteration is still a very serious problem, especially in dietary supplements purchased out of pharmacies. In our study, QUE, KAE, GA, GB, and GC could not be determined qualitatively and quantitatively in H sample containing *G. biloba* obtained from herbalists. In addition, there are differences between the reported values and the found values in the G sample obtained from the herbalist. This situation is similar to other studies reported in the literature [47,48].

3.4. Total Phenol and Flavonoid Analysis

The data summarized in Table 8 showed that, as expected, the highest total phenol, and flavonoid values were found in the sample containing the highest *G. biloba* standard leaf extract (C). On the other hand, the total phenol and flavonoid values determined in the tablet sample obtained from herbalists (G) were at the lowest level compared to the other tablets. Although no bioactive compounds in the standardized *G. biloba* extract was qualitatively detected in the powder sample taken from the herbalist, total phenol, and flavonoid values were at the highest level. This situation suggests that there may be adulteration in the sample.

Table 8. Total phenolic and flavonoid values for the samples (n=3, Mean ± SD).

Sample	Total Phenol mg (GAE)/g	Total Flavonoid mg (KUE)/g
A	35.51 ± 0.52	16.03 ± 0.29
B	36,51 ± 0.37	18.2 ± 0.50
C	40.48 ± 0.11	27.53 ± 0.29
D	38.14 ± 0.14	23.7 ± 0.51
E	37.47 ± 0.10	22.87 ± 0.28

JSR A
Journal of Scientific Reports

F	32.78 ± 0.10	12.37 ± 0.30
G	18.42 ± 0.15	9.03 ± 0.55
H	50.05 ± 0.52	45.37 ± 0.31

4. CONCLUSION

In this study, qualitative and quantitative analysis of drugs and dietary supplements containing *G. biloba* leaf extract available in the Turkish market was performed with a fast, easy, and validated analytical method. The highest total phenol and flavonoid values among the products purchased from the pharmacy were in the tablet containing the highest amount of *G. biloba* leaf extract. The total phenol and flavonoid values for the tablet sample purchased from the herbalist were the lowest. On the contrary, the total phenol and flavonoid values of the powder sample obtained from the herbalist were the highest compared to other pharmaceutical products. In this case, the most surprising point according to the LC-TOF/MS results was that the flavonoid glycosides and ginkgolide A, B, and C found in *G. biloba* were not detected in the powder sample taken from the herbalist. The fact that the dietary supplements showed such high total phenol and flavonoid values while none of the bioactive components of *G. biloba* exist in its content indicates that it may have been adulterated with other botanical materials with lower costs.
Table 9 compares the findings of this study to those of other *G. biloba* studies in the literature. The findings indicate that adulteration is still a significant issue in various *G. biloba* samples.

Table 9. Comparison of the results of the present study and other studies on the analysis of *G. biloba*.

Sample	Method	Finding	Reference
G. biloba food supplements	HPLC‑UV LC‑MS/MS	Adulteration was determined through analyses performed on selected samples.	40
G. biloba L. phytopharmaceuticals	HPLC‑UV	The proposed methods were used successfully to determine terpenes and flavonoids in four phytopharmaceutical preparations from the Egyptian market.	44
G. biloba L. pharmaceuticals	HPLC-DAD LC-MS	The study revealed that food supplements were mixed with rutin to reach the expected amount of flavonoid glycosides.	49
G. biloba solid oral dosage form	HPLC-PDA	According to the findings, appropriate quality control measures should be implemented to ensure the quality, safety, and efficacy of commercially available *G. biloba* products.	50

G. biloba L. drugs and three dietary supplements	LC-TOF/MS	Serious adulteration was noticed in dietary supplements containing *G. biloba* that were not purchased from a pharmacy.	**This study**

The study results reveal that we should be more cautious about the quality of these products, especially given the frequent use of herbal products during the Covid 19 pandemic**.**

Funding: This study was funded by the Mersin University Scientific Research Project Unit with the project no. 2021-1-TP2-4135.

ACKNOWLEDGEMENT

We are thankful to Mersin University Scientific Research Project Unit.

REFERENCES

[1] Mohanta, T.K., Occhipinti, A., Zebelo, S.A., Foti, M., Fliegmann, J., Bossi, S., Maffei, M.E., and Bertea, C.N. (2012). Ginkgo biloba responds to herbivory by activating early signaling and direct defenses. Plos One, 7(3), 1-14.

[2] Lin, H.Y., Li, W.H., Lin, C.F., Wu, H.R., and Zhao, Y.P. (2022). International biological flora: Ginkgo biloba. Journal of Ecology, 110(4), 951-982.

[3] Singh, B., Kaur, P., Gopichand, S.R.D., and Ahuja, P.S. (2008). Biology and chemistry of Ginkgo biloba. Fitoterapia, 79(6), 401–418.

[4] Belwal, T., Giri, L., Bahukhandi, A., Tariq, M., Kewlani, P., Bhatt, I.D., and Rawl, R.S. (2019). Ginkgo Biloba. Nonvitamin and Nonmineral Nutritional Supplements, 241-250.

[5] Tronnier, H. (1968). Clinical-pharmacological studies on the effect of an extract from Ginkgo biloba L. in the postthrombotic syndrome. Arzneimittelforschung, 18 (5), 551–554.

[6] Mussgnug, G., and Alemany, J. (1968). Studies on peripheral arterial blood circulation disorders. XV. On the problems of conservative therapy of obliterating peripheral blood circulation disorders demonstrated on tincture and extract from Ginkgo biloba L. Arzneimittelforschung, 18 (5), 543–550.

[7] Montanini, R., and Gaspari, G. (1969). Use of an extract of Ginkgo biloba (Tebonin) in the therapy of cerebral vascular diseases. Minerva Cardioangiologica, 17 (12), 1096–1102.

[8] Locatelli, G.R., and Sorbini, E. (1969). Effects of Tebonin (extract from leaves of Ginkgo biloba L.) in the treatment of senile peripheral arteriopathies. Minerva Cardioangiologica, 17 (12), 1103–1108.

[9] Kramer, F., and Ortigoza, A. (2018). Ginkgo biloba for the treatment of tinnitus. Medwave, 18 (26), 7295.

[10] Yang, G., Wang, Y., Sun, J., Zhang, K., and Liu, J. (2016). Ginkgo biloba for mild cognitive impairment and Alzheimer's disease: a systematic review and meta-analysis of randomized controlled trials. Current Topics in Medicinal Chemistry, 16(5), 520–528.

[11] Solis, M.I., Acero, N., Morell, F.B., Castillo, E., Rosende, M.E.G., Mingarro, D.M., Ortega, T., Sanahuja, M.A., and Villagrasa, V. (2019). Neuroprotective potential of Ginkgo biloba in retinal diseases. Planta Medica, 85 (17), 1292–1303.

[12] Rodriguez, M., Ringstad, L., Schäefer, P., Just, S., Hofer, H.W., Malmsten, M., and Siegel, G. (2007). Reduction of atherosclerotic nanoplaque formation and size by Ginkgo biloba (EGb 761) in cardiovascular high-risk patients. Atherosclerosis, 192 (2), 438–444.

[13] Oskouei, D.S., Rikhtegar, R., Hashemilar, M., Bazargani, H.S., Bonab, M.S., Hokmabadi, E.S., Zarrintan, S., and Sharifipour, E. (2013). The effect of Ginkgo biloba on functional outcome of patients with acute ischemic stroke:a double-blind, placebo-controlled, randomized clinical trial. Journal of Stroke Cerebrovascular Diseases, 22(8), 557-563.

[14] Muir, A.H., Robb, R., McLaren, M., Daly, F., and Belch, J.J.F. (2002). The use of Ginkgo biloba in Raynaud's disease: a double-blind placebo-controlled trial. Vascular Medicine, 7(4) 265–267.

[15] Zhu, H.W., Shi, Z.F., and Chen, Y.Y. (2005). Effect of extract of Ginkgo biloba leaf on early diabetic nephropathy. Zhongguo Zhong Xi Yi Jie He Za Zhi, 25 (10), 889–910.

[16] Van Beek, T.A. (2002). Chemical analysis of Ginkgo biloba leaves and extracts. Journal Chromatography A, 967(1), 21–55.

[17] Tabassum, N.E., Das, R., Lami, M.S., Chakraborty, A.J., Mitra, S., Tallei, T.E., Idroes, R., Mohamed, A.A.R., Hossain, M.J., Dhama, K., Hedeab, G.M., and Emran, T.B. (2022). Ginkgo biloba: A treasure of functional phytochemicals with multimedicinal applications. Evidence-Based Complementary and Alternative Medicine, 2022,1-30.

[18] Mahadevan, S., and Park, Y. (2008). Multifaceted therapeutic benefits of Ginkgo biloba L.: chemistry, efficacy, safety, and uses. Journal of Food Science, 73(1), 14–19.

[19] RxMediaPharma, (2022), [online], Website https://portal.rxmediapharma.com.tr/ [accessed 25 May 2022].

JSR A
Journal of Scientific Reports

[20] Ma, G.L., Xiong, J., Yang, G.X., Pan, L.L., Hu, C.L., Wang, W., Fan, H., Zhao, Q.H., Zhang, H.Y., and Hu, J.F. (2016). Biginkgosides A–I, unexpected minor dimeric flavonol diglycosidic truxinate and truxillate esters from Ginkgo biloba leaves and their antineuroinflammatory and neuroprotective activities. Journal of Natural Products, 79(5), 1354–1364.

[21] Beck, S., and Stengel, J. (2016). Mass spectrometric imaging of flavonoid glycosides and biflavonoids in Ginkgo biloba L. Phytochemistry, 130, 201–206.

[22] Hasler, A., and Sticher, O. (1992). Identification and determination of flavonoids from Ginkgo biloba by high performance liquid chromatography. Journal of Chromatography A, 605(1), 41–48.

[23] Liu, X.G., Yang, H., Cheng, X.L., Liu, L., Qin, Y., Wang, Q., Qi, L.W., and Li, P. (2014). Direct analysis of 18 flavonol glycosides, aglycones and terpene trilactones in Ginkgo biloba tablets by matrix solid phase dispersion coupled with ultra-high performance liquid chromatography tandem triple quadrupole mass spectrometry. Journal of Pharmaceutical and Biomedical Analysis, (97),123–128.

[24] Lin, L.Z., Chen, P., Ozcan, M., and Harnly, J.M. (2008). Chromatographic profiles and identification of new phenolic components of Ginkgo biloba leaves and selected products. Journal of agricultural and food chemistry, 56(15), 6671–6679.

[25] Van Beek, T.A., and Montoro, P. (2009). Chemical analysis and quality control of Ginkgo biloba leaves, extracts, and phytopharmaceuticals. Journal of Chromatography A, 1216(11), 2002–2032.

[26] Rimmer, C.A., Howerton, S.B., Sharpless, K.E., Sander, L.C., Long, S.E., Murphy, K.E., Porter, B.J., Putzbach, K., Rearick, M.S., Wise, S.A., Wood, L.J., Zeisler, R., Hancock, D.K., Yen, J.H., Betz, J.M., Nguyenpho, A., Yang, L., Scriver, C., Willie, S., Sturgeon, R., Schaneberg, B., Nelson, C., Skamarack, J., Pan, M., Levanseler, K., Gray, D., Waysek, E.H., Blatter, A., and Reich, E. (2007). Characterization of a suite of ginkgo-containing standard reference materials. Analytical and Bioanalaytical Chemistry, 389(1), 179–96.

[27] Chandra, A., Li, Y., Rana, J., Persons, K., Hyun, C., Shen, S., and Mulder, T. (2011). Qualitative categorization of supplement grade Ginkgo biloba leaf extracts for authenticity. Journal of Functional Foods, 3(2), 107–114.

[28] Li,W., and Fitzloff, J.F. (2002). HPLC determination of flavonoids and terpene lactones ın commercıal Gınkgo bıloba products. Journal of Liquid Chromatography & Related Technologies, 25(16), 2501–2514.

[29] Hasler, A., Sticher, O., and Meier, B. (1992). Identification and determination of the flavonoids from Ginkgo biloba by high-performance liquid chromatography. Journal of Chromatography A, 605(1), 41–48.

[30] Kressmann, S., Muller, W.E., and Blume, H.H. (2002). Pharmaceutical quality of different Ginkgo biloba brands. Journal of Pharmacy and Pharmacology, 54(5), 661–669.

[31] Booker, A., Frommenwiler, D., Reich, E., Horsfield, S., and Heinrich, M. (2016). Adulteration and poor quality of Ginkgo biloba supplements. Journal of Herbal Medicine, 6(2), 79–87.

[32] Harnly, J.M., Luthria, D., and Chen, P. (2012). Detection of adulterated ginkgo biloba supplements using chromatographic and spectral fingerprints. Journal of AOAC International, 95(6), 1579–1587.

[33] Liu, X.G., Wu, S.Q., Li, P., and Yang, H. (2015). Advancement in the chemical analysis and quality control of flavonoid in Ginkgo biloba. Journal of Pharmaceutical and Biomedical Analysis, 113, 212–225.

[34] Wohlmuth, H., Savage, K., Dowell, A., and Mouatt, P. (2014). Adulteration of Ginkgo biloba products and a simple method to improve its detection. Phytomedicine, 21(6), 912–918.

[35] López-Gutiérrez, N., Romero-González, R., Vidal, J.L.M., and Frenich, A.G. (2016). Quality control evaluation of nutraceutical products from Ginkgo biloba using liquid chromatography coupled to high resolution mass spectrometry. Journal of Pharmaceutical and Biomedical Analysis, 121, 151–160.

[36] Tokalıoglu, S. (2012). Determination of trace elements in commonly consumed medicinal herbs by ICP-MS and multivariate analysis. Food Chemistry, 134(4), 2504–2508.

[37] Zhao, L.J., Liu, W., Xiong, S.H., Tang, J., Lou, Z.H., Xie, M.X., Xia, B.H., Lin, L.M., and Liao, D.F. (2018). Determination of total flavonoids contents and antioxidant activity of Ginkgo biloba leaf by near-infrared reflectance method. International Journal of Analytical Chemistry, 2018, 1–7.

[38] Li, C.Y., Lin, C.H., Wu, C.C., Lee, K.H., and Wu, T.S. (2004). Efficient 1H nuclear magnetic resonance method for improved quality control analyses of Ginkgo constituents. Journal of Agricultural and Food Chemistry, 52(12), 3721–3725.

[39] Al-kuraishy, H.M., Al-Gareeb, A.I., Kaushik, A., Kujawska, M., and Batiha, G.E.S. (2022). Ginkgo biloba in the management of the COVID-19 severity. Archiv der Pharmazie, 355, 2200188.

[40] Czigle, S., Tóth, J., Jedlinszki, N., Radnai, E.H., Csupor, D., and Tekelová, D. (2018). Ginkgo biloba food supplements on the European Market –adulteration patterns revealed by quality control of selected samples. Planta Medica, 84, 475–482.

[41] Slinkard, K., and Singleton, V.L. (1977). Total phenols analysis: Automation and comparison with manual methods. American Journal of Enology and Viticulture, 28, 49 – 55.

[42] Kim, D.O., Jeong, S.W., and Lee, C.Y. (2003). Antioxidant capacity of phenolic phytochemicals from various cultivars of plums. Food Chemistry, 81(3), 321 – 326.

[43] Park, Y.G., Kim, S.J., Jung, H.Y., Kang, Y.M., Kang, S.M., Prasad, D.T., Kim, S.W., and Choi, M.S. (2004). Variation of ginkgolides and bilobalide contents in leaves and cell cultures of Ginkgo biloba L. Biotechnology and Bioprocess Engineering, 9, 35-40.

[44] Mesbah, M.K., Khalifa, S.I., Gindy, A.E., and Tawfik, KA. (2005). HPLC determination of certain flavonoids and terpene lactones in selected Ginkgo biloba L. Phytopharmaceuticals. Farmaco, 60(6-7),583-590.

[45] Van Beek, T.A. (2005). Ginkgolides and bilobalide: their physical, chromatographic and spectroscopic properties. Bioorganic and Medicinal Chemistry, 13(17), 5001-5012.

[46] Sevindik, O., Guclu, G., Agirman, B., Selli, S., Kadiroglu, P., Bordiga, M., Capanoglu, E., and Kelebek, H. (2022). Impacts of selected lactic acid bacteria strains on the aroma and bioactive compositions of fermented gilaburu (Viburnum opulus) juices. Food Chemistry, 378, 132079.

[47] Fransen, H.P., Pelgrom, S.M.G.J., Stewart-Knox, B., de Kaste, D., and Verhagen, H. (2010). Assessment of health claims, content, and safety of herbal supplements containing Ginkgo biloba. Food and Nutrition Research, 54, 5221.

[48] Chen, P., Ozcan, M., and Harnly, J. (2007). Chromatographic fingerprint analysis for evaluation of Ginkgo biloba products. Analytical and Bioanalytical Chemistry, 389(1), 251–61.

[49] Demirezer, L.Ö., Büyükkaya, A., Uçaktürk, E, Uz, A.K., Güvenalp, Z., and Palaska, E. (2014). Adulteration determining of pharmaceutical forms of Ginkgo biloba extracts from different international manufacturers. Records of Natural Products, 8, 4, 394-400.

[50] Dubber, M.J., and Kanfer, I. (2004). High-performance liquid chromatographic determination of selected flavonols in Ginkgo biloba solid oral dosage forms. Journal of Pharmaceutical Sciences, 24, 7

JSR A
Journal of Scientific Reports

APPENDIX A

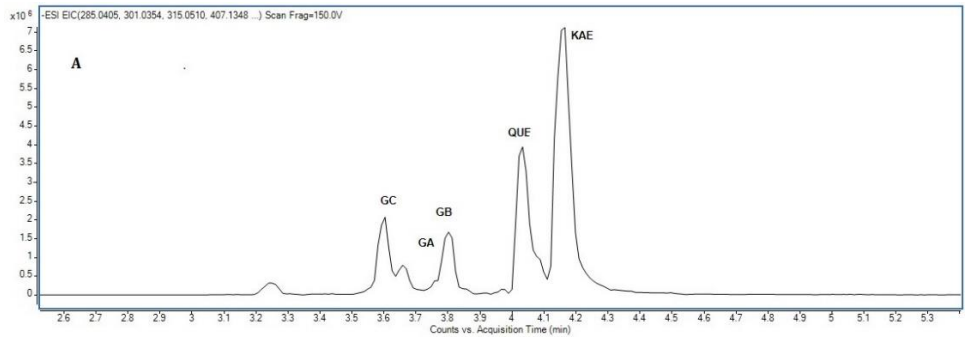

Figure A1. Chromatogram of A (dietary supplement) sample obtained from pharmacy.

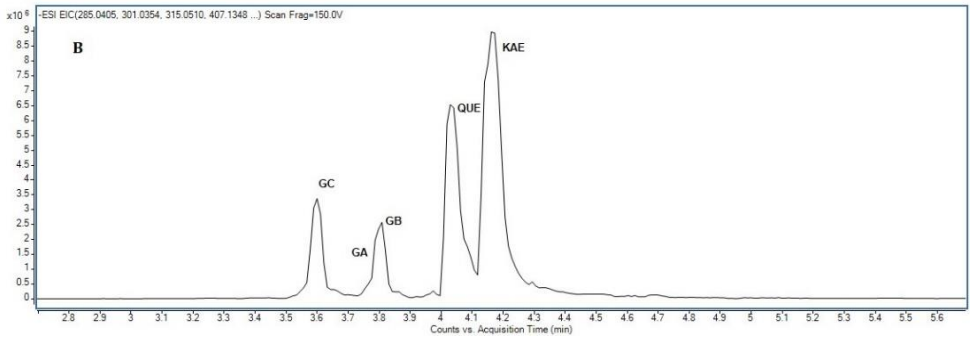

Figure A2. Chromatogram of B (dietary supplement) sample obtained from pharmacy.

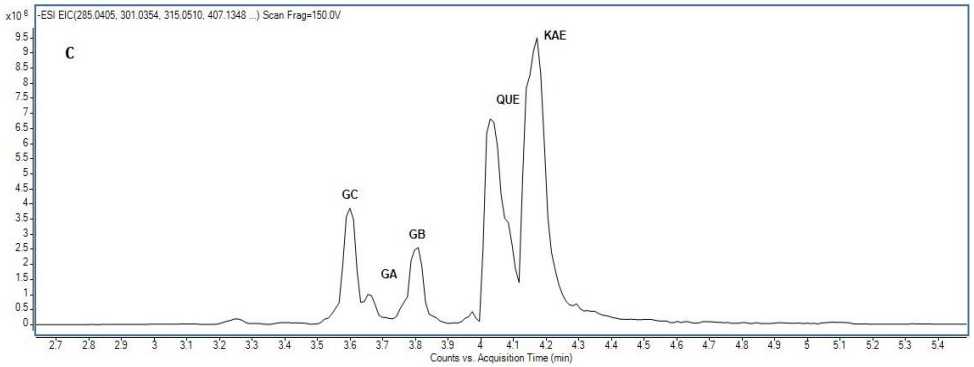

Figure A3. Chromatogram of C (dietary supplement) sample obtained from pharmacy.

JSR A
Journal of Scientific Reports

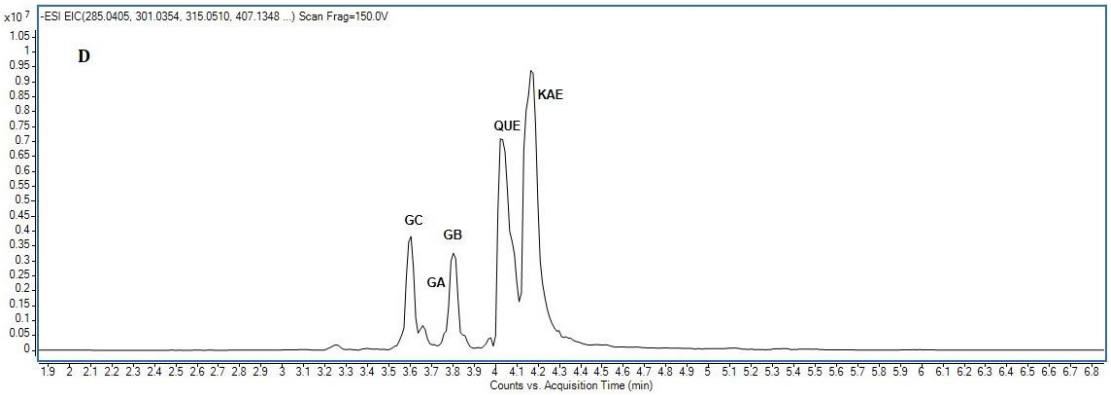

Figure A4. Chromatogram of D (drug) sample obtained from pharmacy.

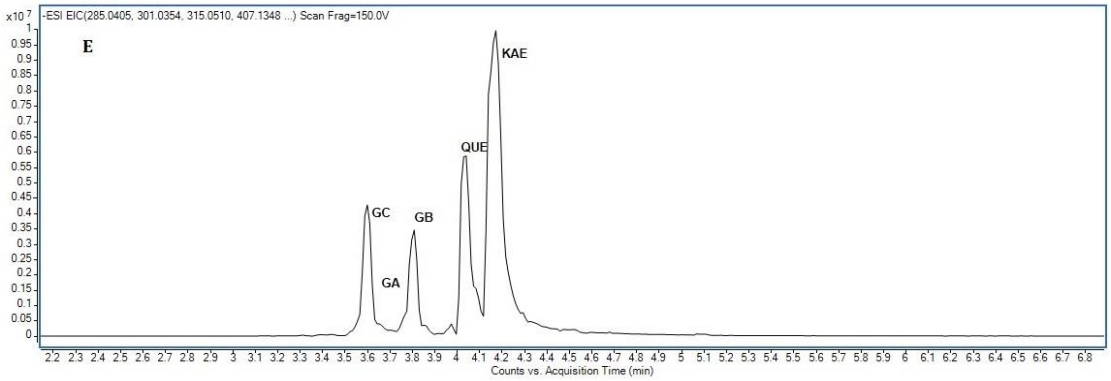

Figure A5. Chromatogram of E (drug) sample obtained from pharmacy.

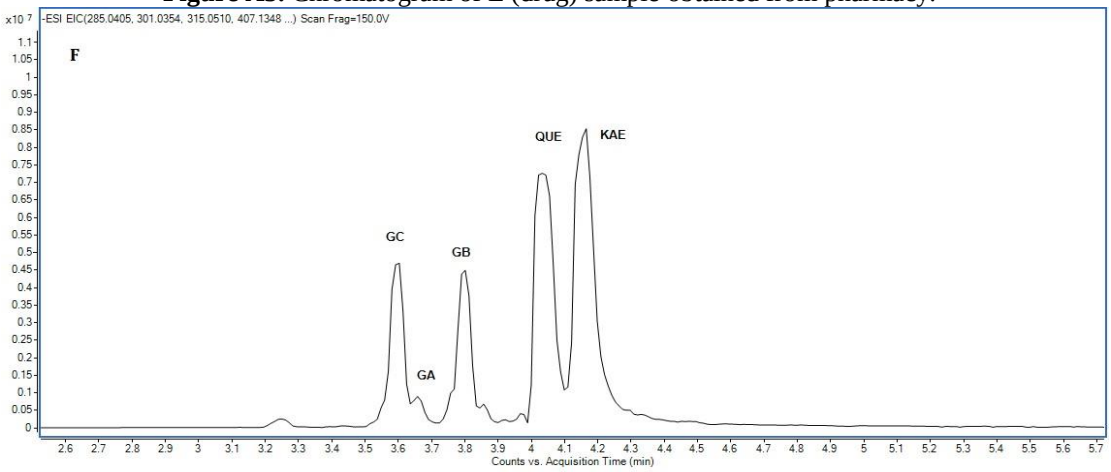

Figure A6. Chromatogram of F (drug) sample obtained from pharmacy.

JSR A
Journal of Scientific Reports

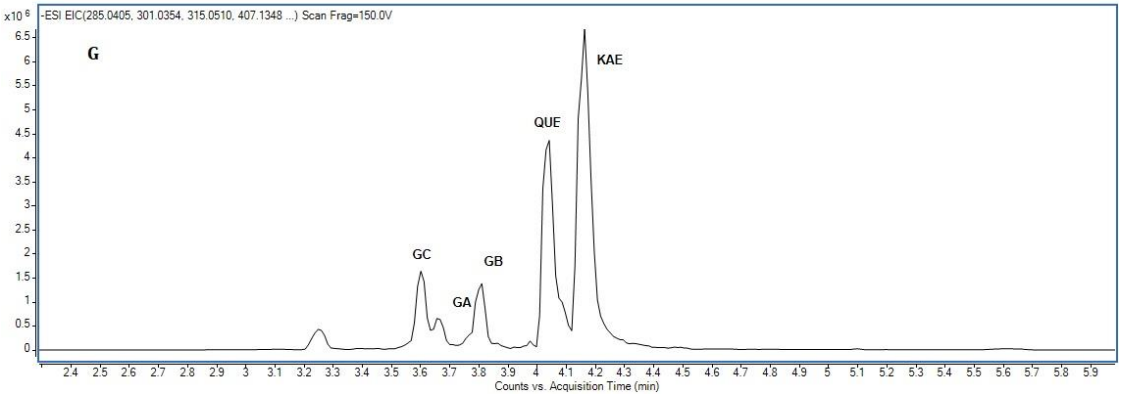

Figure A7. Chromatogram of G (dietary supplement) sample obtained from herbalist.

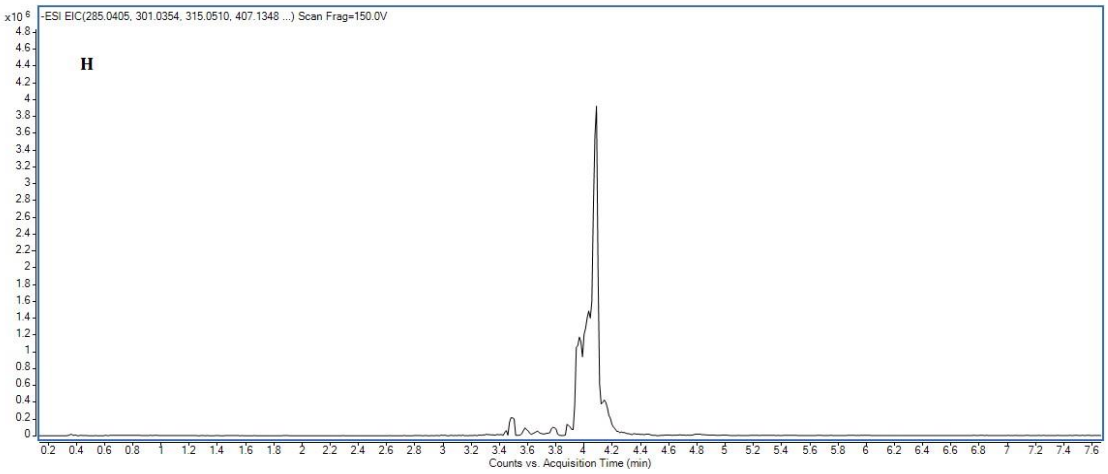

Figure A8. Chromatogram of H (dietary supplement) sample obtained from herbalist.

Kütahya Dumlupınar University
Institute of Graduate Studies

Journal of Scientific
Reports-A
E-ISSN: 2687-6167
Number 53, June 2023

RESEARCH ARTICLE

MULTI-METAL RECOVERY FROM FLOTATION TAILINGS WITH CITRIC ACID ON THE NACL MEDIA

Emine YOĞURTCUOĞLU[1*]

[1]Faculty of Engineering, Department of Mining Engineering, Niğde Ömer Halisdemir University, 51240, Niğde, Turkey, eyogurtcuoglu@ohu.edu.tr, ORCID: 0000-0002-9961-8809

Receive Date:27.01.2023 *Accepted Date: 29.03.2023*

ABSTRACT

After the flotation process of oxidized lead-zinc ores, the high amount of metal (especially zinc metal) in its content cannot be recovered and is stored as tailing. Ore and (therefore) tailings are found together with gangue minerals such as calcite, and dolomite, which are oxide/carbonate minerals. Precious minerals are zinc, lead, silver, and iron-containing minerals such as smithsonite, hydrozincite, plumbojarosite, and goethite. The particle size of the sample taken from this tailing was determined as d_{80}= 78.22µm. In order to recover these ore tailings with high metal content, the dissolution of citric acid, which is a weak organic acid, in NaCl medium was investigated. A basic experimental condition determined was applied as 0.5 M citric acid, 200 g/L NaCl, 1 hour time, 60 ℃ temperature, and 10% solids ratio. As a result, zinc, lead, silver and iron dissolved up to 66.85%, 56.53, 40.68, and 27.74%, respectively. According to the results of this experiment, keeping each of these parameters constant, 0.125-1 M citric acid, 50-400 g/L NaCl, 15-120 minutes leaching time, 25-95 ℃ leaching temperature, and 5-40% solids metal. The efficiency of the gain yields was tried to be determined. When the final results are examined, there are 60-80% zinc, 40-70% lead, 0.01-35% iron, and 11-83% silver recovery efficiencies. In light of these results, it is thought that industrial-scale improvements in multi-metal recovery from oxidized ore tailings may improve positive results.

Keywords: *Flotation tailings, Oxidized lead-zinc, Silver, Citric acid, NaCl, Leaching.*

1. INTRODUCTION

Lead-zinc ores are generally found in oxide, sulfide, and mixed forms. Among these mineralizations, the most enriched ores are sulfide ores, and they can be recovered by the flotation process [1-3]. In oxide ores, recovery for lead can be made by flotation. It is based on the principle of flotation by sulfurizing the ore surface and adding a collector such as a xanthate. One of the deposits in Turkey is located in the Zamantı region [4,5].

JSR A
Journal of Scientific Reports

Important oxidized zinc minerals such as smithsonite ($ZnCO_3$), willemite (Zn_2SiO_4), hydrozincite ($2ZnCO_3.3Zn(OH)_{2)}$, zincite (ZnO), and hemimorphite ($Zn_2SiO_3.H_2O$). Although these ores are generally found together with lead-containing minerals, they cannot be recovered by flotation like these minerals. High-grade zinc and iron minerals and low-grade lead can be found in the wastes of these flotation concentrates [6].

In general, lead oxide minerals are cerusite ($PbCO_3$), anglesite ($PbSO_4$), and jarosite-containing beudantite $PbFe_3(AsO_4)(SO_4)(OH)_6$, plumbojarosite $PbFe_6(SO_4)_4(OH)_{12}$ minerals [3, 7-10].

The dissolution reaction of citric acid ($C_6H_8O_7$) in water (Eq. (1)-(2)-(3)) and the reactions between this acid and some minerals of zinc (Eq. (4)) [11], lead (Eq. (5)), and iron (Eq. (6)) [12-14] are as follows:

$$C_6H_8O_{7(s)} + H_2O_{(l)} \leftrightarrow H_3O^+_{(aq)} + C_6H_7O_7^-{}_{(aq)} \quad (1)$$

$$C_6H_7O_7^-{}_{(s)} + H_2O_{(l)} \leftrightarrow H_3O^+_{(aq)} + C_6H_7O_7^{2-}{}_{(aq)} \quad (2)$$

$$C_6H_7O_7^{2-}{}_{(s)} + H_2O_{(l)} \leftrightarrow H_3O^+_{(aq)} + C_6H_7O_7^{3-}{}_{(aq)} \quad (3)$$

$$3ZnO_{(s)} + 2C_6H_8O_{7(aq)} \rightarrow 3\ Zn^{2+} + 2C_6H_7O_7^{3-}{}_{(aq)} + 3H_2O_{(l)} \quad (4)$$

$$1.5PbO + C_6H_8O_7 \leftrightarrow 1.5Pb^{2+} + C_6H_5O_7^{3-} + 1.5H_2O \quad (5)$$

$$Fe_3O_4 + C_6H_8O_7 + 2e^- \leftrightarrow 3FeO + C_6H_5O_7^{3-} + H_2O + H^+ \quad (6)$$

The reaction of zinc oxide with salt (NaCl) leaching (Eq. (7)) [15,16] occurs as follows:

$$ZnO + iCl^- + 2H^+ \rightarrow ZnCl_i^{2-i} + H_2O \quad (7)$$

i=1, 2, 3, 4

The dissolution of lead oxide minerals by salt leaching (Eq. (8)) [1, 17-21] is as follows:

$$PbSO_4 + 2Cl^- \rightarrow PbCl_2 + SO_4^{2-} \quad (8)$$

The dissolution reaction of silver with salt and/or hydrochloric acid is as follows (Eq. (9)) [22-24]:

$$Ag(s) + 2Cl^- + H^+ + ¼\ O_2(g) = AgCl_2^- + ½\ H_2O \quad (9)$$

For the recovery of lead and silver from lead sulfates in zinc smelter wastes, recovery by roasting, sulfuric acid, and salt leaching were investigated. Sulfides were oxidized step by step, followed by neutral leaching and chlorine dissolution, recoveries of 90-95% Pb, 60-70% Ag were achieved [25]; [26].

JSR A
Journal of Scientific Reports

Pressure leaching was carried out with nitric acid from concentrates containing Pb-Ag sulfide minerals. The best conditions for the study investigated at a nitric acid concentration of 0.13–0.65 M at operating conditions (130-170 °C) higher than the melting temperature of sulfur (119 °C), 90 min leaching time, in 0.65 M nitric acid medium, and leaching time at 130 °C. approximately 90% Ag and 80% Pb recovery was obtained [27].

Recovery of copper, zinc and lead from brass melting slag by hydrometallurgical processes was investigated. Metal extraction increases in acidic environment with an increase in temperature and in terms of the types of these acids, respectively, as sulfuric, hydrochloric and nitric acids [28].

Metal recovery was made from oxidized Zn/Pb ore by performing two-stage alkali leaching process. Firstly, the ore, which was reduced to a certain size (0.2 mm), was dissolved by caustic (NaOH) leaching process at 90℃ alkaline leaching temperature, 120 min leaching time. Then, metal recovery efficiencies of over 80% were obtained by leaching sodium sulfide ($Na_2S{\cdot}9H_2O$) at the same temperature [29].

Metal recoveries from zinc leaching wastes by sulphate roasting and water leaching processes were investigated. In this study, the ferric sulfate/zinc ferrite ratio was 1.2, and then dissolved with water at a roasting temperature of 640 °C for 1 hour. As a result of the experiments, the recovery efficiencies were 92.4% Zn, 93.3% Mn, 99.3% Cu, 91.4% Cd, and 1.1% Fe [30].

In light of all this research, this study was carried out in order to evaluate the metals in oxide ore flotation wastes with the dissolution efficiency of citric acid in a salt medium.

2. MATERIAL and METHOD

2.1. Material

The samples used in the experiments were taken from the oxide lead-zinc flotation tailings of the Havadan Mining (Kayseri, Yahyalı) Plant. The moisture of the tailings was dried at about 105 °C, blended, and the sample splits separated. Citric acid leaching was applied to these tailings in a NaCl medium. As test parameter values; 0.125-1 M citric acid concentration, 50-300 g/L sodium chloride concentration, 15-120 minutes leaching time, 25-95℃ leaching temperature, and 5-40% solids were investigated. All test results were compared with the experiment performed at 0.5 M citric acid and 200 g/L NaCl concentrations, 1-hour time, 60℃ temperature, and 10% solids.

Experiments were carried out in a fume hood with a magnetic stirrer with heater. After dissolving, the liquid solution was separated, and the solid was washed and precipitated. Then these samples by drying were sent for analysis.

When the XRF analysis and chemical analysis results of the test sample were examined (Table 1); 2.29% Pb, and 6.28% Zn were detected. In addition, it was determined that the densest elements were Fe (19.40%) and Si (4.39%).

JSR A
Journal of Scientific Reports

Table 1. The chemical analysis of test sample [10].

Element	%	Element	%
Fe	19.40	**Pb**	2.29
Si	4.39	**As**	0.33
Zn	6.28	**Mg**	0.38
Al	0.98	**K**	0.24
Ca	2.31	**Ti**	0.16

In the particle size distribution analysis of the test sample (Figure 1), it was found that d_{80}= 78.22 µm.

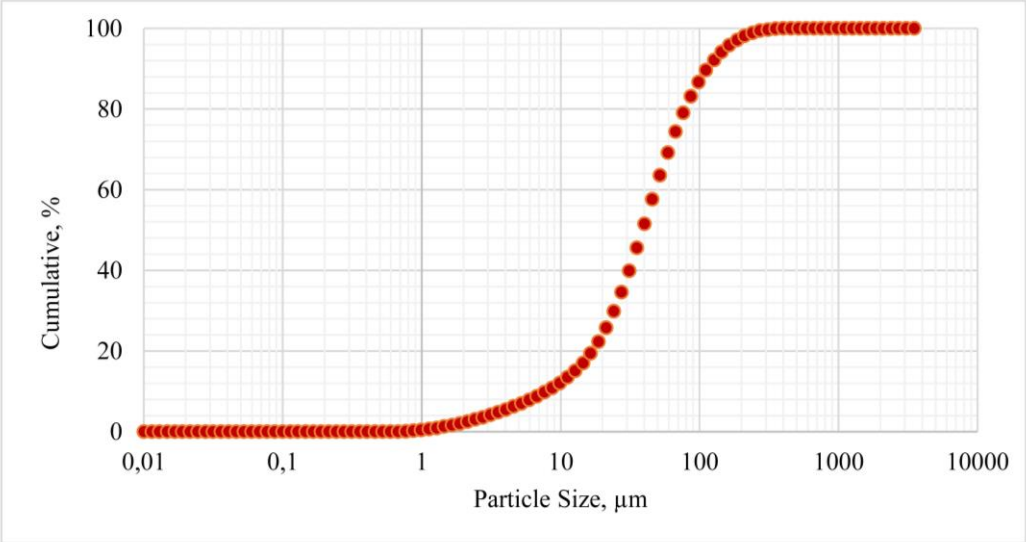

Figure 1. Particle size distribution [10].

In XRD analysis of the test sample (Figure 2), calcite ($CaCO_3$), dolomite ($CaMg(CO_3)_2$), goethite ($FeO(OH)$), hydrozincite ($ZnCO_3.3Zn(OH)_2$), plumbojarosite ($PbFe_6(SO_4)_4(OH)_{12}$), quartz (SiO_2), and smithsonite ($ZnCO_3$) minerals were determined [31].

JSR A
Journal of Scientific Reports

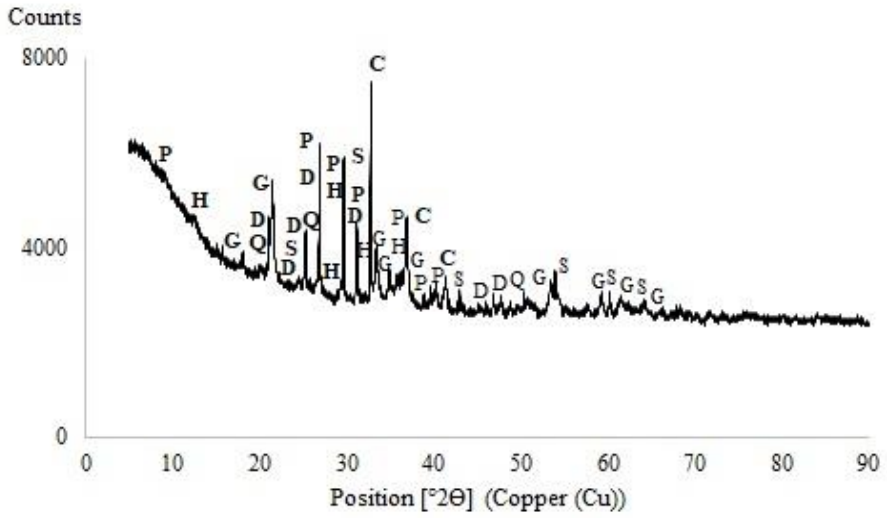

Figure 2. XRD analysis of the tailing sample used in the experiment (C: calcite, D: dolomite, G: goethite, H: hydrozincite, P: plumbojarosite, Q: quartz, S: smithsonite) [31].

3. RESULTS and DISCUSSION

As shown in Figure 3 below, an experiment was conducted under the conditions of 0.5 M citric acid and 200 g/L NaCl concentration, 60℃ leaching temperature, 1 hour leaching time, and 10% solids ratio. As a result of the experiment, the metal recoveries are 40.68%Ag, 56.53%Pb, %66.85Zn, and 27.74%Zn, respectively.

JSR A
Journal of Scientific Reports

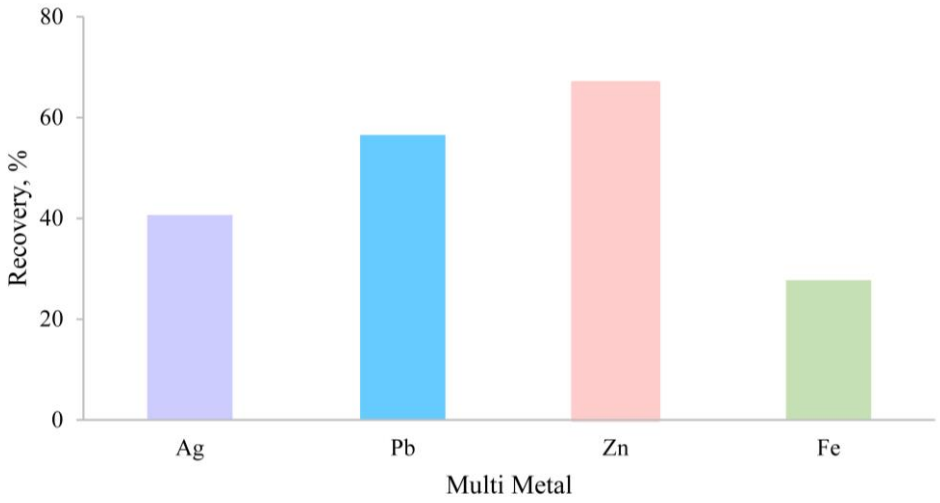

Figure 3. According to stable test, multi-metal recoveries (%) [0.5 M citric acid and 200 g/L NaCl concentration, 60℃ leaching temperature, 1 hour leaching time, 10% solids].

3.1. The Effect of Solid Ratio

In the experiments in which the % solids ratio parameter was examined (Figure 4), 0.5 M citric acid concentration, 200 g/L NaCl concentration, 60℃ leaching temperature and 1 hour leaching time were kept constant. As a result of the experiment, it was observed that the metal recovery efficiency increased as the % solid ratio decreased. Zn recoveries were found to be 17.92-66.85%, Pb recoveries 37.19%-56.53% and Fe 0.12-27.74%. Only Ag recovery efficiencies (26-83%) increased between 20-40%. At the solubility of smithsonite ore in ammonium chloride medium, zinc recovery reached up to 91% in 5 M ammonium chloride, 240 minutes leaching time, 90°C leaching temperature, 84–110 micron grain size and 1/10 solid ratio (g/mL) experiments [32]. In the NaOH dissolution process from refractory hemimorphite zinc oxide ore, 6-12 solid ratio was investigated. Metal recoveries are obtained as 73% Zn, 45% Al, 11% Pb, 5% Cd, and <0.1% Fe at 65-76 µm grain size, 5 M sodium hydroxide, and 10:1 liquid:solid ratio, at 358 K, 2 hours leaching time [33].

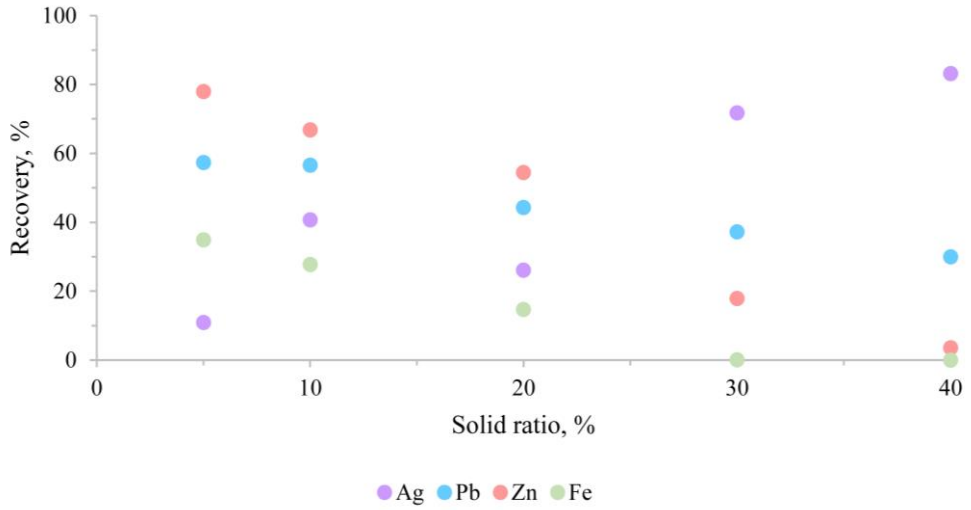

Figure 4. Multi-metal recovery efficiencies obtained according to % solid ratio [0.5 M citric acid concentration, 200 g/L NaCl concentration, 60°C leaching temperature, 1 hour leaching time].

3.2. The Effect of Citric Acid Concentration

In the citric acid concentration difference experiments (Figure 5), 200 g/L NaCl concentration, 60℃ leaching temperature, 1 hour leaching time and 10% solids ratio were kept constant. As a result of the experiment, it was observed that the Zn recovery (16.59-66.85%), Pb recovery (36.16%-56.53%), and Fe recovery (19.39-27.74%) increased as the concentration increased. Recovery of silver decreased by about 20% at 1M citric concentration.

The concentration of citric acid in the range of 0.01-0.5 M in the dissolution of zinc oxide was investigated. It reached up to 70% Zn extraction at a concentration of 0.5 M acid in 60 minutes at 25 °C [12].

JSR A
Journal of Scientific Reports

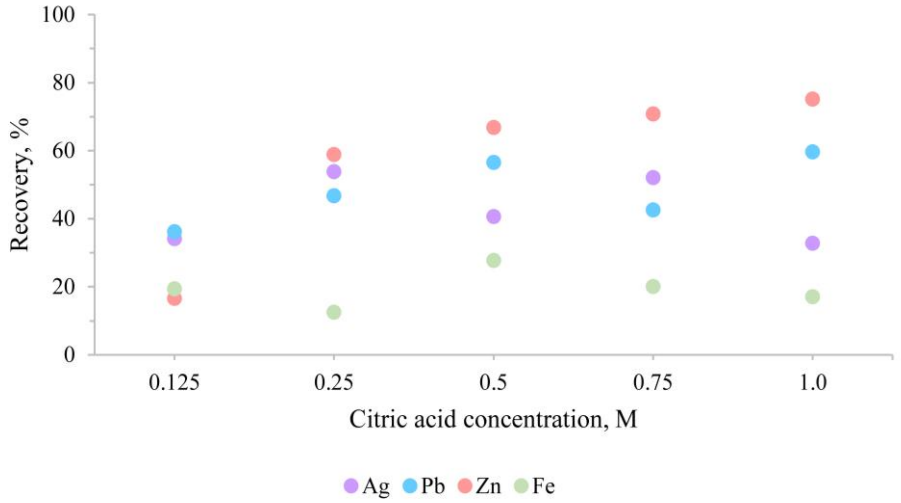

Figure 5. Multi-metal recovery obtained according to citric acid concentration difference [at 200 g/L NaCl concentration, 60°C leaching temperature, 1 hour leaching time, 10% solids].

3.3. The Effect of Leaching Time

In the experiments in which the leaching times were examined (Figure 6), the parameters of 0.5M citric acid concentration, 200 g/L NaCl concentration, 60℃ leaching temperature and 10% solids ratio were selected in the leaching time range of 15-120 minutes. The recoveries of metals are 13.70-40.68% for Ag, 42.89-56.53% for Pb, 47.22-66.85% for Zn, and 14.09-27.74% for Fe. It was observed that the leaching time for Ag, Pb, and Fe increased up to 60 minutes with the increase of the time in this parameter. Extraction of zinc and other precious metals from low grade zinc oxide ore with iminodiacetate aqueous solution was investigated. The leaching time was studied between 1-6 hours. Optimum zinc recovery was achieved at 76.6% in 4 hours leaching time, 70 °C, pH 8, L/S 5:1, and 0.9 M iminodiacetate aqueous solution [34]. Zinc recoveries (42-44%) in the leaching time (between 30-150 minutes) do not differ much in the application of 1/10 solids ratio, 25°C leaching temperature and 0.5 M citric acid on low grade ZnO wastes [35].

JSR A
Journal of Scientific Reports

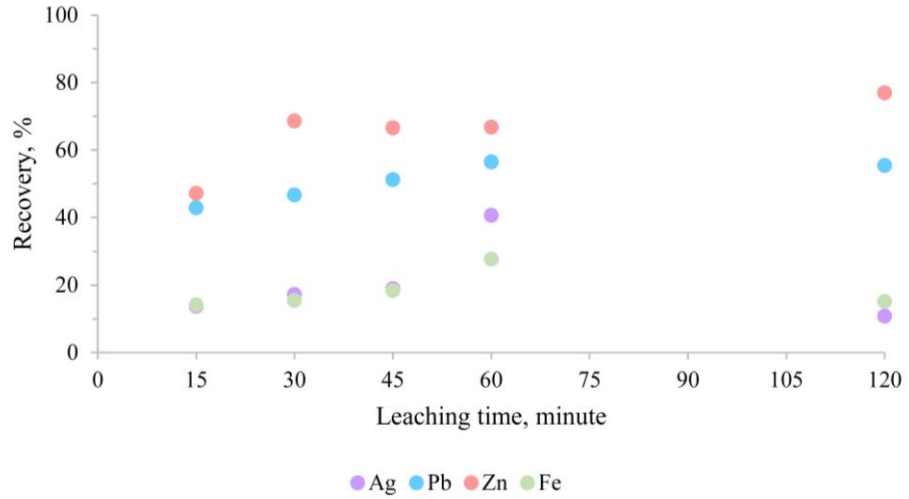

Figure 6. Multi-metal recovery efficiencies obtained according to leaching times [at 0.5M citric acid concentration, 200 g/L NaCl concentration, 60°C leaching temperature, 10% solids].

3.4. The Effect of Leaching Temperature

In the experiments in which leaching temperatures (25-95℃) were investigated (Figure 7), the parameters of 0.5M citric acid concentration, 200 g/L NaCl concentration, 60 minutes leaching time, and 10% solids ratio were selected. In the recovery of metals, it was determined that Ag and Fe recoveries decreased at 95 °C, lead had close values, and zinc increased in direct proportion with the increase (29.15-78.59%) in temperature. In the aforementioned study, where the recovery of ZnO ore with citric acid was mentioned, in the temperature increase examination, the solubility increased towards 60 minutes leaching time at 25-50℃ temperature ranges and was obtained around 90% [12]. When the effect of the leaching temperature parameter of zinc oxide wastes was investigated (30-80℃), the zinc recovery reached up to 65% in 0.5 M concentration of citric acid, 1:10 solid-to-liquid ratio, and 60 min reaction time [35].

JSR A
Journal of Scientific Reports

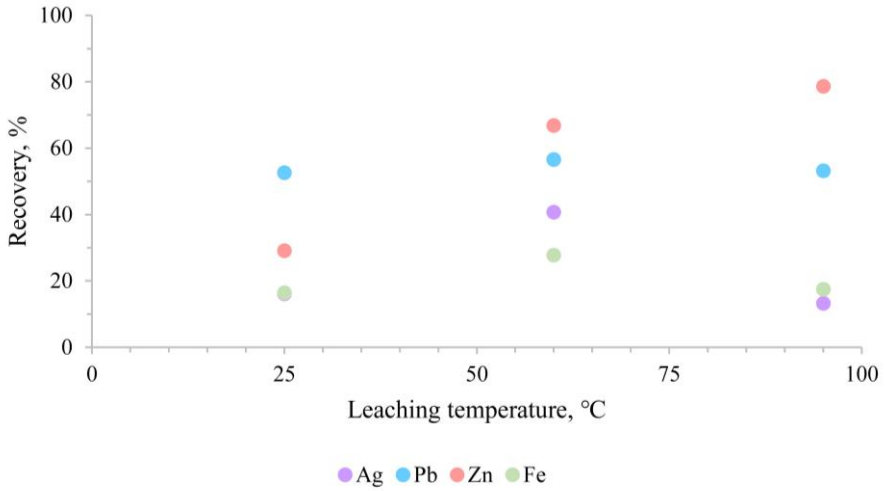

Figure 7. Multi-metal recovery efficiencies according to leaching temperatures [at 0.5M citric acid concentration, 200 g/L NaCl concentration, 1 hour leaching time, 10% solids].

3.5. The Effect of NaCl Concentration

In the experiments where NaCl concentrations were examined (Figure 8), 0.5M citric acid concentration, 60℃ leaching temperature, 1 hour leaching time, and 10% solid ratio were constant. The metal recoveries are 15.02-40-68% for Ag, 42.60-56.53% for Pb, 56.16-78.50% for Zn, and 13.43-27.74% for Fe, respectively. When the citric acid concentration in the chlorine medium (0.05 mol/L) was investigated, it was observed that the zinc solubility reached nearly 100% in leaching times of up to 60 minutes in the temperature range of 25-40 ℃ [12]. Zinc recovery (90%) was obtained after sulphate (H_2SO_4) roasting, and lead (92%) and silver (62%) were recovered in the subsequent NaCl dissolution process. The NaCl concentration range was studied as 60-320 g/L. Ag was obtained in the range of 60-120 g/L with 55-63% and Pb in the range of 60-315 g/L with 17-92% recovery efficiencies [36].

JSR A
Journal of Scientific Reports

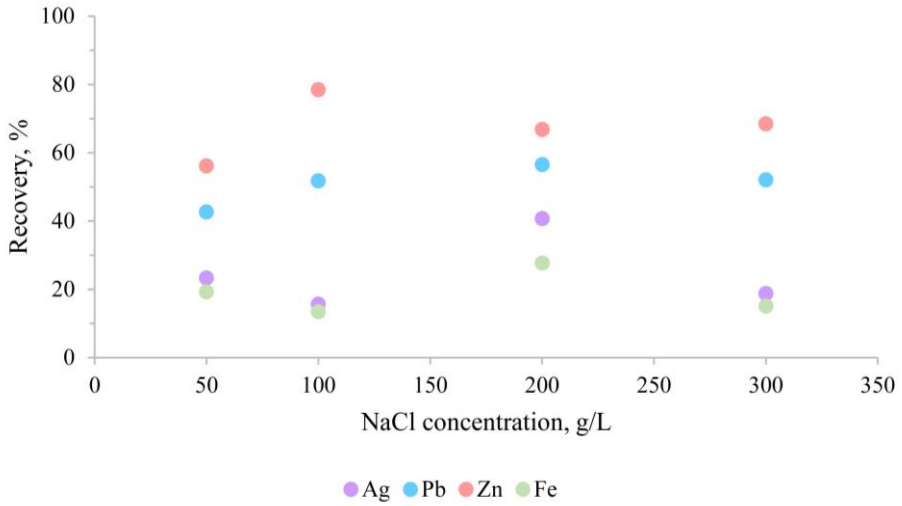

Figure 8. Multi-metal recovery efficiencies according to NaCl concentrations [at 0.5M citric acid concentration, 60°C leaching temperature, 1 hour leaching time, 10% solids].

In the metal recovery of citric acid leaching, it was stated that the metal recovery took place in the following order [13,14] (Eq. (10)):

Citric Acid Zn>Cr>Pb>Mn>Fe (10)

Similarly, in these experiments, it is seen that the most intense zinc is recovered, followed by lead and finally iron. In addition, less recovery of iron in the recovery of precious metals such as lead, zinc and silver is a result of the selective behavior of organic acids [10,11, 37,38].

4. CONCLUSIONS

In this study, flotation tailings of oxidised Pb/Zn ores were investigated in terms of solubility of organic acids in citric acid and NaCl medium.

The tailing sample used in the experiments contains 2-3% Pb, 5.5-6.5% Zn, 19-20% Fe, and 20-35g/t Ag, and generally consists of smithsonite, hydrozincite, plumbojarosite, and goethite minerals. The particle size of the test sample was below about 100 microns, and re-grinding was not required.

In the experiment performed at 0.5 M citric acid and 200 g/L NaCl concentration, 60 minutes leaching time, 60℃ leaching temperature, and 10% solids, the recovery efficiencies of the metals were obtained as 66-67% Zn, 56-57%Pb, 27-28% Fe, and 40-41% Ag. These experimental conditions were compared in all other experiments performed.

When the % solid ratio difference was examined, it was determined that as the ratio decreased, metal recovery efficiencies (18-78% Zn, 37-58% Pb, 0-35% Fe, and 11-84% Ag) increased (except for silver only). This increase in silver can be explained by the reasons such as the low amount of availability and therefore the solubility may be faster than other elements.

According to the experiments investigating the citric acid concentration difference (0.125-1M), 17-76% zinc, 36-60% lead, 13-28% iron, and 33-54% silver metal recovery were obtained.

In the 15-120 minute leaching time differences experiments, similar to the other experiments, it was determined that zinc had the highest recovery efficiency and recovery efficiencies of around 57/80%, especially in terms of Pb/Zn.

It was determined that zinc reached 79% efficiency in 25-95 ℃ leach temperature experiments.
In the NaCl concentration differences experiments, zinc was obtained with recovery efficiencies in the range of 56-79%, lead 43-57%, iron 14-28%, and silver 15-41%.

As a result, it has been determined that chlorine leaching of citric acid, a low-cost organic acid, is possible in the recovery of multi-metals from these oxidised ore tailings, especially in terms of Pb/Zn (60 and 80%). In addition, as an important advantage of these acids, it is thought that iron has lower gains, and silver is important in terms of precious metal recovery, although it varies.

ACKNOWLEDGMENT

I would like to thank Havadan Mining for sample supply and analysis support.

REFERENCES

[1] Turan, M.D., Altundoğan, H.S., and Tümen, F. (2004). Recovery of zinc and lead from zinc plant residue. Hydrometallurgy, 75, 169–176. https://doi.org/10.1016/j.hydromet.2004.07.008

[2] Kursunoglu, S., Top, S., and Kaya, M. (2020). Recovery of zinc and lead from Yahyali non-sulphide flotation tailing by sequential acidic and sodium hydroxide leaching in the presence of potassium sodium tartrate. Transactions of Nonferrous Metals Society of China, 30, 3367–3378. https://doi.org/10.1016/S1003-6326(20)65468-1

[3] Hussaini, S., Kursunoglu, S., Top, S., Ichlas, Z.T., and Kaya, M. (2021). Testing of 17-different leaching agents for the recovery of zinc from a carbonate-type Pb-Zn ore flotation tailing. Miner. Eng., 168, 106935, 1–29. https://doi.org/10.1016/j.mineng.2021.106935

[4] Şentürk, B., Özbayoğlu, G., and Atalay, Ü. (1993). Flotation of lead-zinc carbonate ore of Kayseri-Zamanti district (in Turkish). Türkiye XIII Madencilik Kongresi, 459–466.

[5] Önal, G., Bulut, G., Gül, A., Kangal, O., Perek, K.T., and Arslan, F. (2005). Flotation of Aladağ

oxide lead-zinc ores. Minerals Engineering, 18, 279–282. https://doi.org/10.1016/j.mineng.2004.10.018

[6] Hosseini, S.H. and Taji, M. (2015). Flotation behavior of Iranian oxidized zinc ore using different types of collectors (cationic, anionic and mixed (cationic/anionic)). International Journal of Mining Engineering and Mineral Processing, 4, 18–27. https://doi.org/10.5923/j.mining.20150401.03

[7] Rashchi, F., Dashti, A., Arabpour-Yazdi, M., and Abdizadeh, H. (2005). Anglesite flotation: a study for lead recovery from zinc leach residue. Minerals Engineering, 18, 205–212. https://doi.org/10.1016/j.mineng.2004.10.014

[8] Pirajno, F., Burlow, R., and Huston, D. (2010). The Magellan Pb deposit, Western Australia; a new category within the class of supergene non-sulphide mineral systems. Ore Geology Reviews, 37, 101–113. https://doi.org/10.1016/j.oregeorev.2010.01.001

[9] Koski, R.A. (2010). Supergene ore and gangue characteristics. USGS, 181-189.

[10] Yoğurtcuoğlu, E. (2022). Metal recovery from oxidized ore tailings with organic acid (in Turkish). 2nd International Conference on Environment, Technology and Management (ICETEM), 263–271.

[11] Demir, F., Laçin, O. and Dönmez, B. (2006). Leaching kinetics of calcined magnesite in citric acid solutions. Ind. Eng. Chem. Res., 45, 1307–1311. https://doi.org/10.1016/j.jiec.2009.09.014

[12] Larba, R., Boukerche, I., Alane, N., Habbache, N., Djerad, S., and Tifouti, L. (2013). Citric acid as an alternative lixiviant for zinc oxide dissolution. Hydrometallurgy, 134–135, 117–123. https://doi.org/10.1016/j.hydromet.2013.02.002

[13] Halli, P., Hamuyuni, J., Leikola, M. and Lundström, M. (2018). Developing a sustainable solution for recycling electric arc furnace dust via organic acid leaching. Minerals Engineering, 124, 1–9. https://doi.org/10.1016/j.mineng.2018.05.011

[14] Kaya, M., Hussaini, S., and Kursunoglu, S. (2020). Critical review on secondary zinc resources and their recycling technologies. Hydrometallurgy, 195, 105362. https://doi.org/10.1016/j.hydromet.2020.105362

[15] Cengiç, S. (2007). Recovery of zinc wastes by hydrometallurgical methods (in Turkish). Yildiz Teknik Üniversitesi.

[16] Xia, Z., Zhang, X., Huang, X., Yang, S., Chen, Y., and Ye, L. (2020). Hydrometallurgical stepwise recovery of copper and zinc from smelting slag of waste brass in ammonium chloride solution. Hydrometallurgy, 197, 105475. https://doi.org/10.1016/j.hydromet.2020.105475

[17] Zhang, J., Hendrix, J.L., Kappes, D.W., and Albert, T.E. (1993). Recovery of gold and silver from a sulfidic ore cyanide and chloride leaching after chlorination roasting. Society for Mining, Metallurgy & Exploration, 311–326.

[18] Liao, M.X. and Deng, T.L. (2004). Zinc and lead extraction from complex raw sulfides by sequential bioleaching and acidic brine leach. Minerals Engineering, 17, 17–22. https://doi.org/10.1016/J.MINENG.2003.09.007

[19] Ruşen, A., Sunkar, A.S., and Topkaya, Y.A. (2008). Zinc and lead extraction from Çinkur leach residues by using hydrometallurgical method. Hydrometallurgy, 93, 45–50. https://doi.org/10.1016/J.HYDROMET.2008.02.018

[20] Farahmand, F., Moradkhani, D., Safarzadeh, M.S., and Rashchi, F. (2009). Brine leaching of lead-bearing zinc plant residues: process optimization using orthogonal array design methodology. Hydrometallurgy, 95, 316–324. https://doi.org/10.1016/j.hydromet.2008.07.012

[21] Silwamba, M., Ito, M., Hiroyoshi, N., Tabelin, C.B., Fukushima, T., Park, I., Jeon, S., Igarashi, T., Sato, T., Nyambe, I., Chirwa, M., Banda, K., Nakata, H., Nakayama, S., and Ishizuka, M. (2020). Detoxification of lead-bearing zinc plant leach residues from Kabwe, Zambia by coupled extraction-cementation method. Journal of Environmental Chemical Engineering, 8, 104197. https://doi.org/10.1016/j.jece.2020.104197

[22] Gammons, C.H. and Williams-Tones, A.E. (1995). The solubility of Au-Ag alloy + AgCl in HCl/NaCl solutions at 300°C: new data on the stability of Au (1) chloride complexes in hydrothermal fluids. Geochimica et Cosmochimica Acta, 59, 3453–3468. https://doi.org/10.1016/0016-7037(95)00234-Q

[23] Tagirov, B.R., Zotov, A. V., and Akinfiev, N.N. (1997). Experimental study of dissociation of HCl from 350 to 500°C and from 500 to 2500 bars: thermodynamic properties of HCl°(aq). Geochimica et Cosmochimica Acta, 61, 4267–4280. https://doi.org/10.1016/S0016-7037(97)00274-3

[24] Bahram, B. and Javad, M. (2011). Chloride leaching of lead and silver from refractory zinc plant residue. Research Journal of Chemistry and Environment, 15, 1–8.

[25] Raghavan, R., Mohanan, P.K., and Patnaik, S.C. (1998). Innovative processing technique to produce zinc concentrate from zinc leach residue with simultaneous recovery of lead and silver. Hydrometallurgy, 48, 225–237. https://doi.org/10.1016/S0304-386X(97)00082-0

[26] Raghavan, R., Mohanan, P.K., and Swarnkar, S.R. (2000). Hydrometallurgical processing of lead-bearing materials for the recovery of lead and silver as lead concentrate and lead metal. Hydrometallurgy, 58, 103–116. http,s://doi.org/10.1016/S0304-386X(00)00108-0

[27] Zárate-gutiérrez, R., Lapidus, G.T., and Morales, R.D. (2010). Hydrometallurgy pressure

leaching of a lead–zinc–silver concentrate with nitric acid at moderate temperatures between 130 and 170 °C. Hydrometallurgy, 104, 8–13. https://doi.org/10.1016/j.hydromet.2010.04.001

[28] Basir, S.M.A. and Rabah, M.A. (1999). Hydrometallurgical recovery of metal values from brass melting slag. Hydrometallurgy, 53, 31–44.

[29] Liu, Q., Zhao, Y., and Zhao, G. (2011). Production of zinc and lead concentrates from lean oxidized zinc ores by alkaline leaching followed by two-step precipitation using sulfides. Hydrometallurgy, 110, 79–84. https://doi.org/10.1016/J.HYDROMET.2011.08.009

[30] Jiang, G., Peng, B., Liang, Y., Chai, L., Wang, Q., Li, Q., and Hu, M. (2017). Recovery of valuable metals from zinc leaching residue by sulfate roasting and water leaching. Transactions of Nonferrous Metals Society of China (English edition), 27, 1180–1187. https://doi.org/10.1016/S1003-6326(17)60138-9

[31] Yoğurtcuoğlu, E. (2022). Evaluation of flotation wastes of oxidised ores (in Turkish). IV International Turkic World Congress on Science and Engineering (TURK-COSE), 1098–1104.

[32] Ju, S., Motang, T., Shenghai, Y., and Yingnian, L. (2005). Dissolution kinetics of smithsonite ore in ammonium chloride solution. Hydrometallurgy, 80, 67–74. https://doi.org/10.1016/j.hydromet.2005.07.003

[33] Chen, A., Zhao, Z. W., Jia, X., Long, S., Huo, G., and Chen, X. (2009). Alkaline leaching Zn and its concomitant metals from refractory hemimorphite zinc oxide ore. Hydrometallurgy, 97, 228–232. https://doi.org/10.1016/j.hydromet.2009.01.005

[34] Dou, A.C., Yang, T.Z., Yang, J.X., Wu, J.H., and Wang, A. (2011). Leaching of low grade zinc oxide ores in Ida^{2-}- H_2O system. Transactions of Nonferrous Metals Society of China (English edition), 21, 2548–2553. https://doi.org/10.1016/S1003-6326(11)61049-2

[35] Irannajad, M., Meshkini, M., and Azadmehr, A.R. (2013). Leaching of zinc from low grade oxide ore using organic acid. Physicochemical Problems of Mineral Processing, 49, 547–555. https://doi.org/10.5277/ppmp130215

[36] Güler, E., Seyrankaya, A., and Cöcen, I. (2011). Hydrometallurgical evaluation of zinc leach plant residue. Asian Journal of Chemistry, 23, 2879–2888.

[37] Yoğurtcuoğlu, E. (2022). Usage of acetic acid for boric acid production from boron wastes. Niğde Ömer Halisdemir University Journal of Engineering Sciences, 11, 819–825. https://doi.org/10.28948/ngmuh.

[38] Yoğurtcuoğlu, E. (2022). The citric acid leaching of boron process wastes (early access). Canadian Metallurgical Quarterly, 1–18. https://doi.org/10.1080/00084433.2022.2131132

Kütahya Dumlupınar University
Institute of Graduate Studies

Journal of Scientific
Reports-A
E-ISSN: 2687-6167
Number 53, June 2023

RESEARCH ARTICLE

THE IMPORTANCE OF STATISTICS ON OCCUPATIONAL ACCIDENTS AND OCCUPATIONAL DISEASES IN THE WORLD AND IN TÜRKİYE BETWEEN 2000-2020

Şahin YUVKA[1*], Edip ZORLU[2]

[1] Kutahya Dumlupinar University, Faculty of Engineering, Kutahya, sahin.yuvka@dpu.edu.tr , ORCID: 0000-0002-3219-2321
[2] Malatya Risk JHSU, Malatya, edipzorlu@hotmail.com, ORCID: 0009-0003-7927-3211

Receive Date:24.04.2023 *Accepted Date: 18.05.2023*

ABSTRACT

Increasing industrialization with the developing technology has brought the risk factors that negatively affect the employees in the working environment. Occupational accidents and occupational diseases occur due to these risk factors. With the effective implementation of occupational health and safety rules, occupational accidents and occupational diseases can be prevented. It is very important to regularly record all data related to work accidents and occupational diseases and to take necessary measures by analyzing these data. In particular, the data on the number of work accidents, death rates after work accidents, occupational diseases, and death rates due to occupational diseases are an indicator of the economic and social development of countries. In this study, evaluations were made about preventive and remedial activities by comparing statistical data on work accidents and occupational diseases in our country and in the world.

Keywords: *Occupational Disease, Occupational Accident, Year 2000 and After, World, Türkiye*.

1. INTRODUCTION

Occupational accidents caused by unconscious or unexpected mistakes in business life and occupational diseases arising from the nature of work, which are increasing by industrialization, continue to be an important problem for employees, employers and governments. According to the data of the International Labor Organization (ILO), every year over 2.3 million women and men die at work from an occupational injury or disease. Over 350,000 deaths are due to fatal accidents and almost 2 million deaths are due to fatal work-related diseases. The ILO also estimates that 160 million cases of non-fatal work-related diseases occur annually. These estimates imply that every day approximately 6,400 people die from occupational accidents or diseases and that 860,000 people are injured on the job[1]. The main reason for this is the inadequacy of the inspections for occupational health and safety, and the economic invoice to be created by the cost to be spent for these audits is damaging the economy of employers and states due to occupational accidents and occupational diseases [2],[3] In our country, which is placed near the top of the world ranking in the field of

JSR A
Journal of Scientific Reports

occupational accidents and occupational diseases, according to the data of the Social Security Institution in 2020; there are more than 17 million 4a status employees in Türkiye in 2020 and 384,262 work accidents and 1,231 deaths occurred due to work accidents in the same year. 908 occupational diseases were diagnosed and 5 of them resulted in death [4].

The whole purpose of occupational health and safety practices is to prevent the occurrence of work accidents and occupational diseases. Prevention of occupational accidents and occupational diseases ensures significant gains from the point of employees, employers and government. The loss of people with occupational accidents and occupational diseases, which is the core element of the production, should not be considered only a loss of life and injury. Besides, it creates plenty of unfavorable pictures for employers, employees, and governments such as a decrease in productivity of enterprises, an increase in costs, indemnity payments, treatment, care and recovery expenditures. Occupational health and safety services are becoming an increasingly important issue. The researches on the subject revealed the fact that all occupational accidents could be prevented unless it is a result of unexpected incidents such as natural disasters. Besides, due to the solution to the essential problem is human-oriented, it necessitates the implementation of all preventative practices and carefully monitoring and examination. Preventive approaches related to occupational health and safety have been intensively discussed in public, especially after work accidents in the mining and construction sectors that have occurred in our country in recent years. Under the guidance of the Ministry of Labor, more examinations and research are being made by universities, non-governmental organizations, professional associations, employers and unions to take all precautions about the subject and reports are being published. It is of great importance to act with the logic that taking all kinds of precautions related to occupational accidents and occupational diseases is cheaper than paying the costs of death, disablement and illness which are resultant of the state of not taking precautions. Work accidents have great importance in terms of the sustainability of enterprises due to both costs and environmental impacts and cause serious social and economic problems as a consequence of injuries and loss of lives.

Determining the existing hazards in the workplace and controlling the risks that may occur is effective in reducing work accidents and occupational diseases [5]. In this study, statistical data on occupational accidents and occupational diseases that occurred in the world and in our country were compared. Our positive and negative aspects have been tried to be determined in the view of these obtained data. Evaluations on the subject have been made.

2. GENERAL CONCENPTS RELATED to OCCUPATIONAL HEALTH and SAFETY

2.1. Occupational Health and Safety

According to the principles of the World Health Organization (WHO) and the International Labor Organization (ILO), occupational health and safety is defined as bringing physical, mental and common health, safety and prosperity of all workers to the highest level and preserving this level regardless of their contract types, extinguishing the unhealthy results that may arise from work environment, environmental impacts and production, removing the risk factors that affect mental and physical integrity of workers, creating work environments that protect mental and physical health of employees. There are many estimative or incalculable hazards and risks in every work. This situation

threatens employees, employers, machinery-equipment on the factory floor and environment. Occupational health and safety is essential to remove or reduce these hazards and risks to the lowest level. According to the International Labor Organization and World Health Organization Expert Committee, occupational health is "An area of work in public health to promote and maintain the highest degree of physical, mental and social well-being of workers in all occupations". Five basic principles have been defined for the success of occupational health systems. These; protection and prevention, adaptation, promotion and development, treatment and recovery and primary care health services. As understood from these definitions, occupational health and safety is a multidisciplinary science that requires occupational health and safety specialists, workplace doctors and allied health personnel to collaborate with business officials and act as a team in our country's conditions [6].

2.2. Occupational Accident

There are many definitions of occupational accidents according to each institution. According to WHO, an occupational accident is defined as an "Unplanned event that often leads to personal injuries, damage to machines, tools and equipment, and causes production to stop" [7]. ILO defines it as "Job accident is an unexpected event that leads to a certain harm or injury".

In our country, according to the Social Security and General Health Insurance Law No 5510, the occupational accident is defined as; "It is an event that occurs while the insured is at the workplace, due to the work carried out by the employer, if the insured works independently on his/her own behalf and account due to the work performing, when the insured working for an employer is sent to another place outside the workplace as an employee without performing his/her main job, in the times allocated for breastfeeding insured woman to give milk to her child in accordance with the labor legislation, during the insured's travel to and from the place of work with a vehicle provided by the employer and causes an insured person to become physically or mentally handicapped immediately or afterward [8].

According to the Occupational Health and Safety Law No 6331, "Occupational accident is an event that occurs in the workplace or due to the conduct of the business, causing death or resulting bodily integrity to become mentally or physically disabled". Law No 5510 stipulates that three elements must be together for an incident to be considered as a work accident: "being insured, having encountered an incident, and becoming physically or mentally disabled due to the incident".

Among the dangerous situations that may cause occupational accidents, situations can be listed such as inappropriate protective equipment, using defective tools and equipment, unsafe tools and machines, insufficient or excessive lighting, insufficient ventilation, and unsafe methods and conditions. Examples of dangerous behaviors are unsafe and unnecessary fast work, unsafe loading, transportation, stacking, working in dangerous places, unsafe attitude, not using personal protective equipment, confusion, jokes, and anger.

The main cause of all occupational accidents that result in serious injury or death is dangerous situations and behaviors and near miss incidents that no precautions are taken. Although 300 dangerous situations and behaviors do not cause any harm; If no measures are taken, it will cause 29 loss of limbs and injuries, and if the same negative situation and behavior continues and no

precautions are taken and ignored, it will lead to 1 fatal work accident or serious injury. When every work accident that causes serious injury or death is examined, according to the Work Accident Pyramid. On the basis of 1 serious injury or fatal accident, there are 29 minor injury incidents, and 300 simple non-injury incidents (1-29-300 ratio principle - Heinrich Principle). The causes of all 'near-miss' incidents should be investigated in detail, and all causes of incidents should be corrected and eliminated. A very important feature of this rule is that it allows us to make a projection about the accidents that may occur in the enterprise and gives us an opportunity to think beforehand. Recording and keeping statistics of occupational accidents gives the opportunity to estimate the frequency of accidents in enterprises compared to previous years and to take precautions [9].

2.3. Occupational Disease

Occupational diseases are called the "silent epidemic" of modern times. It is estimated that 7500 people die every day in the world as a result of work accidents or occupational diseases. 6500 of these deaths are due to work related and occupational diseases, and 1000 of them are due to injuries as a result of work accidents. Occupational health and safety related issues come to the fore in the society and the press mostly due to occupational accidents and industrial disasters. However, deaths as a result of occupational diseases and work related diseases are much higher than deaths from work accidents. 2.3 million deaths per year from occupational diseases are much more than deaths from tuberculosis, AIDS and traffic accidents. Cases are more common in low and middle income countries, where manufacturing is most intensive and occupational health and safety rules and practices are often poorly enforced [10][11] Occupational diseases are the common name of diseases that occur primarily due to factors caused by the workplace environment [12]. In international sources such as the World Health Organization and the International Labor Organization, occupational diseases are defined as a group of diseases in which a cause-effect and action-reaction relationship specific to the work being studied can be revealed between a harmful factor and the human body affected by it [13].

According to the Social Security and General Health Insurance Law No 5510, occupational disease is defined as “temporary or permanent illness, physical or mental disability, which the insured person suffers due to a recurring reason due to the nature of the work he/she performs or due to the conditions of the business”. Symptoms of occupational diseases may appear one week or years after the employee's first contact with the factor [14].

2.4. Diagnosis, detection and classification of occupational disease

Occupational diseases are in the group of completely preventable diseases. Occupational diseases are not caused by a single cause, but also by many causes. Nutrition, personal sensitivity, genetic changes, drug use, alcohol and cigarette use and obesity can be counted as causes. With the onset of occupational diseases, personal, familial, social and societal effects occur in employees. Since the effects may occur years later, the diagnosis of occupational diseases depends on the awareness of the employee, specifying the field of work in the hospital, receiving training on this subject, organizations and legal regulations in this regard. Because occupational diseases can only be found if they are sought with a high level of awareness, skepticism and questioning. Another difference in occupational diseases is the existence of their own diagnostic and screening methods. With regular periodic environmental measurements, employment and periodic health examinations, as per the legislation,

JSR A
Journal of Scientific Reports

occupational diseases can be detected in employees without any symptoms and all necessary precautions can be taken. It is very important to inform employers and employees about occupational diseases specific to the field of work, to raise awareness and to increase their sensitivity. If one of the employees is diagnosed with an occupational disease, all colleagues working in the same environment and in a similar way should be evaluated in terms of early diagnosis and treatment. In case of diagnosis of occupational disease, it can be tried to be covered up with a false belief as it brings financial and moral compensation to the employee, additional payments according to incapacity for work, new investments to evaluate and improve the working environment, and criminal responsibilities.

In our country, there are certain legal processes for the diagnosis of occupational disease. There should be a compulsory causal link between the occupational disease and the work itself or the working environment, the person should be covered by SSI, the disease should be included in the list of occupational diseases, the person should be exposed to more than the relevant disease exposure value, the disease should occurred within the period of obligation, the occupational disease must be determined by a doctor report in authorized hospitals, it must be approved by the SSI Health Board and must be from diseases that can be produced experimentally under the same conditions. Exceptionally; The Social Security Institution Supreme Health Council can examine a disease not included in the list and individual differences and accept it as an occupational disease, and can change exposure values according to the personal situation [12].

Health service providers authorized for occupational diseases are Ministry of Health Occupational Diseases Hospitals, Training and Research Hospitals and State University Hospitals. According to the Social Security and General Health Insurance Law, it is determined by the Institution Health Board by examining the following documents that the insured person has an occupational disease due to his work; The health board report duly prepared by the health service providers authorized by the institution, the basis of this report and other medical documents and, if deemed necessary by the institution, the audit reports and other necessary documents revealing the working conditions in the workplace and the medical results related to it [15].

Occupational Diseases in Türkiye are grouped under 5 main groups according to the Regulation on Determination of Working Power and Loss of the Earning Capacity in Occupation. This classification is given in Table 1.

Table 1. Classification of Occupational Diseases [16].

Group A	**Occupational Diseases Caused by Chemical Substances**	**Carbon monoxide, Cadmium, Chromium, Mercury, Lead, Benzene, Arsenic, Organic Phosphorus, Ammonia etc.**
Group B	Occupational Skin Diseases	Skin Cancers and other Skin Diseases etc.
Group C	Pneumoconiosis and Other Occupational Respiratory System Diseases	Coal Miner's Lung, Bronchial Asthma, Silicosis, Asbestosis, Byssinosis etc.

JSR A
Journal of Scientific Reports

Yuvka, Ş. and Zorlu, E., Journal of Scientific Reports-A, Number 53, 74-96, June 2023

Group D	Occupational Contagious Diseases	Bacteria, Viruses, Parasites
Group E	Occupational Diseases Caused by Physical Factors	Noise, Vibration, Pressure, Radiation, Thermal Factors etc.

2.4.1. Medical and legal diagnosis process of occupational diseases

When establishing a work-related disease or occupational disease connection, it is very important to make a clinical evaluation, question the work history in detail, perform the physical examination wholly and completely, make all laboratory evaluations related to the patient's clinic and make workplace environment measurements when necessary.

Occupational disease is not only related to health processes, at the same time, it is a situation in which legal processes are also involved. With this diagnosis, it is proved that all risks of work cannot be fully and completely managed by the employer in the workplace, and therefore the worker is affected, his/her health condition worsens, illness begins or suffers a loss of function. For this reason, during the diagnosis process, there should be people who have been specially trained on this subject, who can act as experts when necessary, and these competent and health institutions.

According to the Social Security and General Health Insurance Law No 5510 published in the Official Gazette No 26200 on 16 June 2006; "It is obligatory to be determined by the Institution Health Board by examining the following documents that the insured person has an occupational disease due to his work; The health board report duly prepared by the health service providers authorized by the institution, the basis of this report and other medical documents and, if deemed necessary by the institution, the audit reports and other necessary documents revealing the working conditions in the workplace and the medical results related to it" [17].

If the occupational disease emerged after leaving the job and it was documented by the health board that it arose due to the job he/she worked as an insured, in order for the insured to benefit from the rights obtained by law, the period of time between leaving his job where he has an occupational disease and the emergence of the disease should not be longer than the period specified by the institution for the disease. Employees who suspect an occupational disease providing this situation can apply to the Social Security Institution with all necessary documents. In cases where occupational disease is determined by clinical and laboratory results and the factor causing occupational disease is determined by workplace examination, even if the liability periods specified in the list of occupational diseases have been exceeded, the detected occupational disease can be considered an occupational disease with the approval of the Social Security Institution or the SSI Higher Health Board upon the application of the employee or his representatives [17].

2.5. Work-Related Illnesses

Work-related diseases are diseases in which other risk factors play a role, along with many causative factors present in the workplace. The cause of the disease is complex and multifactorial. The cause of the disease is not only in the workplace, there may also be different sources together with the workplace. Although it is not directly caused by the workplace, the disease is affected by the causes in the workplace and its course changes. Due to the work done, the disease may start or become

aggravated, accelerated, or exacerbated. Therefore, work-related diseases are more common than occupational diseases. It can be seen widely in the general society as well as the workers [18].

Today, in our country and in the world, there is a health system for diagnosing not all work-related diseases in general, but occupational diseases that develop a clinical picture and cause disease, and the cause of exposure is completely work-specific. However, work-related diseases are defined as physical or mental illnesses and health problems that are partially or completely caused by working conditions or worsening the clinical picture [19]. This definition is more comprehensive and more accurate since it emphasizes not only the workplace but also all life conditions of the employee. For this reason, occupational diseases are only a subgroup of work-related diseases. Perhaps the most problematic aspect of the definition of occupational disease is that the employees only evaluate the disease they are exposed to due to the environment individually, and therefore it does not take into account that the work completely affects the health of the employees. In occupational disease, the main cause of illness is work-specific rather than personal. Occupational diseases; have a special or strong relationship with the profession, they are usually caused by only one factor and are determined by this feature. Work-related diseases; factors in the work environment are effective as well as other risk factors and may play a role in the development of such diseases with a complex etiology (musculoskeletal system diseases, stress). Diseases affecting workers; although there is no causal relationship between illness and work, these are diseases that may be aggravated due to occupational hazards (diabetes, hypertension)[20].

2.6. Frequency of Accidents and Death Rates Caused by Work Accidents

The concept of “accident frequency” is defined as the occupational accident per 100,000 employees and the “death rate” resulting from these accidents, and was developed by the Statistical Office of the European Communities (Eurostat) for the preparation of statistical data of occupational accidents, for comparison between countries, and for comparison of positive and negative changes over time [21].

2.7. Comparison Criteria of Occupational Accidents and Occupational Diseases

Since both the population and the number of employees of each country are different, it would be meaningless to compare the countries only according to the recorded work accidents, occupational diseases and deaths resulting from these. At the same time, since the number of employees changes over the years, it would be misleading to analyze the changes in work accidents, occupational diseases and related deaths in a country by only looking at the numbers in these data. What is important in statistics is the ratio of the number of employees who had an accident in the working group, rather than how many people have had an occupational accident. For this reason, various benchmarks are used between countries and years in comparisons related to work accidents and occupational diseases [21].

3. OVERVIEW of OCCUPATIONAL ACCIDENTS and OCCUPATIONAL DISEASES in TÜRKİYE

Depending on the development level of a country's occupational health and safety, the number of new occupational diseases to be detected in employment should be between 4-12 per thousand [14]. When calculating over 20 million compulsory insured in 2019 and 2020, if the value of 4 per thousand is

JSR A
Journal of Scientific Reports

taken, the expected number of occupational diseases should be 80,000 and if this value is taken as 12 per thousand, the expected number of occupational diseases should be around 240,000. In terms of the number of deaths, deaths due to work-related diseases should be expected to be 5-6 times more than deaths due to work-related accidents.

Numerical data on work accidents and occupational diseases, related deaths and death rates in Türkiye in 2000 and later are given in Table 2. All of these numerical data are statistical information announced annually only by the Social Security Institution. In Table 2, the number of work accidents, occupational diseases, deaths related to these and the death rates calculated according to 100,000 people in deaths after work accidents in Türkiye in 2000 and later are given. When the table is examined, after 2000, a serious decrease is detected in the general accident frequency value throughout Türkiye, although it varies over the years. This means that although there has been an increase in the number of reported accidents at workplaces in our country, there has been a significant decrease in death rates as a result of work accidents. In light of these data, it can be said that as a result of the measures taken and legal regulations, all our employees work in more reliable environments in terms of life safety compared to the beginning of the 2000s [22].

However, it should be noted that, unfortunately, most of the occupational accidents that occur in our country are not officially recorded. While more than 800,000 work accident reports are made annually in Germany, which has a population similar to our country, unfortunately, as seen in Table 2, this number was 70,000 in Türkiye in the 2000s. Although the Occupational Health and Safety Law No 6331 came into force in 2013, it only increased to 400,000 [23].

More importantly, this situation can be seen more clearly when the comparative data in Table 3 of the non-governmental organization named Health and Safety Labor Watch-Türkiye (HESA), which has been announcing deaths due to occupational accidents and occupational diseases in our country since 2012, together with the SSI, annually. According to this table, although it was stated that a total of 11,295 deaths occurred as a result of work accidents according to SSI data in the last eight years, this number was determined as 14,913 according to the HESA Labor Watch. Even more sadly, in the last eight years, only 5 deaths due to occupational diseases were reported in 2020 in our country, and no deaths due to occupational diseases were reported in the other seven years. However, according to the HESA Labor Watch, this number in the last eight years has been determined as 387 in total. One of the important issues in this difference is the length of the legal processes related to work accidents and occupational diseases [24].

Table 2. Number of Occupational Accidents and Occupational Diseases in Türkiye After 2000 [15].

	Number of Work Accidents	**Death Due to Work Accidents**	**Occupational Accident Death Rate (Death Rate per 100,000 Persons)**	**Number of Occupational Diseases**	**Death Due to Occupational Diseases**
2000	74,847	1043	24.6	803	6
2001	72,367	1008	20.6	883	6
2002	72,344	872	16.8	601	6

JSR A
Journal of Scientific Reports

2003	76,668	810	14.4	440	1
2004	83,830	841	13.6	384	2
2005	73,923	1072	15.8	519	24
2006	79,027	1592	20.5	574	9
2007	80,602	1043	12.3	1208	1
2008	72,963	865	9	539	1
2009	64,316	1171	11.9	429	0
2010	62,903	1444	13.3	533	10
2011	69,227	1563	14.4	688	10
2012	74,871	744	5.8	395	1
2013	191,389	1360	8.3	371	0
2014	221,366	1626	9.4	494	0
2015	241,547	1252	6.9	510	0
2016	286,068	1405	7.5	597	0
2017	359,653	1633	8.2	691	0
2018	430,985	1541	7.9	1044	0
2019	422,463	1147	5.9	1088	0
2020	384,262	1231	6	908	5

Although we have insufficient data on occupational diseases, some inferences can be made from more reliable data (according to the number of employment and occupational accidents) in the world and in our country. For example; According to ILO data, the total number of workers in the world in 2008 was 3.09 billion, and the number of people who died as a result of occupational diseases was 2,022,570. The death rate due to occupational diseases in the world is 65.5 per 100,000. If we evaluate these data for our country, according to the death rate, at least 15,363 out of 23,470,000 employees in our country must have died due to occupational diseases in 2008. This constitutes 4.4 percent of all deaths over the age of 15, according to the Turkish Statistical Institute death statistics for 2008. For better understanding, this rate is equal to all non-illness deaths (murder, accident, poisoning) in the same year [24].

The situation in our country is even more dire in the detection of deaths as a result of occupational diseases (Table 3). In the last nine years, the number of deaths due to occupational diseases was determined as 6 according to the SSI data, while this number was determined as 387 according to the data of the HESA Labor Watch. The fact that the number of occupational diseases has been shown to be zero in recent years, even healthcare workers who died during the Covid-19 pandemic were not included in the list in 2020, bringing the obligation to prove the disease-death causal link of the employees who died in the pandemic by the relatives of the deceased, even the difference in the HESA Labor Watch - SSI data shows that we are in a dire situation that cannot be compared with other countries [15] [25].
Comparing only the data of SSI and HESA Labor Watch shows that work accidents and occupational diseases in our country cannot be recorded sufficiently and carefully. In order to reduce work accidents, occupational diseases and their negative consequences that occur in our country, first of all, it is necessary to record the numerical data related to them in a healthy way.

JSR A
Journal of Scientific Reports

Table 3. Occupational Accident and Occupational Disease Deaths Table of SSI and HESA Labor Watch [15] [25].

	Deaths Due to Occupational Accidents		Deaths Due to Occupational Diseases	
Years	**SSI DATA**	**HESA LABOUR WATCH DATA**	**SSI DATA**	**HESA LABOUR WATCH DATA**
2012	744	878	1	0
2013	1360	1235	0	3
2014	1626	1886	0	29
2015	1252	1730	0	13
2016	1405	1970	0	15
2017	1633	2006	0	4
2018	1541	1923	0	10
2019	1147	1736	0	8
2020	1231	2427	5	305*
Total	11295	14913	6	387

*Deaths of Healthcare Workers in the Covid-19 Pandemic in 2020

4. COMPARISON of TÜRKİYE and VARIOUS COUNTRIES in TERMS of OCCUPATIONAL ACCIDENTS and OCCUPATIONAL DISEASES

4.1. Comparison of Occupational Accident and Occupational Accident Death Rates

Death rates resulting from work accidents compiled from the data of the International Labor Organization, Eurostat, Ourworldindata.org and Social Security Institution for various countries are presented as numerical data in Table 4 and Table 5, and graphically in Figure-1 and Figure 2. The low number of deaths and death rates as a result of work accidents is important for the morale and motivation of occupational health and safety professionals in countries, as it shows the severity of the accidents and is a reference and control indicator of the effectiveness of protective measures.

According to ILO statistics, approximately 110 million occupational accidents occur in the world every year, and 1.2 million people die as a result of work accidents or occupational diseases. Occupational accidents and occupational diseases continue to be one of the most important economic and social problems, especially in developing countries such as ours, as a result of countries' deficient implementation of occupational health and safety in enterprises and failure to fully fulfill their supervisory duties within the state mechanism. Occupational accidents and diseases increase as a result of ignoring the measures for occupational health and safety due to reasons such as the increase in competition at the global level, the inability to take preventive actions in parallel with the speed of technological changes, and the uncontrolled reduction of expense costs. The desire to use cheap labor due to costs, lack of knowledge of employers, and deficiencies in occupational health and safety training for employees are also some of the important reasons for the increase in occupational accidents and diseases. In Table 4, the data on average death rates per 100,000 as a result of work accidents in our country and in some countries in the world between the years 2000-2020 are given. In our country, the number of people who died as a result of work accidents per 100,000 employees is

JSR A
Journal of Scientific Reports

seen, which is important in terms of understanding the seriousness of the situation related to deaths as a result of work accidents [15] [25].

Table 4. Occupational Accident Death Rates in Türkiye and Some Countries in the World (Death Rates per 100,000 Workers) [25].

	Türkiye	**Argentina**	**South Korea**	**Canada**	**Spain**	**Russia**
2000	24.6	18.6	14.3	3.4	9.2	14.9
2001	20.6	-	12.3	3.3	8	15
2002	16.8	15.2	12	3.2	6.1	13.8
2003	14.4	15.2	13.3	2.9	5.3	13.1
2004	13.6	15	13.5	2.9	4.9	12.9
2005	15.8	14.3	11.7	3	4.5	12.4
2006	20.5	14.9	10.6	2.7	4.4	11.9
2007	12.3	14.1	9.1	2.3	3.6	12.4
2008	9	-	8.7	2.7	3.3	10.9
2009	11.9	10.6	8.2	2.1	2.6	9
2010	13.3	10.9	7.9	2.2	2.3	9
2011	14.4	7.7	7.9	2.1	2.5	9
2012	5.8	6.8	7.3	2	2.2	9
2013	8.3	-	7.1	2	1.9	8
2014	9.4	4.7	5.8	1.7	2	8
2015	6.9	4.9	5.3	1.7	2.3	7
2016	7.5	4.2	5.3	1.8	1.9	6
2017	8.2	4.4	5.2	1.8	2	6
2018	7.9	3.7	5.1	1.9	2	5
2019	5.9	-	4.6	4.9	1.8	5
2020	6	-	4.7	-	-	5

JSR A
Journal of Scientific Reports

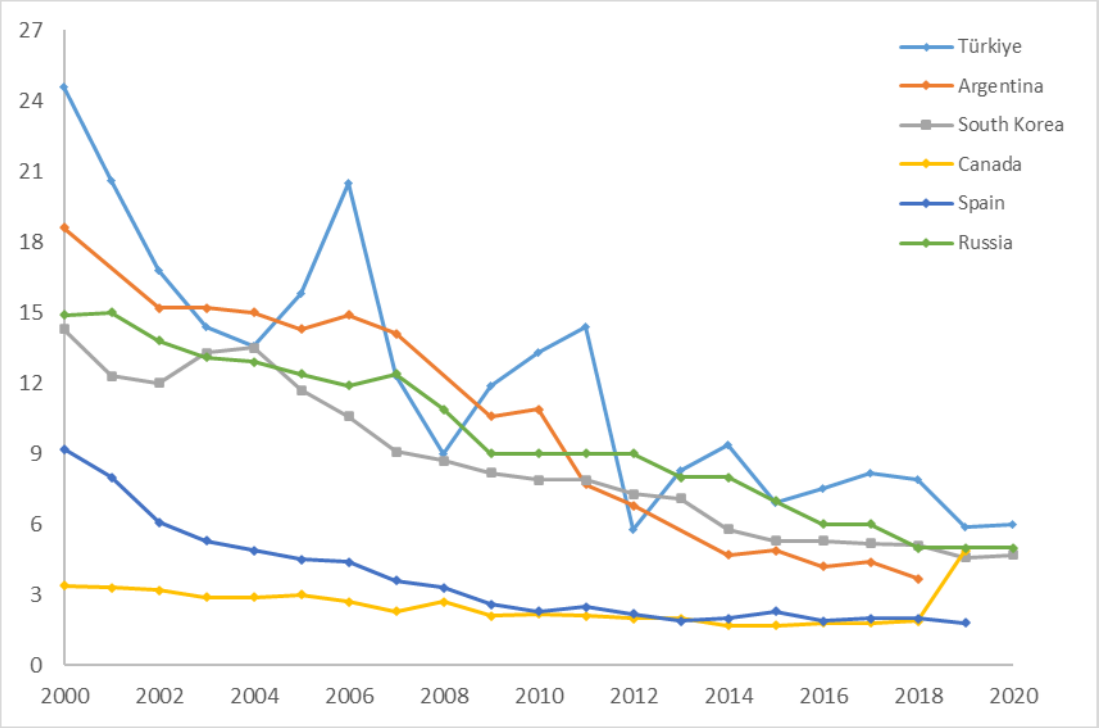

Figure 1. Occupational Accident Death Rates in Türkiye and Some Countries in the World.

According to Table 4 and Figure-1, it can be mentioned that there is a significant decrease in death rates after work accidents in the world, but although there is a decrease in the death rate in Türkiye compared to the countries given in the table, there is no decrease in parallel with other countries. When the death rates of Türkiye, Argentina, South Korea, Canada, Spain and Russia are examined, it is seen that the death rate after a work accident in Spain, which is in the European Union, is lower than other countries, and a constant curve is seen in the figure. It can be said that this depends on the occupational health and safety culture in the European Union countries. After Spain, the lowest post-work accident death rates are seen in Canada. In this country, there is an established occupational health and safety culture compared to other countries. On the other hand, in South Korea, Argentina and Russia, there is a decreasing death rate and shape curve in recent years. However, when compared to other countries, the ups and downs in Türkiye 's numbers and curve draw attention. This shows the existence of an occupational health and safety culture that has not yet settled compared to other countries.

When the Occupational Accident Death Rates in Türkiye and some European Countries in Table 5 and Figure 2 are compared, although the death rate as a result of work accidents in our country has decreased in recent years, it continues to be several times that of these countries. Our death rate after an occupational accident is 3 times the European Union average in our best period and 8 times in our

JSR A
Journal of Scientific Reports

worst period. According to the European Union, the low number of deaths in England can be explained by the good implementation of the occupational health and safety culture in this country.

Table 5. Occupational Accident Death Rates in Türkiye and Some European Union Countries [25].

	Türkiye	**Austria**	**France**	**Italy**	**Hungary**	**EU Average**
2000	24.6	5.3	4	7	4	3.2
2001	20.6	4.5	4.2	6	3.2	3.1
2002	16.8	4.7	3.8	5	4.2	2.9
2003	14.4	3.8	3.7	5	3.4	2.9
2004	13.6	5	3.5	5	4.1	2.7
2005	15.8	4.6	2.7	5	3.2	2.5
2006	20.5	3.9	3	5	3.1	2.8
2007	12.3	3.9	3.4	4	3	2.7
2008	9	4.1	2	4	3	2.4
2009	11.9	4.8	2.2	3	2.7	2
2010	13.3	4.5	2.4	3	2.7	2.1
2011	14.4	3	3.1	2.7	2.4	2
2012	5.8	3.4	2.5	2.6	1.7	1.95
2013	8.3	3.5	2.4	2.3	1.4	1.8
2014	9.4	3.1	2.7	2.3	2.3	1.8
2015	6.9	3.2	2.6	2.4	2.3	1.8
2016	7.5	2	-	-	1.8	-
2017	8.2	-	-	-	-	-
2018	7.9	-	-	-	-	-
2019	5.9	2.5	3.5	2.1	2.1	1.7
2020	6	-	-	-	1.4	-

JSR A
Journal of Scientific Reports

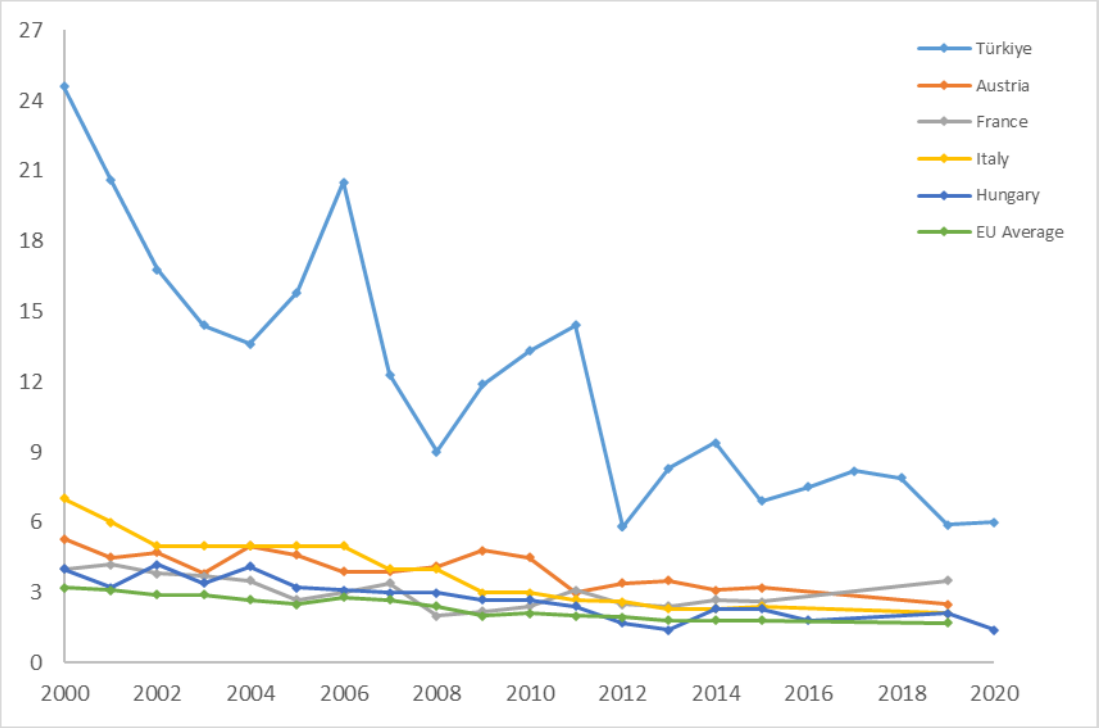

Figure 2. Occupational Accident Death Rates in Türkiye and Some European Union Countries.

The fact that the numbers in the European Union countries show parallelism with each other in a decreasing manner can also be attributed to the same reason. Although Germany, which is the locomotive of the Union, has the same population and number of employees as our country, the number of reported work accidents is 2 to 13 times higher than our country. This shows that the occupational health and safety culture in the country is implemented in a disciplined way, that even the smallest accident notifications are made and measures are taken and as a result, the number and speed of fatal occupational accidents are low. The same can be said for other member states of the European Union.

When we interpret according to the Heinrich Accident Prevention Pyramid, which has been used to prevent accidents since 1931; Table 4 shows 1171 fatal occupational accidents in 2009. When we multiply 1171 by 330 in the pyramid, it can be interpreted that 386,430 occupational accidents have occurred in our country. However, the number of occupational accidents reported in 2009 is seen as 64,316. Almost 5 out of 6 occupational accidents were not reported. When we make the same comment with the 2020 data, 1231 fatal work accidents have occurred and while there should be 406,230 work accident reports, 384,262 case reports were made. The HESA Labor Watch, which was formed by non-governmental organizations that objected to the SSI data and collected their own data, determined that there were 2427 fatal work accidents in 2020. When we multiply this number with the

JSR A
Journal of Scientific Reports

constant multiplier in the Heinrich Accident Pyramid, it is seen that 800,910 occupational accidents occurred in 2020. This number is similar to the number of occupational accidents in Germany. This also shows that; Although it is seen that the Occupational Health and Safety Law No 6331, which came into force in 2013 in our country, has positive effects, it is not possible to detect occupational accidents at a sufficient level when compared to other countries. Unfortunately, it is seen that these data announced annually by SSI do not reflect the truth. Due to the underreporting of the number of work accidents, continues to be the biggest obstacle in preventing deaths as a result of work accidents, which are completely preventable [15] [25].

4.2. Occupational Diseases and Comparison of Deaths Due to Occupational Diseases

As mentioned at the beginning, while the rate of occupational diseases is expected to be high in our country, our inadequacy arises due to many factors such as low capacity to diagnose occupational disease, lack of occupational knowledge of employees, lack of adequate and accurate information about occupational disease, fear of losing rights and positions as a result of the diagnosis of occupational disease, the deterioration of the employee's relationship with the employer, the fear of losing job and the difficulties arising from the occupational disease diagnosis process, so very few diagnoses are made due to reasons such as these. With the rate of economic development among countries, it is expected that between 4 and 12 new occupational diseases per 1000 workers will be seen per year. Considering the rates calculated according to the number of employees in Table 6, the number of occupational diseases in the last twenty years in our country is very low compared to the rate of 4-12 per thousand.

Table 6. Frequency of Occupational Diseases in Türkiye (2000-2020) [15] [25].

	NUMBER OF OCCUPATIONAL DISEASES	NUMBER OF EMPLOYEES X1000	OCCUPATIONAL DISEASE RATE (PER 100,000 PEOPLE)
2000	803	5,254	15.3
2001	883	5,456	16.1
2002	601	5,789	10.4
2003	440	6,231	7.1
2004	384	6,954	5.5
2005	519	7,651	7.5
2006	574	8,582	7.3
2007	1,208	9,198	14.2
2008	539	9,574	6.1
2009	429	9,618	4.8
2010	533	10,575	5.3
2011	688	11,547	6.3
2012	395	12,527	3.2
2013	371	13,136	3.1
2014	494	13,967	3.5
2015	510	14,802	3.4
2016	597	15,535	3.8

JSR A
Journal of Scientific Reports

2017	691	16,369	4.2
2018	1,044	16,054	6.5
2019	1,088	16,010	6.7
2020	908	17,857	5

In Table 7, the expected and detected numbers of occupational diseases in our country and some countries between 2000-2020 are given. As can be seen in this table, there are serious problems in the detection of occupational diseases not only in our country but also all over the world. This is due to the reasons of the employee, the employer and the state and this problem is growing even if not enough attention is paid. However, according to the rate of an occupational disease that should be seen between 4-12 in a thousand cases, unfortunately, an occupational disease can be detected in only one of every 100-300 cases that should be detected annually. The rest are treated without an occupational disease diagnosis due to the lack of occupational health and safety culture. Due to those who could not be diagnosed with an occupational disease, necessary measures cannot be taken to prevent the occurrence of the disease. This has a serious negative impact on employee health.

Table 7. Number of Occupational Diseases Detected in Some Countries in 2000-2020 [15][25][26].

		Countries					
		Sweden	**Finland**	**Norway**	**Latvia**	**Germany**	**Türkiye**
Expected Number of Occupational Diseases by Number of Employees (4-12 per 1000 employees)		17,604-30,144	10,048-30,144	9,772-29,316	4,476-13,428	152,492-457,476	43,000-130,000
Years	2000	23,444	4,991	3,649	495	18,689	803
	2001	26,440	4,923	3,587	726	18,599	883
	2002	22,339	4,807	3,521	883	18,352	601
	2003	25,565	6,329	3,423	965	17,425	440
	2004	20,787	6,132	2,870	1,888	17,413	384
	2005	17,107	7,035	2,737	1,673	16,519	519
	2006	14,186	6,956	3,051	1,111	14,732	574
	2007	11,608	6,487	2,881	1,591	13,932	1208
	2008	10,412	6,312	2,688	2,118	13,546	539
	2009	8,881	6,271	2,439	3,128	16,657	429
	2010	9,074	2,507	2,797	3,471	15,926	533
	2011	9,534	2,106	2,340	2,335	15,880	688
	2012	10,144	1,998	2,862	2,054	15,949	395
	2013	11,088	1,871	2,835	2,845	16,413	371
	2014	11,827	1,625	2,878	3,906	16,969	494
	2015	12,136	1,614	2,364	3,652	18,041	510
	2016	11,696	1,571	-	5,175	22,320	597

JSR A
Journal of Scientific Reports

2017	10,228	1,242	-	5,757	21,772	691
2018	8,894	1,067	-	6,709	21,794	1,044
2019	10,573	930	-	7,710	20,422	1,088
2020	19,899	-	-	6,648	39,551	908

When we look at Table 6 and Table 7, there is a situation in the world where occupational diseases are solved by hiding**.** This is even more evident for our country. As a result, hazards and risks in workplaces cannot be determined. Unfortunately, most of the cases are not recorded unless they are associated with permanent damage, disability, fatal work accident, occupational disease or work-related illness. This situation is not fully reflected in the records of healthcare providers in our country. In our country, the length of the processes of diagnosis of occupational disease and the length of judicial processes in the case of resorting to legal remedies when necessary, exhausts the employees who are victims both financially and morally. In fact, all work-related diseases and occupational diseases can be shown by a causal link by trained specialists of SSI or an insurance institution. This process is both easier and will result in less attrition for the injured employee financially and morally and will provide relief as soon as possible [15][25][26].

The highest decrease was in vocal cord diseases, occupational hearing loss and infectious diseases (30%, 51% and 40%, respectively). Vocal cord pathologies are not considered among occupational diseases in the European Union member countries and the United States of America. It should be especially noted that hoarseness is not considered an occupational disease for teachers in our country. The fact that the definition and detection of occupational diseases are different in each country is the main reason for the inconsistency in the data between countries. Table 8 shows the most common occupational diseases in different countries. Despite the insufficient numbers in our country, it is thought-provoking that pneumoconiosis and musculoskeletal system disorders, which are preventable diseases, are the leading ones. If necessary occupational health and safety measures are taken, these diseases and related deaths can be completely prevented [15][25][26].

Table 8. Most Common Occupational Diseases in Different Countries [27].

Country	**Most Common Occupational Diseases**	**Second Most Common Occupational Diseases**
Argentina	Hearing Loss	Respiratory Diseases
China	Pneumoconiosis	Acute and chronic poisoning
Germany	Skin Diseases	Back diseases - Hearing Loss
South Korea	Musculoskeletal Diseases	Pneumoconiosis
Portugal	Hearing loss	Musculoskeletal Diseases
Russia	Respiratory Diseases	Musculoskeletal Diseases
Sweden	Musculoskeletal Diseases	Diseases Related to Chemicals
Zimbabwe	Pneumoconiosis	Hearing loss
Türkiye	Pneumoconiosis	Musculoskeletal Diseases

JSR A
Journal of Scientific Reports

5. CONCLUSIONS and RECOMMENDATIONS

In this study, work accidents and occupational diseases that occurred in Türkiye and some countries in the world between the years 2000-2020, as well as the number of deaths due to these, were examined; The changes in the accidents over the years were examined by making comparisons according to the death rates in 100,000 cases. As a result of the comparisons made in the research, the following findings were obtained:

While there has been a significant increase in the number of work accidents in Türkiye over the years, there has not been a remarkable decrease in the number of deaths. However, due to the increase in the number of occupational accidents, a significant decrease in the death rate per 100,000 was observed.

It is thought that the main problem in our country is the reporting of occupational accidents to the Social Security Institution. As a matter of fact, the increase in case reporting after the Occupational Health and Safety Law No 6331, which came into force on January 1, 2013, shows this. Despite this, it has been determined by comparisons and calculations that there are still deficiencies in the reporting. The inability to determine the actual numerical data is the biggest obstacle in front of the real dimensions of occupational health and safety problems and the measures that can be taken in our country.

Among the main reasons for the emergence of these results, various factors such as employing uninsured workers, the lack of employment of occupational physicians and occupational safety specialists due to the postponement of the implementation of some articles of the existing law in small-scale enterprises, ignorance of the employer and employees about work accidents and occupational diseases, and inadequacy of current inspections are thought to be effective.

Türkiye has a higher accident frequency than the other world countries examined in the study and the European Union average, in terms of the fatal accident rate, which is calculated as per 100,000 as a result of work accidents.

Our country is in a worse situation than occupational accidents in terms of detection and follow-up of occupational diseases. In occupational diseases that can occur due to multiple reasons, there is a situation almost like ignoring occupational diseases by considering non-occupational reasons. This situation becomes even more evident when comparing the data of the HESA Labor Watch and the SSI data.

When it is expected that between 4 and 12 new occupational diseases will be detected per 1000 workers, depending on the number of employees, between 50,000 and 150,000 new occupational diseases are expected to be detected annually in our country. However, the annual detection of occupational diseases in our country is not even 1000.

In terms of the number of work accidents, Türkiye seems to be in a better situation than South Korea, Germany, France, Spain and European Union countries, but the high rate of death after work accidents per 100,000 can be considered as a contradiction. This is a result of the fact that occupational health

and safety is implemented more carefully and diligently in the mentioned countries than in our country, and even the smallest occupational accident is recorded.

The only source from which we can obtain information on work accidents and occupational diseases in Türkiye is the annual statistics of SSI. However, due to both the fact that the occupational accidents resolved in the workplace health units are not reflected in these data, and due to the reservations to avoid possible inspector examination, they are not reflected by the enterprises. Some of the occupational accidents cannot be added to the system by treating the employees with undeclared practices in public or private health institutions.

Not to employ uninsured workers, to carry out necessary analysis and tests at the start of employment and during periodic examinations, to ensure all necessary health conditions in the workplace, to ensure a clean air flow in the workplace environment, to remove all kinds of harmful factors that come out during the work with appropriate methods, to take into account the warnings of the occupational safety specialist and the workplace doctor, to fully implement the recommendations specified in the reports of occupational health and safety inspections are important in terms of preventing work accidents and occupational diseases.

Not evaluating preventive medicine practices as a priority in the presentation of occupational health, work accidents and occupational diseases are not a priority area in the training policies and programs of occupational physicians and allied health personnel, the inadequacy of the knowledge and sensitivity of the occupational physicians are among the issues that need to be corrected.

Difficulties experienced in the diagnosis of occupational diseases and not paying attention to the importance of this issue in health service providers are also important and need to be corrected.

In addition to providing statistical unity between countries in terms of all health ministries with the ICD-10 (International Statistical Classification of Diseases and Related Health Problems), an international agreement should be reached on occupational accidents and diseases. Any statistical comparison without this provision will be incomplete and meaningless.

The fact that diagnostic guidelines for occupational diseases have not yet been fully developed, systemic inadequacy in occupational disease records, lack of occupational disease diagnosis standards, physicians working in the primary and secondary health care systems are not sensitive to occupational diseases and do not know the procedure are among the issues that need to be corrected.

Considering that employees do not have sufficient and accurate information about work accidents and occupational diseases and do not know their legal rights, fear of loss of rights and positions should be eliminated in the diagnosis of work accidents and occupational diseases and in the following processes and employees should be taught all their rights.

The target of increasing the number of expected but undetected occupational disease cases by 500%, which was targeted in the National Occupational Health and Safety Policy Document previously

prepared by the Ministry of Labor, should be met. The stagnation in the number of occupational disease detections after 2008, when this was targeted, is thought-provoking.

The expected increase in the detection of occupational diseases can be achieved by disseminating and facilitating the procedures related to the diagnosis of occupational diseases, which are one of the indicators of occupational health and safety, which can lead to different negative pictures if no precautions are taken, increasing the knowledge and sensitivity of occupational physicians and all health personnel, all employers and employees, all trade union organizations and professional organizations, providing information in the written and visual media about the subject.

The only data source on work accidents and occupational diseases in Türkiye is the annual statistics of SSI. However, it is obvious that these data do not reflect the real picture, due to the accidents that are not reflected in these data by the enterprises with different reservations and the health examinations and treatments of employees being carried out without notification in official or private health institutions. As all parties of the Employee-Employer-State, this issue and the creation of different statistical sources and auto-control of SSI data are also very important in terms of diagnosis, examination, treatment and measures that can be taken.

In summary, if we were to synthesize all the findings and predictions, thousands of our people lost their lives and lost their rights due to unreported work accidents, occupational diseases and related deaths in our country in 2000 and later. Currently, deaths due to work accidents are under-reported by at least 30% compared to the number of non-governmental organizations, and deaths due to occupational diseases are almost never reported. Due to the fact that the data do not reflect the truth, no efficient analysis can be made for the past, present and future. This will result in failure to take the measures that can be taken in the context of occupational health and safety and will lead to new work accidents, occupational diseases and deaths. In addition to death and disability, billions of liras will be transferred from employees, employers and state treasury to analysis, examination, treatment and compensation.

As a result, the majority of work accidents, occupational diseases and related deaths are preventable. Employees, employers and occupational health and safety workers must work with the state to develop preventive occupational health and safety systems. Unfortunately, as in our country, if the facts continue to be concealed for any reason, all preventive actions to be taken will remain incomplete and defective, leading to new work accidents, occupational diseases, disability and death.

ACKNOWLEDGMENT

The authors thank the reviewers for important questions, valuable comments, careful reading, and helpful suggestions.

JSR A
Journal of Scientific Reports

REFERENCES

[1] ILO. World Day For Safety And Health At Work, 28 April 2015, 01.04.2023, https://www.ilo.org/legacy/english/osh/en/story_content/external_files/fs_st_1-ILO_5_en.pdf

[2] Narter, S. (2015). İş Kazaları ve Meslek Hastalıklarında Tüzel Kişi Organı Olarak Ortak İşverenin Cezai Sorumluluğu, Gazi Üniversitesi İktisadi ve İdari Bilimler Fakültesi Dergisi, 17(2), 229 – 265.

[3] Songur, L., Songur, G. (2018). Ekonomik Büyümede İş Kazası ve Meslek Hastalıklarının Önemi ve Sosyal Tarafların Sorumlulukları, Akademik Bakış Dergisi, 68, 43-55.

[4] Koçali, K. (2021). Sosyal Güvenlik Kurumu'nun 2012-2020 Yılları Arası İş Kazaları Göstergelerinin Standardizasyonu, Akademik Yaklaşımlar Dergisi, 12 (2), 302-327.

[5] Gözüak, M.H., Ceylan, H. (2021). Türkiye'de İnşaat Sektöründe Meydana Gelen İş Kazalarının İş Sağlığı ve Güvenliği Bağlamında Analizi: Güncel Eğilimlere Genel Bir Bakış, Sağlık Akademisyenleri Dergisi, 8(2), 133-143.

[6] Cerev, G., Yıldırım, S. (2018). Çalışanların Kişisel Özelliklerinin İş Kazası ve Meslek Hastalıklarına Etkisi Üzerine Bir İnceleme, Fırat Üniversitesi, İİBF Uluslararsı İktisadi ve İdari Bilimler Dergisi, 2(1), 53-72.

[7] Karaman, H.I.Ö. (2013). Düşme Tehlikesi Olan İşlerde İşçilerin Nörolojik İzlemi, Türk Tabipler Birliği Mesleki Sağlık ve Güvenlik Dergisi, 13(47), 31-38.

[8] 5510 Sayılı Sosyal Sigortalar ve Genel Sağlık Sigortası Kanunu. (2006). Sayı:26200, Tertip:5, Cilt:45.

[9] Pişkin, M., Dalyan, O. (2020). İşyerlerinde Ramak Kala Bildirimlerinin İş Kazalarına Etkisi ve İnşaat Sektöründe Uygulama, Çanakkale Onsekiz Mart Üniversitesi Fen Bilimleri Enstitüsü Dergisi, 6(1), 133-143.

[10] Ocaktan, M.E. (2019). İş Sağlığı ve Güvenliği, 1.Uluslararası 2. Ulusal Sağlık Bakım Hizmetleri Kongresi, 46-50.

[11] Kahraman, A.E. (2020). Meslek hastalığı sürecinin kalitatif değerlendirilmesi, Tıpta Uzmanlık Tezi, Dokuz Eylül Üniversitesi, 1-127.

[12] Kocabaş, F., Aydın U., Özgüler, V.C., İlhan, M.N., Demirkaya, S., Ak, N., Özbaş, C. (2018). Çalışma Ortamında Psikososyal Risk Etmenlerinin İş Kazası, Meslek Hastalıkları ve İşle İlgili Hastalıklarla İlişkisi, Sosyal Güvence Dergisi, 14(7), 28-62.

[13] Yeşiltepe, A., Karadağ, G. (2019). Meslek Hastalığının Boyutları ve Meslek Hastalıklarından Korunmada İş Sağlığı Hemşiresinin Rolleri, DEUHFED, 12 (4), 294-302.

[14] Berk, M., Önal, B., Güven, R. (2011). Meslek Hastalıkları Rehberi, Çalışma ve Sosyal Güvenlik Bakanlığı, Matsa Basımevi, 11-27.

[15] Sosyal Güvenlik Kurumu, İstatistik, SGK İstatistik Yıllıkları, 01.03.2023. https://www.sgk.gov.tr/Istatistik/Yillik/fcd5e59b-6af9-4d90-a451-ee7500eb1cb4/

[16] Akarsu, H., Ayan, B., Çakmak, E., Doğan, B., Eravcı, D.B., Karaman, E., Koçak, D. (2013). Meslek Hastalıkları, ÇASGEM, Özyurt Matbaacılık, 7-45.

[17] Resmi Gazete, (2006). Sosyal Sigortalar ve Genel Sağlık Sigortası Kanunu, Sayı: 26200, Cilt:45.

[18] Çalışma ve Sosyal Güvenlik Bakanlığı, Meslek Hastalıkları ve İşle İlgili Hastalıklar Tanı Rehberi, 2010, 06.03.2023. https://guvenlitarim.csgb.gov.tr/media/4l0jo25f/meslek-hastalıkları-ve-iş-ile-ilgili-hastalıklar-rehberi.pdf

[19] Disk/Genel-İş, "İşe Bağlı Hastalıklar Dosyası 1 "Meslek Hastalığı mı? "İşe Bağlı Hastalık" mı?", 30.10.2019, 06.03.2023. https://www.genel-is.org.tr/ise-bagli-hastaliklar-dosyasi-1-meslek-hastaligi-mi-ise-bagli-hastalik-mi,2,20422

[20] Keleş, M.S. (2020). Meslek Hastalıkları, Atatürk Üniversitesi Açık Öğretim Fakültesi Yayınları, 5-61

[21] Ceylan, H. (2011). Türkiye'deki İş Kazalarının Genel Görünümü ve Gelişmiş Ülkelerle Kıyaslanması, Uluslararası Mühendislik Araştırma ve Geliştirme Dergisi, 3(2), 18-24.

[22] Yardım, N., Çipil, Z. (2007). Türkiye İş Kazaları ve Meslek Hastalıkları: 2000-2005 Yılları Ölüm Hızları, Dicle Tıp Dergisi, 34(4), 264 – 271.

[23] Şen, M., Dursun, S., Murat G. (2018). Türkiye'de İş Kazaları: Avrupa Birliği Ülkeleri Bağlamında Bir Değerlendirme, Uluslararası Toplum Araştırma Dergisi, 9(16), 1167-1190.

[24] İşçi Sağlığı ve İş Güvenliği Meclisi, "Raporlar-İş Cinayeti Raporları", 2021, 06.11.2022. https://www.isigmeclisi.org/is-cinayetleri-raporlari

[25] Our World in Data, "Charts,Fatal Occupational İnjury", 2020, 01.02.2023. https://ourworldindata.org/grapher/fatal-occupational-injuries-among-employees?tab=chart&country

[26] World Health Organization (WHO), "Data-Indicator", 01.09.2022,15.02.2023. https://gateway.euro.who.int/en/indicators/hfa_453-4041-number-of-new-cases-of-occupational-diseases/

[27] Data Akademi, "Meslek Hastalıklarına Giriş, 28.02.2017, 17.03.2023. http://www.dataakademi.com.tr/wp-content/uploads/2017/02/28-MESLEK-HASTALIKLARINA-GİRİŞ.pdf

Kütahya Dumlupınar University
Institute of Graduate Studies

Journal of Scientific
Reports-A
E-ISSN: 2687-6167
Number 53, June 2023

RESEARCH ARTICLE

THE ROLE OF MHD WAVES IN HEATING OF THE SOLAR CORONA

Ebru BAŞ[1], Dicle ZENGİN ÇAMURDAN[2,*]

[1] Department of Astronomy and Space Sciences, Faculty of Science, Ege University, 35100 İzmir, Turkey, ebru.1093.ebru@gmail.com, ORCID: 0000-0002-2055-0259
[2] Department of Astronomy and Space Sciences, Faculty of Science, Ege University, 35100 İzmir, Turkey, dicle.zengincamurdan@ege.edu.tr, ORCID: 0000-0003-2596-1775

Receive Date:02.11.2022 *Accepted Date: 14.05.2023*

ABSTRACT

The million-degree-temperature corona, which exists above the cooler photosphere layer, is an unsolved astrophysical phenomenon. Magnetohydrodynamic (MHD) waves have recently been the favored subject of heating of corona and driving the solar wind research. In order to acquire a better knowledge of wave heating,, we must consider how various dissipation parameters, such as viscosity, temperature anisotropy, and heat conduction can influence the evolution of these phenomena in the coronal plasma. It was recently discovered that plume and inter-plume lanes (PIPL) structure North Polar Coronal Hole (NPCH) in the radial direction, however this has not been taken into consideration in many studies. SOHO/UVCS satellite data show that some parameters (i.e., temperature, particle number density) are different in these regions. We aim to find that whether these regions affect the dispersion properties of the incompressible MHD waves. We assumed a model based on a process of Alfvén/ion cyclotron resonance with O VI ions by using quasi-linear approximation taking into account PL and IPL structre in NPCH, for the first time. Our results show that the damping length scales ($0.2 - 1.8\,R$) and energy flux densities ($\sim 10^6$ erg cm^{-2} s^{-1}) of Alfvén waves are identical for both plumes and interplumes in NPCH. This amount of energy is sufficient to heat the coronal hole and accelerate the solar wind above $2 - 6\,R$.

Keywords: *Solar corona, Magnetohydrodynamic, Alfvén waves, Solar wind.*

1. INTRODUCTION

The solar corona exhibits different characteristics at the different phase of solar cycle (i.e., a quiescent active region, a flaring active region, an equatorial and a polar coronal hole, etc.). As a result, magnetic field strength, temperature, particle number density, and other physical properties vary from one region to another. The temperature of the photosphere which is the inner solar atmosphere is 5780 K. However, the corona which is the outer atmosphere of the Sun is not an isolated layer, and there is mass and energy transfer in both directions between the inner and outer layers via a region known as the transition region, where a sharp shift in temperature is seen (from 20000 K in the upper

JSR A
Journal of Scientific Reports

chromosphere to over 2 MK in the corona) [1]. The main questions are that what process (or mechanisms) is (are) responsible for the coronal heating, and how can this solar atmosphere recover enough energy to maintain a temperature of more than one million K? This is a long-standing problem of solar physics for over sixty years.

Several heating mechanisms have been proposed since the observations revealed the coronal heating problem. These mechanisms are typically divided into models that use alternating current (AC) and direct current (DC). AC models contain mechanisms with the photospheric driving timescale (τ_{ph}) that are smaller than the Alfvén travel-time (τ_A) through a coronal loop and primarily comprise of wave dissipation models ([2], [3], [4]) and MHD Alfvén wave. In the DC models, the photospheric driving timescale that are longer than the Alfvén travel-time ($\tau_{ph} \gg \tau_A$) and the coronal magnetic field becomes tangled and braided by slow footpoint motions. According to these models, the magnetic energy is dissipated via nanoflares and small-scale reconnection events ([5], [6], [7]). A full review of the analytical and numerical studies performed is far beyond the scope of this paper, so we suggest readers interested in the specifics of the heating process to two recent review papers by Cranmer & Winebarger [8] and Viall et al. [9]. Instead, we focus on one of the AC mechanism known as MHD wave heating that is currently the most favoured.

The solar plasma at such temperature has a tendency to lose energy via optically thin radiation and thermal conduction and mass loss with the solar wind and solar activities (flares, mass ejections from corona), which are referred to as macroscopic processes. In addition, small-scale processes like viscosity, electrical resistance, heat conductivity, and forced vibration transmit energy from one area to another. Small-scale processes, referred to as dissipative in terms of energy and heat equations, result in the conversion of mechanical energy into heat and raise the entropy of the plasma. These processes, according to the MHD wave theory, transform mechanical energy stored in the wave's ordered motion into disordered thermal energy of the particles and can serve as a constant supply of energy for the corona. This study uses the propagation properties of these waves, which resonate with O VI ions, to investigate the coronal heating problem in NPCH by wave-particle interactions in the context of the MHD approximation.

Magnetic waves can dissipate their energy in the atmosphere, heating the corona and can be seen all over the corona. To explain the observations, several models have been developed. Extreme Ultraviolet (EUV) observations, performed by Transition Region and Coronal Explorer (TRACE) and the Solar and Heliospheric Observatory (SOHO) satellites, confirm the existence of MHD waves in NPCH ([10], [11], [12], [13], [14]). The line measurements observations of O VI and Mg X ions showed that beyond 1.75 - 2.1 R distance range, the solar plasma was collisionless in NPCH ([15]). These observations revealed the collisionless structure of the NPCH. This indicates that in the relevant distance extend, plasma transport processes should not be studied in the classical Coulomb collission. The ion-cyclotron resonance mechanism could be responsible for the extraordinarily large line widths. Therefore, the widths of the emission lines taken from this region can be used to understand how MHD waves contribute to heating the corona and increasing the speed of the solar wind. Observations of coronal lines formed at high temperatures ($T \geq 10^6$ K) from the solar edge along the radius direction to the solar corona ($R \geq 1.1\ R_\odot$). They provide confirmation for MHD-induced line

JSR A
Journal of Scientific Reports

broadening. Hassler et al. [16] made the first observations in this field. They calculated the effects of opacity, systematic fluid effects, thermal Doppler expansion, and the effects of MHD waves on the line broadening using six EUV emission lines. They came to the conclusion that MHD waves may be reponsible for the non-thermal extraordinarily large line widths of the solar emission lines. In light of data from the Solar Maximum Mission (SMM) satellite's Flat Crystal Spectrometer (FCS), Saba and Strong [17] obtained a similar result. The SOHO satellite provided later work on measurements of the solar coronal emission lines. Doyle et al. [15] found Si VIII λλ 1440.49 and 1445.75 line widths as a measurement of location relative to the solar surface using SOHO/SUMER data. The non-thermal widths of the lines increased from $\sim$24 km s^{-1} at the solar edge to $\sim$28 km s^{-1} at a distance of 35 arcsec from the edge along the radius direction to the solar corona. Patsourakos and Klimchuk [18] demonstrated that non-thermal line broadening may be measured by examining the profiles of highly ionised lines such as Fe XVII. These observations have led them to the conclusion that MHD waves might be responsible for heating the quiescent solar corona. van Ballegooijen et al. [19]] investigated whether or not Alfvén wave turbulence can heat the corona and discovered that the photospheric waves can sustain a temperature of 2.5 MK. On the other hand, the nonthermal line broadening using Hinode/EIS observations was investigated by Brooks and Warren [20] and their findings contradict proposed models of coronal heating: nanoflares, Alfvén wave turbulence, reconnection.

The length and frequency of the damped waves provide guidelines for theoretical computations. Using Extreme Ultraviolet Imaging Telescope (EIT) and Ultraviolet Coronograph Spectrometer white-light channel (UVCS/WLC) measurements, Ofman et al. [21] examined the wave dampening in a gravitationally layered medium carried by a radially changing magnetic field. The damping of slow magnetosonic waves was calculated in this work to be 0.08 R under the compressive viscosity; however, for waves with a 300 s period, this value increases to 0.14 R ($R = r/R_{\odot}$, where $R_{\odot} = 7 \times 10^{10}$cm). They came to the conclusion that the dissipated waves might have an effect on the solar wind's acceleration and so transfer momentum to the collisionless region of the hole, which is located farther from the sun. The impact of nonlinear dissipation of Alfvén waves in coronal holes has been researched by Nakariakov et al. [22] and their results showed that short-period Alfvén waves (< 10 s) and the periods ~ 300 s become diminished within radial distances of $10\,R$ and $1\,R$, respectively. These waves may be responsible for the solar wind's acceleration as well as the heating of the coronal hole plasma. The periodicities and propagation speeds of MHD waves discovered in coronal hole structures were summarized in Table 1 by Banerjee et al. [23]. However, it seems that the related energy flow that the Alfvénic waves are thought to be carrying at the corona is enough to satisfy the requirements for acceleration of the solar wind and/or coronal plasma heating (also see Discussion section).

Furthermore, As can be seen in Fig. 1, the observations of Wilhelm et al. [24] show that NPCH is structured radially by plume lanes (PL) and interplume lanes (PIPL). These structures are considered by many studies ([21], [25], [26], [27]). Thermal conductivity, viscosity and anisotropic resistivity are found in the higher level of chromosphere and corona (see details in Sec. 2). The observed periods for the plume and inter-plume regions in this study are between $600 - 1800$ s. Using Doppler velocity time records of the corona, Morton et al. [27] studied Alfvén wave propagation through the solar atmosphere. Their research revealed the presence of forward- and backward-propagating Alfvén

JSR A
Journal of Scientific Reports

waves in plume (PL) and interplume (IPL) lanes, which are open magnetic field line regions. They noted the presence of turbulence in Alfvén wave, that heats the plasma and speeds up the solar wind. They were able to identify counter-propagating waves from the power spectra they obtained. In addition to this, Banerjee et al. [26] discovered that non-thermal velocities differ between plume and inter-plume plasma, with increased velocities measured in the inter-plume regions.

The goal of this study is to test the hypothesis that waves are indeed what heats the corona and propels the solar wind so both the damping lenght scale of the waves and the energy dissipated by the waves must be quantified. In the present work, we investigate the damping and propagation of Alfvén waves in NPCH in the context of incompressible MHD, and the basis for the current investigation is mainly given by Pekünlü et al. [28]. We investigate the dissipation of MHD waves taking into account the data from SOHO satellite on temperature, variations in non-thermal line widths and electron distribution in the PL/IPL structure of NPCH. The effects of the isotropic viscosity on the propagation characteristics of these waves are taken into account in the constructed model. In order to compute the damping length scales and wave energy flows, we rederive the dispersion relation. In this context, we will discuss the findings on how MHD waves accelerating solar wind and heating the corona. The novelty of our approach is that we focus on how the PL/IPL structure of NPCH affects wave propagation characteristics which has not been studied previously, using incompressible MHD waves.

The novelty of our approach is that we investigate the effect of the PL/IPL structure of NPCH on wave propagation characteristics, which has not been studied previously, using incompressible MHD waves. The propagation characteristics of incompressible MHD waves with periods of 0.0001 - 0.01 s within the range of 1.05 - 1.35 R were examined in the study by Pekünlü et al. [28], R is the radial distance that has no dimensions ($R = r/R_{\odot}$). Furthermore, in contrast to Pekünlü et al. [28], considering the recent literature studies, we chose waves having angular frequency $\omega = 0.01 - 1$ rad/s, that represents a period range of $628 \text{ sec} > P > 6.28$ sec in 1.65 - 3.50 R region.

2. PROPERTIES OF PLASMA and BASIC MODEL for NPCH

2.1. Number Densities in NPCH

Many studies have attempted to estimate the electron number density distribution in the coronal hole ([29], [30], [15], [31]). The measurements of Si VIII line ratio found that the densities of electron in the NPCH were approximately two times less than in low solar activity [32].

The electron number density is calculated for the range 1.65 - 3.50 R. Wilhelm et al. [33] reported that the coronal hole is typically constant, based on observations from many plume and interplume locations over the two Solar minimums. Since the mathematical relationship established by Doyle et al. [15] is compatible with the data of the electron number density change in the plume and interplume region, we used it in our investigation of electron number density variation,

$$N_e = \frac{1 \times 10^8}{r^8} + \frac{2.5 \times 10^3}{r^4} + \frac{2.9 \times 10^5}{r^2} \text{ cm}^{-3} \quad (1)$$

JSR A
Journal of Scientific Reports

relation is used. $R = r/R_{\odot}$ denotes the radial distance that is normalized. In NPCH, mass density is defined as $\rho_0(r) = \tilde{\mu}\, m_p N_e$, where m_p is the mass of proton mass and $\tilde{\mu}$~0.6 is the average atomic weight. According to Priest [34], the pressure scale height Λ_p is as follows:

$$\Lambda_p = 5.0 \times 10^6\, T(r)\, (r/R_{\odot})^2 \text{ cm} \tag{2}$$

NPCH is electrically quasineutral, which indicates that the amount of electrons is equal to the number of protons [35], [36], [37]. The number of electrons in PL is approximately 10 % greater than that in IPL [38].

In our work, we used Devlen and Pekünlü's [39] equation for the distribution of the numerical density of protons in the space of plume conditions, with $N_e = N_p$:

$$N_p^P(R,x) = N_p^{IPL}(R)\left(1 + 0.1\, Sin^2(2\pi x/92.16\, R)\right) \tag{3}$$

The abundances of some elements (such as oxygen) were measured in coronal streamers by Raymond et al. [40]. They discovered that the number density of oxygen is $N_{O\,VI} = 6.8 \times 10^{-5} N_p$. Cranmer et al. [41] provide the highest and lowest values changing between $2.4 \times 10^{-6} N_p - 8 \times 10^{-7} N_p$ in polar coronal holes.

2.2. Temperatures in NPCH

SOHO/UVCS data suggested that the NPCH is configured by bright and dim lanes [42]. According to their findings, the form of the NPCH is consisted of bright, cold, and high-intensity plumes (PL) and dim, warm, and low-intensity interplume bands (IPL). An collisionless plasma is most likely to exhibit temperature anisotropy. Using ion line of sight velocities, SOHO/UVCS data demonstrated that the temperature of the O VI ion observed near the coronal hole is direction dependant [43], [41]. In this condition, the kinetic temperature of ion in the perpendicular direction to the magnetic field, $T_{\perp}$, is higher than its temperature in the parallel direction, $T_{\parallel}$. UVCS data revealed comparable temperature dependences for other rare ions in the coronal hole (He++, Si VIII, Mg X, and etc). The emission line lengths of O VI ions measured in IPL were found to be wider than those measured in PL. This suggests that heating interplume lanes perpendicular to magnetic field lines is more effective than heating plumes [44], [33]. These findings suggest that the ion-cyclotron induced vibration method can heat the coronal plasma.

Because there are no observational data on the temperature distribution of the plasma in NPCH, the temperature is assumed to be isothermal along the line of sight. the temperature along los is considered to be isothermal. On the other hand,, Kohl et al. [43] discovered that O VI line intensity changed in both the radial and x directions.

JSR A
Journal of Scientific Reports

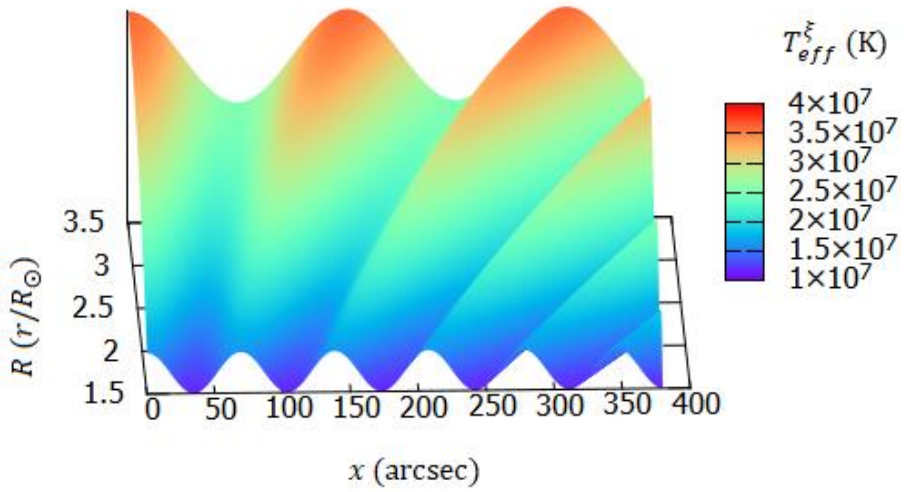

Figure 1. T_{eff}^{ξ} values of the O VI ions depending on the parameters R and x. Wave crests correspond to warmer IPL, and troughs between two ridges correspond to cooler PL in the NPCH. The width of the PIPL change with R. The axis x is measured in arcseconds, as it is in [22]. This figure is reproduced with permission of Devlen et al. [46].

The relationship between ion temperature and effective temperature is identified by Wilhelm et al. [42]

$$T_{eff} = \frac{m_i}{2k_B} v_{1/e}^2 = T_i + \frac{m_i}{2k_B} \xi^2 \tag{4}$$

where the Boltzmann constant, the mass and temperature of ion are denoted by k_B, m_i , T_i , respectively. The most likely velocity of an ion through the los is showed $v_{1/e}$. In an isotropic turbulent velocity field with Gaussian distributions, ξ represents the speed that has the highest likelihood of occurrence based on the probability density function. Esser et al. [45] defined the relation between wave amplitude and ξ, $\langle \delta v^2 \rangle = 2\xi^2$.

According to Wilhelm et al. [42], T_{eff} (O VI) in IPL is approximately 30% greater than that of PL. The two-dimensional effective temperature calculated by Devlen et al. [26] was used in our study based on this observation. Figure 1 illustrates the observed variation as well.

According to Devlen and Pekünlü [39],

$$T_{eff}(R) = -7.941 \times 10^7 R^2 + 4.9487 \times 10^8 R - 5.7625 \times 10^8 \tag{5}$$

JSR A
Journal of Scientific Reports

Table 1. The effective temperature (T_{eff}), the ion temperature (T_i), and the component of the effective temperature that is not related to thermal processes (T_{eff}^{ξ}) in the interplume and plume region for O VI ion, are presented as an expression of distance along the radial axis (R). Temperature units are 10^7 K.

	Interplume			***Plume***		
R	T_{eff}	T_i	T_{eff}^{ξ}	T_{eff}	T_i	T_{eff}^{ξ}
1.7	3.55	1.61	1.94	2.49	1.13	1.36
1.8	5.72	3.62	2.10	4.01	2.54	1.47
1.9	7.73	5.48	2.26	5.46	3.86	1.59
2.0	9.58	7.18	2.40	6.83	5.12	1.71
2.1	11.28	8.74	2.54	8.14	6.31	1.83
2.2	12.81	10.15	2.66	9.37	7.43	1.95
2.3	14.19	11.40	2.78	10.53	8.47	2.07
2.4	15.40	12.51	2.90	11.60	9.42	2.18
2.5	16.46	13.46	3.00	12.58	10.28	2.29
2.6	17.36	14.26	3.10	13.45	11.05	2.40
2.7	18.10	14.92	3.18	14.21	11.71	2.50
2.8	18.68	15.42	3.26	14.85	12.25	2.59
2.9	19.10	15.77	3.34	15.36	12.68	2.68
3.0	19.37	15.97	3.40	15.75	12.99	2.77
3.1	19.47	16.02	3.46	16.00	13.16	2.84
3.2	19.42	15.91	3.50	16.12	13.21	2.91
3.3	19.20	15.66	3.54	16.09	13.12	2.97
3.4	18.83	15.26	3.58	15.91	12.89	3.02
3.5	19.30	14.70	3.60	15.59	12.52	3.07

The value ranges of ξ for Mg X and O VI ions are precisely comparable to one another and change in the identical direction as R, as revealed by Esser et al. [45]. Taking all of this into consideration, Devlen and Pekünlü [39] calculated a polynomial expression for the component of the effective temperature that is not related to thermal processes of O VI ions using Mg X data for ξ, which we use in our study, as shown below.

$$T_{eff}^{\xi} = -4 \times 10^6 R^2 + 3 \times 10^7 R - 2 \times 10^7 \quad (6)$$

$$T_{eff}^{P}(R, x) = T_{eff}^{IPL}(R)\left(1 + 0.3\, Sin^2(2\pi x / 92.16\, R)\right) \quad (7)$$

In this study, we calculated the variations of T_{eff}, T_i, T_{eff}^{ξ} with radial distance using Equations (5)-(7) for both plume and interplume lanes, which are listed in Table 1.

JSR A
Journal of Scientific Reports

2.3. The Solar Magnetic Field Intensity in NPCH

The magnetic field (B) variation with R in NPCH as determined by Hollweg [47] is given in Equ. 8. Because there is no data in the literature on how B varies in the PL and IPL, in particular with respect to the x direction, we will suppose that the following formula employs to both PL and IPL.

$$B = 1.5(f_{max} - 1)R^{-3.5} + 1.5R^{-2} \text{ G} \tag{8}$$

with $f_{max} = 9$.

3. MHD EQUATIONS

The equations of motion, magnetic flux conservation, and magnetic induction are the fundamental equations for the propagation of waves and dissipation within an incompressible fluid. [48]:

$$\rho \frac{D\mathbf{v}}{Dt} = (\nabla \times \mathbf{B}) \times \frac{\mathbf{B}}{\mu} + \rho v \left[\frac{4}{3}\nabla(\nabla \cdot \mathbf{v}) - \nabla \times \nabla \times \mathbf{v}\right] \tag{9}$$

$$\frac{\partial \mathbf{B}}{\partial t} = \nabla \times (\nabla \times \mathbf{B}) + \eta \nabla^2 \mathrm{B} \tag{10}$$

$$\nabla \cdot \mathbf{B} = 0 \tag{11}$$

In these equations, B , v , ρ represent the magnetic field vector, the fluid velocity, the mass density of gas and v , μ represent kinematic viscosity and magnetic permeability. $\eta = 5.2 \times 10^{11} T^{-3/2} \ln \Lambda$ $\mathrm{cm^2\ s^{-1}}$ refers magnetic diffusivity.

The viscosity coefficient is given by Spitzer [49],

$$\rho v = 2.21 \times 10^{-15} \frac{T^{5/2}}{ln\Lambda} \text{ g cm}^{-1}\text{s}^{-1} \tag{12}$$

here $ln\Lambda\ (= 22)$ represents the Coulomb logarithm.

$$D/Dt = \partial/\partial t + \mathrm{v} \cdot \nabla \tag{13}$$

represent the Lagrangian derivative.

We applied a conventional WKB (Wentzel-Kramers-Brillouin) perturbation analysis to examine the equilibrium state. All variables are represented in this examination by adds of equilibrium and a minor perturbed quantity where "0" and "1" subscript indicates these parameters, respectively, i.e. $\rho = \rho_0 + \rho_1$, $\mathrm{B=B_0 + B_1}$ etc.

The linearized equations derived from Eq. 8 - Eq.10 are as follows:

JSR A
Journal of Scientific Reports

$$\rho_0 \frac{D\mathrm{v_1}}{Dt} = \frac{1}{\mu}(\mathrm{B_0}\cdot\nabla)\mathrm{B_1} + \rho_0 v\nabla^2\mathrm{v_1} \tag{14}$$

$$\frac{\partial \mathrm{B_1}}{\partial t} = (\mathrm{B_0}\cdot\nabla)\mathrm{v_1} + \eta\nabla^2\mathrm{B_1} \tag{15}$$

$$\nabla\cdot\mathrm{B_1} = 0 \tag{16}$$

Perturbed values are generally thought to be small in compared to equilibrium values in the linear approximation., i.e. $\rho_1\cdot\rho_1 = 0$ and $\mathrm{B_1}\cdot\mathrm{B_1} = 0$ etc.

We assume that the perturbation quantities vary as $\exp[i(\mathbf{k}.\mathrm{r} - \omega t)]$. For Eq. 14 - Eq.16, we use the following replacements: $\partial/\partial t \rightarrow -i\omega$ and $\nabla \rightarrow ik$. We applied scalar product Eq. 14 - Eq.16 with $\widehat{\mathrm{B_0}}$ unit vector;

$$\rho_0(i\omega)\left(\mathrm{v_1}\cdot\widehat{\mathrm{B_0}}\right) + \frac{1}{\mu}i(\mathrm{B_0}\cdot\mathbf{k})\left(\mathrm{B_1}\cdot\widehat{\mathrm{B_0}}\right) - v\rho_0 k^2\left(\mathrm{v_1}\cdot\widehat{\mathrm{B_0}}\right) = 0 \tag{17}$$

$$(i\omega)\left(\mathrm{B_1}\cdot\widehat{\mathrm{B_0}}\right) + i(\mathrm{B_0}\cdot\mathbf{k})\left(\mathrm{v_1}\cdot\widehat{\mathrm{B_0}}\right) - \eta k^2\left(\mathrm{B_1}\cdot\widehat{\mathrm{B_0}}\right) = 0 \tag{18}$$

We can derive the dispersion relation from equations (17) and (18) as follows:

$$\eta v k^4 + \left({v_A}^2 - i\omega(v+\eta)\right)k^2 - \omega^2 = 0 \tag{19}$$

where $v_A = B_0/\sqrt{\mu\rho_0}$ is Alfvén velocity.

We solved the equation (19) numerically using Matlab code, and we get two different complex values of k (wave number), negative and positive of the same value. A negative value for k indicates that the wave is damped as it propagates outward from the sun. Reversing the imaginary part of the smaller k value yielded the wave's damping length scale.

For the range of 1.65-3.50 R, the wave energy flux density is calculated using Priest's [48] formula.

$$F = \rho\langle\delta v^2\rangle\frac{\partial\omega}{\partial k} \tag{21}$$

where $\partial\omega/\partial k$ is the wave's group velocity, and $\langle\delta v^2\rangle = 2\xi^2$ corresponds to the non-thermal part of the velocity which is related to fine-scale turbulent structures that remain unresolved [39].

The polynomial function provided by Esser et al. [45] was used by Devlen and Pekünlü [39] to express the non-thermal velocities of OVI ions as follows:

$$\xi = 0.2\times10^7 R^3 - 10^7 R^2 + 4\times10^7 R - 3\times10^7 \tag{22}$$

JSR A
Journal of Scientific Reports

Table 2. The energy flux density and length scale for damping of Alfvén waves of different periods propagating along a plume in the radial direction of R. x is chosen 40″ for plotting purpose. The viscosity value was assumed as 10^{20} cm^2 s^{-1} in the calculations.

P (s)	R	$1/k_i$ ($R_\odot$)	F(erg cm^{-2} s^{-1})
6	1.6	0.1983	1.01×10^7
	1.8	0.1983	6.79×10^6
	2.0	0.1983	4.70×10^6
	2.2	0.1982	3.45×10^6
	2.4	0.1982	2.72×10^6
	2.6	0.1982	2.31×10^6
	2.8	0.1983	2.10×10^6
	3.0	0.1983	2.01×10^6
60	1.6	0.6207	3.20×10^6
	1.8	0.6196	2.15×10^6
	2.0	0.6186	1.49×10^6
	2.2	0.6180	1.09×10^6
	2.4	0.6179	8.61×10^5
	2.6	0.6182	7.31×10^5
	2.8	0.6188	6.63×10^5
	3.0	0.6197	6.37×10^5
600	1.6	1.8142	1.04×10^6
	1.8	1.7977	7.05×10^5
	2.0	1.7855	4.93×10^5
	2.2	1.7785	3.64×10^5
	2.4	1.7768	2.87×10^5
	2.6	1.7802	2.43×10^5
	2.8	1.7883	2.19×10^5
	3.0	1.8003	2.09×10^5

The wavelength $\lambda(= 2\pi/k_r)$ is compared with the value of the local pressure scale height (Λ_p). The scientific reliability of the "slowly varying medium" approach is examined for preferred frequencies and radial distances. We obtained that the criterion of "slowly varying medium", namely $\lambda/\Lambda_p \ll 1$, is satisfied for the period less than 60 s in the considered radial range. One should, however, keep in mind that this condition is not satisfied for the periods, $P > 60$ s. Nonetheless, we consider them worthy of use because the observations have unambiguously shown that these waves are present in the NPCH [22],[23]. However, one should take caution when interpreting the results from this study for waves with longer periods.

Because viscosity coefficient is not well-constrained in the conditions of the solar corona, we need to specify that we adopted this coefficients as a free parameter.

JSR A
Journal of Scientific Reports

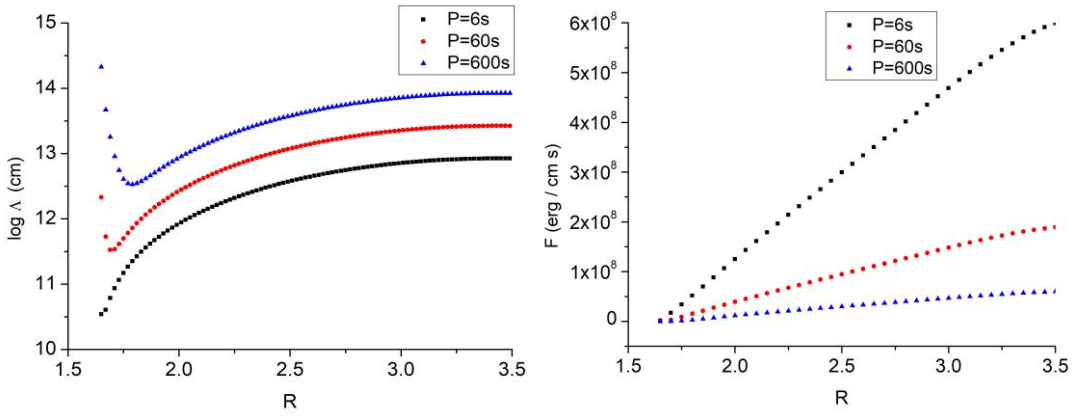

Figure 2. Comparison the damping length scale $(1/k_i)$ with R, where k_i is the imaginary part of the wave vector. The variation of the wave energy flux density with respect to R normalized radial distance is showed in bottom pannel.

4. DISCUSSION

In a collisionless plasma, like the NPCH region in sun, the effectiveness of Alfvén waves in heating and the propagation characteristics has not yet been studied in detail. We tried to comprehend to understand how ions such as O VI react to the propagation of these waves within NPCH as far as 1.5 – 3.5 R at frequencies that are close to their cyclotron frequency in this study. In addition to this, assuming that the solar plasma is an incompressible plasma, we examine the impact of the PL/IPL formation of coronal hole on the properties of wave propagation which has never been investigated before.

The first step in the study is to compute the length scales for damping and to determine whether the waves with the appropriate value have the required energy that will cause coronal heating and the solar wind's acceleration. In the context of incompressible MHD, for ω was given a value in the range $6 < P < 600$ covering the radial distance of 1.5– 3.5 R, we investigate how the ion-cyclotron waves propagate. The variation in length scale for damping $(1/k_i)$ of the wave obtained using Equ. (19) and Figure 2 presents the variation of this parameter in solar radius as a function of radial location relative to the sun (left). According to Fig. 2 (left), as the wave period increases, so does the damping length scale. The figure shows that that R also causes an increase in the wave's damping length scale. Figure 2 (right) demonstrates the change in energy flux density of the waves as a function of radial location relative to the sun. It is evident that the waves's energy flux density increases with increasing radial distance and decreases with increasing wave period. The length scale for damping of the high frequency waves has larger values ($> 5\ R$), as can be seen in Fig. 2 (left).

We made the first attempt to build a numerical solution of the dispersion relation for these waves to comprehend the properties of MHD wave propagation along the plume and interplume structure. For

JSR A
Journal of Scientific Reports

this purpose, we calculated the energy flux densities and damping length scales in the radially using $x = 40''$ as the plume's midpoint distance. Assuming viscosity has a value of 10^{20} cm^2 s^{-1}, at some radial distances, Table 2 shows the calculated parameters of waves for periods 6,60 and 600 s. As can be seen in the Table 2, as distance increases, the fluxes tend to decrease and this decrease in flux is more significant at shorter periods.

Figure 3 illustrates how frequency and viscosity effects variations in the energy flux density (bottom) and the length scale for damping (top) of a waves in a plume at $R = 1.7\ R$. We used false colors in this figure that display length-scales from 0.01 to 6.5 R (top figure) and the logaritmic energy flux density of the waves (Log *F)* between 5.5 and 8.5 (bottom figure). Viscosity is observed to rise linearly with frequency. For example, the damping length scale is $\sim 2.5 - 3\ R$ when the viscosity value is approximately 10^{21} cm^2 s^{-1} and the period of the wave is ~ 60 s, i.e., the logarithmic frequency is -1.0 s^{-1}. Since the viscosity coefficient in coronal conditions is uncertain, it appears that it is a crucial parameter in determining the distance at which the waves are damped, and for these waves that plays a role to the coronal's heating, its value should be greater than 10^{20} cm^2 s^{-1}.

Studies suggest that for appropriate values of damping scale length, an energy flux density of MHD waves roughly $10^6 - 10^7$ erg cm^{-2} s^{-1} is sufficient. The energy flux density of the wave is observed to increase with increasing viscosity when the frequency is fixed at a specific value. These waves have identical length scales for dissipation and energy flux densities for plumes and interplumes. On the other hand, as suggested by Cranmer et al. [44], the heating interplume lanes perpendicular to magnetic field lines is more effective than heating plumes. Similarly, Dogan and Pekunlu [50] obtained that the resonance mechanism in the IPL is far more effective than in the PL using a model based on the kinetic theory. However, we could not find any evidence that the resonance mechanism works more efficiently in any of these regions. We consider that the incompressible plasma assumption for NPCH in our model may not be valid for this region, or the variations between the PL and IPL regions can be revealed by taking into account different ion contributions in the modelling as opposed to heating with the only O VI ion.

In Figure 4, when waves with a wider period range ($P = 0.0001 - 600$ sec) are examined at $R = 1.7\ R$, it is noticed that L values of these waves is in the range of 1-1.5 R for all frequencies when the viscosity is $< 10^{20}$ cm^2 s^{-1}. The L is greater than $2\ R$ for the frequency range of $0.001 - 100$ s^{-1} when the viscosity value is greater than 10^{20} cm^2 s^{-1}. At higher frequencies, the L value is less than $1.5\ R$.

JSR A
Journal of Scientific Reports

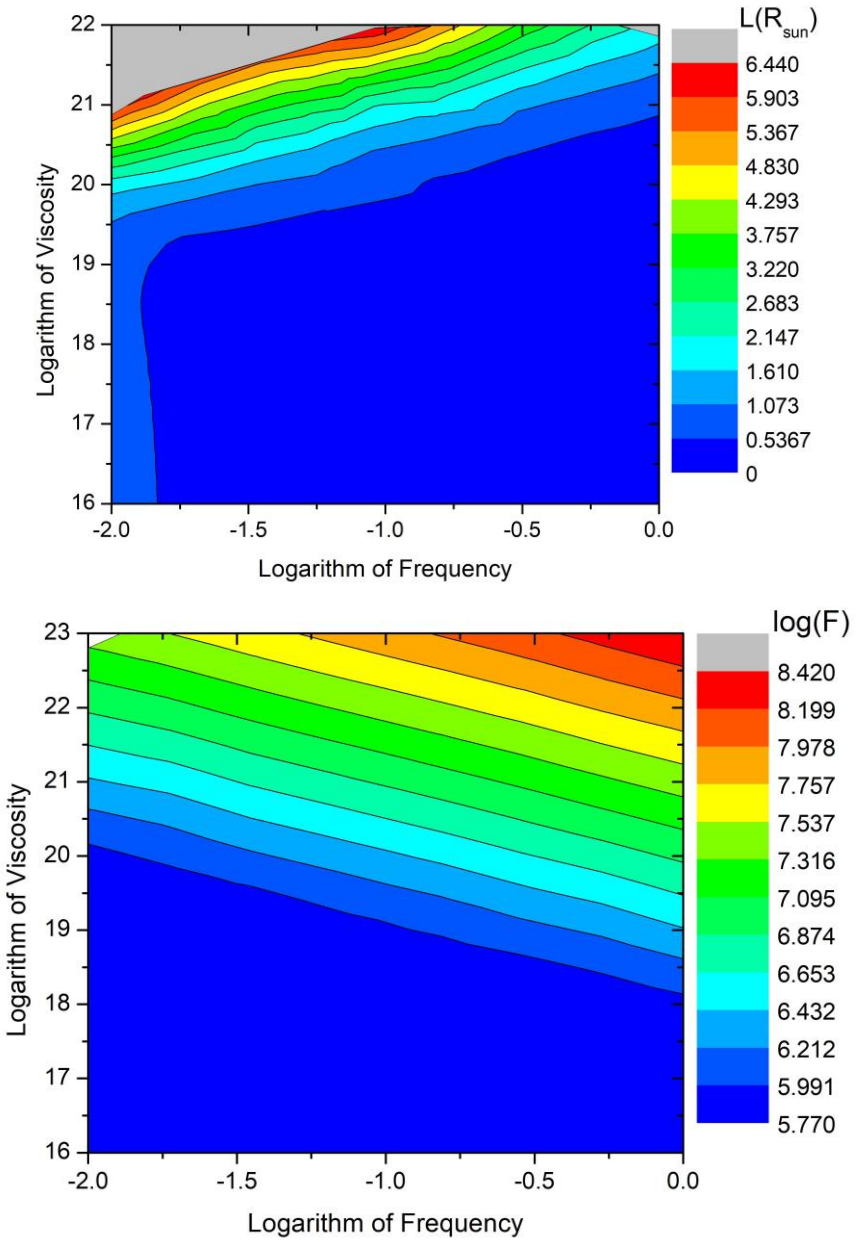

Figure 3. The length-scale for damping contours in R_{sun} unit (top) and flux densities (bottom) shown versus viscosity and frequency in logaritmic scales in the case of waves transmitting in a plume.

JSR A
Journal of Scientific Reports

Table 2 shows that the waves's flux densities continuously reduce as the radial direction increases. This energy decay suggests that waves and ions in plume structure in coronal hole are exchanging energy through ion cyclotron resonance process. The literature provides some information concerning energy fluxes and the wave's length scales for damping and is used to compare the results obtained in our study (see Table 3). According to Hollweg [51] and Hollweg and Johson [52], the essential energy density flux for heating the corona is 5×10^5 erg cm^{-2} s^{-1}. According to [53], 8×10^5 erg cm^{-2} s^{-1} is the MHD wave energy flux needed for heating this region. McIntosh et al. [54] examined spectral observations from the Solar Dynamics Observatory's (SDO) Atmospheric Imaging Assembly (AIA). They discovered that small amplitude waves in a NPCH region contain enough energy to account for the heating needs of coronal holes ($1 - 2 \times 10^5$ erg cm^{-2} s^{-1}). Magnetic wave energy dissipation is important not just for coronal heating in coronal holes, but also for the acceleration of the fast solar wind (for details see [55], [23]). According to Hahn et al. [56], the observed fast decline in line widths is needed to heat the NPCH and promote the solar wind acceleration. Hahn and Savin [57] calculated the energy flow density to be 6.7×10^5 erg cm^{-2} s^{-1}. In addition to this, anisotropic heat conduction and isotropic viscosity effects on MHD wave propagation in the NPCH were examined by Devlen et al. [46] for compressible MHD waves. Their findings demonstrate that the wave propagation characteristics are novelly introduced by the perpendicular heat conduction. Alfvén waves have energy flux densities that range from $10^6 - 10^{8.6}$ erg cm^{-2} s^{-1}. Their findings imply that transformed magnetoacoustic waves might be the primary driver of the O VI ion heating and preferential acceleration that has been observed, as well as an additional accelarator concerning the fast solar wind in this region.

The these waves's flux densities in our investigation were calculated to be an interval of $10^5 - 10^7$ erg cm^{-2} s^{-1}, as indicated in Table 2. For example, L and F are $2\,R$ and 1.5×10^6 erg cm^{-2} s^{-1} respectively, for $P = 60$ s and viscosity coefficient around Spitzer value (10^{20} cm^2 s^{-1}). Our findings imply that Alfvén waves deposit energy in the NPCH, supplying as a critical resource of heating this layer and primarily favored heating of oxygen ions. This quantity is expected to replace the energy lost in NPCH due to heat conduction to lower regions and optically thin emission.

Table 3. An overview of some of the research on the waves's energy flux density in various areas of solar corona.

Region	$\boldsymbol{F}$(erg cm^{-2} s^{-1})	**References**
Coronal Hole	8×10^5	Withbroe & Noyes [53]
Corona	4-5 $\times 10^5$	Hollweg [51] Hollweg &Johson [52]
NPCH	5×10^5	Banerjee et al. [31]
Coronal Hole	1-2 10^5	McIntosh et al. [54]
Polar Coronal Hole	6.7×10^5	Hahn & Savin [57]
NPCH	$10^6 - 10^{8.6}$	Devlen et al. [46]
NPCH	$10^5 - 10^7$	This study

JSR A
Journal of Scientific Reports

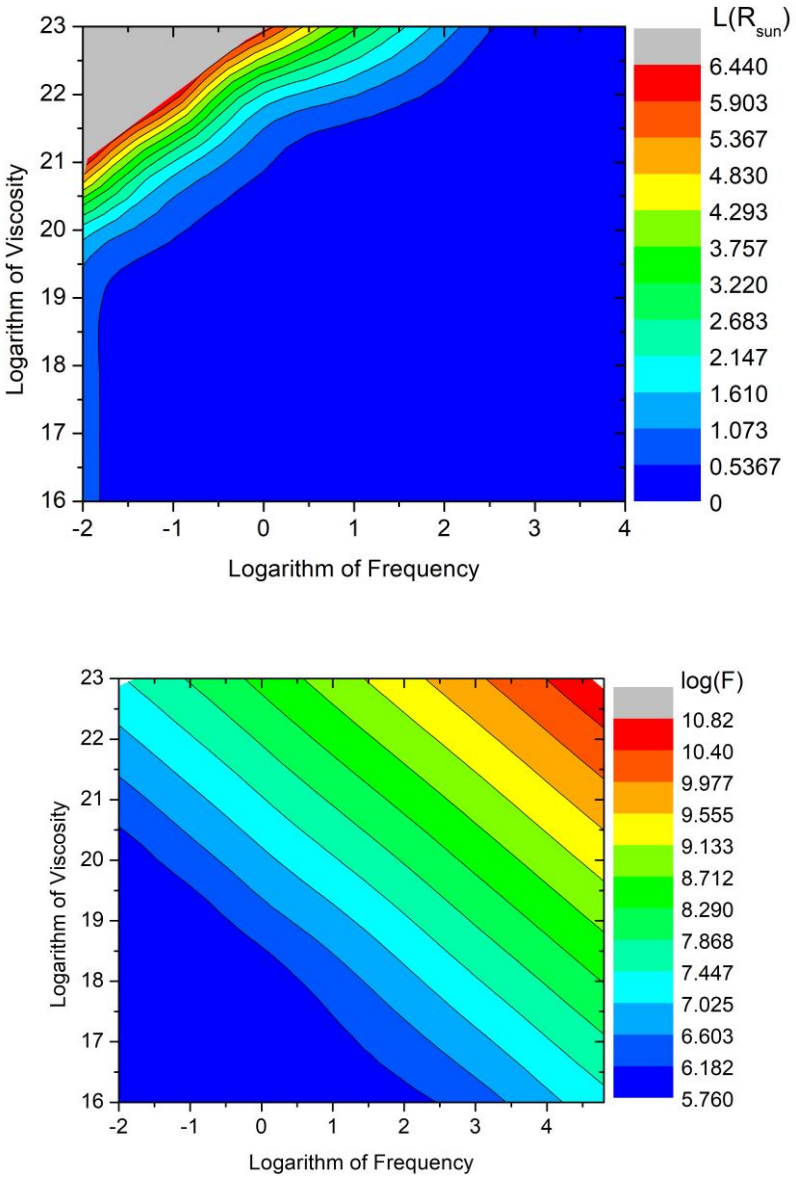

Figure 4. The length-scale for damping contours in R_{sun} unit (top) and flux densities (bottom) shown versus viscosity and frequency in logaritmic scales in the case of waves transmitting in a plume. The frequency range is between 0.0001 sec < *P* < 600 sec.

As shown by Antonucci et al. [58], coronal UVCS data can be utilized to detect an acceleration of the solar wind beyond $1.5 - 2\ R$. The data collected indicates the presence of compelling evidence of the fast solar wind within the central region of polar coronal holes, following the path of exposed magnetic fields. According to Telloni et al. [59], it is stated that Alfvén waves that are in resonance with ions cause energy dissipation in the outer corona across the magnetic field at a maximum rate around $1.9\ R$ which means the energy release can contribute to increase the wind speed. As a results, according to our findings, Alfvén waves have a greater damping length-scale ($2 - 6\ R$), Alfvén waves both in PL and IPL may be responsible for the extra the enhanced velocity of the fast solar wind that has been observed.

5. CONCLUSION

Our model, for the first time, takes into account the MHD wave propagation characteristics assuming an incompressible coronal plasma taking into account PL/IPL region in NPCH. Our investigation of the effect of the PL/IPL structure on Alfvén wave propagation characteristics yielded such results that the transmitting Alfvén waves's lenght scales for damping and energy flux densities along the Pl and IPL regions are remarkably similar. Alfvén waves with periods less than 60 seconds can contribute to and accelerate the solar wind beyond a heliocentric range of $2\ R$ and transport sufficient energy flux to heat this region. The Alfvén waves's propagation properties in NPCH show results that these waves possess sufficient energy flux to heat the corona. The wave mechanical flux density is in the order of 10^6 erg cm^{-2} s^{-1}. It is possible that the longer dissipation length-scale of these waves, which exist in both in both PL and IPL, is contributing to the measured increase in speed of the fast solar wind.
Various studies on the solar corona clearly show that this region's heating is not solely caused by the MHD wave dissipation. There are definitely various proposed mechanism at work, each with a different efficiency, in various areas of the solar corona. These include small-scale reconnection, the drifting of heating layers in phase mixing/resonant absorption known as nanoflare heating event, and others.

In order to solve the heating problem, we need improved observations. In the near future, new telescope and instrument data will soon provide high quality observations of the solar atmosphere. Recognizing the properties of coronal hole plasma will advantage from upcoming measurements of electron temperatures in the corona using the Solar Orbiter's SPICE spectrometer or polarimetric studies of the magnetic field in the corona utilizing the Daniel K. Inoue Solar Telescope. With the availability of additional data, we intend to improve our model for NPCH. The plasma fluid description in our model is a rough approximation to the coronal condition. The model we constructed in this study will be utilized to examine the wave dissipation characteristics in NPCH applying the solution of the collisionless Vlasov equation.

ACKNOWLEDGEMENT

This work is a part of the study of the MS thesis of E. Baş

REFERENCES

[1] Wedemeyer-Böhm, S., Lagg, A. , Nordlund, A., (2009), The Origin and Dynamics of Solar Magnetism, Space Sciences Series of ISSI, Volume 32. ISBN 978-1-4419-0238-2, Springer New York, p. 317.

[2] Ofman, L., Davila, J. M., Steinolfson, R. S.,(1994), Nonlinear studies of coronal heating by the resonant absorption of Alfvén waves, Geophysical Research Letters, Volume 21, Issue 20, p. 2259-2262.

[3] Pagano, P., De Moortel, I., (2017), Contribution of mode-coupling and phase-mixing of Alfvén waves to coronal heating, Astronomy & Astrophysics, Volume 601, id.A107, 13 pp.

[4] Pagano, P., Pascoe, D. J., De Moortel, I., (2018), Contribution of phase-mixing of Alfvén waves to coronal heating in multi-harmonic loop oscillations, Astronomy & Astrophysics, Volume 616, id.A125, 12 pp.

[5] Cargill, Peter J., Klimchuk, James A., (2004), Nanoflare Heating of the Corona Revisited, The Astrophysical Journal, Volume 605, Issue 2, pp. 911-920.

[6] Klimchuk, J. A., (2006), On Solving the Coronal Heating Problem, Solar Physics, Volume 234, Issue 1, pp.41-77.

[7] Chitta, L. P., Peter, H., Solanki, S. K., (2018), Nature of the energy source powering solar coronal loops driven by nanoflares, Astronomy & Astrophysics, Volume 615, id.L9, 6 pp.

[8] Cranmer, S. R., Winebarger, A. R., (2019), The Properties of the Solar Corona and Its Connection to the Solar Wind, Annual Review of Astronomy and Astrophysics, vol. 57, p.157-187.

[9] Viall, N. M., De Moortel, I.,Downs, C., Klimchuk, J. A., Parenti, S., Reale, F., (2021), The Heating of the Solar Corona, Space Physics and Aeronomy, Volume 1, Solar Physics and Solar Wind, Geophysical Monograph Series, Vol. 258. ISBN: 978-1-119-50753-6, 320 pp. American Geophysical Union, Wiley, 2021, p.35.

[10] Tomczyk, S., McIntosh, S. W., Keil, S. L., Judge, P. G., Schad, T., Seeley, D. H., Edmondson, J., (2007), Alfvén Waves in the Solar Corona, Science, Volume 317, Issue 5842, pp. 1192.

[11] Landi, E., Cranmer, S. R., (2009), Ion Temperatures in the Low Solar Corona: Polar Coronal Holes at Solar Minimum, The Astrophysical Journal, Volume 691, Issue 1, pp. 794-805.

[12] Gupta, G. R., Banerjee, D., Teriaca, L., Imada, S., Solanki, S, (2010), Accelerating Waves in Polar Coronal Holes as Seen by EIS and SUMER, The Astrophysical Journal, Volume 718, Issue 1, pp. 11-22.

[13] Bemporad, A., Abbo, L., (2012), Spectroscopic Signature of Alfvén Waves Damping in a Polar Coronal Hole up to 0.4 Solar Radii, The Astrophysical Journal, Volume 751, Issue 2, 110, 13 pp.

[14] Cranmer, S. R., Gibson, S. E., Riley, P., (2017), Origins of the Ambient Solar Wind: Implications for Space Weather, Space Science Reviews, Volume 212, Issue 3-4, pp. 1345-1384.

[15] Doyle J., Teriaca L., Banerjee D., (1999), Coronal hole diagnostics out to 8 R. Astronomy and Astrophysics, 349, 956.

[16] Hassler D. M., Rottman G. J., Shoub E. C., Holzer T. E., (1990), Line broadening of MG X 609 and 625 A coronal emission lines observed above the solar limb. The Astrophysical Journal, 348, L77-80.

[17] Saba J. L., Strong K. T., 1991. Coronal dynamics of a quiescent active region. The Astrophysical Journal, 375, 789-799.

[18] Patsourakos, S., Klimchuk, J. A., (2006), Nonthermal Spectral Line Broadening and the Nanoflare Model, The Astrophysical Journal, Volume 647, Issue 2, pp. 1452-1465.

[19] van Ballegooijen, A. A., Asgari-Targhi, M., Voss, A., (2017), The Heating of Solar Coronal Loops by Alfvén Wave Turbulence, The Astrophysical Journal, Volume 849, Issue 1, article id. 46, 23 pp.

[20] Brooks, David H., Warren, Harry P., (2016), Measurements of Non-thermal Line Widths in Solar Active Regions, The Astrophysical Journal, Volume 820, Issue 1, article id. 63, 14 pp.

[21] Ofman L., Nakariakov V., Sehgal N., (2000) Dissipation of slow magnetosonic waves in coronal plumes. The Astrophysical Journal, 533, 1071.

[22] Nakariakov V. M., Ofman L., Arber T. D., (2000), Nonlinear dissipative spherical Alfvén waves in solar coronal holes. The Astronomy and Astrophysics, 353, 741-748.

[23] Banerjee D., Gupta G. R., Teriaca L., (2011) Propagating MHD Waves in Coronal Holes. Space Science Reviews, 158, 267-288.

[24] Wilhelm K., Marsch E., Dwivedi B. N., Hassler D. M., Lemaire P., Gabriel A. H., Huber M. C., (1998), The solar corona above polar coronal holes as seen by SUMER on SOHO. The Astrophysical Journal, 500, 1023.

[25] Ruderman, M. S., Oliver, R., Erdélyi, R., Ballester, J. L., Goossens, M., (2000), Slow surface wave damping in plasmas with anisotropic viscosity and thermal conductivity, Astronomy and Astrophysics, v.354, p.261-276.

[26] Banerjee, D., Pérez-Suárez, D., Doyle, J. G., (2009), Signatures of Alfvén waves in the polar coronal holes as seen by EIS/Hinode, Astronomy and Astrophysics, Volume 501, Issue 3, 2009, pp.L15-L18.

[27] Morton R., Tomczyk S., Pinto R., 2015. Investigating Alfvénic wave propagation in coronal open-field regions. Nature Communications, 6, 1-12.

[28] Pekünlü E. R., Bozkurt Z., Afsar M., Soydugan E., Soydugan F., (2002), Alfvén waves in the inner polar coronal hole. Monthly Notices of the Royal Astronomical Society, 336, 1195-1200.

[29] Fisher R., Guhathakurta M., (1995), Physical properties of polar coronal rays and holes as observed with the Spartan 201-01 coronagraph. The Astrophysical Journal Letters, 447, L139.

[30] Guhathakurta M., Fisher R., (1998), Solar Wind Consequences of a Coronal Hole Density Profile: Spartan 201-03 Coronagraph and Ulysses Observations from 1.15 R to 4 AU. The Astrophysical Journal Letters, 499, L215.

[31] Banerjee D., Teriaca L., Doyle J., Wilhelm K., (1998), Broadening of SI VIII lines observed in the solar polar coronal holes. Astronomy and Astrophysics, 339, 208-214.

[32] Doschek G., Warren H., Laming J., Mariska J., Wilhelm K., Lemaire P., Schühle U., Moran T., (1997), Electron densities in the solar polar coronal holes from density-sensitive line ratios of Si VIII and Sx. The Astrophysical Journal Letters, 482, L109.

[33] Wilhelm K., Abbo, L., Aucre, F., and et al., (2011), Morphology, dynamics and plasma parameters of plumes and inter-plume regions in solar coronal holes. The Astronomy and Astrophysics Review, 19, 35.

[34] Priest E., Kirk J., Melrose D., (1994), Plasma astrophysics. Berlin: Springer-Verlag.

[35] Marsch E., (1999), Solar wind models from the Sun to 1 AU: Constraints by in situ and remote sensing measurements. Coronal holes and solar wind acceleration, 1–24.

[36] Endeve E., Leer E., (2001), Coronal heating and solar wind acceleration; gyrotropic electron-proton solar wind. Solar Physics, 200, 235-250.

[37] Voitenko Y., Goossens M., (2002), Excitation of high-frequency Alfvén waves by plasma outflows from coronal reconnection events. Solar Physics, 206, 285-313.

[38] Cranmer S. R., Kohl, J.L. and Noci, G. And et al., (1999), An empirical model of a polar coronal hole at solar minimum. The Astrophysical Journal, 511, 481.

[39] Devlen E., Pekünlü E. R., (2010), MHD waves in the solar north polar coronal hole. Astronomische Nachrichten, 331, 716-724.

[40] Raymond, J. C., Kohl, J. L., Noci, G., et al., (1997), Composition of Coronal Streamers from the SOHO Ultraviolet Coronagraph Spectrometer, Solar Physics, Volume 175, Issue 2, pp 645–665.

[41] Cranmer S. R., Panasyuk A. V., Kohl J. L., (2008), The Astrophysical Journal, 678, 1480.

[42] Wilhelm K., Marsch E., Dwivedi B. N., Hassler D. M., Lemaire P., Gabriel A. H., Huber M. C., (1998) The solar corona above polar coronal holes as seen by SUMER on SOHO. The Astrophysical Journal, 500, 1023.

[43] Kohl J., Noci, G. and Antonucci, E., et al., (1997), The First Results from SOHO. Springer, pp 613–644.

[44] Cranmer S. R., Panasyuk A. V., Kohl J. L., (2008), The Astrophysical Journal, 678, 1480.

[45] Esser R., Fineschi S., Dobrzycka D., Habbal S. R., Edgar R. J., Raymond J. C., Kohl J. L., Guhathakurta M., 1998. Plasma properties in coronal holes derived from measurements of minor ion spectral lines and polarized white light intensity. The Astrophysical Journal Letters, 510, L63.

[46] Devlen E., Zengin Çamurdan D., Yardımcı M., Pekünlü E. R., (2017), A new model for heating of the Solar North Polar Coronal Hole. Monthly Notices of the Royal Astronomical Society, 467, 133-144.

[47] Hollweg J. V., 1999. Kinetic Alfvén wave revisited. Journal of Geophysical Research: Space Physics, 104, 14811-14819.

[48] Priest E. R., 1987. Solar magneto-hydrodynamics. D. Reidel Pub. Co.

[49] Spitzer Jr L., 1962. Physics of Fully Ionized Gases 2nd edition Interscience. New York.

[50] Doğan, S., Pekünlü, E. R., (2012), Ion-cyclotron waves in solar coronal hole, New Astronomy, Volume 17, Issue 3, p. 316-324.

[51] Hollweg, J. V., (1986), Transition region, corona, and solar wind in coronal holes, Journal of Geophysical Research, Volume 91, Issue A4, p. 4111-4125.

[52] Hollweg J. V., Johnson W., 1988. Transition region, corona, and solar wind in coronal holes: Some two-fluid models. Journal of Geophysical Research: Space Physics, 93, 9547-9554.

[53] Withbroe G. L., Noyes R. W., 1977. Mass and energy flow in the solar chromosphere and corona. Annual review of astronomy and astrophysics, 15, 363-387.

[54] McIntosh, S. W., de Pontieu, B., Carlsson, M., Hansteen, V., Boerner, P., Goossens, M., (2011), Alfvénic waves with sufficient energy to power the quiet solar corona and fast solar wind, Nature, Volume 475, Issue 7357, pp. 477-480.

[55] Cranmer, S. R., Matthaeus, W. H., Breech, B. A., Kasper, J. C., (2009), Empirical Constraints on Proton and Electron Heating in the Fast Solar Wind, The Astrophysical Journal, Volume 702, Issue 2, pp. 1604-1614.

[56] Hahn, M., Landi, E., Savin, D. W., (2012), Evidence of Wave Damping at Low Heights in a Polar Coronal Hole, The Astrophysical Journal, Volume 753, Issue 1, article id. 36, 9 pp.

[57] Hahn, M., Savin, D. W., (2013), Observational Quantification of the Energy Dissipated by Alfvén Waves in a Polar Coronal Hole: Evidence that Waves Drive the Fast Solar Wind, The Astrophysical Journal, Volume 776, Issue 2, article id. 78, 10 pp.

[58] Antonucci E., Dodero M. A., Giordano S., 2000. Oxygen temperature anisotropy and solar wind heating above coronal holes out to 5 R. Solar Physics, 197, 115-134.

[59] Telloni D., Antonucci E., Dodero M. A., 2007. Oxygen temperature anisotropy and solar wind heating above coronal holes out to 5 R. The Astronomy and Astrophysics, 476, 1341-1346.

Kütahya Dumlupınar University
Institute of Graduate Studies

Journal of Scientific
Reports-A
E-ISSN: 2687-6167
Number 53, June 2023

RESEARCH ARTICLE

ANALYSIS OF TiFe INTERMETALLIC COMPOUND BY DFT

Emre TAŞ[*,1], İlknur KARS DURUKAN[2], Yasemin ÖZTEKİN ÇİFTCİ[3]

[1] Gazi University, Faculty of Sciences, Department of Physics, 06500, Ankara, emre.tas@gazi.edu.tr,
ORCID: 0000-0003-2527-9434
[2] Gazi University, Faculty of Sciences, Department of Physics, 06500, Ankara, ilknurdurukan@gazi.edu.tr,
ORCID: 0000-0001-5697-0530
[3] Gazi University, Faculty of Sciences, Department of Physics, 06500, Ankara, yasemin@gazi.edu.tr,
ORCID: 0000-0003-1796-0270

Receive Date:04.12.2022 *Accepted Date: 27.03.2023*

ABSTRACT

The structural, mechanical, anisotropy, and optical properties of the TiFe compound, which is the effective hydrogen storage material, were analyzed using the DFT method with the CASTEP program. The elastic constants of the cubic system, which have been determined by the stress-strain method, are stable according to the Born stability criteria. According to the mechanical properties, the compound was brittle and hard. Anisotropy properties were examined in 2D and 3D with the EIAM code. Finally, the optical properties using the complex dielectric function based on the electronic structure of TiFe; parameters such as dielectric constants, reflectivity, extinction coefficient, refractive index, and loss function were examined in the range of 0-50 eV. Generally, our obtained results are comparable with literature values.

Keywords: *Anisotropy, Hard Material, Brittle, Optic Properties.*

1. INTRODUCTION

Today, the rapid development of technology, in parallel with the increasing population, has brought the need for energy and fuel [1]. Over the years, this energy need has turned from solid-source coal to liquid-source oil and natural gas. All these fossil fuels pollute the air by releasing CO, CO2, NOx, and SOx. While air pollution threatens all life, oil spills also threaten aquatic life. In addition to all these negativities, it is necessary to meet the increasing energy and fuel needs. Unfortunately, the oil will not meet the world's energy needs in the coming years.

Hydrogen is an environmentally friendly fuel with a high potential to meet the world's energy needs [2,3]. However, hydrogen is an energy carrier, not an energy source like oil; not available directly [4,5]. Although it can be produced using other sources, it must be transported and stored after being built. Today, hydrogen storage materials have become attractive to many researchers due to their

JSR A
Journal of Scientific Reports

applications in the energy field. Hydrogen storage materials are material classes whose primary material is metal [6,7].

Generally, B2-type intermetallic compounds can be used for technological applications such as energy and optoelectronics due to having a high melting point and ordering energy and showing high strength, good corrosion resistance, and high phase stability [8]. Ti compounds with a B2 structure are the most widely used hydrogen storage material [9]. In addition, the partially filled d states of Ti-based compounds add extraordinary properties to the compounds formed. Titanium is particularly interested in the aerospace industry and high-friction materials [10]. In particular, TiFe is one of the most attractive materials due to its abundant and low-cost raw material, high strength, and mild hydrogenation conditions [11]. For this reason, we have attempted to review many theoretical and experimental studies on TiFe intermetallic compounds in the literature. Pawar et al. investigated the structural, electronic, phonon, and superconductivity properties of TiFe compounds using the QUANTUM ESPRESSO code based on the DFT method. They found that the compound is metallic and thermodynamically stable, and the transition temperature to superconductivity is 1.15 K [10]. Ko et al. calculated the role of ternary alloying elements in TiFe-based hydrogen storage alloys with the DFT-based VASP code. This study analyzed the effect of ternary elements on hydrogen storage with pressure composition and temperature curves [12]. Ciric et al. synthesized $TiFe_{1-x}$ Ni_x (X:0.2-0.6) by melt spinning. They analyzed the crystal structure, bond structure, and hybridization properties by varying the Fe and Ni concentration ratios. In this study, they determined that the increase in Ni concentration leads to a shift in hydrogen desorption temperatures to higher values and a decrease in the maximum amount of hydrogen absorbed under the same conditions [13]. Fodorougbo et al. analyzed the hydrogen production properties of $TiFe_{1-x}M_x$ (M=Al, Be, Co, Cr, Cu, Mn, and Ni) compounds in the light of activation, kinetic and thermodynamic properties by DFT [14]. Sujan et al. evaluated the fabrication process of TiFe intermetallic compounds from fabrication to hydrogen storage in detail.[15] Kong et al. calculated the electronic and thermodynamic properties of TiM (M: Fe, Ru, and Os) compounds using the CASTEP code based on the DFT method. They determined the sensitivity of the thermal expansion coefficient at high temperature-high pressure, where the compounds are thermodynamically stable, and that this coefficient decreases with increasing pressure.[16] Bakulin et al. investigated the effect of impurities on the diffusivity of TiFe compounds by DFT. They found that impurities change the hydrogen absorption energy at the nearest positions and neighborhoods [17]. Eladati et al. studied the effect of plastic deformation on hydrogen storage and microstructure of $TiFe_{1-x}$ Mn_x(x: 0, 0.15, and 0.3) compounds. Since the hydrogen storage performance is due to lattice defects and amorphous regions, it was determined that adding Mn expands the lattice and reduces the hydride formation energy, thereby lowering the hydrogenation/activation pressure [18]. Oliveira et al. experimentally determined hydrogen desorption kinetics at room temperature and hydrogen absorption kinetics for a cold-rolled TiFe IMC alloy processed under an inert atmosphere.[19] Dematteis et al. experimentally prepared TiFe-based alloys and provided information on the kinetics of adding Mn and copper in hydrogen storage. They also emphasized that the prepared samples have fast kinetics and high hydrogen storage properties [20]. Du et al. experimentally and theoretically analyzed the thermophysical properties of TiFe alloys [21]. In another experimental study, Yang et al. determined the microstructure and hydrogen storage properties of chromium, manganese, and irium elements in TiFe-based alloys [22].

JSR A
Journal of Scientific Reports

Conventional experimental methods allow us to grasp and evaluate general changes caused by element substitution. Still, changes at a much more fundamental level are beyond the reach of standard experimental tools. In this sense, computational approaches, such as first-principle density functional theory (DFT) calculations, are of great interest as they allow better evaluation and monitoring of even small changes in good physical properties. Due to its widespread use in technology, the TiFe compound has attracted the attention of many experimental and theoretical working groups. Many studies have continued in this direction, especially after the use of TiFe intermetallic compound in hydrogen energy became known. Hydrogen-storing compounds with a B2-type structure utilizes the interatomic hydrogen storage mechanism. When hydrogen atoms are inserted into compounds, the lattice structure of the compound is disrupted by high temperature and pressure. Due to these changes during the hydrogen absorption and desorption, the material can be affected by elastic and plastic deformation. In the cycling process of hydrogen storage for the materials, poor plasticity can cause residual stress accumulates and defects which affect hydrogen storage performance. So mechanical properties of hydrogen storage material significantly affect the hydrogen storage performance. Selecting suitable materials to meet renewable energy needs is science's center. To expand this problem in a certain way, obtaining and optimizing the available materials is necessary. Optical properties need to be discussed because these properties are helpful to understand better the fundamental properties such as crystal vibrations, excitons, impurity levels, localized defects, and band structure to understand optical switching and optoelectronics applications. The optical properties of the material are attributed to electronic properties. Besides all these known facts, some physical properties of TiFe intermetallic compounds have not been observed. To contribute to the literature, TiFe compound was examined theoretically. Structural, Elastic, anisotropic and optical properties were analyzed in detail with the CASTEP program using the DFT based on the first-principles method. Before the synthesis procedure, utilizing such calculations, a very time-consuming effort, is very important.

2. MATERIAL METHOD

The structural, elastic, anisotropy, and optical properties of TiFe compound have been calculated using the Ab initio method. Ab-initio is essential in determining many macroscopic properties important in technology based on fundamental quantum mechanical theory. The main advantage of ab-initio approaches is their independence from experimental data. When appropriate algorithms and software using ab-initio calculation methods are used, results close to experimental values can be obtained. The CASTEP package program used density functional theory (DFT) [23,24] to perform all calculations. Plane-wave basis sets with 300 eV energy cutoff and 10x10x10 Monkhorst and Pack [25] k-points in the Brillouin region are used for the TiFe compound. Interactions between ions and electrons were captured using Ultrasoft Vanderbilt pseudopotential [26,27]. The electronic valence configurations for each atomic species were chosen as Ti: $3d^2\ 4s^2$, Fe: $3d^6\ 4s^2$. The parameters we used in our calculations were obtained by optimizing the TiFe compound. The stress-strain method is used to estimate the elastic properties [28]. Three-dimensional representation of anisotropy properties, EIAM code [29]. Finally, optical parameters were evaluated in the 0-50 eV range.

JSR A
Journal of Scientific Reports

3. RESULTS and DISCUSSION

3.1. Structural and Elastic Properties

TiFe is found in 221 space groups in the CsCl structure. The representation of the atoms in the compound in the unit cell is as Fe atom in the center and Ti atom at the corners. It is presented in Fig. 1a. The Bulk modulus and first derivative were calculated by fitting the Murnaghan equation of the graph given in Figure 1b. Structural parameters are listed in Table 1 and compared with the literature. The calculated values are comparable with previous studies [16,31-33]. It is possible to determine the material's structural stability by the formation's enthalpy.

$$\Delta H^{\mathrm{TiFe}} = E_{tot}^{\mathrm{TiFe}} - E_t^{\mathrm{Ti}} - E_t^{\mathrm{Fe}} \quad (1)$$

Here, E_{tot}^{TiFe} is the total energy of TiFe per unit cell, and E_t^{Ti}, E_t^{Fe} shows the computed energies per unit cell at 0K and 0GPa. The negative ΔH is indicative of its stability and experimental feasibility. The computed formation enthalpy value of TiFe is -1.495 eV/f.u. The negative value of ΔH^{TiFe} shows the stability of TiFe thermodynamically.

Table 1. The structural parameters of TiFe.

	Lattice constant (Å)	**B(GPa)**	**B'**
TiFe	2.960	182.34	3.90
Ref.	2.961[16] 2.978[1] 2.969[2] 2.965[3]	174.64[16]	2.135[16]

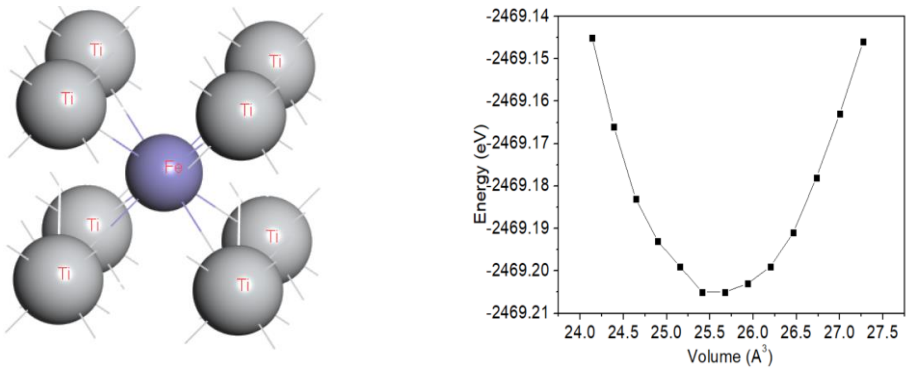

a) **b)**

Figure 1. a) The unitcell of TiFe, **b)** Total energy - volume curve.

JSR A
Journal of Scientific Reports

Elastic properties, determining the physical response of the material, are fundamental in understanding its effectiveness in device applications. In addition, the thermodynamic behavior of the material can be learned by knowing the elastic properties. Three elastic constants are required for the cubic system, while the elastic properties determine the material's response to stress. C_{11} determines the presence of rigidity of the material, while C_{12} determines the transverse expansion. C_{44} is related to shear deformation. These three elastic constants are essential in determining the stability of the material. The stability conditions of the cubic system, known as the Born-Huang criteria [34], are related to fulfilling the four criteria listed below.

C_{11}-$C_{12} > 0$ (2)

$C_{11} > 0$ (3)

$C_{44} > 0$ (4)

$C_{11}+2C_{12} > 0$ (5)

The mechanical properties can be calculated by the equations presented below by determining the elastic constants [35].

$$B = \frac{1}{3}(C_{11} + 2C_{12}) \quad (6)$$

$$G = \frac{1}{5}(C_{11} - C_{12} + 3C_{44}) \quad (7)$$

$$E = \frac{9BG}{3B+G} \quad (8)$$

$$H_v = 2\left(\left(\frac{G}{B}\right)^2 G\right)^{0.585} - 3 \quad (9)$$

C''= C_{12}-C_{44}

$$\upsilon = \frac{3B-2G}{2(3B+G)} \quad (10)$$

$$A = \frac{2C_{44}}{C_{11}-C_{12}} \quad (11)$$

Elastic constants and mechanical properties are calculated and presented in Table 2. C_{11}, C_{12}, and C_{44}, satisfied the stability state. XTi(X=Fe, Co, Ni, Ru) compounds in the B2 structure presented in Table 2 also have stable structures [36,37]. The Bulk modulus (B, GPa) indicates the material's compressibility and ability to resist fracture. The larger this value, the more difficult it is to compress the material. The Shear module (G, GPa) defines the resistance to plastic deformation. Young's modulus (E, GPa) is the stress per unit strain mainly related to the chemical bond of the atoms in the materials. E also gives information about the hardness of the material. Because of E value, TiFe compound is hard. When compared with the XTi(X=Fe, Co, Ni, Ru) compounds in the literature, it

JSR A
Journal of Scientific Reports

was determined by our calculations that the hardest compound was TiFe [36,37], indicating the stronger chemical bond. The ductile or brittle behavior is determined from the B/G ratio, the Paugh ratio, and C'' Cauchy pressure. If this ratio is greater than 1.75, it is ductile. Otherwise, it is brittle. It is ductile if positive for Cauchy pressure and brittle if negative. TiFe is brittle according to Cauchy pressure and Paugh ratio. However, XTi (X=Fe, Co, Ni, Ru) compounds show ductile properties in Table 2 [36,37]. The Poisson ratio (v) describes the bonding forces in solids and is the center of interatomic force in a material if v ranges from 0.25 to 0.50. When the v is 0.5, the material is nearly incompressible. The forces of the TiFe and XTi(X=Fe, Co, Ni, Ru) compounds are central [36,37]. Hv is a parameter that defines the stiffness against deformation. For the B2 structure the hardness increase with constant elastic C_{44}[34]. If the value of this parameter is above 10, it is hard; if it is above 40, it is super-hard. TiFe compound has a hard structure with a value of 13.00. Higher values of the bulk modulus, shear modulus, B/G ratio, and Poisson's ratio indicate that the hydrogen enhances the ability of TiFe to resist fracture and plastic deformation and improve ductility and cycle performance. Zener anisotropy A is calculated from elastic constants. It is isotropic when this value equals 1, and anisotropic when it is small or large. TiFe and XTi(X=Fe, Co, Ni, Ru) compounds have an anisotropic nature [36,37].

Table 2. Elastic constants (C_{11}, C_{12}, C_{44}), Bulk modulus (B, GPa), Shear modulus (G, GPa), Young modulus (E, GPa), Paugh ratio (B/G), Cauchy pressure (C''= C_{12}-C_{44}), Poisson ratio (v), Hardness (Hv),. Anizotropy(A) of TiFe and other compounds.

	C_{11}	C_{12}	C_{44}	B	G	E	B/G	C''	v	Hv	A
TiFe	369.742	72.059	82.038	171.287	99.989	251.106	1.713	-9.979	0.267	13	0.438
FeTi(2)	372.95	87.1	68.63	182.38	92.49	237.36	1.97	18.47	0.28		0.48
CoTi(2)	286.51	113.79	74.66	173.56	79.13	205.74	2.16	39.13	0.29		0.86
NiTi(2)	195.93	157.59	62.9	160.03	39.14	109.09	4.35	94.68	0.39		3.28
RuTi(3)	386.97	135.37	109.27	220.97	133.69	138.32	1.81	10.04	0.26		0.58

The mechanical parameters, Young's modulus (E_{min} and E_{max}, GPa), Shear modulus (G_{min} and G_{max}, GPa), and Poisson's ratio (v_{min}, v_{max}), are presented in Table 3. The minimum and maximum values of mechanical parameters are given in Table 3; all parameters are anisotropic. Mechanical parameters were plotted using the ELATE code. The mechanical parameters Young's modulus, shear modulus, and Poisson's ratio depending on the two-three-dimensional orientation, are presented in Figure 2. Deviation from sphericity in the figures indicates anisotropy; it is anisotropic like other intermetallic compounds [36,37]. Minimum values are shown in green, while maximum values are shown in blue.

Table 3. Variation of mechanical parameters.

	E_{min} (GPa)	E_{max} (GPa)	G_{min}(GPa)	G_{max}(GPa)	v_{min}	v_{max}
TiFe	212.23	346.24	82.038	148.84	0.110	0.432
Anisotropy	1.631		1.814		3.903	

JSR A
Journal of Scientific Reports

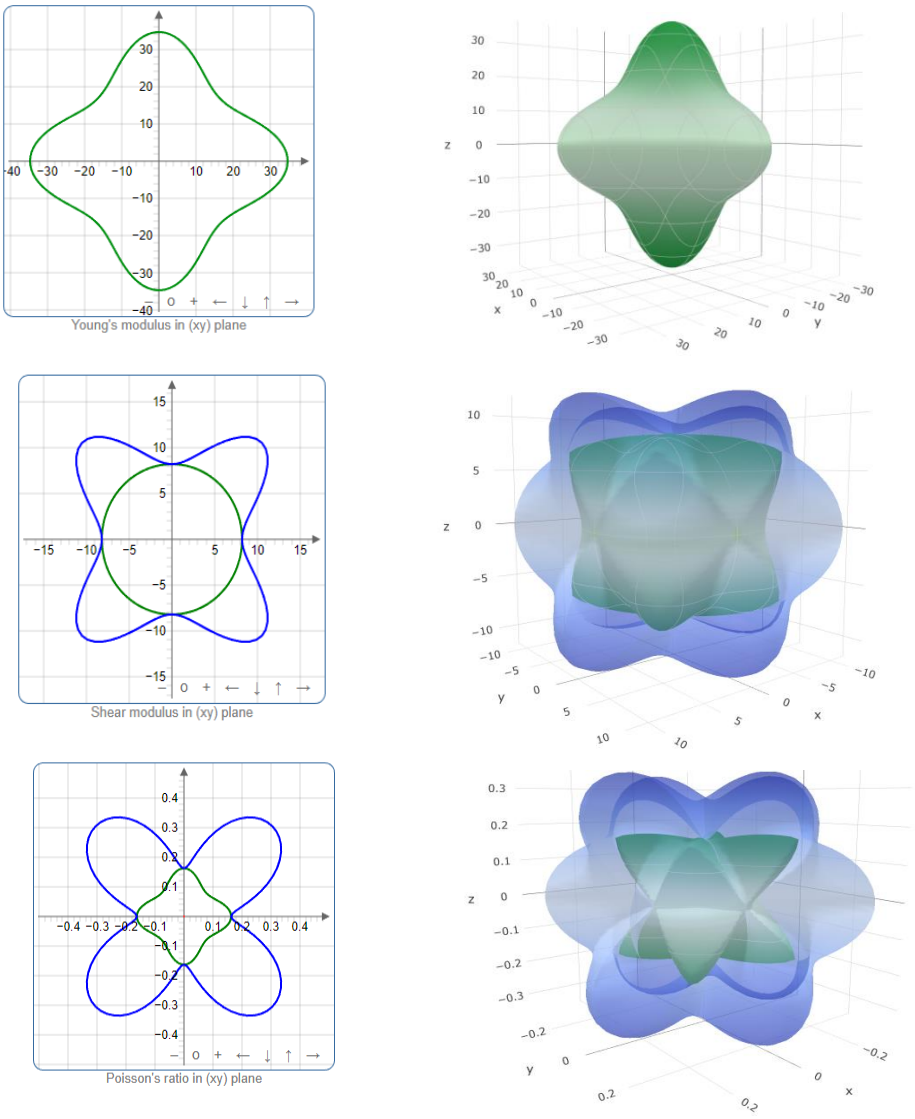

Figure 2. The Calculated two- and three-dimensional elastic anisotropy parameters of TiFe.

3.2 Optic Properties

Optical properties are the compound's response to electromagnetic waves. Optical constants are obtained using the complex dielectric function.

$$\varepsilon(E) = \varepsilon_1(E) + i\,\varepsilon_2(E) \tag{12}$$

JSR A
Journal of Scientific Reports

It is the wave vector's polarization response to the external electromagnetic field in a given system. The photon's electric field allows transitions between the occupied and unoccupied wave vector states. $\varepsilon_1(\omega)$ shows the dispersion of incoming photons by the materials, while ε_2 (ω) is related to the energy absorbed by the material [38]. In Fig. 3a, the variation of the real part $\varepsilon_1(\omega)$ and the real part $\varepsilon_2(\omega)$ of the dielectric function in the energy range from 0 to 50 eV is given. The limit value $\varepsilon_1(0)$ = 45.73, corresponding to the near-zero radiation frequency, is called the static dielectric constant. $\varepsilon_1(\omega)$ shows that the zero crossing of the spectrum means no scattering. Between [2.86–16.71eV] and [35.86–35.35 eV], $\varepsilon_1(\omega)$ exhibits negative values, in which case the compound shows metallic character [39]. The fluctuations in the dielectric function's real part indicate localized absorption and reflection maxima. The dielectric function's imaginary part $\varepsilon_2(\omega)$, indicating the electronic excitations between 0 and 50 eV, was also examined. It was determined that it peaked in the visible region and took the maximum value. Values indicate optical absorption when the dielectric function is greater than zero. Absorption and reflection decrease toward zero in the UV region.

The graph of the refractive index n(ω) and the extinction coefficient k(ω) according to the energy change is given in Fig 3b. When a light beam changes medium, it changes direction, and refraction occurs due to the change in propagation speed. The behavior of the n(ω) against energy is similar to the real part of the dielectric constant. The square of the n(ω) at zero frequency equals the $\varepsilon 1(\omega)$. While the points where the refractive index is maximum are in the IR region, it decreases in the Visible region and fluctuates in the UV region. The extinction coefficient peaks k(ω), which indicates the transition between bands in the range of 0-10 eV, then after 10 eV, fluctuations occur in the UV region.

In Figure 3c, the variation of the absorption of the material against the energy values indicating the portion of energy lost by the wave when passed through the material is given. The region with the highest absorption is the UV region with fluctuations in this region. The maximum absorption is 5.68 105 cm-1, corresponding to an energy value of 36.18 eV. These results show TiFe as a prospective material for optoelectronics in the ultraviolet region mainly due to its extremely sharp cut-off response, particularly in this region.

The reflectivity of the material, expressed as a percentage, is given in Fig 3d. R(w) can be defined as the ratio between reflected and incident luminous flux. Different peaks are indicative of the reflection of photons from the material surface. R (0) is high at zero energy, and its value is 54%. At low energies, R(w) fluctuates and reaches a maximum of 70% in the UV range, with a maximum value of around 60% in the visible range (1.73–3.4 eV). The highest reflective region of TiFe is UV, with a reflectance value of 70 percent.

The energy loss function L(ω) is the energy loss of an electron moving through a material, indicating the energy lost by the high-speed electron, and is presented in Figure 3e. The energy loss function L(ω) has no significant peak in the visible and near-infrared regions. This situation can be interpreted as $\varepsilon_2(\omega)$ showing large values in these ranges. The prominent peak in the figure is called the plasma frequency, which indicates the combined performance of the loosely bounded electrons in the valence and conduction bands. Its value is about 4.48.

JSR A
Journal of Scientific Reports

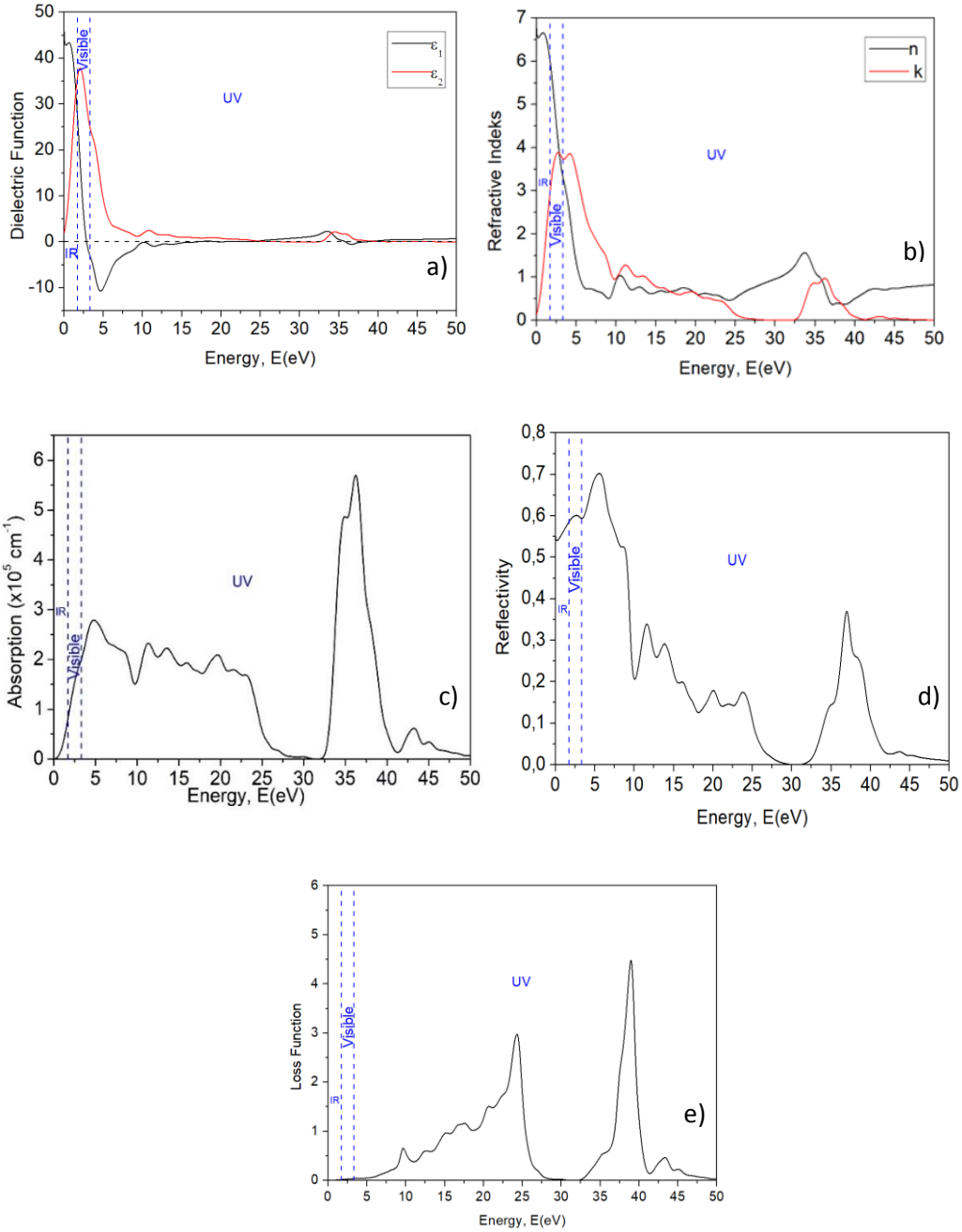

Figure 3. Optical properties of TiFe.

JSR A
Journal of Scientific Reports

4. CONCLUSION

Structural, Elastic, anisotropic, and optical properties of TiFe were analyzed by the first-principles method using DFT. The CASTEP program was used in our calculations as a purely theoretical study. The structural and mechanical properties for TiFe were compared with experimental and theoretical results available in the literature. The results were found to be generally in agreement with the literature data. Second-order elastic constants and mechanical parameters of the TiFe compound at zero pressure were calculated. TiFe compound shows a hard and brittle structure. The mechanical parameters of the TiFe compound calculated with the 2D and 3D ELATE program also show anisotropy (A) properties. Optical properties were examined in the range of 0-50 eV to understand the improved application status of TiFe compound. It has a refractive index of 6.76 and a reflectivity of 70 percent in the UV region. Obtained results in this study could help improve the hydrogen storage performance of TiFe as a promising candidate for optoelectronic devices.

ACKNOWLEDGEMENT

The authors declare that they have no conflict of interest.

REFERENCES

[1] Niaz, S., Manzoor, T., Pandith, A.H. (2015). Hydrogen storage: Materials, methods and perspectives. Renewable and Sustainable Energy Reviews, 50, 457-469.

[2] Nazir, G., Tariq, S., Mahmood, Q., Saad, S., Mahmood, A., Tariq, S. (2018). Under Pressure DFT Investigations on Optical and Electronic Properties of Under Pressure DFT Investigations on Optical and Electronic Properties of PbZrO 3. Acta Physica Polonica A, 133, 105-113.

[3] Vezirolu, T.N., Barbir, F. (1992). Hydrogen: the wonder fuel. International Journal of Hydrogen Energy, 17(6), 391-404.

[4] Andreas, Z. (2004). Hydrogen storage methods. Published online, 91, 157-172.

[5] Graetz, J. (2009). New approaches to hydrogen storage. Chemical Society Reviews, 38(1), 73-82.

[6] Collins, D.J., Zhou, H.C. (2007). Hydrogen storage in metal – organic frameworks. Journal of Materials Chemistry, 17(30), 3154-3160.

[7] Long, J.R., Murray, L.J., Dinca, M. (2009). Hydrogen storage in metal – organic frameworks. Chemical Society Reviews, 38(5), 1294-1314.

[8] Kaneno, Y., Takasugi, T. (2003). Effects of microstructure and environment on room-temperature tensile properties of B2-type polycrystalline CoTi intermetallic compound. Journal of materials science, 38, 869-876.

[9] Guo, Q., Kleppa, O.J. (1998). Standard enthalpies of formation of some alloys formed between group IV elements and group VIII elements, determined by high-temperature direct synthesis calorimetry II. Alloys of (Ti, Zr, Hf) with (Co, Ni). Journal of Alloys and Compounds, 269, 181-186.

[10] Pawar, H., Shugani, M., Aynyas, M., Sanyal, S.P. (2019). Electronic structural, lattice dynamics and superconducting properties of tife intermetallic compound: A first-principles study. AIP Conference Proceedings, 2115, 030336.

[11] Edalati, K., Matsuda, J., Arita, M., Daio, T., Akiba, E., Horita, Z. (2013). Mechanism of activation of TiFe intermetallics for hydrogen storage by severe plastic deformation using high-pressure torsion. Applied Physics Letters, 103, 143902.

[12] Ko, W.S., Park, K.B., Park, H.K. (2021). Density functional theory study on the role of ternary alloying elements in TiFe-based hydrogen storage alloys. Journal of Materials Science & Technology, 92, 148-158.

[13] Ćirić, K.D., Kocjan, A., Gradišek, A., Koteski, V.J., Kalijadis, A.M., Ivanovski, V.N., Laušević, Z.V., Stojić, D.L. (2012). A study on crystal structure, bonding and hydriding properties of Ti–Fe–Ni intermetallics – Behind substitution of iron by nickel. İnternational journal of hydrogen energy, 37, 8408-8417.

[14] Fadonougbo, J.O., Park, K.B., Na, T.W., Park, C.S., Park, H.K., Ko, W.S. (2022). An integrated computational and experimental method for predicting hydrogen plateau pressures of TiFe1-xMx-based room temperature hydrides. İnternational journal of hydrogen energy, 47, 17673-17682.

[15] Sujan, G.K., Pan, Z., Li, H., Liang, D., Alam, N. (2019). An overview on TiFe intermetallic for solid-state hydrogen storage: microstructure, hydrogenation and fabrication processes. Critical Reviews in Solid State and Materials Sciences, 45(5), 410-427.

[16] Kong, Z., Duan, Y., Peng, M., Qu, D., Bao, L. (2019). Theoretical predictions of thermodynamic and electronic properties of TiM (M= Fe, Ru and Os). Physica B: Condensed Matter, 573, 13-21.

[17] Bakulin, A.V., Kulkov, A.S., Kulkova, S.E. (2023). Impurity influence on the hydrogen diffusivity in B2-TiFe. İnternational journal of hydrogen energy, 48, 232-242.

[18] Edalati, K., Matsuo, M., Emami, H., Itano, S., Alhamidi, A., Staykov, A., Smith, D.J., Orimo, S-i., Akiba, E., Horita, Z. (2016). Impact of severe plastic deformation on microstructure and hydrogen storage of titanium-iron-manganese intermetallics. Scripta Materialia, 124, 108-111.

[19] Oliveira, V.B., Beatrice, C.A.G., Leal Neto, R.M., Silva, W.B., Pessan, L.A., Botta, W.J., Leiva, D.R. (2021). Hydrogen absorption/desorption behavior of a cold-rolled tife intermetallic compound. Materials Research, 24(6), 2021-0204.

[20] Dematteis, E.M., Cuevas, F., Latroche, M. (2020). Hydrogen storage properties of Mn and Cu for Fe substitution in TiFe0. 9 intermetallic compound. Journal of Alloys and Compounds, 851, 156075.

[21] Du, L.Y., Wang, L., Zhai W., Hu, L., Liu, J.M., Wei, B. (2018). Liquid state property, structural evolution and mechanical behavior of TiFe alloy solidified under electrostatic levitation condition. Materials and Design, 160, 48-57.

[22] Yang, T., Wang, P., Xia, C., Liu, N., Liang, C., Yin, F., Li, Q. (2020). Effect of chromium, manganese and yttrium on microstructure and hydrogen storage properties of TiFe-based alloy. International Journal of Hydrogen Energy, 45, 12071-12081.

[23] Mehmood, N., Ahmad, R., Murtaza, G. (2017). Ab Initio Investigations of Structural, Elastic, Mechanical, Electronic, Magnetic, and Optical Properties of Half-Heusler Compounds RhCrZ (Z = Si, Ge). Journal of Superconductivity and Novel Magnetism, 30(9), 2481-2488.

[24] Kresse, G., Hafner, J. (1993). Ab initio molecular dynamics for liquid metals. Physical Review B, 47(1), 558-561.

[25] Le Page, Y., Saxe, P. (2002). Symmetry-general least-squares extraction of elastic data for strained materials from ab initio calculations of stress. Physical Review B - Condensed Matter and Materials Physics, 65(10), 1-14.

[26] Perdew, J.P., Chevary, J.A., Vosko, S.H., Jackson, K.A., Pederson, M.R., Singh, D.J., Fiolhais, C. (1992). Atoms, molecules, solids, and surfaces: Applications of the generalized gradient approximation for exchange and correlation. Physical review B, 46(11), 6671-6687.

[27] Vanderbilt, D. (1990). Soft self-consistent pseudopotentials in a generalized eigenvalue formalism. Physical review B, 41(11), 7892-7895.

[28] Mehl, M.J., Osburn, J.E., Papaconstantopoulos, D.A., Klein, B.M. (1990). Structural properties of ordered high-melting-temperature intermetallic alloys from first-principles total-energy calculations. Physical Review B, 41(15), 10311-10323.

[29] Marmier, A., Lethbridge, Z.A.D., Walton, R.I., Smith, C.W., Parker, S.C., Evans, K.E. (2010). ElAM : A computer program for the analysis and representation of anisotropic elastic properties. Computer Physics Communications, 181(12), 2102-2115.

[30] Murnaghan, F.D. (1944). The compressibility of media under extreme pressure. Proceedings of the National Academy of Sciences. 30(9), 244-247.

[31] Melnyk, G., Tremel, W. (2003). The titanium–iron–antimony ternary system and the crystal and electronic structure of the interstitial compound Ti5FeSb2. Journal of alloys and compounds, 349(1-2), 164-171.

[32] Duwez, P., Taylor, J. (1950). The structure of intermediate phases in alloys of titanium with iron, cobalt, and nickel. Journal of Metals, 188, 1173-1176.

[33] Fischer, P., Hälg, W., Schlapbach, L., Stucki, F., Andresen, A.F. (1978). Deuterium storage in FeTi. Measurement of desorption isotherms and structural studies by means of neutron diffraction. Materials Research Bulletin, 13(9), 931-946.

[34] Mouhat, F., Coudert, F.X. (2014). Necessary and sufficient elastic stability conditions in various crystal systems. Physical Review B - Condensed Matter and Materials Physics, 90(22), 1-4.

[35] Kars Durukan, I., Oztekin Ciftci, Y. (2020). First-principles calculations of vibrational and optical properties of half-Heusler NaScSi. Indian Journal of Physics, Published online, 95, 2303-2312.

[36] Acharya, N., Fatima, B., Chouhan, S.S., Sanyal, S.P. (2013). First Principles Study on Structural , Electronic , Elastic and Thermal Properties of Equiatomic MTi (M = Fe , Co , Ni). Chemistry and Materials Research, 3, 22-30.

[37] Jain, E., Pagare, G., Chouhan, S.S., Sanyal, S.P. (2014). Electronic structure, phase stability and elastic properties of ruthenium based four intermetallic compounds: Ab-initio study. Intermetallics, 54, 79-85.

[38] Liu, Z.T.Y., Gall, D., Khare, S.V. (2014). Electronic and bonding analysis of hardness in pyrite-type transition-metal pernitrides. Physical review B, 90(13), 134102.

[39] Anissa, B., Radouan, D., Durukan I.K. (2022). Study of structural, electronic, elastic, optical and thermoelectric properties of half‐Heusler compound RbScSn: A TB‐mBJ DFT study. Optical and Quantum Electronics, 54(6), 1-17.

Kütahya Dumlupınar University
Institute of Graduate Studies

Journal of Scientific
Reports-A
E-ISSN: 2687-6167
Number 53, June 2023

RESEARCH ARTICLE

EVALUATION OF GROUND VIBRATION AND AIR BLAST MEASUREMENTS INDUCED BY BLASTING IN A QUARRY MINE

Bahadır ŞENGÜN[1], Yavuz GÜL[2]

[1]Sivas Cumhuriyet University, Engineering Faculty, Civil Engineering, bsengun@cumhuriyet.edu.tr,
ORCID: 0000-0003-0413-1748
[2] Sivas Cumhuriyet University, Engineering Faculty, Civil Engineering,ygul@cumhuriyet.edu.tr,
ORCID: 0000-0002-2969-577X

Receive Date:27.12.2022 *Accepted Date: 24.04.2023*

ABSTRACT

The energy released during blasting in underground and surface mines for excavation purposes can cause flyrock, excessive level of ground vibration and air blast. In this study, ground vibration and air blast induced by blasting were measured and evaluated for a quarry mine in the Kangal district of Sivas province. Within the scope of this study, observations and measurements were made before, during, and after two blasting operations in a quarry mine to evaluate the environmental effects of blasting. The environmental effects of blasting were assessed by considering both the blasting parameters and the ground vibration and air blast measurement results.

Keywords: *Quarry mine, Blasting, Ground vibration, Air blast*

1. INTRODUCTION

The use of explosives in underground and surface mines continues to increase. The energy newly entering the environment as a result of blasting disrupts the equilibrium position in the environment and causes land motions. If the blasted environment does not show an elastic property to the new incoming energy, the energy is damped and only reflected as waves with reduced vibrations. If the environment exhibits elastic properties, the neighboring environments leave the equilibrium position as a result of the disrupted environment and create an oscillation similar to the spring-weight mechanism [1]. Ground vibration, airblast, and fly rocks problems may occur as a result of these oscillating movements. Parameters related to ground vibrations can be divided into two main classes as controllable (blast geometry parameters) and uncontrollable parameters (rock characteristics and site geology) (Siskind et al., 1980). The peak particle velocity (PPV) is considered most appropriate and accurate indicator of the damaging capabilities blast vibration [2].

Nowadays, environmental effects during blasting are monitored, evaluated and necessary precautions are taken in order to determine and control the environmental effects caused by blasting. Particle velocity and frequency are taken into account in most blasting safe limit criteria developed by

JSR A
Journal of Scientific Reports

numerous researchers [3 – 12]. In addition to these studies, the principles regarding the control of environmental vibration induced by various vibration sources have been determined under the heading of "Environmental Vibration Principles and Criteria" of the environmental noise assessment and management regulation in Turkey dated 04.06.2010. Approaches based on predicting the particle velocity depending on the scaled distance have been introduced with the development and use of geophones and pressure sensing microphones. The scaled distance-based prediction of the peak particle velocity has been accepted in most studies in the literature [13].

Within the scope of this study, ground vibration and air blast were measured at 6 points for two different blasts in a quarry (basalt) mine, and the effects of blasts on the Kangal-Zara highway, which is located at a distance varying between 50-100 m from the mining site, were evaluated.

2. MATERIAL and METHODOLOGY

2.1. Study Area

Basalt is produced by the open pit mine method in a quarry mine located in the Kangal district of Sivas province (Figure 1). Basalt masses (30-150 cm) fragmented-loosed by blasting are loaded on the truck with an excavator and transported to the crusher in the mine. The Kangal-Zara highway (which is separated from the D260 Sivas-Divriği highway) passes parallel to the east boundary of the mine at distances varying between 50-100 m.

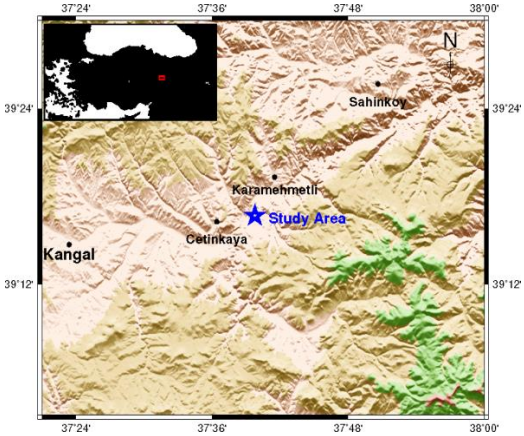

Figure 1. Studied area.

3. OBSERVATION and MEASUREMENT RESULTS

A detailed research was carried out before, during, and after two blasts performed at different times in the study area [14]. Ground vibration and air blast measurements of the blasts performed within the mine area were selected from among the points close to the highway. Two trial blasts were planned and implemented to reveal the environmental effects of controlled bench blasting in the quarry. In these trial blasts, there are no two free faces in bench blasting, but there is only one free face since

JSR A
Journal of Scientific Reports

Before Blasting (First Blasting)

After Blasting (First Blasting)

Before Blasting (Second Blasting)

After Blasting (Second Blasting)

Figure 2. Controlling of blasting area.

JSR A
Journal of Scientific Reports

only the top part of the blasted mass is open. Ground vibration and air blast were measured simultaneously at three points during the trial blasts (Figure 2). The specific charge amount of the first blast was calculated as 0,444 kg/m^3, whereas the specific charge amount of the second blast was calculated as 0,449 kg/m^3. The specific charge amounts in question may be reduced to lower values due to the presence of two free faces in bench blasting. In this case, lower ground vibration and air blast values can be obtained because the maximum charge per delay will decrease. Table 1 contains the blasting parameters applied in these blasts. In the surface mine using ANFO as an explosive, the average charge per hole was applied as 35,65 kg in the first blast and 56,95 kg in the second blast. Since a single hole is blasted simultaneously in both blasts (Table 2), the maximum charge per delay values are the same as the charge per hole values. Moreover, a delay of at least 8 ms, predicted in the literature [15], was ensured between the holes in both blasts (Figure 3). First, data on the basic blasting parameters of the above-mentioned blasts were obtained. After performing detailed examinations in the field for each blast, geophones and pressure sensing microphones were placed to measure ground vibration and air blast along the east boundary of the mine, and their distances from the blasting point were found (Figure 4 and 5). The locations of the geophones and pressure sensing microphones used in the blasts are presented in Figures 6 and 7. In the first blast, the geophones and pressure sensing microphones coded CUM-1 were placed closest to the blasting point (Distance: 168 m), while the other two (CUM-5 and CUM-3) were placed along the highway north of CUM-1 (Figure 6). The distances of CUM-5 and CUM-3 to the blasting point are 185 m and 253 m, respectively (Table 3). In the second blast, the geophones and pressure sensing microphones coded CUM-5 were placed closest to the blasting point (Distance: 150 m), and the other two (CUM-1 and CUM-3) were placed along the highway north and south of CUM-5 (Figure 7). Table 3 contains the distances of the geophones and pressure sensing microphones to the blasting point.

The results of ground vibration and air blast measurements induced by blasting are presented in Table 3. The peak particle velocity and frequency were measured as 4,57 mm/s and 39 Hz, respectively, and the peak noise was measured as 119,2 dB in the first blast, while the peak particle velocity and frequency were measured as 15,10 mm/s and 37 Hz, respectively, and the peak noise was measured as 114,0 dB in the second blast. While the peak particle velocity varied between 2,03-15,10 mm/s in the blasts, the frequencies varied between 27-39 Hz. Furthermore, the calculated scaled distance values are presented in Table 3. Scaled distance is a concept introduced using the amount of explosive that affects the distance and the basis of seismic waves or creates energy in air blasts. The scaled distance is correlated with the amount of land motions' blasting levels at varying distances. Scale is a unitless factor used depending on distance [16]. The scaled distance is derived from combinations of charge per delay, impacting seismic development and air blast energy, and the distance between the blast and the measurement point. The formula of the scaled distance (SD_1) most frequently used in the literature and this study is presented below. The safe distance can also be computed using the same formula. Furthermore, it is used in air blast predictions (SD_2).

$$SD_1 = R/\sqrt{W} \quad ; \quad R = SD\sqrt{W}$$
$$SD_2 = R/\sqrt[3]{W}$$

Here,

JSR A
Journal of Scientific Reports

SD : Scaled distance
R : Distance to blasting point or safe distance (m)
W : Maximum charge per delay (kg)

Since the charge shape used in surface mine studies is usually cylindrical (if the charging level-hole diameter ratio is ≥ 6, it is considered cylindrical, if the ratio is < 6, the charge is considered spherical), the waves from the column charge are propagated with the expanding shape of this cylinder. It is an accepted approach that the volume of this pressure cylinder varies with the square of its radius.

Table 1. Blasting parameters.

Blasting Parameters	First Blasting	Second Blasting
Type of blasting	Loose	Loose
Hole diameter (mm)	89	102
Hole slope (˚)	85-90	85-90
Drilling patern	Staggered	-
Burden (m)	2,5	3,5
Spacing (m)	3,5	3,5
Hole depth (m)	10	11
Subdrill (m)	1,0	1.0
Stemming (m)	2,0	2,9
Stemming material	Hole material	Hole material
Charge type	Colon	Colon
Charge per hole (kg)	35,65 (35 kg ANFO+0,5 kg Dyn.)	56,95 (55 kg ANFO+1,5 kg Dyn.)
***Specific charge (kg Anfo)/m^3)**	0,444	0,449
Number of holes	48	10
Number of rows	4	1
Maximum charge per delay (kg)	35,65 (35 kg ANFO+0,5*1,3Dyn.)	56,95 (55 kg ANFO+1,5*1,3 Dyn.)
Total charge (kg)	1680 kg ANFO 24 kg Dynamite	550 kg ANFO 15 kg Dynamite
Firing system	Non-electric capsule	Non-electric capsule
Delay order		
• **In the hole (ms)**	0	0
• **Between holes (ms)**	25	25
• **Between rows (ms)**	42	-

** Specific charge= kg Anfo/(Burden x Spacing x (Hole depth - subdrill))*

JSR A
Journal of Scientific Reports

Table 2. Firing times of blast holes.

First Blasting							
Row_A Hole_#	**Time (ms)**	**Row_B Hole_#**	**Time (ms)**	**Row_C Hole_#**	**Time (ms)**	**Row_D Hole_#**	**Time (ms)**
#1	25	#13	92	#25	159	#37	226
#2	50	#14	117	#26	184	#38	251
#3	75	#15	142	#27	209	#39	276
#4	100	#16	167	#28	234	#40	301
#5	125	#17	192	#29	259	#41	326
#6	150	#18	217	#30	284	#42	351
#7	175	#19	242	#31	309	#43	376
#8	200	#20	267	#32	334	#44	401
#9	225	#21	292	#33	359	#45	426
#10	250	#22	317	#34	384	#46	451
#11	275	#23	342	#35	409	#47	476
#12	300	#24	367	#36	434	#48	501
Second Blasting (Single Row)							
#1	25	#4	100	#7	175	#9	225
#2	50	#5	125	#8	200	#10	250
#3	75	#6	150				

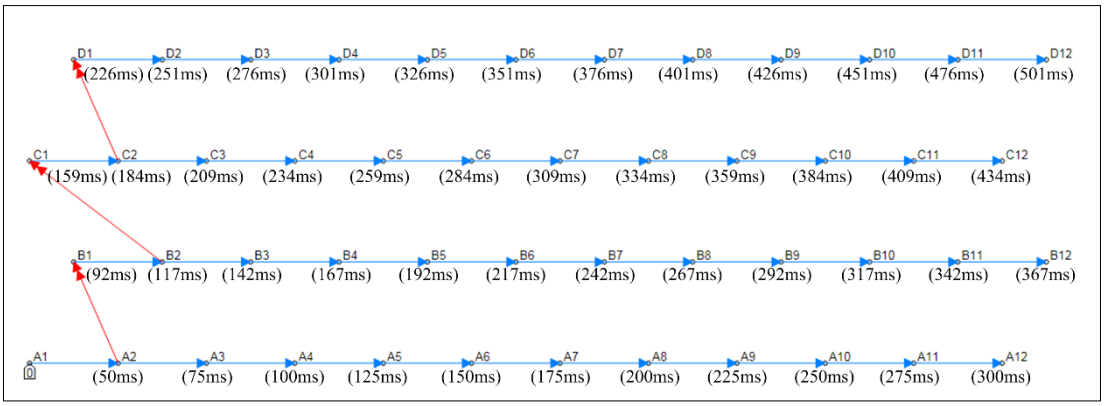

Figure 3. Drilling patern and firing times of first blasting holes.

JSR A
Journal of Scientific Reports

CUM-1

CUM-3

CUM-5

Figure 4. Placing of geophones and microphones (First blasting).

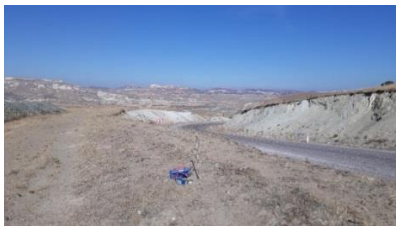

CUM-1

CUM-3

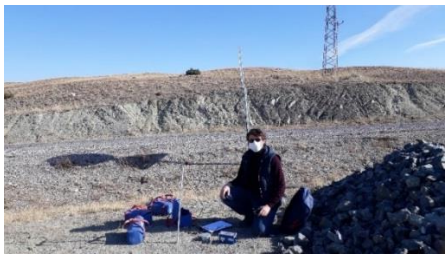

CUM-5

Figure 5. Placing of geophones and microphones (Second blasting).

JSR A
Journal of Scientific Reports

Figure 6. Measurement points of ground vibration and air blast (First blasting).

JSR A
Journal of Scientific Reports

Figure 7. Measurement points of ground vibration and air blast (Second blasting).

JSR A
Journal of Scientific Reports

Şengün, B. and Gül, Y., Journal of Scientific Reports-A, Number 53, 131-146, June 2023

Table 3. Measurement results of ground vibration and air blast.

Geophone Number	Partical Velocity (Transverse) PVT mm/s [Frequency,Hz]	Partical Velocity (Vertical) PVV mm/s [Frequency,Hz]	Partical Velocity (Longitudinal) PVL mm/s [Frequency, Hz]	Peak Partical Velocity PPV inch/s (mm/s) [Frequency, Hz]	Noise N dB (Pa)	Distance R (m)	Scaled Distance SD	
							SD_1	SD_2
First Blasting								
CUM-1	3,05 [57]	2,67 [30]	4,57 [39]	**0,180** (4,57) [39]	**119,2** (18,3)	168	28,14	51,04
CUM-5	3,30 [37]	2,29 [37]	2,79 [51]	**0,130** (3,30) [37]	**115,4** (11,8)	185	30,98	56,21
CUM-3	2,03 [73]	1,14 [85]	2,03 [27]	**0,08** (2,03) [27]	**110,9** (7,0)	253	42,37	76,81
Second Blasting								
CUM-1	3,56 [32]	2,41 [18]	2,41 [43]	**0,140** (3,56) [32]	**106,5** (4,25)	271	35,91	70,44
CUM-5	5,21 [30]	7,75 [34]	9,02 [30]	**0,355** (9,02) [30]	**114,0** (10,0)	150	19,88	38,99
CUM-3	9,91 [32]	6,60 [37]	15,10 [37]	**0,594** (15,10) [37]	**108,0** (5,0)	173	22,92	44,97

4. EVALUATION of the MEASUREMENT RESULTS

4.1. Evaluation of ground vibration measurement results

In the current study, the calculated scaled distance (SD_1) values varied between 28,14 - 42,37 in the first blast and 19,88 – 35,91 in the second blast (Table 3). Numerous studies in the literature state that there is no need for seismic recording as long as the scaled distance factors (Table 4) of the U.S. Office of Surface Mining (OSM) are applied. Considering the distance values from the blasting points in the trial blasts, the SD value must be higher than 55 to perform blasting without seismic recording.

JSR A
Journal of Scientific Reports

The fact that all the SD values calculated are lower than 55 indicates the necessity of vibration and air blast measurements.

Table 4. Recommended scaled distance factors for lack of siesmic monitoring [7].

Distance from the blast site		**Scaled distance to be applied without seismic monitoring**
ft	**m**	**(SD)**
0 – 300	0 – 90	50
301 – 5000	91 – 1500	55
>5001	>1500	65

The ground vibration and air blast values measured simultaneously at three points in both blasts were evaluated by considering the approaches of some researchers [3 - 7] and the "Regulation on Evaluation and Management of Environmental Noise; Environmental Vibration Criteria in Buildings (28.07.2013) in force in our country. It was found that the ground vibration and air blast measurement values (Table 3) did not have the risk of damaging any structure in the places where the measurements were performed according to these damage criteria.

The ground vibration and air blast measurement results (Table 3) were evaluated by considering the OSM, 1983 alternative criterion analysis approach, which is commonly employed nowadays and overlaps with the regulation in Turkey (Figure 8). As seen in Figure 8, the ground vibration values induced by the blasts were in the permitted region and did not carry any risk.

Simple regression analysis was conducted between the measured particle velocity and scaled distance values (Table 3), and as in the literature, the highest correlation was acquired in the power relationship (Figure 9). Figure 10 shows the correlation between the particle velocity acquired using this relationship and the measured particle velocity values. As is known, it is recommended in the literature to have more than 30 data pairs so that this relationship, in which site factors are determined, can be more reliable and more highly correlated. In the present study, 6 different measurements were carried out. Since bench blasting will be performed during the operation phase, lower particle velocities can be expected. However, ground vibration measurements should be made at more than 30 points to make the relationship between particle velocity and scaled distance (Figure 9) more reliable. Nevertheless, controlled bench blasting can be performed by considering this relationship to be acquired.

JSR A
Journal of Scientific Reports

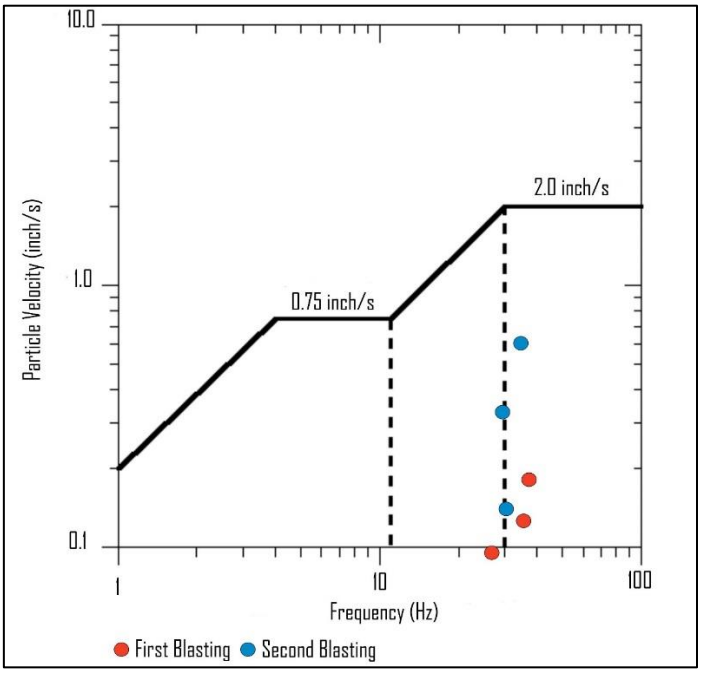

Figure 8. **S**afe limit criteria [7].

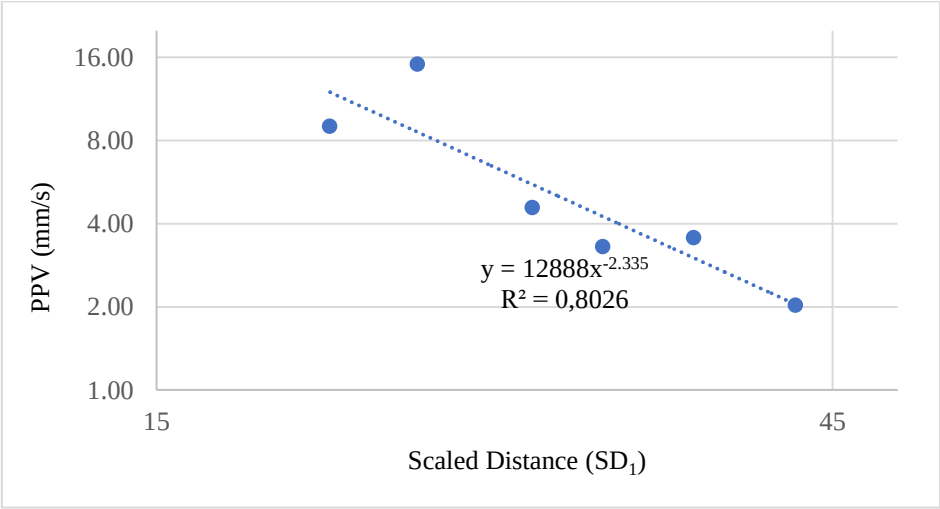

Figure 9. Relationship between peak particle velocity and scaled distance.

JSR A
Journal of Scientific Reports

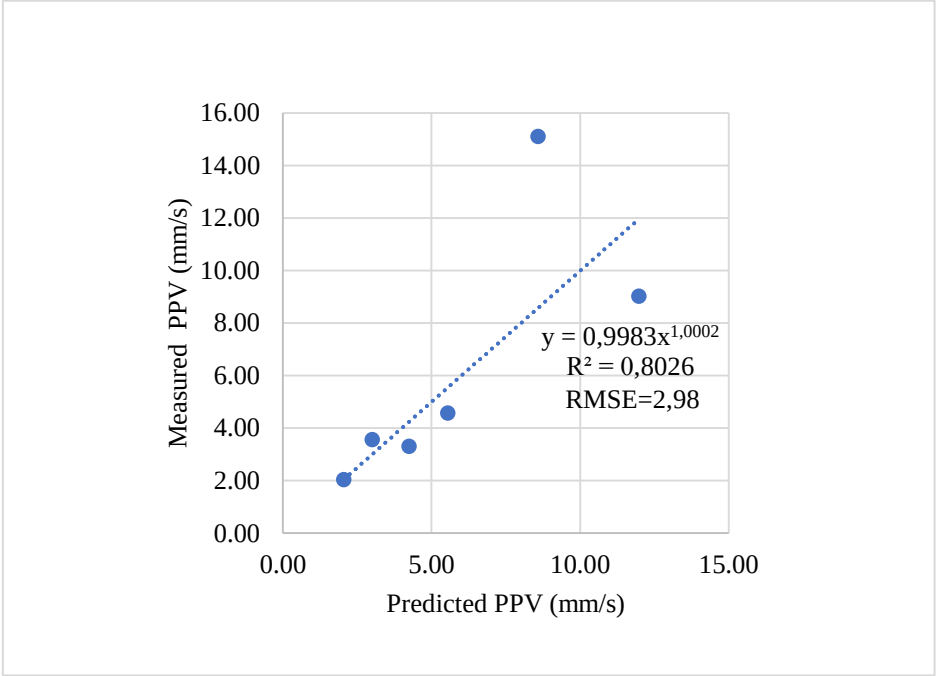

Figure 10. Relationship between measured and predicted peak particle velocities.

4.2. Evaluation of Air Blast Measurement Results

It is known that the propagation of the blast-induced air blast wave depends on atmospheric and topographic conditions, such as temperature, wind, and altitude. Even cloud closure at a particular distance can sometimes cause the pressure wave to be reflected back to the ground. The intensity of the audible parts of the blasts is usually between the noise caused by pneumatic breakers and the aircraft during landing. In the legal regulations in the US [5, 7], the air blast level corresponding to 140 decibels is determined as the starting level of damage and the top level of noise. In Turkey, the daily exposure limit values were given as (LEX, 8 hours) = 87 dB(A) or (Peak) = 200 Pa [140 dB(C) re. 20 µPa] under the heading of the "Exposure duration values and exposure limit values" (Second Section, Article 5) of the Regulation on the Protection of Employees from Risks Related to Noise, published in the Official Gazette dated 28.07.2013. The peak air blast values measured as 119.2 dB (18,3 Pa) and 114.0 dB (10,0 Pa), respectively, in the first and second blasts in the study area are below the starting level of damage and the top level of noise predicted by both regulations, and the exposure duration is very short (< 1 minute). Simple regression analysis was also carried out between the air blast and scaled distance values (Table 3). An acceptable correlation (R^2=0,0526) between air blast and SD_1 could not be acquired. However, an acceptable correlation (R^2=0,6642) was determined between air blast and SD_2 (Figure 11).

JSR A
Journal of Scientific Reports

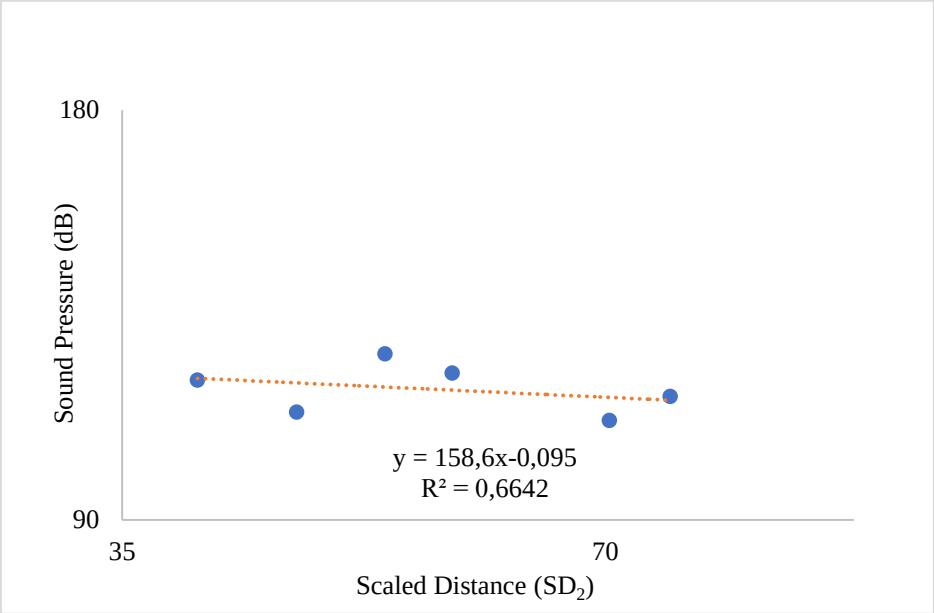

Figure 11. Relationship between sound pressure and scaled distance.

5. CONCLUSIONS and RECOMMENDATIONS

This study evaluated the ground vibration and air blast measurement results induced by two trial blasts performed for controlled blasting in a quarry mine.

ANFO was used as an explosive in the trial blasts, and the maximum charge per delay was applied as 35,65 kg in the first blast and 56,95 kg in the second blast. The specific charge amounts were calculated as 0,444 kg/m^3 and 0,449 kg/m^3 in the first and second blasts, respectively. It was indicated that the specific charge amounts could be reduced to lower values due to the presence of two free faces in bench blasting, and in this case, lower ground vibration and air blast values could be acquired since the maximum charge amount per delay would also decrease. Ground vibration and air blast measurements were performed simultaneously at three points during each of the blasts, and it was revealed that the blasts to be performed over a distance of 50-100 m did not have the risk of damaging the highway and/or any structure or building located after this distance. Simple regression analysis was carried out between the measured particle velocity and scaled distance values, and a highly correlated relationship was developed. Furthermore, a good correlation was found between the particle velocity obtained using this relationship and the measured particle velocity values. On the other hand, similar evaluations were performed for the air blast. It was seen that the measured air blast values were below the starting level of damage and the top level of noise. An acceptable correlated relationship was also acquired between the air blast and the scaled distance.

It was indicated that lower particle velocities could be expected since bench blasting would be performed during the operation phase. However, it was recommended to perform ground vibration measurements at more than 30 different points in order to make the particle velocity and scaled distance relationship more reliable for controlled bench blasting.

ACKNOWLEDGEMENT

The authors gratefully acknowledge Nettaş Mining Company. Also, the authors are grateful to Prof. Dr. Atilla CEYLANOĞLU for support in controlling and evaluating field measurements.

REFERENCES

[1] Ceylanoğlu, A., Kahriman, A. (1996). Measurement and analysis of ground vibration induced by bench blasting in a celestite open-pit mine in Turkey", Fourth International Symposium on Environmental Issues and Waste Management in Energy and Mineral Production, October 7-11, Cagliari, Italy, Volume 1, 283-290.

[2] Singh, T.N., Singh, V. (2005). An intelligent approach to prediction and control ground vibration in mines, Geotechnical and Geological Engineering, 23, 249-262, doi: 10.1007/s10706-004-7068-x.

[3] Langefors, U., Khilström, B., Westerberg, H. (1957). Ground vibrations in blasting, Water Power.

[4] Edwards, A.T., Northwood, T.D. (1959). Experimental blasting studies, National Resarch Council, Ottawa-Kanada.

[5] Siskind, D. E., Stagg, M. S., Kopp, J. W., & Dowding, C. (1980). Structure response and damage produced by ground vibration from surface mine blasting, USBM RI 8507. Pittsburgh: United States Department of the Interior.

[6] Bauer, A., Calder , P.N. (1977). Pit slope manual, Canmet Report, 77-14.

[7] OSM (Office of Surface Mining Reclamation and Enforcement), (1983). Federal Register, 30 CFR Parts, 715, 780, 816 and 817, Vol. 48, No. 46, Rules and Regulations (governing the blasts associated with surface and underground mines). Washington, DC., USA.

[8] Kuzu, C., Ergin, H. (2005). An assessment of environmental impacts of quarry-blasting operation: a case study in Istanbul, Turkey, Environmental Geology, 48, 211-217, doi: 10.1007/s00254-005-1291-5.

[9] Khandelwal, M., Singh, T.N. (2009). Prediction of blast-induced ground vibration using artificial neural network, International Journal of Rock Mechanics & Mining Sciences, 46, 1214-1222, doi: 10.1016/j.ijrmms.2009.03.004.

[10] Dehghani, H., Ataee-pour, M. (2011). Development of a model to predict peak particle velocity in a blasting operation, International Journal of Rock Mechanics & Mining Sciences, 48, 51-58, doi:10.1016/j.ijrmms.2010.08.005.

[11] Uysal, Ö., Cavus, M. (2013). Effect of a pre-split plane on the frequencies of blast induced ground vibrations, Acta Montanistica Slovaca, 18(2), 101-109.

[12] Yuvka, S., Beyhan, S., and Uysal, Ö. (2017). The effect of the number of holes on blast-induced ground vibrations, Environmental Earth Sciences, (76), 621, doi: 10.1007/s12665-017-6959-0.

[13] Ceylanoğlu A., Arpaz E. (2000). Divriği demir ve Kangal kömür açık işletmelerinde patlatma kaynaklı yersarsıntısı ve hava şoku ölçümlerinin sonuçları (in Turkish), 4th Drilling and Blasting Symposium, Ankara, Türkiye, ISBN 975-395-380-1, 135-145.

[14] Gül, Y., Şengün, B. (2020). 80524 ruhsat 3274527 erişim no'lu sahadaki gabro açık ocağında patlatmadan kaynaklanan yer sarsıntısı ve hava şoku ölçümlerinin değerlendirilmesi (in Turkish), Project report, Sivas Cumhuriyet University, Türkiye, 10.

[15] Kopp, J.W., Siskind, D.E. (1986). Effects of millisecond-delay intervals on vibration and airblast from surface coal mine blasting. United States Bureau of Mines RI 9026.

[16] Dick, R.A., Fletcher, L.R., D'Andrea, D.V. (1983). Explosives and blasting procedures manual, USBM IC 8560, USA, 44.

Kütahya Dumlupınar University
Institute of Graduate Studies

Journal of Scientific
Reports-A
E-ISSN: 2687-6167
Number 53, June 2023

RESEARCH ARTICLE

CHANGES IN HEART TYPE FATTY ACID BINDING PROTEIN (H-FABP) AND CERTAIN BIOCHEMICAL PARAMETERS DURING CHRONIC ARTERY DISEASES

Ercan GÜNEŞ[1], Nihat Mert[2], Yüksel KAYA[3], Nizamettin Günbatar[4*], Handan Mert[5]

[1]Van Yüzüncü Yıl University, Faculty of Veterinary Medicine, Department of Biochemistry, Van, erco-gunes@hotmail.com, ORCID: 0000-0001-6378-0049
[2]Van Yüzüncü Yıl University, Faculty of Veterinary Medicine, Department of Biochemistry, Van, nmert@yyu.edu.tr, ORCID: 0000-0001-7185-3316
[3]Van Yüzüncü Yıl University ,Faculty of Medicine, Department of Internal Medicine, Department of Cardiology, Van, yukselkaya@yyu.edu.tr, ORCID: 0000-0002-3007-9501
[4]Van Yüzüncü Yıl University Faculty of Health Sciences, Van, nizam_gun2011@hotmail.com, ORCID: 0000-0002-6684-3970
[5]Van Yüzüncü Yıl University, Faculty of Veterinary Medicine, Department of Biochemistry, Van, hmert@yyu.edu.tr, ORCID: 0000-0001-9827-7996

Receive Date:28.12.2022 *Accepted Date: 10.05.2023*

ABSTRACT

Coronary artery disease (CAD) is one of the leading causes of death and morbidity in our country, which is also true for the world in general as well. CAD generally develops atop atherosclerosis events. In this study, changes in heart-type fatty acid binding protein (H-FABP) and certain other biomarker levels during chronic artery diseases were investigated.. For the present paper, serum samples collected from patients who applied to Van Yüzüncü Yıl University Dursun Odabaş Medical Center Emergency Department and Cardiology Polyclinics with acute ischemic chest pain between January - June of 2019 were evaluated. Patients were not given any drugs or other kinds of substances before sample collection. Of the patients who applied to the cardiology clinic, 24 of these patients were diagnosed with chronic arteritis, 12 patients with cardiological problems were diagnosed with diabetes mellitus (DM), 12 patients with hypertension (HT) problems and heart complaints, and 12 healthy individuals (who were not diagnosed with diabetes, hypertension or CAD) were included as research materials.

Certain markers like Troponin, CK, CK-MB, AST, ALT, LDL-Cholesterol, HDL-Cholesterol, LDH, Glucose, and Creatinine in the blood samples were biochemically determined using an autoanalyzer (Abbott ci16200),while H-FABP values were determined using ELISA method.

As a result of the analyses carried out : LDL-cholesterol values reached their highest in the CAD group (108,06 ± 6,82 MG/DL), while HDL-Cholesterol and LDH values peaked in the CAD+HT group (51,52 ± 3,92 MG/DL), (318,83 ± 37,42 MG/DL), and CK, CK-MB, cTnI, AST, Glucose, creatinine, and H-FABP levels were found to be high in the DM+CAD group. Meanwhile, cTnI

JSR A
Journal of Scientific Reports

values were increased in people with HT or DM as well as CAD, but there was no statistical significance. Similarly, LDL-cholesterol levels stayed similar between the groups. Intergroup changes in other biomarkers examined showed the importance of CK and Glucose levels at p≤ 0.001, AST p≤ 0.002, LDH p≤ 0.003, CK-MB p≤ 0.004, HDL-Cholesterol p≤ 0.049, Creatinine p≤ 0.011, and H-FABP p≤ 0.050. H-FABP has recently taken its place in the field of cardiology with increasing importance in the diagnosis of CAD and MI. The findings obtained in this study show that the H-FABP level was increased in all groups except the test group, and we recommend its use as a practical parameter in cardiology clinics.

Keywords: *Diabetes mellitus, Hypertension, H-FABP, Cardiac markers, Coronary artery disease*

1. INTRODUCTION

Coronary artery disease (CAD) is quite prevalent in the world and is associated with serious cardiac effects in many patients. Coronary artery disease is often triggered by physical or psychological stress. Symptoms related to it usually don't last long. That being said, a coronary artery is completely blocked during the disease which can cause permanent damage to the heart muscles (myocardial infarction) if not diagnosed and treated early. This can cause severe symptoms which usually occur in the form of chest pain and shortness of breath. In certain cases, it can result in death. Diabetes, hypertension, smoking, hypercholesterolemia, inactive life, obesity, and genetic factors are possible risk factors for CAD. Rarely, patients with CAD may show no symptoms. Cardiomyocytes are extremely rich in various proteins and enzymes, including troponin, creatine kinase (CK), creatine kinase MB (CK-MB), and lactic dehydrogenase (LDH). These proteins and enzymes can be released and dispersed into the bloodstream following cardiomyocyte necrosis and breakdown. These are then broken down and mixed into the blood and can be used as vital markers for the early diagnosis of coronary artery disease. In addition to these cardiomyocytes Heart-type fatty acid-binding protein (H-FABP), which may be introduced into the blood even earlier, can help facilitate early diagnosis [1].

Although H-FABP is expressed mainly in cardiomyocytes, it also occurs in much lower concentrations in skeletal muscle, renal distal tubular cells, and the brain. There is also the use of H-FABP as a sensitive marker for exercise-induced skeletal injury [2]. Myocardial infarction, congestive heart failure and angina pectoris [3] in the damaged area of the heart, for example, the heart isoform of the first described biochemical marker creatine kinase (CK-MB) has found its place in the clinic as a 'gold standard' protein. [4] Plasma H-FABP concentrations increase and decrease faster than creatine kinase (CK), indicating that H-FABP is more useful than CK for early diagnosis of such damage and monitoring of damage during repeated exercise sessions. The potential use of H-FABP as a rapidly changing biomarker to diagnose the early stages of acute myocardial infarction was studied in [5]. The results of this study were later put to test by many other researchers as well. Normally, plasma or interstitial fluid contains no H-FABP, which is only released following cellular injury to the heart. This release occurs approximately 2 hours following the onset of the symptoms, and studies suggest that it peaks at approximately 4 to 6 hours. Return to its normal baseline occurs within 20 hours. For the next 3 to 4 hours following the symptom onset, H-FABP has more than 80% sensitivity for AMI events. Other heart markers (CK), such as creatine kinase, CK-muscle and brain (MB) (mass or activity), cardiac troponin I (cTnI), and cardiac troponin T (cTnT) will only begin to accumulate in

plasma within 0-6 hours of symptom onset, and their sensitivity has been reported to be around 64% [5].

The main causes of coronary artery disease are the result of the loss of elasticity of the coronary arteries. CAD occurs with lipid plaque accumulation and hardening and rupture of the vessels. These plaques have a high tendency to cause deterioration of the vascular structure and subsequent formation of clots. A significant part of the CAD can result in AMI, and even death if the intervention is late. Most such sudden and untimely deaths are due to atherosclerosis, which often goes unnoticed due to its associated risk factors being prone to modification, prevention, or reduction.

A heart attack occurs due to the death of cells in the heart tissue, which in turn is the result of the blockage of one or more of the main vessels in the heart that feed that particular tissue. This scenario can lead to fatal results. Depending on the severity of the obstruction, symptoms such as sweating, nausea, vomiting, and sometimes fainting may occur, which may be accompanied by severe pain in the chest. Although chest pain indicates a heart attack, it may sometimes be felt in the upper abdomen and stomach area in some people. Such pain is often ignored, thinking that it's just a temporary discomfort caused by the stomach. Generally, in elderly people, the crisis may occur in the form of shortness of breath that increases with effort. These symptoms can be seen in 75-80 out of 100 people. The other 20% occur in a condition called "silent heart attack", which shows no symptoms. The first symptom in these cases is often death [6].

Factors like nutritional disorders, overeating, a fatty diet, consuming too many ready-made foods, hypertension, high cholesterol, coronary arteriosclerosis (Atherosclerosis), diabetes, smoking, obesity, and an inactive life are among the leading causes of heart problems [7].

2. MATERIALS and METHODS

This research was conducted on a total of 60 patients between the ages of 20 and 100, between January 2019 and June 2019, after obtaining permission with the Ethics Committee Approval No: 12.10.2018 decision no 06. Of these 60 individuals, 48 were patients and 12 were healthy.

The relationship between H-FABP and some biochemical and cardiac parameter values (CK-MB, Troponin, AST, ALT, LDL-Cholesterol, HDL-Cholesterol, LDH, Glucose, and Creatinine) of patients admitted to emergency departments of hospitals and cardiology outpatient clinics (with complaints of coronary artery disease and chest pain) were examined.

2.1. Patient Selection

In this study, blood samples collected from patients who applied to Van Yüzüncü Yıl University Dursun Odabaş Medical Center Emergency Department and Cardiology Polyclinics between January 2019 and June 2019 were evaluated. No medication or other substance was given to these people or no application was made. Of the patients who came to the cardiology with similar demographic characteristics, 24 patients (CAD=24) with acute ischemic chest pain and diagnosed with chronic arteritis disease, 12 patients with cardiological problems diagnosed with diabetes mellitus (DM+CAD=12), 12 patients with hypertension problems and again came to the clinic with a heart

JSR A
Journal of Scientific Reports

complaint (HT+CAD=12) and 12 healthy people who were not diagnosed with diabetes, hypertension and with similar demographic characteristics CAD (CONTROL=12) as research material it was used. Certain markers like Troponin, CK, CK-MB, AST, ALT, LDL-Cholesterol, HDL-Cholesterol, LDH, Glucose, and Creatinine in the blood samples were biochemically determined using an autoanalyzer (Abbott ci16200), while H-FABP values were determined using ELISA method.

2.1.1. Human heart fatty acid binding protein (H-FABP)

Principle: ELISA Kit Biont, Catalog No: YLA1747HU. This kit uses enzyme-linked immunosorbent assay (ELISA) based on biotin double antibody sandwich technology to assay human heart fatty acid binding protein (H-FABP). H-FABP is added to pre-coated cavities with monoclonal antibodies and then incubated. After that, anti-H-FABP antibodies labeled with biotin are added to combine with streptavidin-HRP, which forms an immune complex. After incubation and washing, unbound enzymes are removed. Substrates A and B are added. Then the solution turns blue, and under the influence of acid, turns yellow. The colorimetric tones of the solution and the concentration of H-FABP are positively correlated.

2.1.2. Assay procedure summary

1. Prepare all reagents, samples and standards.
2. Prepared samples, standards and ELISA solutions are added. They are allowed to react for 60 min at 37 °C.
3. The plate is washed five times. Chromogen solutions A and B are added for color development. Incubate at 37 °C for 10 minutes.
4. The stop solution is added.
5. The OD value is read and calculated within 10 minutes.

Working range： 0.05 ng/ml → 20 ng/ml 25

Sensitivity：0.01 ng/ml

2.1.3. Statistical analysis

For the descriptive statistics for the features emphasized, the average is expressed as the SEM value. The Kruskal-Wallis test was used to compare the groups in terms of these features. In the calculations, the statistical significance level was taken as 5%. SPSS (ver: 21) statistical package program was used for the calculations.

3. RESULTS

Table 1. Control and change of biochemical parameters studied in chronic arterial disease.

Group **Test**	**CAD** **avg ± SEM** **n=24**	**DM+CAD** **avg ± SEM** **n=12**	**HT+CAD** **avg ± SEM** **n=12**	**Control** **avg ± SEM** **n=12**	**P**
CK (U/L)	67.23 ± 9.12^{b}	135.95 ± 17.91^{a}	73.33 ± 11.86^{b}	40.80 ± 5.72^{b}	0.001
CK-MB (U/L)	22.11 ± 4.31^{b}	45.81 ± 9.99^{a}	19.04 ± 5.38^{b}	14.20 ± 1.56^{b}	0.004
CTnI (NG/ML)	0.60 ± 0.44	6.76 ± 3.78	4.07 ± 4.05	0.023 ± 0.002	0.269

JSR A
Journal of Scientific Reports

H-FABP (MG/L)	8.43 ± 1.45^{c}	16.16 ± 0.92m	11.82±0.97^{b}	1.86 ±0.43m	0.050
ALT (U/L)	29.58±5.82^{ab}	39.91 ± 6.08^{a}	22.42±2.91^{b}	18.50±1.45^{b}	0.048
AST (U/L)	31.21 ± 3.96^{b}	89.36 ± 29.36^{a}	31.67±6.10^{b}	23.00±1.34^{b}	0.002
LDH (MG/DL)	298.29±26.81^{a}	292.64±3.04^{a}	318.83±37.42^{a}	160.92±6.87^{b}	0.003
HDL (MG/DL)	50.20 ± 3.69^{a}	36.55 ± 2.90^{b}	51.52± 3.92^{a}	45.63±2.51^{ab}	0.049
LDL (MG/DL)	108.06 ± 6.82	101.75 ± 10.77	90.59±11.44	82.57±5.30	0.143
CREATININE (MG/DL)	0.85 ± 0.18b	1.32 ± 0.25m	1.05± 0.07^{ab}	0.93±0.03^{b}	0.011
GLUCOSE (MMOL/L)	110.04±4.47^{b}	239.36±40.08^{a}	111.92±6.18^{b}	97.42±2.56^{b}	0.001

a,b,c,d The difference between the means shown with different letters in each column is statistically significant

According to these findings, the CK enzyme, which shows changes in muscular destruction, followed a profile similar to the AST level. CK values for the DM+CAD group were calculated to be 3.5 times higher than the controls, and 2 times higher than the other 2 groups (135.95 U/L). This shows how strongly DM is correlated to heart damage (Table 1) ($p \leq 0.001$).

CK-MB, one of the three important isoenzymes of the CK enzyme, is very important as a cardiac marker. A similar table to that of AST-CK can also be found here. The same conclusions reached for the CK analysis can also be used for the interpretation of CK-MB (Table 1). The 14.2 U/L activity observed in the controls reached up to 45.81 U/L in the DM+CAD group ($p\leq 0.004$).
The values for cTn1, which is an important cardiac marker, have also increased significantly in the HT+CAD and DM+CAD groups. As shown in (Table 1), the level was almost zero in the controls, increasing to 6.76 ng/ml in the DM+CAD group. Once again the negative effects of diabetes can be observed ($p\geq 0.269$).

While control group H-FABP level was 1.86, the peak was 11.82 mg/l in the hypertension group and 8.43 mg/l in the CAD group, while it was 16.16 mg/l in the DM+CAD group. This result further emphasizes the negative effect of diabetes on the heart ($p\leq 0.050$).

While the ALT enzyme was measured as 18.50 U/L in the control group, the highest level was found in the DM+CAD group. This shows that diabetes also has negative effects on the liver (Table 1) ($p\leq 0.048$)

AST increases liver or muscle damage and was used as a good diagnostic enzyme to determine heart muscle damage in the past. Here, AST levels were shown to undergo significant changes in CAD cases.The peak value was observed in the DM+CAD group (89.36 U/L) and similar levels were measured in CAD and HT+CAD groups. All three groups had higher AST levels than the controls (Table 1) ($p\leq 0.002$).

The detected HDL-cholesterol levels appear to have decreased, predisposing the patients to heart diseases (Table 1) shows the HDL-cholesterol levels of the other 2 groups, as well as the controls ($p\leq 0.049$).

JSR A
Journal of Scientific Reports

LDH levels were increased in the HT+CAD group compared to the control's (318.83 – 160.92 U/L). Similar elevations were found in all 3 groups related to CAD compared to the control ($p \leq 0.003$).

When LDL-cholesterol levels are high, the risk of heart and circulatory diseases increases. Accordingly, (Table 1) has a very good graphical appearance. The lower level in controls (82.57 mg/dl) reached 108.06 mg/dl in the CAD group ($p \geq 0.143$).

Although creatinine, whose clinical significance as a kidney function test is not discussed, did not show much change, the highest value was once again seen in the DM+CAD group (1.32 mg/dl) ($p \leq 0.011$).

As expected, the hunger glucose level was high in the diabetic group and significant changes were detected in the other groups. In Table 1, the value of the DM+CAD group 239.36mmol/L was significantly higher than the others ($p \leq 0.001$).

4. DISCUSSION

The incidence and mortality of cardiovascular disease are increasing worldwide [8] and acute myocardial infarction (AMI) has become an important cause of death [9]. In addition, AMI exhibits a rapid growth trend in young and low-income groups [10]. It is possible to detect these proteins and determine the potential location, severity and course of tissue damage. As such, these are often referred to as biochemical markers, and their correct and quick evaluation is essential to formulate correct treatment and discharge plans. If the rise and fall of these markers in the blood can be detected in time, they can also help discharge or redirect patients who are not actually suffering from tissue damage, or to determine when their recovery is complete. This, in turn, helps reduce hospitalization costs.

That being said, use of such markers accurately to formulate a treatment plan depends on a range of factors. These markers have different release times and rates into the circulatory system, and their elimination rates and paths also vary. Taken both of these into consideration yields the plasma reference levels, which are essential for correct diagnosis and treatment. As such, efforts are focused on identifying tissue-specific proteins that have previously been raised above plasma reference values from biomarker proteins used today. Second, new technologies need to be applied for faster determination of these markers levels to allow for rapid outcomes. In particular, the development of the tests that are applied in the patient room, also known as the point-of-care tests, is attracting a lot of attention, significantly promoting the clinical application of biochemical marker proteins.

Fatty acid-binding proteins (FABPs) are small cytoplasmic proteins that are readily available in large quantities in tissues with active fatty acid metabolisms. Examples of such tissues include the heart and liver. As of this study, nine different types of the FABP families are identified. The most studied is heart-type FABP (H-FABP) largely due to its abundant presence in cardiomyocytes.

Many researchers have studied H-FABP to determine if it can be used as a myocardial damage indicator [5, 11, 12]. Early clinical markers of myocardial infarction include myoglobin (Myo),

JSR A
Journal of Scientific Reports

creatine kinase-Mb (CK-MB), cardiac troponin T (cTnT), and cardiac troponin I (cTnI) (13). A new myocardial marker, heart type fatty acid binding protein (H-FABP), has been discovered for the early diagnosis of AMI (14). Under normal physiological conditions, H-FABP is not seen in plasma or tissue fluids and can only be detected in the case of myocardial injury; H-FABP begins to increase 1-3 hours after the onset of acute coronary syndrome. It peaks after 6-8 hours and returns to normal after 12-24 hours. It is one of the earliest markers released into the circulating blood during myocardial injury (15).

All these findings show that, different biomarkers have different utilization windows, and some of this potential can be hidden or lost by the time of initial hospitalization. Many studies have taken this into consideration and compared the potential usability of H-FABP, myoglobin, cTnT, and cTnI for the rapid detection of AMI. The results mostly conclude that H-FABP is an prime candidate as a biomarker for rapid diagnosis and differentiation of clinical events [14]. Table 1 contains the summarized results of 5 similar comparison studies that study how early H-FABP can be used as a marker candidate in hospital-presenting patients with complaints of chest pain suggestive of AMI (Table 1). In each study, the recipient study for accepted blood samples from all patients showed that H-FABP was significantly higher than myoglobin, which demonstrated superior performance.

H-FABP plasma levels usually reach their maximum about 6-8 hours after the first symptoms, and fall back to their normal levels within approximately 1-2 days. Although H-FABP concentration level changes are similar to that of myoglobin (quick to release and clear), its cardiac specificity is approximately 15-20 times greater, so it is a much more effective indicator for myocardial damage. Additionally, the normal serum/plasma levels of H-FABP are significantly lower than that of myoglobin, making it much safer in terms of false-positives.

In some cases, serum H-FABP levels were found to increase within half an hour of ischemic events, making it possible to detect them early. This possibility was tested in numerous studies on bypass graft patients and cardiopulmonary bypass (CPB) pump cases [16,17]. In these studies, it was found that H-FABP has more sensitivity and specificity than troponins and myoglobin. Wider-scope prospective studies were also performed, and in one such study with a cardiac surgery patient count of 1298, various biomarkers like CK-MB, CPB, and H-FABP levels were analyzed. As a result, H-FABP was revealed as an independent marker which could be used to predict death in both the post-op period and beyond [18].

While troponin-I and H-FABP have some a certain degree of variance in terms of their post tissue damage biochemical behaviors, many studies have shown that their plasma levels share similar and often overlapping curves [16,17]. Ischemia can be driven forth as an explanation for this similarity. That being said, neither the reperfusion nor the cytotoxic events caused by neurohormones in plasma are specific to AMI, which also correlates to any troponin-I value beyond the reference. High-sensitivity troponin-I may increase during perioperative myocardial stress as a result of increasing cardiomyocyte apoptosis, stretching of the myocardial wall, or due to proteolysis of the contractile apparatus. None of these cases have myocardial necrosis but high sensitivity troponin-I may increase nonetheless.

JSR A
Journal of Scientific Reports

For H-FABP, levels above 26 ng/mL18.2-51.5 ng/mL were found to be a sensitive indicator of ventricular dysfunction, extended hospitalization periods, and mortality rates. One particular study determined a cut-off value of 6.8ng/mL to distinguish myocardial damage in patients undergoing bypass grafting at the pump [19]. The ROC curve-based cutting value was 19.7ng/mL (sensitivity 77%, specificity 75%). The correlation between the various types of biomarkers examined in the present study is slightly different from the studies mentioned above. As a result, it was seen that the largest correlation was found between H-FABP and CK-MB. The correlation between Troponin I and H-FABP is low.

CK-MB is an auxiliary parameter for diagnosis in cases of myocardial injury or infarction. In this study, CK-MB values increased from 14.20 U/L in controls to 45.81 U/L in the DM+CAD group. The most valuable finding of this study is that similar results have been observed in many of the studied parameters related to the heart. The increase in troponin levels is also seen here,where the difference between patient groups and control was statistically significant ($p \leq 0.004$). CK levels also showed a similar profile, resulting in a similar increase in myocardial damage levels ($p \leq 0.001$).

In clinical practices, troponins are now widely adopted as the markers MI detection [20]. However, they are not very well suited to diagnose congestive heart failure and unbalanced angina Pectoris. The same holds true for certain any disorders including ventricular remodeling, or for the cases where extracellular matrix undergoes alterations. Minor myocardial injuries and calcium regulation disorders also challenge the successful use of troponins. Death of cardiac muscle cells was also studied in the literature [21,22]. According to the observations of Setsuda et al., only 48.3% of the CHF patients displayed increased cTnT levels, whereas H-FABP was found to have a success rate of 72.4%. This finding clearly shows that H-FABP was much more sensitive to small cardiomyocyte necrosis compared to cTnT [3].

Another study similar to that of Setsuda et al. was performed with the difference being the tissue damage location. This new study has investigated the differences between sensitivity and accuracy of biomarkers in cases of skeletal muscle injury [23]. The results show that the plasma myoglobin/H-FABP ratio was lower than 1 to 15, proving no correlation between skeletal muscle damage and H-FABP levels (ratio <15) [3]. Therefore, high H-FABP levels only emerge as a result of cardiomyocyte damage.

In that particular study, cTnT levels were found to have raised in CHF and UAP cases, whereas H-FABP levels were found to have stayed the same. This can be explained by the cases being minor MI's, in which H-FABP is rapidly eliminated from the blood but cTnT initially stayed high. This finding is especially profound when we consider the fact that patients displayed no other symptoms that could indicate AMI. This underlies that finding sensitive markers for different tissue damage cases is truly important, and is indicative that H-FABP has a higher sensitivity compared to cTnT for the determination of mild muscle cell damage.

In the presented study, the H-FABP level was measured as 1.86 mg/l in the control group, 11.82 mg/l in the hypertension group, 8.43 mg/l in the CAD group, and 16.16 mg/l in the DM+CAD group ($p \leq 0.050$). Since the difference in the H-FABP mean of the 4 groups examined shows statistical

JSR A
Journal of Scientific Reports

importance, this parameter can be suggested as a biomarker in cardiac destructive pathologies. When the H-FABP values were compared proportionally, a 4.5-fold increase was detected in the CAD group compared to the controls. This increase was found to be 6.5 times compared to the HT group and 8.7 times to the DM+CAD group. These elevations seem to be important as a descriptor of a heart problem that will be shaped by different reasons in the patient and will help guide the clinical diagnosis.

Current clinical norm is that ALT and AST tests are the primary methods of determining and monitoring the course of hepatocellular injuries and various other types liver diseases [24]. Current liver function tests are sufficiently specific for liver disease despite their lack of sensitivity. While it's true that ALT analysis has become rapid, cheap and easily accessible thanks to wide range of clinical analyzers, it still has the issue that ALT is a large molecule (96 kD) and it only starts to increase in circulation after severe cell damage or death. Various cytoplasmic proteins share the same problem, but owing to the fact that hepatocytes lack an interstitial barrier due to their large endothelial clefts and are in close contact with vasculature, protein with smaller molecular size diffuse in plasma faster compared to their large counterparts, as in damaged cardiomyocytes, and therefore increase beyond their normal values earlier in serum compared to their larger counterparts. All things considered, new specific and sensitive liver injury markers are generally needed for acute hepatocellular injury diagnosis and treatment [24].

α-GST has been suggested as one such marker for hepatocellular damage due to its strong sensitivity and specificity. Found in the liver, kidneys, and intestines, this cytoplasmic 26 kD protein is quick to be released to the circulation from even slightly-damaged liver cells. α-GST also has a relatively shorter plasma presence [25,26]. That being said it's not specificity is still not as sharp as that of H-FABP, as this has been shown in some studies [20] . Still, α-GST was shown to be a great biomarker in post liver-transplant rejection cases [2].

In the present study, when the ALT level was examined, the highest activity was found in the DM + CAD group. As can be seen in Table 1, the intergroup significance was determined at the level of $p<0.048$. While a value close to that of the controls was determined in the HT-CAD group, higher values were calculated in the CAD group.

Creatinine levels are important for kidney function. In this study, creatinine level was highest in the DM+CAD group. The nephropathic effect of diabetes is underlined by this finding. In the statistical interpretation of the mean between the groups, importance was found at the level of $p\leq0.011$ (Table 1).

Considering all of these, H-FABP stands above others as an early cardiac tissue damage marker. Smaller proteins are released to the circulation faster than their larger counterparts in case of cell damage [4], and H-FABP is lighter compared to many other markers. Another factor influencing the rate of increase of a marker in circulation is its amount in the cells, the more a tissue contains that particular marker, the faster it will rise beyond its reference serum value. Therefore, the best marker for the detection of injuries on a given tissue has to be specific to that particular tissue [27,28]. It should also be protein with a relatively smaller molecular size, as this is usually related to early

release. Similarly, the marker should be readily available on that particular tissue, while simultaneously having a low plasma presence in healthy individuals. H-FABP meets all these criteria for cardiac muscle damage.

Troponins are also good candidates due to their good cardiac specificity, however they are still late markers compared to H-FABP [29]. This delay is due to the fact that they are broken down from tropomyosin, which takes time. Another shortcoming of troponins is their extended plasma presence, which may last days.

LDH enzyme activity showed a lot of variation in this study. An LDH level of 160.92 U/L was determined in the control group, which was 298.29, 292.64,and 318.83 U/L in the CAD, DM+CAD, and HT+CAD groups respectively($p \leq 0.003$).

H-FABP and myoglobin are similar in many regards regarding cardiac tissue damage. They both increase beyond their reference values rapidly, and they both are eliminated from the circulation quickly through the kidney path. This makes both elements good candidates for early markers, from the onset of symptoms to approximately 1-2 days. Their plasma levels reach the peak within 6 - 12 hours of MI, and return to normal within 1 day (36 hours if no thrombolytics are used). However it's still possible to consider H-FABP as a better choice compared to myoglobin as the preferred early cardiac marker [20]. The level difference of H-FABP concentration in healthy and CAD individuals [30] and the high sensitivity of H-FABP to minor myocardial damages, will enable it to be used in diagnosis - even in patients with chronic heart failure or unbalanced angina Pectoris [31,32].

FABP seems to be a bright candidate for future rapid tissue damage diagnosis parameters. While some members of the family are not tissue-specific (H and L-FABP), they are still reported as the most sensitive early diagnosis markers for myocardial, bone, kidney, brain, liver, and intestine damage. Other members of FABP family are tissue specific, where L-FABP shows liver damage, while I-FABP shows intestine and B-FABP shows brain damage.

New rapid testing systems that implement specific monoclonal antibodies and antigens will enable FABP to become a very rapid diagnosis tool in clinics, especially in conjunction with other clinical findings. This can lead to reduced mortality and morbidity.

In the presented study, the changes in biochemical parameters due to combinations of CAD with different diseases and conditions (Hypertension and Diabetes) were examined. The most severe changes in the studied parameters were observed in individuals with diabetes. The increase in H-FABP was mostly shaped in the Diabetic group, and the differences in the parameters between the groups were important for all markers, except for cTnI and LDL. These are important results for cardiological studies.

As a result: clinically, CAD and MI are diagnosed with biochemical measurements such as troponin, CK-MB, LDH, AST, CK, and early treatment plans were shaped according to such findings. The results of this study, however, show that H-FABP levels in different groups such as CAD, DM+CAD, and HT+CAD had changed significantly compared to the control. This means that H-FABP can be

used as a biochemical cardiomarker, and should be taken into account from the first minutes of damage. Due to its early occurrence, specificity and sensitivity compared to other cardiac markers as stated by the literature and as shown here, it can be included in routine biochemistry tests. We hope that our findings will contribute to H-FABP being considered in clinical use.

ACKNOWLEDGMENTS

This study was derived from the master's thesis

REREFENCES

[1] Haskell, W.L., Alderman, E.L., Fair, J.M., Maron, D.J., Mackey, S.F., Superko, H.R., Williams, P.T., Johnstone, I.M., Champagne, M.A., and Krauss, R.M. (1994). Effects of intensive multiple risk factor reduction on coronary ath-erosclerosis and clinical cardiac events in men and women with coronary artery disease. The Stanford Coronary Risk Intervention Project (SCRIP). Circulation. 89, 975-990.

[2] Hughes, V.F., Trull, A.K., Gimson, A., Friend, P.J., and Jamieson, N. (1997). Randomized trial to evaluate the clinical benefits of serum α-glutathione-s-transferase concentration monitoring after liver transplantation. Transplantation. 64, 1446-1452.

[3] Setsuta, K., Seino, Y., Ogawa, T., Arao, M., and Miyatake, Y. (2002). Use of cytosolic and myofibril markers in the detec-tion of ongoing myocardial damage in patients with chronic heart failure. The American Journal of Medicine. 113, 717-722.

[4] Alpert, J.S., Thygesen, K., Antman, E., and Bassand, J.P. (2000). Myocardial infarction redefined-A consensus document of The Joint European Society of Cardiology/American College of Cardiology Committee for the redefinition of myocardial infarction. Journal of the American College of Cardiology. 36, 959-969.

[5] Glatz, J.F., Van Bilsen, M., Paulussen, R.J., Veerkamp, J.H., Van der Vusse, G.J., and Reneman, R.S. (1998). Release of fatty acid-binding protein from isolated rat heart subjected to ischemia and reperfusion or to the calcium paradox. Biochimica Biophys Acta. 961, 148–152.

[6] Petersen, S., Peto, V., Rayner, M., Leal, J., Luengo-Fernández, R., and Gray, A. (2008). European Cardiovascular Disease Statistics: 2008 edition. London: British Heart Foundation.

[7] Johnstone, M.T., and Nesto, R. (2005). Diabetes mellitus and heart disease. In: Pickup JC, Williams G, editors. Joslin's Diabetes Mellitus. 14th ed. Philadelphia: Lippincott Williams and Wilkins; P. 975- 998.

[8] Nemet, I., Saha, P.P., Gupta, N., Zhu, W., Romano, K.A., Skye, S.M., Cajka, T., Mohan, M.L., Li, L., and Wu, Y. (2020). A cardiovascular disease-linked gut microbial metabolite acts via adrenergic receptors. Cell. 180, 862–877.

[9] Roth, G.A., Johnson, C., Abajobir, A., Abd-Allah, F., Abera, S.F., Abyu, G., Ahmed, M., Aksut, B., Alam, T., and Alam, K. (2017). Global, regional, and national burden of cardiovascular diseases for 10 causes, 1990 to 2015. J Am Coll Cardiol. 70, 1–25.

[10] Arora, S., Stouffer, G.A., Kucharska-Newton, A.M., Qamar, A., Vaduganathan, M., Pandey, A., Porterfield, D., Blankstein, R., Rosamond, W.D., Bhatt, D.L and Caughey, and M.C. (2019). Twenty year trends and sex differences in young adults hospitalized with acute myocardial infarction. Circulation. 139,1047–1056.

[11] Ishii, J., Wang, J.H., Naruse, H., Taga, S., Kinoshita, M., and Kurokawa, H. (1997). Serum concentrations of myoglobin vs human heart-type cytoplasmic fatty acid-binding protein in early detection of acute myocardial infarction. Clinical Chemistry. 43, 1372–1378.

[12] Nakata, T., Hashimoto, A., Hase, M., Tsuchihaski, K., and Shimamoto, K. (2003). Human heart-type fatty acid-binding protein as an early diagnostic and prognostic marker in acute coronary syndromes. Cardiology. 99, 96-104.

[13] Wang, Y., Yang, Y., Chen, C., Wang, S., Wang, H., Jing, W., and Tao, N. (2020). One-step digital immunoassay for rapid and sensitive detection of cardiac troponin I. ACS Sens. 5,1126–1131.

[14] Fung, E., Järvelin, M.R., Doshi, R.N., Shinbane, J.S., Carlson, S.K., Grazette, L.P., Chang, P. M., Sangha, R.S., Huikuri, H.V., and Peters, N.S. (2015). Electrocardiographic patch devices and contemporary wireless cardiac monitoring. Front Physiol. 6, 1-49.

[15] Ye, X.D., He, Y., Wang, S., Wong, G.T., Irwin, M.G., and Xia, Z. (2018). Heart-type fatty acid binding protein (H-FABP) as a biomarker for acute myocardial injury and long-term post-ischemic prognosis. Acta Pharmacol Sin. 39,1155–1163.

[16] Muehlschlegel, J.D., Perry, T.E., Liu, K.Y., Fox, A.A., Collard, C.D., and Shernan, S.K. (2010). Heart-type fatty acid binding protein is an independent predictor of death and ventricular dysfunction after coronary artery bypass graft surgery Anesthesia Analgesia. 111, PP. 1101-1109.

[17] Chowdhury, U.K., Malik, V., Yadav, R., Seth, S., Ramakrishnan, L., and Kalaivani, M. (2008). Myocardiyal injury in coronary artery bypass grafting: on-pump versus off-pump comparison by measuring high-sensitivity C-reactive protein, cardiac troponin I, heart-type fatty acid-binding protein, creatine kinase-MB, and myoglobin release. The Journal of Thoracic and Cardiovasculer Surgery. 135, PP. 1110-11-19.

JSR A
Journal of Scientific Reports

[18] Wodzig, K.W., Kragten, J.A., Modrzejewski, W., Gorski, J., and Van Dieijen-Visser, M.P. (1998). Thrombolytic therapy does not change the release ratios of enzymatic and non-enzymatic myocardial marker proteins. Clinica Chimica Acta. 272, 209-223.

[19] Mair, J. (1997). Cardiac troponin I and T: are enzymes still relevant as cardiac markers? Clinica Chimica Acta. 257, 99-115.

[20] Hermens, W.T., Pelsers, M.M.A.L., Mullers-Boumans, M.L., de Zwaan, C., and Glatz, J.F.C. (1998). Combined use of markers of muscle necrosis and fibrinogen conversion in the early differentiation of myocardial infarction and unstable angina. Clinical Chemistry. 44, 890-892.

[21] Davies, C.H., Harding, S.E., and Poole-Wilson, P.A. (1996). Cellular mechanisms of contractile dysfunction in human heart failure. European Heart Journal.17, 189-198.

[22] Olivetti, G., Abbi, R., Quaini, F., Kajstura, J., and Cheng, W. (1997). Apoptosis in the failing heart. The New England Journal of Medicine. 336, 1131-1141.

[23] Van Nieuwenhoven, F.A., Kleine, A.H., Wodzig, K.W.H., Hermens, W.T., and Kragten, J.A. (1995). Discrimination between myocardial and skeletal muscle injury by assessment of the plasma ratio of myoglobin over fatty acid-binding protein. Circulation. 92, 2548-2554.

[24] Dufour, D.R., Lott, J.A., Nolte, F.S., Gretch, D.R., and Koff, R.S. (2000). Diagnosis and monitoring of hepatic injury. I. Per-formance characteristics of laboratory tests. Clinical Chemistry. 46, 2027-2049.

[25] Trull, A.K. (2001). The clinical validation of novel strategies for monitoring transplant recipients. Clin Biochemistry. 34, 3-7.

[26] Platz, K.P., Mueller, A.R., Haller, G.W., Müller, C., and Wenig, M. (1997). Determination of α- and π-Gluthatione-S-transferase will improve monitoring after liver transplantation. Transplantation Proceeding 29, 2827-2829.

[27] Haastrup, B., Gill, S., Kristensen, SR., Jorgensen, P.J., and Glatz, J.F.C. (2002). Biochemical markers of ischemia for the early identification of acute myocardial infarction without ST segment elevation. Cardiology. 94, 254-261.

[28] Chan, C.P.Y., Sanderson, J.E., Glatz, J.F.C., Cheng, W.S., and Hempel, A. (2004). A superior early myocardiyal infarction marker-human heart-type fatty acid-binding protein. Zeitschrift fur Kardiologie. 93(5), 388-397.

[29] Newby, L.K., Goldmann, B.U., and Ohman, E.M. (2003). Troponin: an important prognostic marker and risk stratification tool in non-ST-segment elevation acute coronary syndromes. Journal of the American College of Cardiology. 41, 31-36.

JSR A
Journal of Scientific Reports

[30] Pelsers, M.M., Chapelle, J.P., Knapen, M., Vermeer, C., and Muijtjens, A.M.M. (1999). Influence of age, sex and day-to-day and within-day biological variation on plasma concentrations of fatty acid-binding protein and myoglobin in healthy subjects. Clinical Chemistry. 45, 441-443.

[31] Katrukha, A., Bereznikova, A., and Filatov, V. (1999). Improved detection of minor ischemic cardiac injury in patients with unstable angina by measurement of cTnI and fatty acid-binding protein (FABP). Clinical Chemistry. 45, A 139.

[32] Pelsers, M., Hanhoff, T., van der Voort, D., de Kruijk, J., and Twijnstra, A. (2003). Tissue specific types of fatty acid-binding proteins, B- and H-FABP, as novel markers for detection of brain injury. Clinical Chemistry and laboratory Medicine. 41, P7-98.

JSR A
Journal of Scientific Reports

APPENDIX

T.C.
VAN YÜZÜNCÜ YIL ÜNİVERSİTESİ
GİRİŞİMSEL OLMAYAN
KLİNİK ARAŞTIRMALAR ETİK KURULU
KARAR FORMU

	Prof. Dr. Nihat MERT sorumluluğunda yapılması tasarlanan ve yukarıda başvuru bilgileri verilen "Kronik Arter Hastalıklarında Kalp Tipi Yağ Asidi Bağlayıcı Protein (H-FABP) ve Bazı Biyokimyasal Parametrelerin Değişimi" isimli bilimsel araştırma başvuru dosyası ve ilgili belgeler araştırmanın gerekçe, amaç, yaklaşım ve yöntemleri dikkate alınarak incelenmiştir. Araştırmacıların Van Yüzüncü Yıl Üniversitesi Girişimsel Olmayan Klinik Araştırmalar Etik Kurulunun Çalışma Esasları Hakkında Yönergesinde belirtilen hususları yerine getirdikleri belirlenmiş olup, çalışmaları ile ilgili tüm sorumluluk araştırmacılara ait olmak üzere, söz konusu çalışmanın gerçekleştirilmesinde sakınca bulunmadığına, toplantıya katılan Etik Kurul üye tam sayısının salt çoğunluğu/oy birliği ile karar verilmiştir.
GİRİŞİMSEL OLMAYAN KLİNİK ARAŞTIRMALAR ETİK KURULU	
ETİK KURULUN ÇALIŞMA ESASI	Klinik Araştırmalar Hakkında Yönetmelik, İyi Klinik Uygulamaları Kılavuzu
BAŞKANIN UNVANI / ADI / SOYADI:	**Prof. Dr. Yasin TÜLÜCE**

Unvanı/Adı/Soyadı	Uzmanlık Alanı	Kurumu	Cinsiyet		Araştırma ile ilişki		Katılım *		İmza
Prof. Dr. Yasin TÜLÜCE	Tıbbi Biyoloji	Van Yüzüncü Yıl Üniversitesi Tıp Fakültesi	E☒	K☐	E☐	H☒	E☒	H☐	
Prof. Dr. Sıddık KESKİN	İstatistik Uzmanı	Van Yüzüncü Yıl Üniversitesi Tıp Fakültesi	E☒	K☐	E☐	H☒	E☒	H☐	
Prof. Dr. Özgür KEMİK	Genel Cerrahi	Van Yüzüncü Yıl Üniversitesi Tıp Fakültesi	E☒	K☐	E☐	H☒	E☐	H☒	
Doç. Dr. Serap GÜNEŞ BİLGİLİ	Dermatoloji	Van Yüzüncü Yıl Üniversitesi Tıp Fakültesi	E☐	K☒	E☐	H☒	E☒	H☐	
Doç. Dr. Mahmut SÜNNETÇİOĞLU	Klinik Bakteriyoloji ve Enfeksiyon	Van Yüzüncü Yıl Üniversitesi Tıp Fakültesi	E☒	K☐	E☐	H☒	E☐	H☒	
Dr. Öğr. Üyesi Mahammed BATUR	Göz Hastalıkları	Van Yüzüncü Yıl Üniversitesi Tıp Fakültesi	E☒	K☐	E☐	H☒	E☒	H☐	
Dr. Öğr. Üyesi Emine TÜRKMENOĞLU	Deontoloji	Van Yüzüncü Yıl Üniversitesi Veteriner Fakültesi	E☐	K☒	E☐	H☒	E☒	H☐	
Dr. Öğr. Üyesi Orxe ALLAHVERDİYEV	Tıbbi Farmakoloji	Van Yüzüncü Yıl Üniversitesi Eczacılık Fakültesi	E☒	K☐	E☐	H☒	E☒	H☐	
Dr. Öğr. Üyesi Zehra KAYA	Tıbbi Biyoloji	Van Yüzüncü Yıl Üniversitesi Tıp Fakültesi	E☐	K☒	E☐	H☒	E☐	H☒	
Dr. Öğr. Üyesi Sermin ALGÜL	Fizyoloji	Van Yüzüncü Yıl Üniversitesi Tıp Fakültesi	E☐	K☒	E☐	H☒	E☒	H☐	
Dr. Öğr. Üyesi Özgür GENÇ ŞEN	Endodonti	Van Yüzüncü Yıl Üniversitesi Diş Hekimliği Fakültesi	E☐	K☒	E☐	H☒	E☒	H☐	
Nazlı AKTAŞ	Avukat	Van Yüzüncü Yıl Üniversitesi Hukuk Müşavirliği	E☐	K☒	E☐	H☒	E☒	H☐	
Lütfu POLAT	Eczacı	Van Polat ECZANESİ	E☒	K☐	E☐	H☒	E☒	H☐	
Özge Burak DEĞER	Sağlık Meslegi Mensubu Olmayan Üye	Van Sanayiciler ve İş Kadınları Derneği	E☐	K☒	E☐	H☒	E☒	H☐	
Adnan SELÇUK	Sağlık Meslegi Mensubu Olmayan Üye	Van İş Geliştirme Merkezi	E☒	K☐	E☐	H☒	E☐	H☒	

Sayfa 2

Adres : Van Yüzüncü Yıl Üniversitesi Rektörlük Binası Merkez Kampüsü Van
Tel : 432- 2251701-05
Faks : 432-2251091
e-posta: etikkur@yyu.edu.tr

Kütahya Dumlupınar University
Institute of Graduate Studies

Journal of Scientific
Reports-A
E-ISSN: 2687-6167
Number 53, June 2023

RESEARCH ARTICLE

TRANSPORTATION OF *SPOROSARCINA PASTEURII* IN POROUS MEDIA WITH DIFFERENT PARTICLE SIZES

Kağan ERYÜRÜK*

[1]Necmettin Erbakan University, Faculty of Engineering, Department of Civil Engineering, Konya, TÜRKİYE,
keryuruk@erbakan.edu.tr, ORCID: 0000-0003-3993-839X

Receive Date:17.01.2023 *Accepted Date: 26.05.2023*

ABSTRACT

The current study aimed to determine the transportation distance of *Sporosarcina pasteurii* (ATCC 11859) and the number of cells present in porous media. The experiments were carried out in continuous-flow columns, which were plastic columns with an inner diameter of 2.4 cm and a height of 50 cm, and which contained glass beads with average diameters of 0.25 mm, 0.50 mm and 1 mm to mimic porous media. To investigate cell transport through columns, suspension of *Sporosarcina pasteurii* was introduced into columns at a flow rate of 2 mL/min and the cell densities of OD_{600} 0.15, 0.75, 2.25. To count the bacteria in each section, the column was divided into five equal parts. The results showed that the most cells, which were counted as $1.72*10^{10}$ cells, were deposited in the columns packed with 0.25 mm glass beads for the experiments with OD_{600} 2.25, while the deposited cell number decreased at the bottom of the column. The cell deposition was greater at the bottom of the column in the case of columns packed with 1 mm glass beads. According to the findings, while using smaller glass beads resulted in more cell deposition in the porous media, using larger glass beads resulted in more cell transport through the porous media. It can be concluded that larger particle sizes may result in easier transportation conditions for cells transporting deep into porous media.

Keywords: *Cells, column, glass beads, porous media, Sporosarcina pasteurii.*

1. INTRODUCTION

Nowadays, transportation of bacterial cells gains importance due to the importance of developing environmentally friendly technologies, which can be listed in biotechnology methods including bioaugmentation and biotreatment, for many fields. Bacterial precipitation, which is related for producing insoluble organic and inorganic compounds using bacteria, is one of the environmentally friendly technology [1-2]. Bacterial precipitation has been used by many researchers to improve the soil properties [3-5], seal cracks [6], reduce hydraulic conductivity of porous media [7-8]. *Sporosarcina pasteurii* was used by many researchers for bacterial precipitation [9-12] because *Sporosarcina pasteurii* is a nonpathogenic bacterium with high urea activity [7]. The process of

JSR A
Journal of Scientific Reports

bacterial precipitation carried out by *Sporosarcina pasteurii* relies on the metabolic activity of the bacteria. *Sporosarcina pasteurii* utilizes urease to break down urea into ammonia and carbon dioxide, leading to an increase in pH levels. This rise in pH triggers the precipitation of calcite in the presence of calcium ions [13]. In the most studies, the researchers used urea hydrolysis in a solution containing calcium chloride to introduce Ca^{2+} ions [14-15].

Various factors, including pH, temperature, nutrient presence, nutrient concentration, precipitation reagent concentration, and oxygen availability, influence the effectiveness of the bacterial precipitation process [16-17]. Another of these influencing factors is cell density, which correlates with the urease enzyme [9]. According to Eryürük, the amount of bacterial precipitation can be expressed as a function of the bacterial biomass deposited in the column [18]. Therefore, it is critical to understand the transportation distance of cells through the column to achieve bacterial precipitation. Glass beads of varying diameters were used to pack the columns in the current study, and the transportation distance was evaluated by introducing *Sporosarcina pasteurii* cell suspensions of varying densities.

2. MATERIAL and METHOD

2.1. Preparation of cell culture and measurement of OD

In this study, the transportation of cells was examined using *Sporosarcina pasteurii* (ATCC 11859) as the experimental bacterium. To create the culture medium (Tris-YE), a combination of Tris buffer (130 mM, pH 9.0), ammonium sulfate (10 g/L), and yeast extract (20 g/L) was utilized. To obtain a solid medium for stock culture, a mixture of 2% agar was added to 1000 milliliters of liquid medium. Prior to being mixed together, all of the components were subjected to separate autoclaving at a temperature of 121 °C for a duration of 15 minutes [7]. *Sporosarcina pasteurii* cells were acquired by introducing cells into Tris-YE medium and allowing them to incubate overnight at a temperature of 30 °C. The incubation process involved continuous shaking at a rate of 120 rpm. The collected cells were separated by centrifugation at 10,000 times the force of gravity (10,000 * g) for a duration of 10 minutes [7]. Afterward, the cells were washed twice with distilled water [7]. Finally, 200 mL of distilled water was used to obtain the cell suspension with the optical densities (OD) at 600 nm for 0.15, 0.75, and 2.25 (abbreviated as OD_{600} 0.15, 0.75, and 2.25) [7]. To measure the optical density (OD) values, a Hitachi U-1900 Spectrophotometer from Tokyo, Japan, was employed [7].

2.2. Experimental Setup and Conditions

The columns in the experiments were made of a plastic pipe with an inner diameter of 2.4 cm and a height of 50 cm (Figure 1).

JSR A
Journal of Scientific Reports

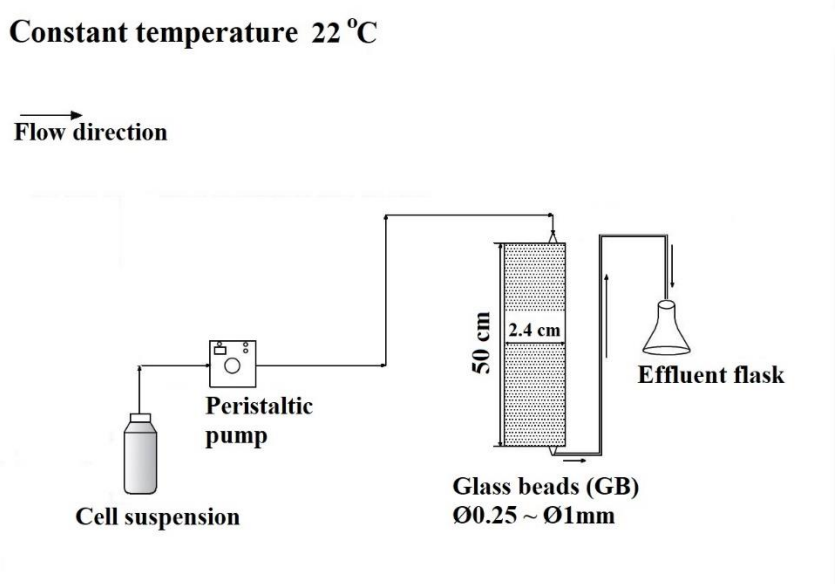

Figure 1. Experimental Setup.

In the experiments, glass beads of varying average diameters (0.25 mm, 0.50 mm, and 1.0 mm) were utilized as the porous media. Prior to each experiment, the glass beads were subjected to a cleansing process in which they were first washed with an acidic solution of 0.1 N HCl. Following that, the cells were subjected to multiple rinses with deionized water until pH was attained as 7.0. Saturated conditions were ensured for each experiment. A consistent temperature of 22 °C was maintained throughout all experiments, and the influent rate in the downward direction was regulated using a peristaltic pump. A suspension of *Sporosarcina pasteurii* cells, equivalent to four pore volumes of glass beads placed in columns, was introduced into the column at a flow rate of 2 mL/min. To ensure a uniform cell suspension during the introduction process, a magnetic stirrer was employed. Figure 2 indicates that the measured optical densities for 2.25, 0.75, and 0.15 at 600 nm were reflective of the following cell concentrations: $2.15 * 10^9$ cells/mL, $8.10 * 10^8$ cells/mL, and $5.89 * 10^8$ cells/mL, respectively.

JSR A
Journal of Scientific Reports

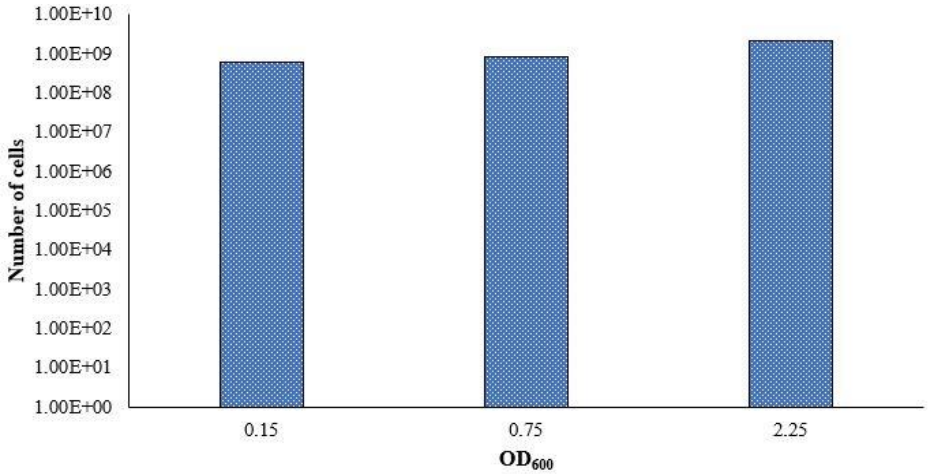

Figure 2. Number of cells for OD_{600} 0.15, 0.75, and 2.25.

The conditions for all the experiments were summarized in Table 1.

Table 1. Conditions for the experiments.

Glass beads size (mm)	OD_{600}
0.25	0.15
0.50	0.75
1	2.25

The column was divided into five equal parts. To determine the number of cells in each part, the glass beads from the corresponding part were transferred to a beaker and distilled water was added to the beaker. The quantity of cells deposited in the respective section was determined by sampling from the beaker. To quantify the cell population, a microscope model Olympus BX50WI from Tokyo, Japan, was employed.

3. RESULTS and DISCUSSION

This study was carried out to investigate the transportation of cells through porous media. As shown in Figure 3, in the columns consisting of small glass beads, cell accumulation was more in the upper parts of the column ($1.72*10^{10}$ cells in the columns filled with glass beads measuring 0.25 mm in diameter and introduction of OD_{600} 2.25 for 0-10 cm) comparing to lower parts ($5.50*10^{9}$ cells in the columns filled with glass beads measuring 0.25 mm in diameter and introduction of OD_{600} 2.25 for 0-10 cm 40-50 cm , while the cell accumulation increased in the lower parts of the column as the glass bead size increased ($2.05*10^{9}$ cells in the columns packed with 1 mm and introduction of OD_{600} 2.25 for 40-50 cm) comparing to upper parts ($7.00*10^{8}$ cells in the columns packed with 1 mm and introduction of OD_{600} 2.25 for 0-10 cm) . The accumulation of cells in the lower sections of the columns, which were packed with larger-sized glass beads, can be attributed to the enlargement of

JSR A
Journal of Scientific Reports

pore size in those beads. The smaller glass beads have smaller pore size which led more cell deposition in the columns packed with smaller glass beads size. The quantity of accumulated cells was additionally influenced by the cell densities of the introduced cell suspensions. Lower densities of the cell suspension led to a reduced number of cells accumulating in the column.

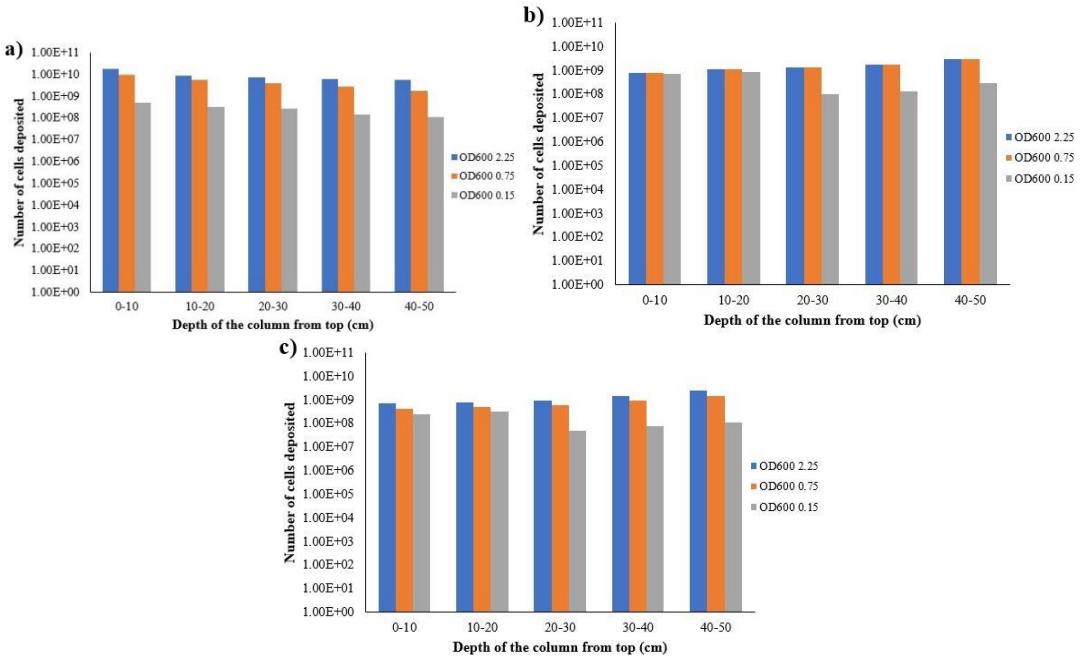

Figure 3. The total quantity of cells deposited in the packed columns with a) 0.25 mm GB b) 0.50 mm GB c)1 mm GB introducing cells suspensions with OD_{600} 0.15, 0.75, 2.25.

Figure 4 indicates that the total number of cells deposited in the columns. While the most cells accumulated in the column packed with 0.25 mm glass beads, the least cells accumulated in the column packed with 1 mm. This could be explained by the small pore size of porous media. In the column consisting of 0.25 mm glass beads, the cells deposited more because the pore size was smaller. Since the pore size was larger in the column consisting of 1 mm glass beads, the cells could not adhere to the glass beads and flowed away.

JSR A
Journal of Scientific Reports

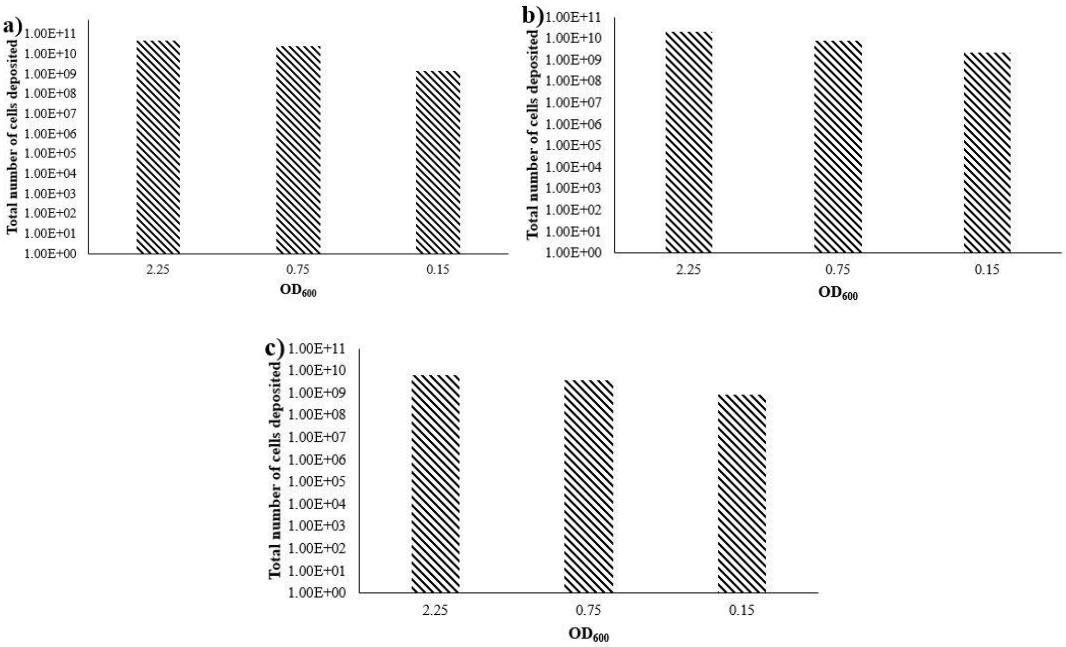

Figure 4. The number of total cells deposited in the columns packed with a) 0.25 mm GB b) 0.50 mm GB c)1 mm GB.

It can be said that the suggested method would be used in bioremediation methods by creating an impermeable layer by transporting bacteria to the deeper parts of the ground.

4. CONCLUSION

In this study, transportation of cells, which is crucial for environmentally friendly biotechnology methods, was investigated. It can be seen from the obtained results that the transportation of cells was effective when the porous media have larger size of particles. However, the total number of cells deposited indicated that more cell accumulation was achieved with smaller particle sizes. The smaller average pore size and correspondingly the pore volume could be reasoning more cell deposition in smaller glass beads. There was more accumulation in the upper parts of the columns containing small glass beads indicated that the biotechnology method to be developed will be effective at the surface level. On the contrary, there was more accumulation in the lower parts of the columns containing large glass beads indicated that the biotechnology method to be developed will also be effective at the lower levels.

This study indicated that density of cell introduced and the particle size of porous media would be crucial factors for improving biotechnology methods. This study can serve as an important motivation for future academic studies on bacterial transportation especially the transportation of *Sporosarcina*

pasteurii, a commonly utilized bacterium among researchers, has contributed to the advancement of biotechnology methods.

ACKNOWLEDGEMENT

This research received no financial supports from any funding agency in public, commercial or nonprofit sectors.

REFERENCES

[1] Stocks-Fischer, S., Galinat, J. K., and Bang, S. S., (1999), Microbial precipitation of $CaCO_3$, Soil Biology and Biochemistry, 31, 1563–1571.

[2] Chou, C.-W., Seagren, E. A., Aydilek, A. H., and Lai, M., (2011), Biocalcification of sand through ureolysis, Journal of Geotechnical and Geoenvironmental Engineering, 137, 1179–1189.

[3] Eryürük, K., Suzuki, D., Mizuno, S., Akatsuka, T., Tsuchiya, T., Yang, S., Kitano, H., and Katayama, A., (2016), Decrease in Hydraulic Conductivity of a Paddy Field using Biocalcification *in situ*, Geomicrobiology Journal, 33 (8), 690–698.

[4] Arpajirakul, S., Pungrasmi, W., and Likitlersuang, S., (2021), Efficiency of microbially-induced calcite precipitation in natural clays for ground improvement. Construction and Building Materials, 282, 122722.

[5] Gao, X., Han, S., Yang, Y., Zhang, W., Zou, T., and Cheng, L., (2022), Mechanical Behavior and Microstructural Study of Biocemented Sand under Various Treatment Methods, Geofluids, 6015335.

[6] Chen, B., Sun, W., Sun, X., Cui, C., Lai, J., Wang, Y., and Feng, J., (2021), Crack sealing evaluation of self-healing mortar with *Sporosarcina pasteurii*: Influence of bacterial concentration and air-entraining agent, Process Biochemistry, 107, 100–111.

[7] Eryürük, K., Yang, S., Suzuki, D., Sakaguchi, I., Akatsuka, T., Tsuchiya, T., and Katayama, A., (2015), Reducing hydraulic conductivity of porous media using $CaCO_3$ precipitation induced by *Sporosarcina pasteurii*, Journal of Bioscience and Bioengineering, 119(3), 331–336.

[8] Eryürük, K., Yang, S., Suzuki, D., Sakaguchi, I., and Katayama, A., (2015), Effects of bentonite and yeast extract as nutrient on decrease in hydraulic conductivity of porous media due to $CaCO_3$ precipitation induced by *Sporosarcina pasteurii*, Journal of Bioscience and Bioengineering, 120(4), 411–418.

[9] Al Imran, M., Shinmura, M., Nakashima, K., and Kawasaki, S., (2018), Effects of Various Factors on Carbonate Particle Growth Using Ureolytic Bacteria, Materials Transactions, 59(9), 1520–1527.

[10] Seifan, M., and Berenjian, A., (2019), Microbially induced calcium carbonate precipitation: a widespread phenomenon in the biological world, Applied Microbiology and Biotechnology, 103, 4693–4708.

[11] Ghosh, T., Bhaduri, S., Montemagno, C., and Kumar, A., (2019), *Sporosarcina pasteurii* can form nanoscale calcium carbonate crystals on cell surface, PLoS ONE, 14(1): e0210339.

[12] Jain, S., and Arnepalli, D. N., (2019), Biochemically Induced Carbonate Precipitation in Aerobic and Anaerobic Environments by *Sporosarcina pasteurii*, Geomicrobiology Journal, 36(5), 443–451.

[13] Wu, J., Wang, X. B., Wang, H. F., Zeng, R. J., (2017) Microbially induced calcium carbonate precipitation driven by ureolysis to enhance oil recovery. RSC Advances, 7(59), 37382–37391.

[14] Hammes, F., and Verstraete, W., (2002), Key roles of pH and calcium metabolism in microbial carbonate precipitation, Reviews in Environmental Science and Bio/Technology, 1, 3–7.

[15] Hsu, C. M., Yi-Hsun, H., Vanita, R., Wen-Chien, L., How-Ji, C., Yi-Hao, K., Chung-Ho, H., Chien-Cheng, C., and Chien-Yen, C., (2018), Comparative Study on the Sand Bioconsolidation through Calcium Carbonate Precipitation by *Sporosarcina pasteurii* and *Bacillus subtilis*, Crystals, 8 (5): 189.

[16] Saricicek, Y. E., Gurbanov, R., Pekcan, O., and Gozen, A. G., (2019), Comparison of microbially induced calcium carbonate precipitation eligibility using *sporosarcina pasteurii* and *bacillus licheniformis* on two different sands, Geomicrobiology Journal, 36(1), 42–52.

[17] Li, M., Wen, K., Li, Y., and Zhu, L., (2018), Impact of Oxygen Availability on Microbially Induced Calcite Precipitation (MICP) Treatment, Geomicrobiology Journal, 35(1), 15–22.

[18] Eryürük, K., (2022), Effect of cell density on decrease in hydraulic conductivity by microbial calcite precipitation, AMB Express, 12, 104.

Kütahya Dumlupınar University
Institute of Graduate Studies

Journal of Scientific
Reports-A
E-ISSN: 2687-6167
Number 53, June 2023

RESEARCH ARTICLE

ESTIMATION OF EDSS FROM EEG SIGNALS OF MULTIPLE SCLEROSIS PATIENTS

Seda ŞAŞMAZ KARACAN[1,*], Hamdi Melih SARAOĞLU[2], Sibel CANBAZ KABAY[3]

[1] Kütahya Dumlupınar University, Engineering Faculty, Electrical and Electronics Engineering Department, Kütahya
sd.sasmaz@gmail.com, ORCID: 0000-0002-0334-260X
[2] Kütahya Dumlupınar University, Engineering Faculty, Electrical and Electronics Engineering Department, Kütahya,
hmelih.saraoglu@dpu.edu.tr, ORCID: 0000-0002-5075-9504
[3] Kütahya Health Sciences University, Medicine Faculty, Department of Neurology, Kütahya,
scanbazkabay@yahoo.com, ORCID: 0000-0003-4808-2191

Receive Date:19.02.2023 *Accepted Date: 08.05.2023*

ABSTRACT

Multiple sclerosis (MS) is an autoimmune, neurodegenerative, chronic disease that affects the central nervous system and manifests itself with attacks. Although there is no definite cure for the disease, it is possible to control these attacks. Follow-up of the disease has great importance in terms of disability. An Extended Disability Status Scale (EDSS) is used to show how much the disease affects. This score is determined by specialized clinicians. In this study, the EDSS score, previously determined by neurologists, was attempted to be estimated using the EEG signals. 32-channel EEG signals were recorded while 17 MS patients with EDSS 1.0, 1.5, and 2.0 were performing a working memory task. Using the band power of these 6-minute EEG signals, EDSS estimation was performed with the Decision Tree Regressor, resulting in a Mean Absolute Error (MAE) of 0.088. With the Leave One Out Cross-Validation, 17 trees were extracted and 12 were found to be identical. As a result, the band power features of F7 and CP2 EEG channels were found to be successful in predicting 3-level EDSS scores with a decision tree regressor with 0.0 MAE. Additionally, the relationship between the scores obtained in the working memory task and the EDSS scores of MS patients was statistically calculated with One-way ANOVA. There was no significant difference between the EDSS score and the task scores ($p>.05$).

Keywords: *Multiple sclerosis (MS), EEG, EDSS, Working Memory, Decision Tree Regressor.*

1. INTRODUCTION

Multiple sclerosis (MS) is a chronic, autoimmune disease of the central nervous system that affects the brain, cerebellum, brain stem, and spinal cord. The immune system attacks the myelin sheath that surrounds the nerve cells, causing damage. Plaques called sclerosis form in damaged tissues. Depending on the involvement of these plaques, various symptoms are observed in patients [1]. The main symptoms are cognitive problems, fatigue, muscle weakness, vision problems, lack of

JSR A
Journal of Scientific Reports

coordination, tingling and numbness, bowel, bladder and sexual problems, mood swings, dizziness, and double vision. The disease is commonly detected using magnetic resonance images (MRI), evoked potentials (EP), and electroencephalography (EEG) signals. Although there is no cure for the disease, the attacks can be brought under control, and the damage caused by the disease can be minimized or reduced to zero. Approximately 2.5 million individuals worldwide are afflicted with MS [2]. Early diagnosis of the disease, monitoring, and controlling its progression are great importance. The disease course of multiple sclerosis (MS) can be classified into five types: Benign MS, Relapsing-Remitting MS (RRMS), Primary Progressive MS (PPMS), Secondary Progressive MS (SPMS), and Progressive Relapsing MS (PRMS) [3]. About 85% of MS patients have the RRMS type. The Extended Disability Status Scale (EDSS), presented by Kurtzke, is used as an indicator of the impact of MS patients [4]. Despite its flaws, it is the most widely used scale in the clinic due to its ease of application. It combines disability and impairment, has moderate inter-rater reliability, and primarily focuses on ambulation-related disability [5]. It is used to monitor the level of disability rather than measuring treatment effects [6]. Additionally, the EDSS scale remains valid [7]–[9], although other scales besides the EDSS [10], [11] are also available in the literature. The EDSS, determined by a detailed neurological examination, corresponds to a value between 0 and 10. Disability status according to the EDSS scores [12], [13] is given in Table 1.

Table 1. Disability status according to the EDSS scores.

EDSS Score	Description
0 - 3.5	No obvious disability.
4.0 - 5.5	Patients have difficulty walking and climbing stairs. They need assistance at distances longer than 100 meters.
6.0 - 6.5	Patients need assistance while walking.
7.0 - 7.5	Wheelchair-dependent.
8.0 - 8.5	The bedridden state.
9.0 - 9.5	Completely immobile with no ability to communicate or safely consume food orally.
10.0	MS-caused death.

Upon reviewing the existing literature, it is evident that no studies have estimated the EDSS score using EEG signals. However, Alexandra et al. [14] demonstrated that cognitive reserve has a significant impact on the association between EDSS score and specific cognitive domains such as processing efficiency, visuospatial learning and memory, and verbal memory disposition. Interestingly, no negative correlation was observed between these cognitive domains and EDSS scores in MS patients with high cognitive reserve.

Kaufmann et al. [15] estimated EDSS based on patient feedback. Based on three questions about patients' mobility, they developed a three-category (EDSS≤3.5, EDSS=4–6.5, EDSS≥7) self-reported disability status scale. With self-reported disability status results, they achieved an accuracy rate of 88.4% in estimating the EDDS determined by clinicians.

Zurawski et al. [16] studied the relationship between time and EDSS. They showed that the time interval between specific EDSS levels showed significant variation. They emphasized that certain functional system scores demonstrated higher predictive ability for future EDDS-related disability, even among patients with the same current EDDS level.

Xiaodong et al. [17] investigated the relationship between Cervical Spinal Cord Atrophy (CSCA) and EDSS scores by synthesizing existing data from MRI images in their review. They analyzed 22 eligible studies involving 1933 participants and showed that the correlation between CSCA and EDSS scores was significant but moderate.

Cao et al. [18] estimated EDSS from posturographic data. The study included 118 volunteers with a range of EDSS scores from 0 to 4.5, who performed the test with their eyes closed. They used second-order polynomial regression models to estimate EDSS based on two postural sway parameters (length and surface) and four recurrence quantification analysis parameters (%Rec, Shannon entropy, mean diagonal line length (LL), and trapping time). To identify the most accurate method for estimating EDSS, they compared the clinical and estimated EDSS scores and demonstrated that the estimates based on surface, %Rec, and LL parameters were correlated with the clinical scores.

In another study by Cao et al. [19], a novel method was presented that utilized decision tree analysis for evaluating the EDSS score using posturographic data. Multiple decision trees were constructed using the training data and evaluated using the test data. A decision tree was presented demonstrating 75% agreement between the clinical and estimated EDSS scores in the test group. The results indicated that the decision tree model effectively automated the evaluation of EDSS scores, and both linear and nonlinear postural sway measures were capable in distinguishing between different EDSS scores.

In a study by Alves et al. [20], the EDSS was estimated using notes and EDSS scores recorded by clinicians in the "OM1 MS Registry data" through the use of machine learning algorithms. The performance of the model was evaluated using metrics such as the area under the curve (AUC), positive predictive value (PPV), and negative predictive value (NPV). The proposed model achieved a PPV of 0.85, an NPV of 0.85, and an AUC of 0.91.

Salim et al. [21] investigated evidence of gray matter brain lesions in patients with MS by evaluating the alpha rhythm of brain electrical activity at rest using EEG recordings. The study included 50 patients diagnosed with MS and 50 control participants. The researchers examined posterior dominant rhythm (PDR) parameters, including wave frequency and amplitude, in the EEG recordings. Functional disability among MS patients was evaluated using the EDSS. One-way analysis of variance and t-test were used to determine the statistical significance. The study found significantly lower PDR frequency and amplitude values in MS patients compared to the control group ($p< .01$), with 34% of MS patients exhibiting PDR frequency lower than 8.5 Hz. Moreover, a negative correlation was found between PDR frequency and the level of functional disability in MS patients ($p<.001$). The study showed that monitoring of the PDR spectrum with EEG could be used as an alternative or complementary tool to other imaging techniques for detecting and monitoring cerebral cortical lesions in MS patients.

JSR A
Journal of Scientific Reports

Gschwind et al. [22] investigated whether the millisecond time range in topographic EEG analysis was altered in patients with RRMS, and whether the temporal characteristics of the millisecond time range reflected a link to the clinical characteristics of the patients. The study included 53 patients with RRMS (EDSS $\leq$ 4, mean 2.2) and 49 healthy controls, and 256-channel EEG signals were used for analysis. The researchers analyzed 5-minute EEG segments at rest and identified four dominant millisecond time ranges for both groups using established clustering methods. Significant differences were found in the temporal dynamics of the EEG signals between RRMS patients and healthy controls. Using stepwise multiple linear regression models with 8-fold cross-validation, they obtained evidence that these electrophysiological measures predict a patient's total disease duration, annual relapse rate, disability score, as well as depression score, and cognitive fatigue measure.

Vázquez-Marrufo et al. [23] conducted a study examining the relationship between EEG signal characteristics and EDSS in MS patients and a healthy control group. They performed correlation analysis using behavioral, neuropsychological test scores, EDSS scores, event-related potentials (ERP), and event-related desynchronization (ERD) parameters, as well as correlation scores between individual participants' P3/ERD maps and the overall average P3/ERD maps. They found that the strongest correlation was between EDSS and reaction time, ERD, and ERP.

Considering the existing literature, it is noted that there is a gap in research on EDSS estimation using EEG signals recorded during cognitive tasks. Therefore, the aim of this study was to contribute to the literature by investigating the estimated EDSS score obtained from EEG signals of MS patients while they performed a working memory task. EDSS was attempted to be estimated using the Decision Tree Regressor based on EEG signals obtained during the working memory task of 17 MS patients with EDSS scores of 1.0, 1.5, and 2.0.

A generalized tree model, which included only 2 features of the EEG signal, was presented for estimating EDSS using the Decision Tree Regressor method. The band power features of the F7 and CP2 EEG channels were identified to be effective in predicting 3-level EDSS scores using a generalized decision tree model, achieving MAE of 0.0. In addition to EDSS estimation, the statistical relationship between the scores obtained in the working memory task and the EDSS scores of MS patients was calculated using One-way ANOVA. The p-value for the comparison between the EDSS score and the task scores was greater than 0.05, indicating that there was no significant difference between the two.

The study flow diagram is given in Figure 1.

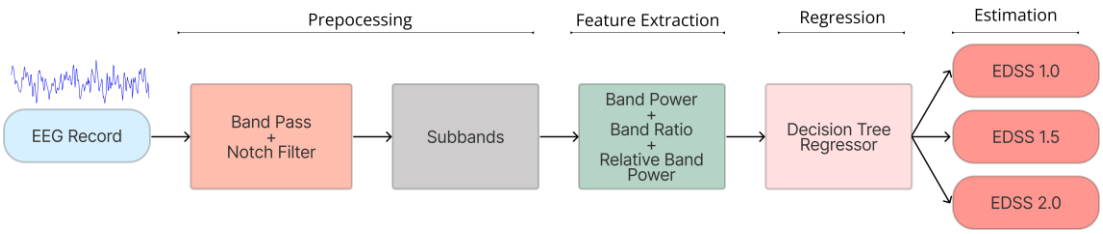

Figure 1. Study flow diagram.

JSR A
Journal of Scientific Reports

In the second part of the study, titled "Material and Method", participants, experimental procedure, signal preprocessing, feature extraction, Decision Tree Regressor, and the proposed method are provided. In the third part, the obtained regression and statistical results are presented. The fourth section discusses the results in comparison with other relevant studies. Finally, the conclusion of the study is presented in the final section.

2. MATERIAL and METHOD

2.1. Participants

In this study, EEG signals from 17 patients diagnosed with RRMS and having EDSS score of 2.0 or lower (EDSS=1.0, EDSS=1.5, EDSS=2.0) were used. Healthy individuals were excluded from the study because a detailed examination is required to determine the EDSS score in healthy individuals. The characteristics of MS patients included in the study are as follows:

- No attacks in the last 6 months
- Not taking cortisone treatment
- No comorbid diseases

The distribution of MS patients is given in Table 2.

Table 2. The distribution of MS patients.

Feature	Distribution
Count (Female/Male)	17 (11/6)
EDSS (Score+SD)	1.4± 0.38
Age (Mean+SD)	31.11±8.27

2.2 .Experimental Procedure

Study permission was obtained from the Clinical Research Ethics Committee of Kütahya Health Sciences University (18.06.2021-2021/03). In the continuation of our previous study [24], the number of MS patients was increased, and EEG signals were recorded during different cognitive tasks. The experiments were conducted at Kütahya Dumlupınar University Neurotechnology Education, Application and Research Center. MS patients performed a cognitive task for working memory on the computer for 6 minutes [25]. This task is a Visual Pattern Test [26] based task for short-term visual memory and visual attention. The patients were shown a square matrix with a pattern and asked to keep it in their memory and to draw the pattern again with the help of the mouse when the matrix disappeared. As the correct moves were made, the square matrix increased in size, and the level became more difficult. The level decreased with the number of wrong moves. Each participant received a score after the task.

2.3. Data Acquisition and Preprocessing

EEG signals of the volunteers were recorded for 6 minutes with a 32-channel active electrode Brain Products ActiChamp EEG device during the memory task. The sampling frequency was 500 Hz. Electrode placements were made according to the international 10-20 system, and electrode impedances were kept below 10 kohm. The Cz electrode was chosen as the reference.

JSR A
Journal of Scientific Reports

As a part of signal preprocessing, a bandpass filter with a frequency range of 0.1-50 Hz was used to eliminate any undesired noise or signal outside of this frequency range. Furthermore, a notch filter with a frequency of 50 Hz was employed to eradicate any electrical interference at this specific frequency. The EEG signal, which was acquired for a duration of 6 minutes, underwent the filtering procedure before subsequent analyses were performed. The filtering process was performed using the MNE library. A 50-second segment of the filtered EEG signal recorded from the participants during the task, according to their EDSS scores, is presented in Figure 2.

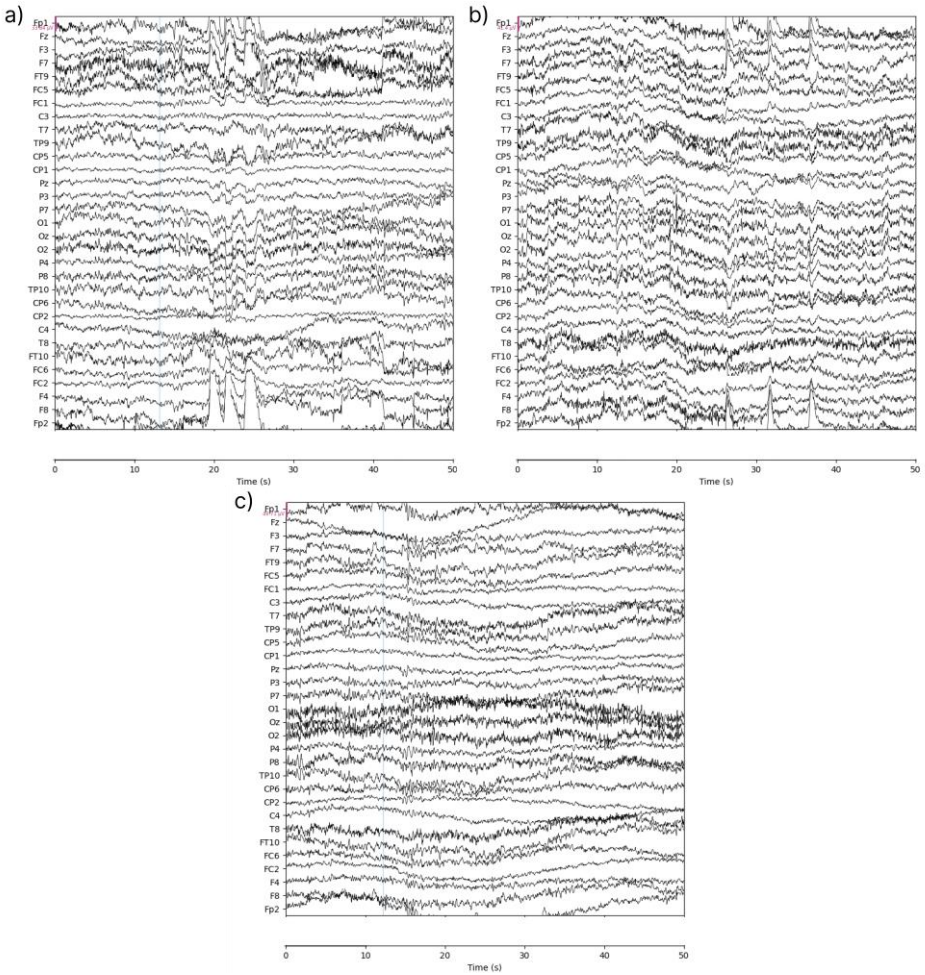

Figure 2. A 50-second segment obtained from volunteers during the task. a) EDSS=1.0. b) EDSS=1.5. c) EDSS=2.0.

JSR A
Journal of Scientific Reports

2.4. Feature Extraction

The filtered 32-channel EEG signals were divided into subbands using the Welch method. These subbands were delta (δ: 0.5-4 Hz), theta (θ: 4-8 Hz), alpha (α: 8-16 Hz), beta (β: 16-31 Hz), and gamma (γ: 31-50 Hz).

Power Spectral Density (PSD), band ratios, and relative band powers were extracted as features. The features were obtained using the MNE library in Python [27].

2.4.1. Power spectral density

During the feature extraction, the power spectral density of the subbands of the EEG signal was calculated using the Fourier Transform-based Welch method.

The EEG signal was divided into windows with power of 2, and the improved periodogram was calculated for these windows. In the Welch method, which is the improved version of the periodogram method, the windows can overlap while the EEG signal is windowed. Eq. 1 shows the data segments.

$$x_i(n) = x(n + iD);\ i = 0, 1, \dots, L-1;\ n = 0, 1, \dots, M-1 \tag{1}$$

An improved periodogram is calculated for these windows, and then the average of these sections is obtained [28].

i. improved periodogram is given in Eq. 2. *f*, *K*, and *w(n)* demonstrate a normalized frequency, normalization factor, and windowing function, respectively.

$$\hat{P}_{xx}^{(i)}(f) = \frac{1}{K.M}\left|\sum_{n=0}^{M\hat{}1} x_i(n)w(n)e^{-j2\pi fn}\right|^2,\ i=0,1,\dots,\ L-1 \tag{2}$$

In Eq. 3, the normalization factor is given.

$$K = \frac{1}{M}\sum_{n=0}^{M-1}(w^2(\mathrm{n})) \tag{3}$$

Eq. 4 shows the power spectrum density.

$$PSD = \hat{P}_{xx}^{w}(f) = \frac{1}{L}\left|\sum_{i=0}^{L-1}\hat{P}_{xx}(f)\right| \tag{4}$$

2.4.2. Band ratios

The band ratios of the EEG signal divided into subbands were calculated and used as a feature in this study. The band ratios used are as follows: α/β, α/γ, α/δ, α/θ, β/γ, β/θ, β/δ, θ/γ, θ/δ, δ/γ.

2.4.3. Relative band powers

After calculating the total PSD of the EEG signal, the relative band powers were calculated using the formulas given in Eq. 5, Eq. 6, Eq. 7, Eq. 8, Eq. 9, and Eq. 10. These relative band powers were used as features in the study.

$$\sum PSD = PSD(\alpha\ +\ \beta\ +\theta\ +\ \delta\ +\gamma\ ) \tag{5}$$

JSR A
Journal of Scientific Reports

$$Relative\ \alpha = \frac{\alpha}{\Sigma PSD} \quad (6)$$

$$Relative\ \beta = \frac{\beta}{\Sigma PSD} \quad (7)$$

$$Relative\ \theta = \frac{\theta}{\Sigma PSD} \quad (8)$$

$$Relative\ \delta = \frac{\delta}{\Sigma PSD} \quad (9)$$

$$Relative\ \gamma = \frac{\gamma}{\Sigma PSD} \quad (10)$$

2.5. Decision Tree Regression

In the study, a Decision Tree Regressor from the Python Scikit-Learn library [29] was used for regression analysis. Unlike the classification, the aim of regression is to predict continuous numerical values. Independent variables were ranked based on the information gain values, and a comparison is made with this ranking during the testing step. Mean Squared Error (MSE) was used as the measurement for feature selection.

2.6. Proposed Method

In the study, EEG signals were recorded during the working memory task. The recorded EEG signals were filtered using a bandpass filter of 0.1-50 Hz and notch filter of 50 Hz. Subsequently, the EEG signals were separated into sub-bands (alpha, beta, gamma, delta, and theta) using the Welch method on the MNE library in the Python programming language [27]. Spectral features (band powers, power ratios, and relative powers) were extracted from each subband. Using these features, a total of 17 decision trees were trained using a Decision Tree Regressor with Leave One Out Cross Validation (LOOCV). It was observed that 12 out of these 17 trees were identical to each other, and any of these 12 trees could be proposed as a generalized tree. The block diagram of the proposed method is shown in Figure 3.

JSR A
Journal of Scientific Reports

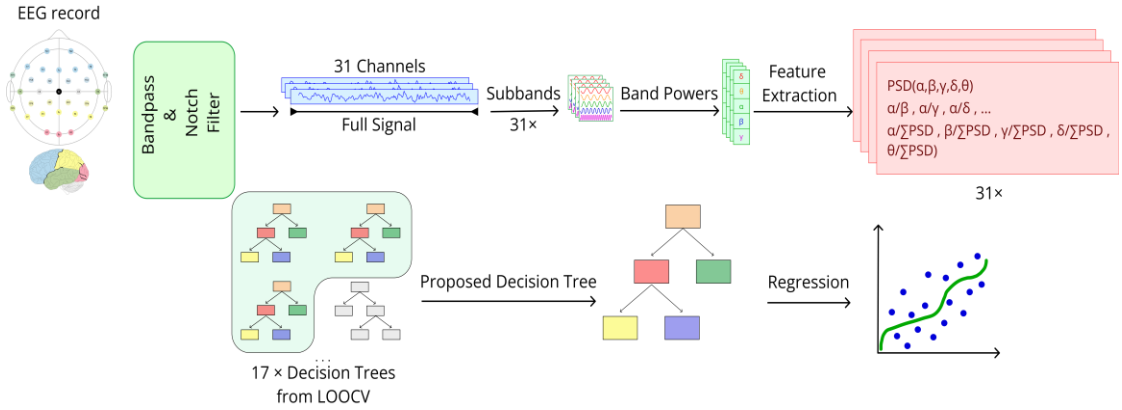

Figure 3. The proposed method block diagram.

2.7. Performance Evaluation Metrics

2.7.1. Mean absolute error

The Mean Absolute Error (MAE) given in Eq. 11 represents the mean of the absolute values of the differences between the real data and the predicted data [30].

$$MAE = \frac{1}{N}\sum_{i=1}^{N}\left|x_i^{real} - x_i^{predicted}\right| \tag{11}$$

2.7.2. Mean squared error

Mean Squared Error (MSE) given in Eq. 12 represents the mean of the squared differences between the real data and the predicted data [30].

$$MSE = \frac{1}{N}\sum_{i=1}^{N}\left|x_i^{real} - x_i^{predicted}\right|^2 \tag{12}$$

2.7.3. Coefficient of determination

The coefficient of determination (R^2) given in Eq. 13 represents the ratio of the variance in the dependent variable that is explained by the linear regression model [31].

$$R^2 = 1 - \frac{\sum\left|x_i^{real} - x^{predicted}\right|^2}{\sum\left|x_i^{real} - x^{mean}\right|^2} \tag{13}$$

3. RESULTS

The statistical features of the EEG signals recorded from the participants during the task are presented in Table 3. The selected features on the nodes of the 17 trees were F7 theta/gamma, FC6 relative alpha, CP2 relative beta, and P3 delta/gamma. These trees are given in Figure 4, showing that 12 of them were identical when analyzing the EEG signals of 17 MS patients using the Decision Tree Regressor with Leave One Out Cross Validation. It was observed that the F7 theta/gamma and CP2

JSR A
Journal of Scientific Reports

relative beta feature pairs were used repeatedly in 14 trees. It was also observed that all decision trees could separate the EDSS level using two nodes.

The graphs created according to the EDSS of the features used by the trees are given in Figure 5. F7 theta/gamma and CP2 relative beta features were found to be distinctive in EDSS.

Table 3. Statistical parameters of the EEG signals recorded from the participants during the task.

Channel	Min	Max	SD	Skewness	Kurtosis	VPP
Fp1	-0.00075	0.00101	0.00013	1.54492	19.49554	0.00176
Fz	-0.00011	0.00014	0.00003	0.42954	5.51061	0.00025
F3	-0.00035	0.00035	0.00007	0.18917	6.55013	0.00070
F7	-0.00034	0.00041	0.00007	0.18918	10.81776	0.00074
FT9	-0.00026	0.00033	0.00005	0.81777	15.57779	0.00059
FC5	-0.00020	0.00019	0.00004	-0.06336	5.69386	0.00038
FC1	-0.00015	0.00015	0.00003	-0.13508	5.64678	0.00030
C3	-0.00009	0.00009	0.00002	-0.00865	4.28930	0.00018
T7	-0.00041	0.00059	0.00008	0.43319	13.30249	0.00100
TP9	-0.00038	0.00064	0.00009	0.75868	12.69678	0.00102
CP5	-0.00010	0.00009	0.00002	-0.18525	4.89025	0.00019
CP1	-0.00011	0.00008	0.00002	-0.30563	6.86306	0.00019
Pz	-0.00017	0.00025	0.00003	0.14124	4.89261	0.00041
P3	-0.00008	0.00008	0.00002	0.10255	4.48578	0.00016
P7	-0.00026	0.00023	0.00005	-0.08180	5.14539	0.00049
O1	-0.00020	0.00019	0.00003	-0.05169	6.29524	0.00039
Oz	-0.00016	0.00016	0.00003	0.00548	4.55911	0.00033
O2	-0.00019	0.00019	0.00004	-0.04872	4.88903	0.00038
P4	-0.00007	0.00007	0.00002	0.02542	3.94477	0.00014
P8	-0.00027	0.00027	0.00005	-0.16267	7.75689	0.00054
TP10	-0.00030	0.00039	0.00006	0.37740	8.53761	0.00069
CP6	-0.00010	0.00010	0.00002	-0.19806	6.31914	0.00020
CP2	-0.00008	0.00007	0.00002	-0.18043	5.89390	0.00015
C4	-0.00009	0.00008	0.00002	-0.12843	4.83436	0.00017
T8	-0.00031	0.00029	0.00005	-0.44179	13.14973	0.00060
FT10	-0.00054	0.00070	0.00011	0.65780	14.32443	0.00125
FC6	-0.00020	0.00023	0.00004	-0.02664	5.63375	0.00043
FC2	-0.00007	0.00007	0.00002	0.04355	3.66873	0.00014
F4	-0.00019	0.00020	0.00004	0.11452	5.68868	0.00038

F8	-0.00053	0.00067	0.00012	0.10190	9.45513	0.00120
Fp2	-0.00036	0.00049	0.00007	1.60709	14.17754	0.00084

VPP: Amplitude of peak to peak **SD:** Standard Deviation

JSR A
Journal of Scientific Reports

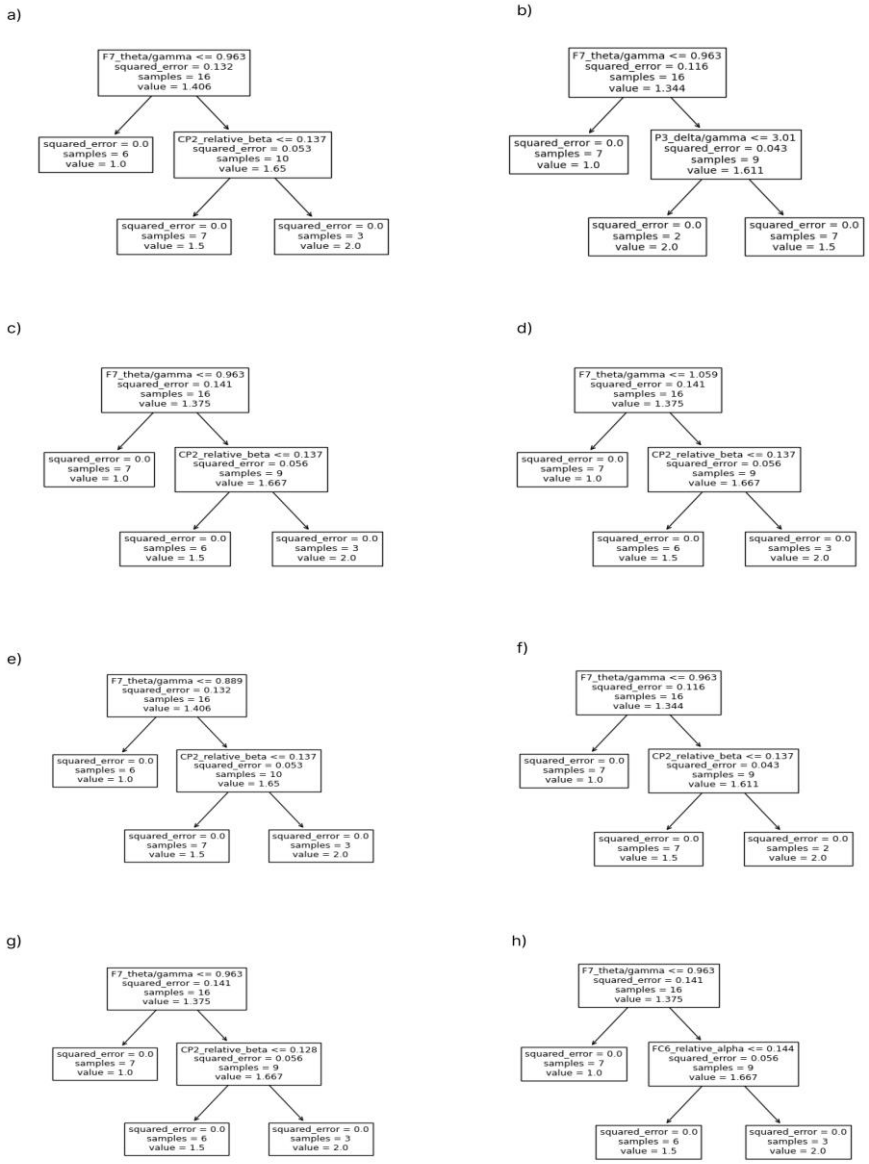

Figure 4. Decision Trees obtained in the LOOCV step a) tree_0, tree_1, tree_2, tree_4, tree_5, and tree_14 b) tree_3 c) tree_6, tree_9, tree_10, and tree_11 d) tree_7 e) tree_8 f) tree_12 and tree_15 g) tree_13 h) tree_16.

JSR A
Journal of Scientific Reports

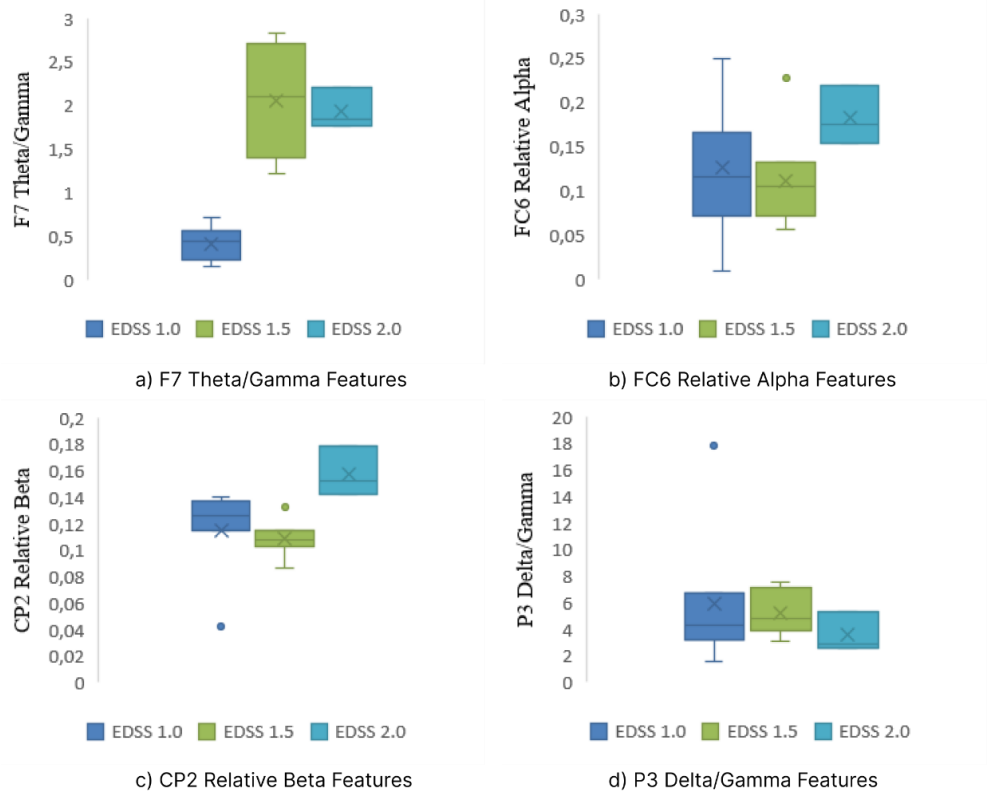

Figure 5. Feature-EDSS graphs used by the decision tree regressor.

The performances of the trees obtained from the Leave One Out Cross Validation steps are presented in Table 4. It is observed that the performances of tree_3, tree_13, and tree_16 are relatively lower compared to the other trees. When the other 14 tree models were used for testing, EDSS scores in the range of 1.0-2.0 (EDSS:1.0, EDSS:1.5, EDSS:2.0) were estimated with an MAE of 0.0, indicating accurate prediction. The overall EDSS estimation using Leave One Out Cross Validation was made with MAE of 0.088.

Table 4. The performances of the trees belonging to the Leave One Out Cross Validation steps.

tree_ID	EDSS	MAE	MSE	R^2	EEG Features
tree_0*	1.0	0	0	1	F7 theta/gamma, CP2 relative beta
tree_1*	1.0	0	0	1	F7 theta/gamma, CP2 relative beta
tree_2*	1.0	0	0	1	F7 theta/gamma, CP2 relative beta
tree_3	2.0	0.029	0.015	0.890	F7 theta/gamma, P3 delta/gamma

JSR A
Journal of Scientific Reports

tree_4*	1.0	0	0	1	F7 theta/gamma, CP2 relative beta
tree_5*	1.0	0	0	1	F7 theta/gamma, CP2 relative beta
tree_6*	1.5	0	0	1	F7 theta/gamma, CP2 relative beta
tree_7	1.5	0	0	1	F7 theta/gamma, CP2 relative beta
tree_8	1.0	0	0	1	F7 theta/gamma, CP2 relative beta
tree_9*	1.5	0	0	1	F7 theta/gamma, CP2 relative beta
tree_10*	1.5	0	0	1	F7 theta/gamma, CP2 relative beta
tree_11*	1.5	0	0	1	F7 theta/gamma, CP2 relative beta
tree_12*	2.0	0	0	1	F7 theta/gamma, CP2 relative beta
tree_13	1.5	0.029	0.015	0.890	F7 theta/gamma, CP2 relative beta
tree_14*	1.0	0	0	1	F7 theta/gamma, CP2 relative beta
tree_15*	2.0	0	0	1	F7 theta/gamma, CP2 relative beta
tree_16	1.5	0.029	0.015	0.890	F7 theta/gamma, FC6 relative alpha
LOOCV	**-**	**0.088**	**0.044**	**0.669**	

tree_ID: States the subject selected from MS patients for the Leave One Out Cross Validation steps. Identical trees are indicated with asterisks (*).

While making the EDSS estimation, 12 decision trees with the same node parameters were obtained in the LOOCV steps. The proposed decision tree is shown in Figure 6.

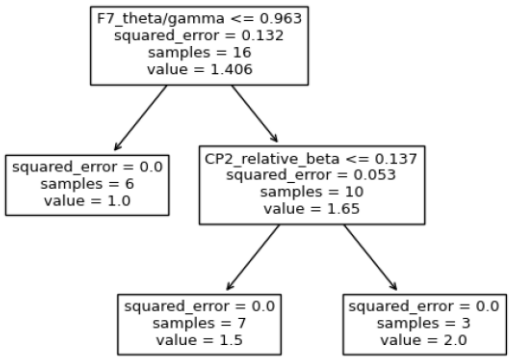

Figure 6. The proposed decision tree.

JSR A
Journal of Scientific Reports

The actual-predict performance of the decision tree is shown in Figure 7.

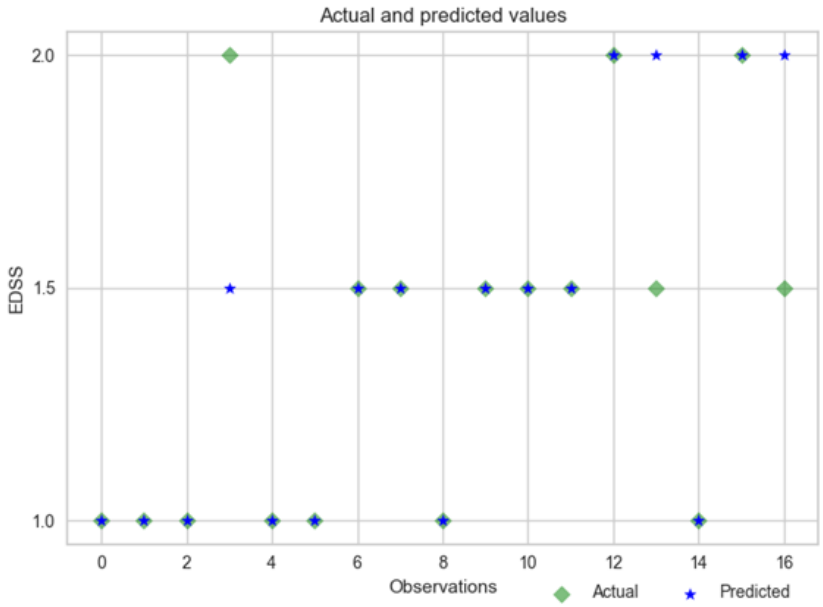

Figure 7. The actual-predict performance of the decision tree.

Statistical results of MS patients' scores obtained during the task according to EDSS are presented in Table 5. One-way ANOVA results showed that there was no significant difference between the cognitive task scores of MS patients with EDSS 1.0, 1.5, and 2.0 (p>.05). However, it was observed that the mean task score decreased as the EDSS increased.

Table 5. Statistical results of MS patients' task scores according to the EDSS score.

EDSS		N	Task Score (Max)	Task Score (Min)	Task Score (Mean)	SD	p
1.0	1.5 2.0	7	83.00	49.00	66.00	10.89	.907 .082
1.5	1.0 2.0	7	86.00	28.00	62.43	20.02	.907 .144
2.0	1.0 1.5	3	53.00	25.00	40.33	14.19	.082 .144

SD denotes the standard deviation, **p** denotes the p-value obtained as a result of the One-way ANOVA test.

JSR A
Journal of Scientific Reports

4. DISCUSSION

Since MS is a chronic and inflammatory disease of the central nervous system, monitoring disease progression and control is crucial. MRI is commonly used for disease follow-up as the lesions seen on MRI are known to correlate with EDSS scores. However, in this study, EDSS estimation was performed using EEG signals, which are more accessible and easier to apply compared to MRI. By using the theta/gamma ratio of the F7 channel and the CP2 relative beta features, accurate EDSS score estimations were achieved for 17 MS patients using a decision tree regressor. Table 6 presents comparisons with relevant studies from the literature that have also attempted EDSS estimation.

Table 6. The EDSS estimation studies in the literature.

Study	**Subject**	**EDSS**	**Feature**	**Method**	**Performance Metrics**
Kaufmann et al. [15]	173 MS	≤3.5, 4–6.5, ≥7	Self-report on patient mobility	Statistical analysis	Accuracy:88.4%
Cao et al. [18]	89 MS 29 Healthy	0-4.5	Postural sway parameters	Second-order polynomial regression models	Agreement:70.49% Mean error:0.63
Cao et al. [19]	89 MS 29 Healthy	0-4.5	Postural sway parameters	Decision trees	Agreement:75.00%
Alves et al. [20]	684 MS	0-10	Clinical notes from neurologist visits (OM1 MS Registry data)	XGBoost gradient-boosting regression models	PPV: 0,85 NPV: 0,85 AUC: 0,91
Gschwind et al. [22]	53 MS 49 Healthy	0-4.0	EEG topographies	Stepwise Multiple Linear Regression Models	R^2:0.97
This Study	**17 MS**	**1.0, 1.5, 2.0**	**EEG band powers**	**Decision Tree Regressor (LOOCV)** **Decision Tree Regressor (Proposed Tree)**	**MAE: 0.088** **MSE: 0.044** **R^2: 0.669** **MAE: 0.0** **MSE: 0.0** **R^2: 1.0**

In previous studies, Kaufmann et al. achieved an accuracy of 88.4% in classifying 3-class EDSS estimation based on self-reported mobility status of MS patients with EDSS scores between 0-10 using statistical methods. Cao et al. estimated EDSSs between 0 and 4.5 with a mean error of 0.63 using second-order polynomial regression models based on postural sway parameters of MS patients. In another study by Cao et al., EDSS estimation with 75.00% agreement was achieved using the Decision Tree method with the same data. Alves et al., used the XGBoost gradient regression model to estimate EDSS scores between 0 and 10 using data recorded by neurologists, achieving an AUC of 0.91. Gschwind et al. Obtained an r-squared value of 0.97 using Stepwise Multiple Linear Regression Models based on EEG topographies of MS patients with EDSS scores between 0-4. In the current study, the Decision Tree Regressor method was used with features extracted from the band powers of EEG signals. It was observed that 14 out of the 17 decision trees obtained in the LOOCV steps were similar, with 12 of them being identical. Using these 12 identical trees, accurate 3-category EDSS estimation with 0.0 MAE was achieved.

The results of the study showed that the theta/gamma ratio of the F7 channel and the relative beta features of the CP2 channel were significant in the EDSS estimation between 0-2.0.

The study has several limitations, including the inclusion of a limited number of MS patients with only the RRMS type and the low range of EDSS scores. Further research with larger sample sizes and inclusion of other types of MS patients in a more homogeneously distributed population is needed. Thus, the stability and reliability of the proposed method will be understood.

5. CONCLUSION

In the study, for the first time, EDSS was estimated using decision tree regression with PSD features of EEG signals from volunteers with MS during a cognitive task. The proposed tree model achieved EDSS estimation with 0.0 MAE, indicating high accuracy. This proposed method could be an important tool for the monitoring the progression of MS disease. The theta/gamma features of the F7 channel and the relative beta features of the CP2 channel were found to be significant in the proposed decision tree; however, further investigation is warranted for these features.

ACKNOWLEDGMENT

No funds, grants, or other support was received.

REFERENCES

[1] Multiple sclerosis - Symptoms and causes - Mayo Clinic. (2022). Mayo Clinic. https://www.mayoclinic.org/diseases-conditions/multiple-sclerosis/symptoms-causes/syc-20350269 (accessed Feb. 17, 2023).

[2] Goris, A., Vandebergh, M., McCauley, J. L., Saarela, J., and Cotsapas, C. (2022). Genetics of multiple sclerosis: lessons from polygenicity. Lancet. Neurol., 21(9), 830–842.

[3] Mental Health and Substance Use. (2006). Neurological Disorders: Public Health Challenges. https://www.who.int/publications/i/item/9789241563369 (accessed Feb. 17, 2023).

[4] Kurtzke, J. F. (1983). Rating neurologic impairment in multiple sclerosis: an expanded disability status scale (EDSS). Neurology, 33(11), 1444–1452.

[5] Sharrack, B. and Hughes, R. A. C. (1996). Clinical scales for multiple sclerosis. J. Neurol. Sci., 135(1), 1–9.

[6] Tombak, K. B, Armutlu, K. and Karabudak, R. (2010). The Effect of Walking Distance on EDSS Score in Patients with Multiple Sclerosis. Turkish Journal of Neurology, 16(2), 72–77.

[7] McMillan, L. and Moore, K. A. (2006). The Development and Validation of the Impact of Multiple Sclerosis Scale and the Symptoms of Multiple Sclerosis Scale. Arch. Phys. Med. Rehabil., 87(6), 832–841.

[8] Lynch, S., Baker, S., Nashatizadeh, M., Thuringer, A., Thelen, J., and Bruce, J. (2021). Disability measurement in Multiple Sclerosis patients 55 years and older: What is the Expanded Disability Status Scale really telling clinicians?. Mult. Scler. Relat. Disord., 49(102724).

[9] Ellenberger, D. et al. (2020). Is benign MS really benign? What a meaningful classification beyond the EDSS must take into consideration. Mult. Scler. Relat. Disord., 46(102485).

[10] Koziol, J. A., Lucero, A., Sipe, J. C., Romine, J. S. and Beutler, E. (1999). Responsiveness of the Scripps neurologic rating scale during a multiple sclerosis clinical trial. Can. J. Neurol. Sci., 26(4), 283–289.

[11] Fischer, J. S., Rudick, R. A., Cutter, G. R., and Reingold, S. C. (1999). The Multiple Sclerosis Functional Composite Measure (MSFC): an integrated approach to MS clinical outcome assessment. National MS Society Clinical Outcomes Assessment Task Force. Mult. Scler., 5(4), 244–250.

[12] Walz, L., Brooks, J. C., Shavelle, R. M., Robertson, N. and Harding, K. E. (2022). Life expectancy in multiple sclerosis by EDSS score. Mult. Scler. Relat. Disord., 68(104219).

[13] Şen, S. (2018). Neurostatus and EDSS Calculation with Cases. Arch. Neuropsychiatry, 55(1), 80-83.

[14] Alexandra, T., Kim, C., Estefania, B., Elaine, R., Pierre, D. and Isabelle, R. (2023). Cognitive reserve as a moderating factor between EDSS and cognition in multiple sclerosis. Mult. Scler. Relat. Disord., 70(104482).

[15] Kaufmann, M. et al. (2020). Development and validation of the self-reported disability status

scale (SRDSS) to estimate EDSS-categories. Mult. Scler. Relat. Disord., 42(102148).

[16] Zurawski, J. et al. (2019). Time between expanded disability status scale (EDSS) scores. Mult. Scler. Relat. Disord., 30(2019), 98–103.

[17] Song, X. et al. (2020). Correlation between EDSS scores and cervical spinal cord atrophy at 3T MRI in multiple sclerosis: A systematic review and meta-analysis. Mult. Scler. Relat. Disord., 37(101426).

[18] Cao, H. et al. (2013). Expanded Disability Status Scale (EDSS) estimation in multiple sclerosis from posturographic data. Gait Posture, 37(2), 242–245.

[19] Cao, H. et al. (2013). Automatic Assessment of Expanded Disability Status Scale (EDSS) in Multiple Sclerosis Using a Decision Tree. Engineering, 5(10), 566–569.

[20] Alves, P. et al.(2022). Validation of a machine learning approach to estimate expanded disability status scale scores for multiple sclerosis. Mult. Scler. J. - Exp. Transl. Clin., 8(2).

[21] Salim, A. A., Ali, S. H., Hussain, A. M., and Ibrahim, W. N. (2021). Electroencephalographic evidence of gray matter lesions among multiple sclerosis patients: A case-control study. Medicine (Baltimore), 100(33).

[22] Gschwind, M. et al. (2016). Fluctuations of spontaneous EEG topographies predict disease state in relapsing-remitting multiple sclerosis. NeuroImage Clin., 12(2016), 466–477.

[23] Vázquez-Marrufo, M. et al.(2019). Altered individual behavioral and EEG parameters are related to the EDSS score in relapsing-remitting multiple sclerosis patients. PLoS One, 14(7).

[24] Karacan, S.S., Saraoglu, H. M., Kabay, S. C., Akdag, G., Keskinkilic, C., and Tosun, M.(2022). EEG Based Environment Classification During Cognitive Task of Multiple Sclerosis Patients. In 4th Int. Congr. Human-Computer Interact. Optim. Robot. Appl. Proc (HORA), 1-4.

[25] Karacan, S.S., Saraoglu, H. M., Kabay, S. C., Akdag, G., Keskinkilic, C., and Tosun, M. (2023). EEG-based mental workload estimation of multiple sclerosis patients. Signal, Image Video Process., 1–9.

[26] Della Sala, S., Gray, C., Baddeley, A., and Wilson, L. (1967). Visual patterns test: a test of short-term visual recall, Thames Valley Test Company, UK.

[27] Gramfort, A. et al. (2013). MEG and EEG data analysis with MNE-Python. Front. Neurosci., 7(267), 1-13.

[28] Welch, P. D. (1967). The Use of Fast Fourier Transform for the Estimation of Power Spectra: A Method Based on Time Averaging Over Short, Modified Periodograms. IEEE Trans. Audio Electroacoust., 15(2), 70–73.

[29] Pedregosa, F. (2011). Scikit-learn: Machine Learning in Python. J. Mach. Learn. Res., 12, 2825–2830.

[30] J. Qi, J., Du, J., Siniscalchi, S. M., Ma, X., and Lee, C. H. (2020). On Mean Absolute Error for Deep Neural Network Based Vector-to-Vector Regression. IEEE Signal Process. Lett.,27, 1485–1489.

[31] Gelman, A., Goodrich, B., Gabry, J., and Vehtari, A. (2019). R-squared for Bayesian Regression Models. The American Statistician, 73(3), 307-309.

Kütahya Dumlupınar University
Institute of Graduate Studies

Journal of Scientific
Reports-A
E-ISSN: 2687-6167
Number 53, June 2023

RESEARCH ARTICLE

THE EFFECTS OF CIRCULAR INSERTS ON THE THERMAL AND FLOW CHARACTERISTICS IN A HORIZONTAL PIPE EXCHANGER: A NUMERICAL INVESTIGATION

Muhammet Kaan YEŞILYURT[1], Nesrin ADIGÜZEL[2*], Orhan YILDIRIM[3], Ömer ÇOMAKLI[4], Faraz AFSHARI[5]

[1]Vocational School of Technical Sciences, Ataturk University, Erzurum,kaan.yesilyurt@atauni.edu.tr
ORCID: 0000-0002-7207-1743
[2]Department of Mechanical Engineering, Ataturk University, Erzurum, nesrin.adiguzel@atauni.edu.tr
ORCID: 0000-0001-7610-2757
[3]Department of Mechanical Engineering, Ataturk University, Erzurum, orhan.yildirim@atauni.edu.tr
ORCID: 0000-0001-8780-1297
[4]Department of Mechanical Engineering, Ataturk University, Erzurum, ocomakli@atauni.edu.tr
ORCID: 0000-0003-4631-7989
[5]Department of Mechanical Engineering, Erzurum Technical University, Erzurum, faraz.afshari@erzurum.edu.tr
ORCID: 0000-0001-9192-5604

Receive Date:11.08.2022 *Accepted Date: 06.03.2023*

ABSTRACT

The aim of the present study was to numerically investigate the effects of circular inserts placed inside a circular tube in order to evaluate the heat transfer characteristics under different operating conditions. Computational Fluid Dynamics methods were used to solve the model, which is a heat pipe with an outer diameter of 21 mm equipped with circular inserts with a distance of 20 cm. Different mass flow rates of the heat transfer fluid, including 25, 50, 75, 100, and 125 g/s were examined, and the thermal behavior of the turbulators and the flow structure were investigated. R19.0 version of ANSYS Fluent software was used as the CFD program to obtain the desired results and contours. From the results, it was found that circular inserts can be used in heat pipes to produce vortices and thus improve the heat transfer.

Keywords: *Vortex generator, Turbulator, Circular Pipe Inserts, Numerical study, ANSYS Fluent, Turbulent flow, Friction factor, Heat Transfer*

1. INTRODUCTION

Whether running on renewables or fossil fuels, i.e., coal, oil, or gas, thermal systems that transport energy from one medium to another are always put into use in numerous applications. Improving the heat exchanger performance and ensuring maximum thermal transmission while also keeping the system as small as possible with high efficiency is of great importance [1]. The efficiency of these systems is primarily determined by their heat transfer characteristics, and several approaches aimed at

JSR A
Journal of Scientific Reports

improving the heat transfer processes have been developed over the last decades. As such, there has been an exponential increase in the number of studies focused on heat transfer enhancement, in parallel with the increasing number of patents and products [2].

Heat transfer enhancement technologies are based on active systems that rely on the use of external power sources and passive systems that do not require external power but rather take advantage of geometrical changes, arrangements, or modifications, rough surfaces, swirling flow devices, etc. [3]. One of the most considered approaches is dealing with the flow regime throughout the system and improving the heat transfer, enabling development of more compact systems, with a smaller room requirement for installation [4], reduced initial cost and lower payback time. In this area, studies involve numerical and experimental methods and mostly employ a circular single tube or pipe as the test section through which lies an insert (which are also called swirl/vortex generator or turbulator) to create turbulent flow [5–13]. Inserted into the pipes or tubes as blades [14], rods [15, 16], rings [17, 18], tapes [8, 19], strips [8, 20] or coils [21, 22], tube inserts enhance heat transfer by providing increased flow mixing and thus creating turbulent flow induced by longitudinal vortices. Among the parameters that affect the enhancement rate induced by the turbulators are their shapes, geometry, placement, spacing or pitch, flow attack angle, material, effective diameter, Reynolds number, and further modifications such as perforations, wings, etc. [1]. Surveying the literature, numerous studies are available on the improvement of heat transfer using inserts, turbulators, and swirl/vortex generators. Some involve only numerical/analytical and some only experimental studies, whereas others involve both numerical and experimental studies in a comparative and confirmative manner. In a study by Tatsumi *et al.* [23], 3D unsteady flow was analyzed in a square channel with rough walls, in the cases where full-span ribs or discrete ribs were attached in sets to the wall of the channel. The flow and associated heat transfer in the channel were reported to be 3D even in the case of full-span ribs when the ratio of rib height to channel height was small. Large-scale downstream eddies that rotate in counter directions were reported to have accompanied the flow through the ribs and thus have improved flow mixing in the case of discrete ribs, resulting in higher wall heat transfer.

In a study aimed at investigating the effects of conical ring inserts, placed as having 10, 20 and 30 mm spacing, on the performance characteristics through entropy generation minimization and efficiency improvements. For this purpose, maximum entropy generation was determined at same Re number for each configuration. In terms of entropy generation, conical ring inserts were thermodynamically advantageous up to Re 8000. The efficiency increased as the pitch decreased from 0.86 to 1.16 [24]. Salman *et al.* [25] carried out a comparative numerical investigation of the effects of V-cut and classical twisted tape inserts with different twist ratios on heat transfer and friction factor. The enhancement factor was reported to have been found to be positively related to the Re number and inversely related to the twist ratio for both the classical and V-cut twisted tape inserts. Furthermore, the V-cut twisted tape provided a better surface for fluid contact and hence a greater heat transfer coefficient compared to right-left helical tape inserts. The overall maximum heat transfer enhancement was reported to be 107%.

In order to experimentally investigate the effect of coiled wire inserts on the occurrence of dynamic instabilities in a straight tube for forced convection boiling test tube, experiments were carried out in a circular tube with and without the inserts using water as the working fluid at different inlet temperatures and the results were compared. Circularly coiled wire inserts with two different pitch

ratios were tested under the conditions that a constant temperature was applied to the outer surface of the test tube and a constant outlet restriction was used at mass flow rates ranging from 110 to 20 g/s. As a result, density waves and pressure drops were reported to have occurred at each configuration and the oscillations occurred at all inlet temperatures [26].

In another study, a comprehensive literature review was presented to investigate heat transfer and flow structure in air ducts. It has been found that perforation in ribs/chambers/blocks and a combined rib and delta fin combination resulted in better thermo-hydraulic performance [27]. Using an uncommon insert material and geometry, Razzaghi *et al.* [28] investigated overall heat transfer along 10 rows of staggered bundle of elliptic tubes with changeable transverse and longitudinal pitches and aluminum foam porous media inserts. Despite increased pressure drop at higher Reynolds numbers, the results suggested that the use of aluminum foams has brought on a significant improvement in the heat transfer and overall efficiency while flow regime remained laminar. An array of conical rings having different pitches were employed in a horizontal tube as tube inserts by Yeşilyurt [29] in a forced-convection boiling two-phase flow system in order to investigate their effects on the flow instabilities as well as the heat transfer characteristics under constant pressure, constant inlet temperature, constant heat flux and output restriction conditions. The characteristic curve of the flow system was reported to have shifted to the right with the smallest increase in the input thermal power, resulting in increased pressure drops at any mass flow rate. The hydraulic and thermal performance of a water-to-air heat exchanger, where air passed through the outer pipes and water flowed through inner pipe, was investigated in the presence of perforated and typical helical fins at different pitch ratios and Re number. Using NSGA II and ANSYS Fluent14, thermal performance, Darcy friction factor and Nu number were obtained using proposed empirical equations [30].

Karagoz *et al.* [14] used cylindrical inserts with different attack angles and pitches (101, 216, 340) to create turbulent flow in the heat exchanger tube at different flow rates and Reynolds numbers (6000, 11,000, 17,000) and investigated the effects of Nusselt number, Reynolds number and friction factor on the heat transfer rate. The inserts in the heat exchanger tube were reported to have led to a significant increase in Nu number and energy efficiency. Zheng *et al.* [15] numerically studied the effect of rod type swirl generators placed in a heat exchanger tube on the thermal and the hydraulic performance of the system and showed that multiple vortices were induced by the introduction of inserts. The slope of the rod, diameter ratio and Re were considered to affect the heat transfer rate and friction factor significantly. Artificial neural networks were also used to supports a multi-objective optimization model in order to ensure maximum heat transfer, minimum pressure drop, and an optimal Pareto front. Applying a thermal-hydraulic performance evaluation criterion, the greatest improvement in the heat transfer were achieved with the 0.058 diameter and 57.057° inclined vortex rod at 426.767 Re number. Li *et al.* [31] investigated the turbulent flow and heat transfer through a tube equipped with drainage inserts. By diverting the fluid running at the central section of the pipe towards the wall, the drainage inserts were reported to improve the mixing of cold and hot fluid as well as create vortices that agitate the fluid. The results obtained from the numerical analyses as well as their confirmation with the experimental data revealed that a 3.3 pitch ratio and a 45° inclination angle of the insert were reported to be the optimum arrangement to yield the greatest performance evaluation criteria, hence better heat transfer and flow performance. The thermal and hydraulic properties of nanofluid flow in a turbulent forced convection regime in a circular tube equipped with cone-shaped inserts were analyzed with numerical studies using the finite volume method.

JSR A
Journal of Scientific Reports

Karuppasamy *et al.* [32] used Al_2O_3 and CuO whereas Mohammed *et al.* [10] used Al_2O_3, CuO, SiO_2 and ZnO particles of various diameter at different volume fractions in water as the carrier fluid. While Karuppasamy *et al.* [32] achieved the highest improvement with Al_2O_3 Mohammed *et al.* [10] reported highest increase in the Nu number and friction factor with SiO_2. In a study, helical-surface disc inserts were examined for their effects on the pressure drop and heat transfer characteristics in a double-tube heat exchanger (DTHE) where hot water flowed through the inner pipe, and cold air flowed inside the annulus. Having tested different values of spacing, helix angle (ϕ) and diameter ratio (DR), the best improvement in the overall heat transfer, Nu and friction factor was reported with DR = 0.42, which was the smallest of all tested, and helix angle of $\phi = 40°$, which was the greatest of all tested [33].

In another study, heat transfer and flow characteristics of mist/steam refrigerant in a U-shaped gas turbine were investigated and the mass ratio and mist to steam as well as the mist diameter were carefully analyzed. With the increase in the mist-to-steam mass ratio, the heat transfer from the ribbed wall has increased proportionally. When the mist diameter was 10μm, the mass ratio of the mist increased from 2% to 10%, whereas the increase in the average Nu number in the first and second passages were 60.13% and 112.5%, respectively [34]. In another study, the turbulent thermal behavior of CuO-distilled HO-based nanomaterials resulting from the placement of a new turbulator was modeled. Four different cases with different geometries, namely straight pipe, twisted band, barrier twisted band, and perforated barrier twisted band, were considered and a two-phase mixing model was applied. The intensification of turbulence by the addition of barriers led to a remarkable improvement in the heat transfer and an increase in the pressure drop was noted due to placement of barrier on the twisted tapes [35]. Recent technological advances have led to significant advances towards more compact and efficient heating.
The development of novel heat transfer improvement techniques remained a hot topic in the global research. Over several decades, various active and passive heat transfer improvement techniques were developed for convective heat transfer. While passive methods are favorable for their simplicity and not needing external energy consumption, active methods enable the modification and deterioration of the thermal boundary layer. Such a technique is the use of tube inserts that create fluid mixing and secondary flows, diverting and/or rerouting the flow stream [20].

The convective heat transfer in an oval channel exposed to a constant heat flow from the bottom was modeled as two-phase water-Al_2O_3 mixture nanofluid and the effects of Re number, nanofluid volume ratio and different combinations of co-conical inward inserts (CCI-in), counter-conical inserts (CoCI) and co-conical outward inserts (CCI-out) on the flow pattern and heat transfer characteristics were investigated. The highest heat transfer coefficient was observed with the CCI-inward inserts, by approximately 17% higher than the plain tube, owing to the induction of secondary flows [20]. In another study, heat transfer characteristics and flow properties of a mist-steam two-phase flow were numerically investigated and experimentally validated in different channels with different void ratios (ε) and rib designs. With ε greater than 0.264, the thermal recovery performance obtained with column-row-ribs was better than with solid ones. On the other hand, the increase in the mist droplet diameter was reported to worsen thermal enhancement factor and increased instabilities in the heat transfer [36]. In another study, the effect of spherical troughs on exergy efficiency and thermos-hydraulic performance of a MWCNT-Al_2O_3/water hybrid parabolic solar collector was investigated through the Nu number, pressure loss and exergy performance. Results showed that the groove height

JSR A
Journal of Scientific Reports

was associated with higher heat transfer, higher exergy efficiency whereas pressure loss was associated with higher Re number and φ [37]. The effects of conical and fusiform inserts in a DTHE with circular and rectangular tubes on heat transfer and turbulent flow patterns were investigated using 21 different configurations at Re 4000, 7000, 10000 and 13000. The highest convection coefficient was reached when the inner tube of the DTHE was circular [38]. The effects of water-to-water aluminum oxide addition in a six-toothed disc turbulator double-pipe heat exchanger were numerically investigated; Nanoparticles with 1%, 4% and 6% concentrations were added to the hot liquid and flowed in a tube with a Reynolds range of 3000 to 13000. At Reynolds 500, cold water flows through the shell and a six-toothed disc turbulator is located in the shell. The increase in the local Nu number by about 70%, hence the improved heat transfer, induced by the collision of the fluid with the surface of the inserts and due to the breaking of the boundary layer resulted in increased the thermal efficiency [39]. The effects of ring turbulators on the flow instabilities were also investigated in another study on an experimental forced-convection two-phase flow system featuring a straight horizontal tube. The effects of a series of rings in variable fluid inlet flow rate were investigated, keeping the pressure, inlet temperature, and thermal power constant. In addition, the wall temperatures and pressure-flow changes of the pipes were also investigated and it was found that at a given mass flow rate, the pressure increased with thermal power at any mass flow rate [18]. In a study, Shivamallaiah and Fernandes [13] numerically investigated the friction characteristics of air flowing through a circular pipe with semi-elliptical inserts at varying aspect ratios, flow attack angles and longitudinal pitches in the range of Re 8000–26000 turbulent flow regime to simulate the heat transfer along the pipe. The presence of semielliptical inserts was reported to have a remarkable effect on the friction characteristics and the Nu number by generating strong longitudinal eddies that intensify fluid mixing in the vicinity of tube wall. While attach angle, pitch and aspect ratio, all had significant effects on friction, aspect ratio's effect on heat transfer was more significant. The enhancement in Nu was 2.1 folds whereas the greatest friction increase was 6.34 folds at 30 mm pitch.

Analyzing available studies in the literature indicated the importance of turbulators and tube inserts as well as CFD simulation. In the present study, the effects of ring inserts, placed inside a circular tube with an interval of 20cm, on the heat transfer along the tube was investigated. The originality of this work is proposing the CFD methods to solve engineering problems in the field of heat exchangers. In this context, the study by Yeşilyurt [29] on the effects tube inserts consisting of conically wound spring arrays on the enhancement of heat transfer and flow instabilities was considered and model simulation of the problem was performed. Further, the present study is based on CFD numerical calculations and the main results of the current study flow structure and temperature distribution contours were obtained and discussed in detail.

2. PHYSICAL MODEL and GEOMETRIC CONFIGURATION

As a common test section used in several other studies in the literature, a circular pipe was used in the test setup in this study. The dimensions of the pipe are the same as in Yeşilyurt [29] but the length of the test section was limited to 500 mm. The inner diameter, outer diameter and wall thickness of the pipe are 17 mm, 21 mm, and 4 mm, respectively. Ring inserts made of 13 mm diameter aluminum wire attached on two sides to two straight aluminum rods at an interval of 20 cm were designed and modeled as the turbulators to be employed in the pipe (Figure 1).

JSR A
Journal of Scientific Reports

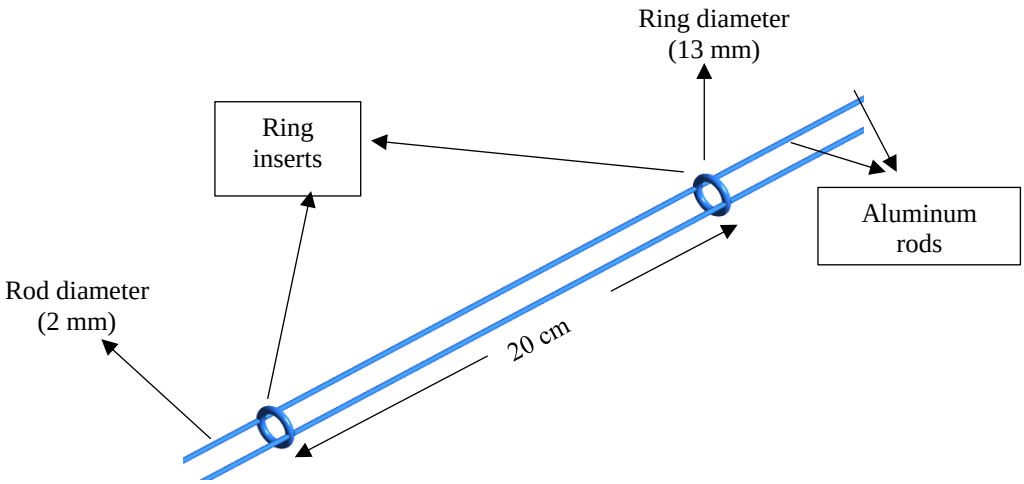

Figure 1. The arrangement and geometric details of the ring turbulators modeled to be employed in the study.

3. COMPUTATIONAL FLUID DYNAMICS ANALYSIS

In the CFD method, several numerical calculations, such as finite elements, finite volumes and finite differences, can be used to solve problems numerically and determine flow characteristics, heat and mass transfer and make predictions about the solutions of real-life problems. CFD solves the conservation equations by making use of equation sets prepared according to control volumes. ANSYS Fluent, a commercial CFD software, that is one of the most popular choices for numerical analyses, was used to carry out the numerical investigation in this study. The analyses were conducted as per the basic steps given below:

- Creating the physical model to be analyzed,
- Designing and meshing the model with a proper mesh quality,
- Constructing the numerical model based on the mathematical set of equations that describe the flow and setting the boundary conditions,
- Running the solution and iterating through all elements,
- Reviewing the results obtained from the solution with the boundary conditions applied,
- Assessing the results in terms of accuracy and precision and starting over the process making any necessary improvements to the model or mesh structure, if necessary.

In this respect, the physical model was first simulated in ANSYS Fluent. The pipe, the insert and the fluid were defined and other necessary definitions were made at first. Afterwards, the mesh was defined and validated. Having ensured that the mesh covers all required zones and is duly sized with all dimensions correct, the solver was chosen and the boundary conditions of the system were defined. After the preparation of the model, solver was established and the equations that govern the flow were

JSR A
Journal of Scientific Reports

solved iteratively to determine the parameters' values in the flow domain. The number of iterations was about 1000 depending on the required precision and the available time allocated for the solution to converge.

The numerical analysis was first carried out for the plain pipe (without the insert placed in) and the values of parameters were saved and analyzed to be referred to as baseline data. Thus, the second numerical analysis will be able to reveal the effect of introducing the insert into the pipe on the values of parameters. The analyses of the water flow through the 500 mm circular heat pipe, with and without the insert, were carried out at a constant wall heat of 6.5 kW, seeking insight into heat transfer characteristics and friction induced by the ring inserts.

3.1. Governing Equations and Assumptions

In the numerical analyses, the exact solution of real life models may be very time-consuming and unnecessarily complex, as such, as a general approach, some assumptions have been made to enable flow and energy equations to be applied in the model.

In the present study, the working fluid was water, and the assumptions made in the analysis are as follows:

i. constant physical properties of the fluid,
ii. incompressible flow,
iii. steady, three-dimensional and fully-developed flow,
iv. gravity acts on the flow.

The two-equation k–ε model, a widely used turbulence model available in most CFD software, such as Fluent, was used in this study to solve the flow field through our circular pipe. The k–ε model can also explicate history effects, such as convection and diffusion of turbulent energy by the virtue that it represents the turbulent properties of the flow by two extra transport equations: the turbulent kinetic energy, k, and the turbulent dissipation, ε, [40].
The first of the transport equations, k, as the name suggests, determines the energy in the turbulence whereas the second, ε, determines the scale of the turbulence, i.e. the rate of dissipation of turbulent kinetic energy.

Considering the abovementioned assumptions, the continuity equation, conservation of momentum and conservation of energy equations, turbulent kinetic energy equation, and turbulent dissipation energy equations, which are given below in sequential order, have been involved in the computational domain.
The continuity equation is expressed as:

$$\frac{\partial \rho}{\partial t} + \frac{\partial \rho u}{\partial x} + \frac{\partial \rho v}{\partial y} + \frac{\partial \rho w}{\partial z} = 0 \quad (1)$$

Momentum equation:

$$\frac{\partial \rho}{\partial t} + \vec{\nabla}.(\rho\vec{V}) = \frac{\partial \rho}{\partial t} + \vec{V}.\vec{\nabla}\rho + \rho\vec{\nabla}.\vec{V} = 0 \quad (2)$$

Energy equation:

$$\rho c_v \frac{dT}{dt} = k\nabla^2 T + \Phi \quad (3)$$

The turbulence kinetic energy equation, k, is expressed as follows:

$$\frac{\partial}{\partial t}(\rho k) + \frac{\partial}{\partial x_i}(\rho k u_i) = \frac{\partial}{\partial x_j}\left((\mu + \frac{\mu}{\sigma_k})\frac{\partial k}{\partial x_f}\right) + G_k + G_b + \rho\varepsilon - Y_M + S_k \quad (4)$$

and the dissipation rate of turbulent kinetic energy, ε, is given as:

$$\frac{\partial}{\partial t}(\rho\varepsilon) + \frac{\partial}{\partial x_i}(\rho\varepsilon u_i) = \frac{\partial}{\partial x_j}\left((\mu + \frac{\mu_t}{\sigma_e})\frac{\partial e}{\partial x_j}\right) + C_{1\epsilon}\frac{\varepsilon}{k}(G_k + C_{3\epsilon}G_b) + C_{2\epsilon}\rho\frac{\varepsilon^2}{k} + S_e \quad (5)$$

where G_k is the turbulent kinetic energy generation due to average velocity magnitudes; G_b is the turbulent kinetic energy generation from buoyancy; Y_M is the effect of increasing or decreasing compressible turbulence on the overall dissipation rate; $C_{1\varepsilon}$, $C_{2\varepsilon}$, $C_{3\varepsilon}$ and C_μ are constants; σ_k and σ_ε are the Prandtl numbers for k and ε, respectively; and S_k and S_e user-defined source terms.
The turbulent viscosity (μ_t) is calculated with Equation 6;

$$\mu_t = \rho C_\mu \frac{k^2}{\varepsilon} \quad (6)$$

JSR A
Journal of Scientific Reports

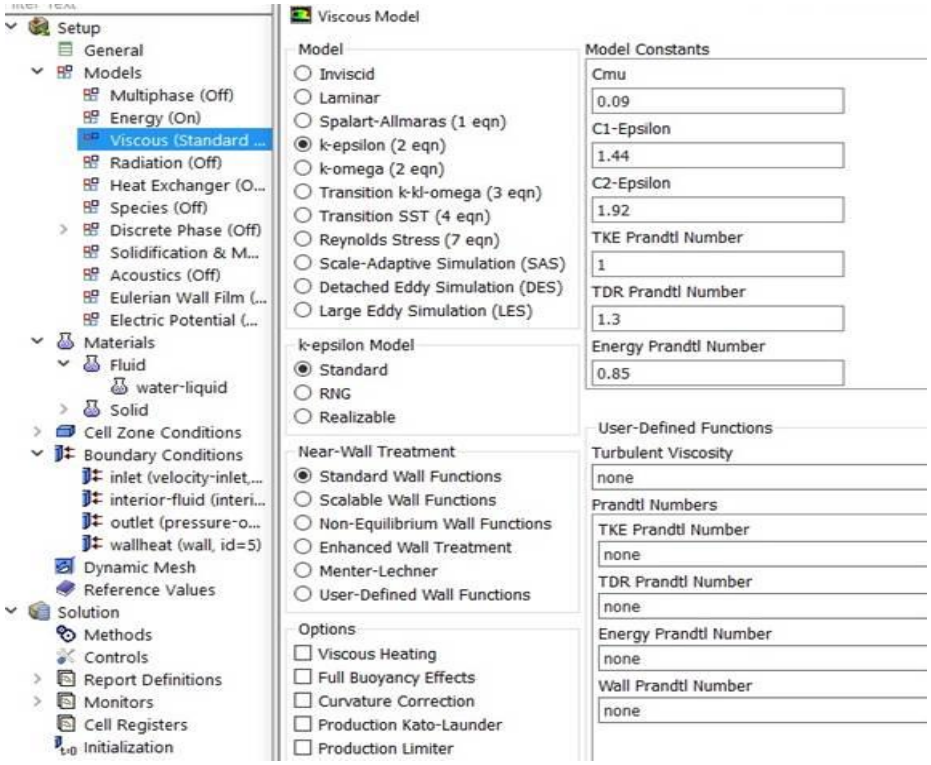

Figure 2. Model selection.

The constants in the model are set as shown in Figure 2. The energy equation used in convection heat and mass transfer in standard k-ε models of turbulent flow is calculated as given in Equation 7;

$$\frac{\partial}{\partial t}(\rho E) + \frac{\partial}{\partial x_i}(u_i(\rho E + \rho)) = \frac{\partial}{\partial x_j}\left(k_{eff}\frac{\partial T}{\partial x_j} + u_i(\tau_{ij})_{eff}\right) + S_h \quad (7)$$

where E is the total energy, k_{eff} is the effective heat transfer coefficient, and τ_{ij} is the deviatoric stress tensor.

3.2. Boundary Conditions

The model was designed based on the experimental system used in Adiguzel and Göcücü [18] and Yeşilyurt [29]. The boundary conditions for the numerical analysis to be carried out in ANSYS Fluent were, therefore, determined with reference to the data obtained from the experimental system. As such, the temperature, velocity and pressure values determined during the experiments were used as the boundary conditions in the model. The temperature of water at the inlet was uniform at 292 K and the inlet velocity varied based on the preset mass flow rates. The relative average pressure at the outlet has been defined as zero since it discharges to open air at atmospheric pressure. The Reynolds number was determined by the velocity of water at the inlet, as well as the hydraulic diameter. A constant heat

flow rate of 6.5 kW was defined at the pipe wall surface, and a no-slip velocity condition was considered on the pipe wall.

3.3. Meshing and Mesh Validation (Grid Independence Test)

In the 3D analysis, "tetrahexonal" type mesh was used and boundary layer theory was applied by choosing the "infiltration" option on the pipe wall (Figure 3).

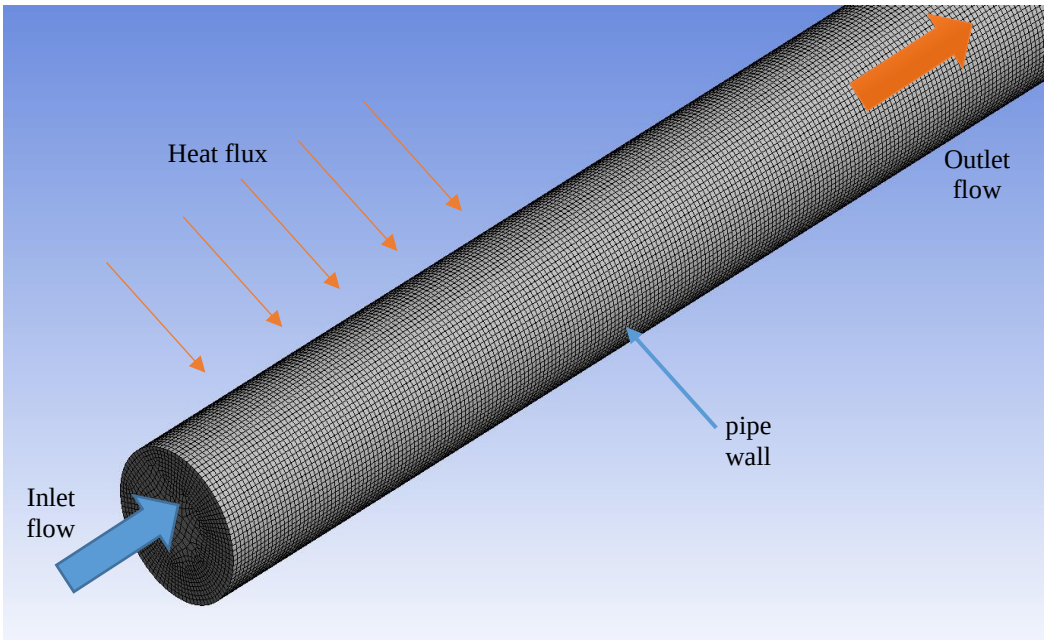

Figure 3. Pipe and mesh structure analyzed.

The mesh structure was created on the determined model and the mesh quality was adjusted. The number of these elements is important to converge to the correct solution. In order to determine the mesh quality, the "skewness" criterion was taken as a reference among the relevant options. Values below the threshold of 0.94 are considered applicable values, and it is generally aimed to further decrease this value.

Excellent	Very good	Good	Acceptable	Bad	Unacceptable
0-0.25	0.25-0.50	0.50-0.80	0.80-0.94	0.95-0.97	0.98-1.00

Figure 4. Mesh skewness spectrum and the scales for the Skewness criterion.

Errors due to mesh structure are a problem that results in an unsuccessful or erroneous analysis. Consideration must be given to cell type, cell count, and mesh quality to ensure the correct solution

and obtain reliable results. Therefore, mesh independence tests are necessary to ensure accurate results while also avoiding an excessive mesh number, hence a longer analysis time. First of all, independence from mesh number analyses were performed. After the mesh structure was arranged, the solution part was passed. k-ε turbulence model was selected to solve the problem. Figure 2 shows the operations performed in the solution part. While performing flow and heat analysis, water was chosen as the heat transfer fluid and only the flow region was defined. At this stage, the results of the analyzed model were examined.

4. RESULTS and DISCUSSION

In Figure 5, the geometry of the experimental setup, the inlet and outlet and the heat transfer application have been illustrated in three dimensions in the form of a schematic view of the pipe length. The circular turbulators inside the pipe can be seen in the picture. Circular turbulators have been located at the same distances inside the pipe as shown in the figure.

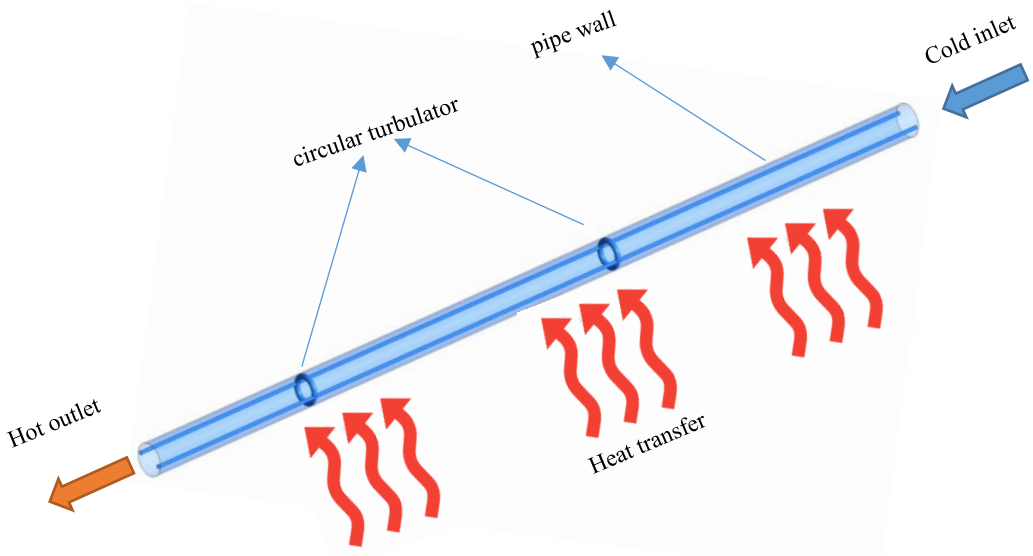

Figure 5. 3-D boundary condition and geometry of the pipe and circular pipe inserts.

In this study, after the mesh independence was ensured for the defined domain, solutions were performed and the results were compared. Various cell configurations and sizes were also performed and no remarkable change was observed. As a result of mesh analysis, the defined geometry was meshed using a maximum cell number of 4,000,000 cells. It should be noted in the meshing process that the defined meshes are well concentrated in the regions close to the wall and circular turbulators in order to get results with the desired accuracy. In the meshing procedure, the skewness value was 0.84 with a growth rate of 1.2. In Figure 6, two views of the mesh configuration have been presented to show the quality of the applied mesh inside the pipe and circular turbulator.

JSR A
Journal of Scientific Reports

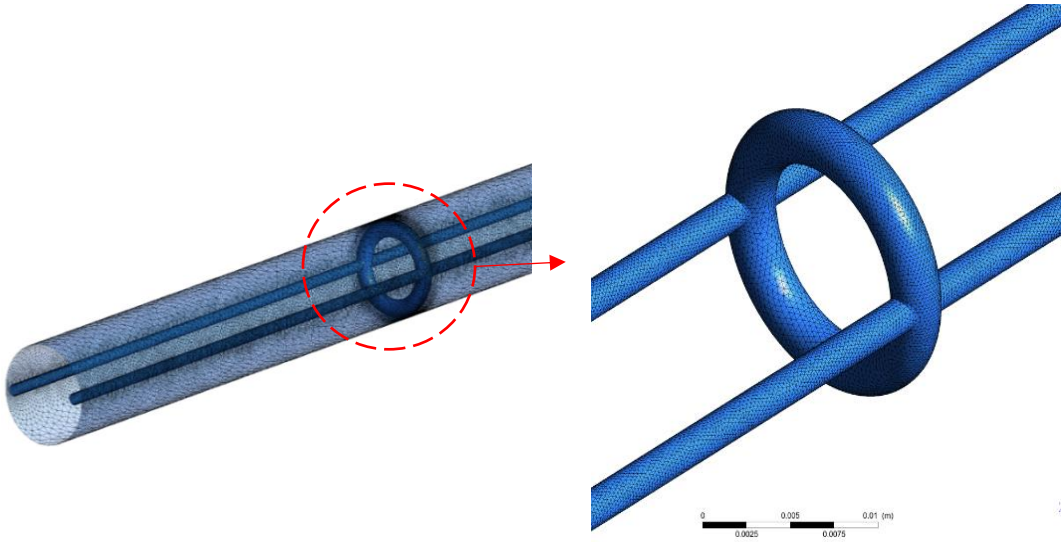

Figure 6. Mesh quality of pipe and circular turbulator.

To ensure the accuracy of the solutions, a simulation was performed for plain pipe (with no turbulators placed in) and the necessary contours were obtained. The velocity and temperature distributions obtained for plain pipe are in good agreement with the existing studies in the literature as shown in the following figures. In Figure 7, the velocity contours for plain pipe have been presented at different mass flow rates from 0.25 g/s to 125 g/s. With increasing mass flow rates, velocity increases gradually. In Figure 8, temperature contours for the plain pipe have also been presented. The effect of mass flow rate on the temperature distribution can be clearly seen in the figure. Moreover, the higher temperature of the regions near the boundary wall can be s in the obtained contours.

JSR A
Journal of Scientific Reports

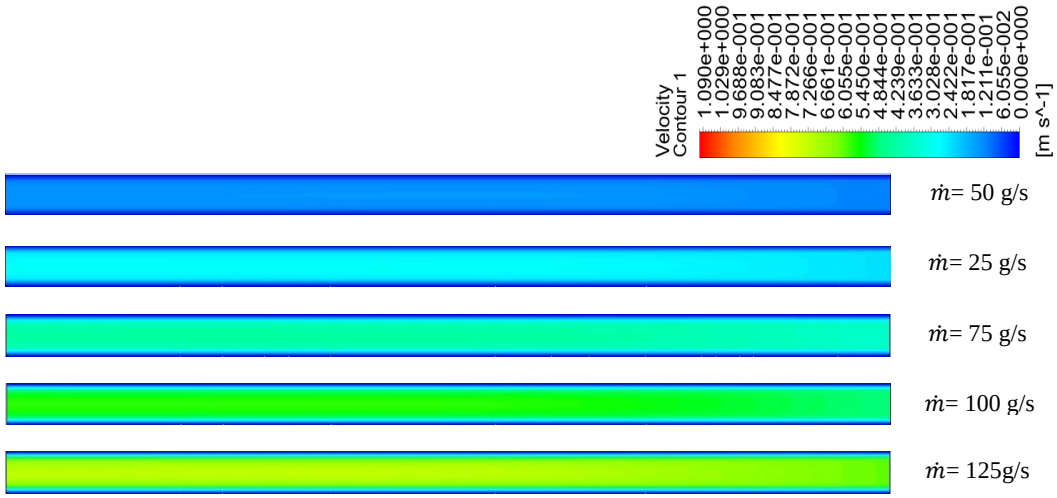

Figure 7. Velocity contours for plain pipe at different mass flow rates.

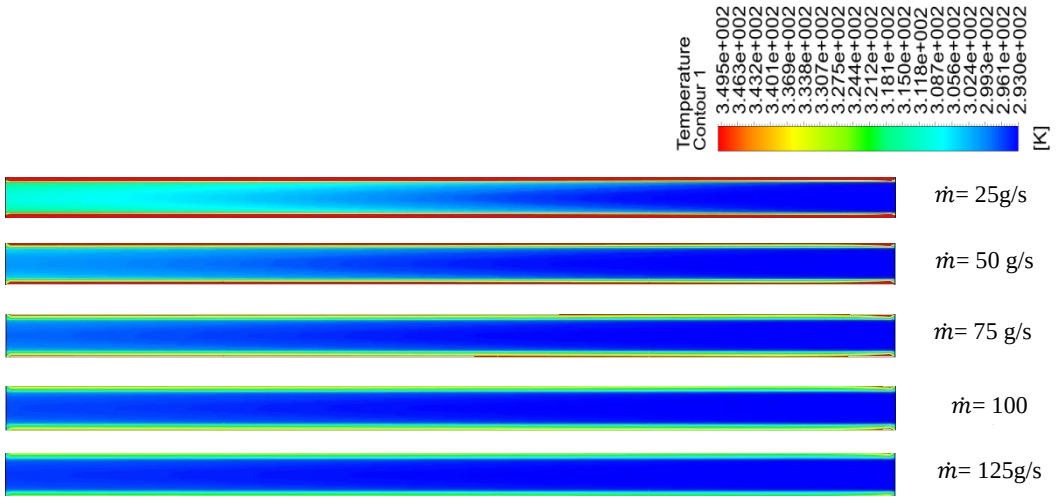

Figure 8. Temperature contours for plain pipe at different mass flow rates.

JSR A
Journal of Scientific Reports

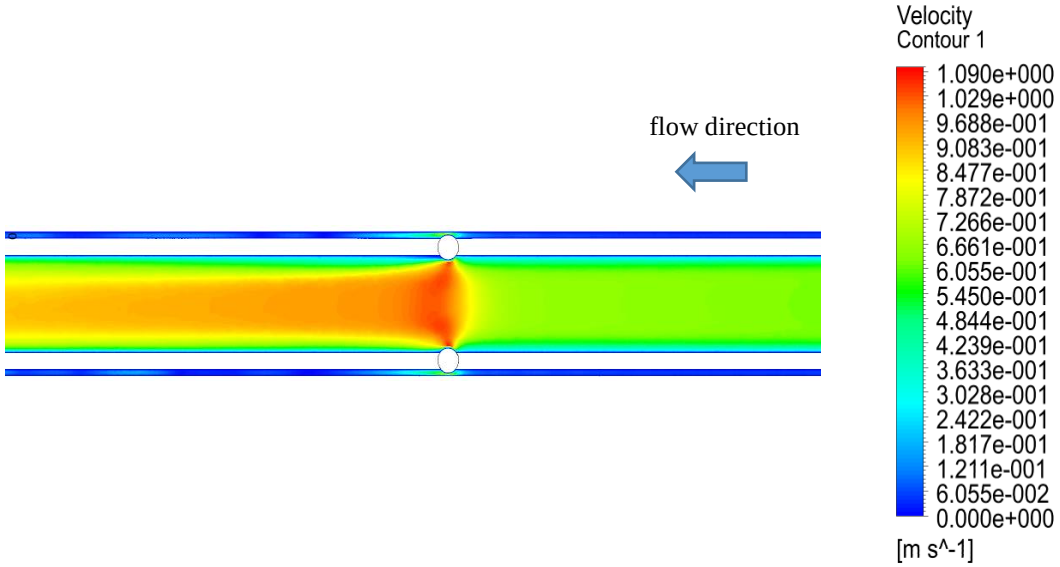

Figure 9. Velocity contour inside pipe at flow rate of 125 g/s.

In Figure 9, the velocity contour of the model has been shown at the fluid flow rate of 125 g/s. The circular turbulators have a favorable effect on disturbing and fluid mixing, and it can be seen that the maximum velocity is in the center of the pipe and the area inside the circular turbulators. The direction of fluid flow has been indicated by an arrow from right to left.

Additionally, velocity contours for pipe inserts (circular turbulators) have been presented in Figure 10 for different fluid flow rates of 25, 50, 75, 100, and 125 g/s. The numerical study was carried out to reveal the influence of installing circular turbulators on flow structure and heat transfer characteristics. It can be observed that Figure 10 demonstrates the fluid flow behavior inside the used pipe from the side view. By increasing the mass flow rate, the velocity variations for all experiments can be compared with those of the presented results.

JSR A
Journal of Scientific Reports

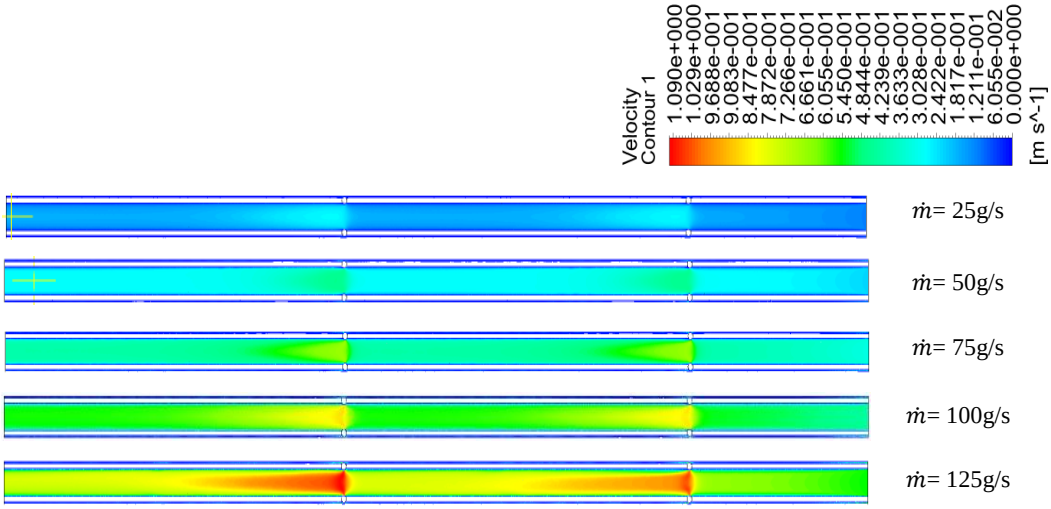

Figure 10. Velocity contours for pipe inserts at different mass flow rates.

To demonstrate the temperature distribution along the pipe equipped with circular turbulators for given mass flow rates, the temperature contours between two turbulators are presented in Figure 11. Temperature variation inside the pipe demonstrates the growth of thermal boundary layers through pipe length and regions around circular turbulators at different fluid mass flow rates. By analyzing temperature contours for different mass flow rates of 25, 50, 75, 100, and 125 g/s, it can be seen that the temperature gradient becomes larger in the boundary layer at lower mass flow rates. The figure also shows the effect of the turbulators on the temperature profile along the pipe.

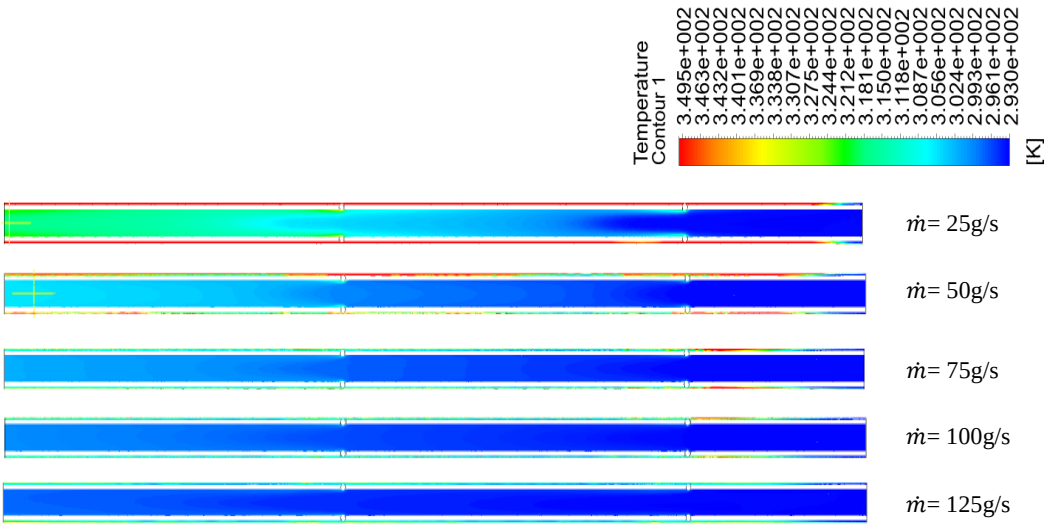

Figure 11. Temperature contours for pipe inserts at different mass flow rates.

5. CONCLUSION

In this study, the numerical results obtained for plain pipe were compared to those obtained for the pipe equipped with circular inserts. Adding the circular pipe inserts into the pipe and producing turbulence flow definitely improved the heat transfer characteristics of the water flow throughout the circular pipe, which received a constant heat flux. In the numerical experiments, different water mass flow rates were examined and by using simulation and visualization techniques, the thermal behavior and structure of the flow were characterized and significant contours were provided.

ACKNOWLEDGMENT

This research has not received any grants.

REFERENCES

[1] Min, C., Li, H., Gao, X., Wang, K., and Xie, L. (2021). Numerical investigation of convective heat transfer enhancement by a combination of vortex generator and in-tube inserts, International Communications in Heat and Mass Transfer, 127, 105490, doi: 10.1016/j.icheatmasstransfer.2021.105490.

[2] Sarada, S. N., Raju, A. V. Sita Rama, and Radha, K. K. (2010). Experimental numerical analysis enhancement of heat transfer in a horizontal circular tube using mesh inserts in turbulent region, European Journal of Mechanical and Environmental Engineering, 2, 3–18. [Online]. Available: http://www.bsmee.be/ejmee/ejmee20102.pdf

[3] Cao, Z., Wu, Z., Luan, H., and Sunden, B. (2017). Numerical study on heat transfer enhancement for laminar flow in a tube with mesh conical frustum inserts, Numerical Heat Transfer, Part A: Applications, 72, 1, 21–39, doi: 10.1080/10407782.2017.1353386.

[4] Mousa, M. H., Miljkovic, N., and Nawaz, K. (2021). Review of heat transfer enhancement techniques for single phase flows, Renewable and Sustainable Energy Reviews, 137, 110566, doi: 10.1016/j.rser.2020.110566.

[5] Jassim, N. A., Abdul Hussin, K., and Abdul Abbass, N. Y. (2017). Numerical investigation of Heat Transfer Enhancement in Circular Tube using Twisted Tape Inserts and Nanotechnology, ejuow, 5, 2, 42–54, doi: 10.31185/ejuow.Vol5.Iss2.57.

[6] Jinxing, W., Chao, W., Mingqiang, W., Yanhui, L., and Yafei, L. (2017). Numerical Simulation of Turbulent Fluid Flow and Heat Transfer in a Circular Tube with Twisted Tape Inserts, Journal of Zhengzhou University (Engineering Science). [Online]. Available: https://en.cnki.com.cn/article_en/cjfdtotal-zzgy201703003.htm

[7] Chamoli, S., Lu, R., Xie, J., and Yu, P. (2018). Numerical study on flow structure and heat transfer in a circular tube integrated with novel anchor shaped inserts, Applıed Thermal Engıneerıng, 135, 304–324, doi: 10.1016/j.applthermaleng.2018.02.052.

[8] Liu, P., Zheng, N., Shan, F., Liu, Z., and Liu, W. (2018). An experimental and numerical study on the laminar heat transfer and flow characteristics of a circular tube fitted with multiple conical strips inserts, Internatıonal Journal of Heat and Mass Transfer, 117, 691–709, doi: 10.1016/j.ijheatmasstransfer.2017.10.035.

[9] Waghole, D. R. (2018). Experimental and numerical investigation on heat transfer augmentation in a circular tube under forced convection with annular differential blockages/inserts (in En;en). Heat Mass Transfer, 54, 6, 1841–1846, doi: 10.1007/s00231-018-2276-8.

[10] Mohammed, H. A., Ali Abuobeida, I. A., Vuthaluru, H. B., and Liu, S. (2019). Two-phase forced convection of nanofluids flow in circular tubes using convergent and divergent conical rings inserts, International Communications in Heat and Mass Transfer, 101, 10–20, doi: 10.1016/j.icheatmasstransfer.2018.12.010.

[11] Nikoozadeh, A., Behzadmehr, A., and Payan, S. (2020). Numerical investigation of turbulent heat transfer enhancement using combined propeller-type turbulator and nanofluid in a circular tube (in En;en). J Therm Anal Calorim, 140, 3, 1029–1044, doi: 10.1007/s10973-019-08578-x.

[12] Liu, H., Zheng, G., Man, C., Jiang, K., and Lv, X. (2021). Numerical and Experimental Studies on Heat Transfer Enhancement in a Circular Tube Inserted with Twisted Tape Inserts, AJEE, 9, 2, 30, doi: 10.11648/j.ajee.20210902.12.

[13] Shivamallaiah, M. M. and Fernandes, D. V. (2021). Numerical investigation of heat transfer and friction factor characteristics of circular tube fitted with an array of semi-elliptical vortex generator inserts, Cogent Engineering, 8, 1, doi: 10.1080/23311916.2021.1968742.

[14] Karagoz, S., Afshari, F., Yildirim, O., and Comakli, O. (2017). Experimental and numerical investigation of the cylindrical blade tube inserts effect on the heat transfer enhancement in the horizontal pipe exchangers, Heat Mass Transfer, 53, 9, 2769–2784, doi: 10.1007/s00231-017-2021-8.

[15] Zheng, N., Liu, P., Wang, X., Shan, F., Liu, Z., and Liu, W. (2017). Numerical simulation and optimization of heat transfer enhancement in a heat exchanger tube fitted with vortex rod inserts, Applied Thermal Engineering, 123, 471–484, doi: 10.1016/j.applthermaleng.2017.05.112.

[16] Raheemah, S. H., Ashham, M. A., and Salman, K. (2019). Numerical investigation on enhancement of heat transfer using rod inserts in single pipe heat exchanger, JMES, 13, 4, 6112–6124, doi: 10.15282/jmes.13.4.2019.24.0480.

[17] Anvari, A. R., Javaherdeh, K., Emami-Meibodi, M., and Rashidi, A. M. (2014). Numerical and experimental investigation of heat transfer behavior in a round tube with the special conical ring

inserts, Energy Conversion and Management, 88, 214–217, doi: 10.1016/j.enconman.2014.08.030.

[18] Adiguzel, N. and Göcücü, A. (2021). Experimental Investigation of the Effects of Ring Turbulators on Heat Transfer in Two-Phase Flow (in En;en). Iran J Sci Technol Trans Mech Eng, 1–10, doi: 10.1007/s40997-021-00472-y.

[19] Outokesh, M., Ajarostaghi, S. S. M., Bozorgzadeh, A., and Sedighi, K. (2020). Numerical evaluation of the effect of utilizing twisted tape with curved profile as a turbulator on heat transfer enhancement in a pipe (in En;en). J Therm Anal Calorim, 140, 3, 1537–1553, doi: 10.1007/s10973-020-09336-0.

[20] Mashayekhi, R., Arasteh, H., Toghraie, D., Motaharpour, S. H., Keshmiri, A., and Afrand, M. (2020). Heat transfer enhancement of Water-Al2O3 nanofluid in an oval channel equipped with two rows of twisted conical strip inserts in various directions: A two-phase approach, Computers & Mathematics with Applications, 79, 8, 2203–2215, doi: 10.1016/j.camwa.2019.10.024.

[21] Agrebi, S., Solano, J. P., Snoussi, A., and ben Brahim, A. (2015). Numerical simulation of convective heat transfer in tube with wire coil inserts in *2015 World Symposium on Mechatronics Engineering & Applied Physics (WSMEAP)*.

[22] Abas, E. F., Weis, M. M., and Ridha, A. S. (2018). Experimental and Numerical Study of Heat Transfer Enhancement in a Shell and Tube Heat Exchanger using Helical Coiled Wire Inserts, Tikrit j. eng. sci., 25, 2, doi: 10.25130/tjes.25.2.10.

[23] Tatsumi, K., Iwai, H., and Inaoka, K. (2002). Numerical simulation for heat and fluid characteristics of square duct with discrete rib turbulators, Internatıonal Journal of Heat and Mass Transfer, 45, 21, 4353–4359, doi: 10.1016/S0017-9310(02)00141-2.

[24] Yakut, K., Sahin, B., and Canbazoglu, S. (2004). Performance and flow-induced vibration characteristics for conical-ring turbulators, Applied Energy, 79, 1, 65–76, doi: 10.1016/j.apenergy.2003.11.002.

[25] Salman, S. D., Kadhum, A. A. H., Takriff, M. S., and Mohamad, A. B. (2013). Numerical investigation of heat transfer and friction factor characteristics in a circular tube fitted with V-cut twisted tape inserts, Scıentıfic World Journal, 2013, 492762, doi: 10.1155/2013/492762.

[26] Omeroglu, G., Comakli, O., Karagoz, S., and Sahin, B. (2013). Experimental Research of Dynamic Instabilities in the Presence of Coiled Wire Inserts on Two-Phase Flow, Scıentıfic World Journal, doi: 10.1155/2013/714180.

[27] Alam, T., Saini, R. P., and Saini, J. S. (2014). Heat and flow characteristics of air heater ducts provided with turbulators—A review, Renewable and Sustainable Energy Reviews, 31, 289–304, doi: 10.1016/j.rser.2013.11.050.

[28] Razzaghi, H., Layeghi, M., Goodarzi, S., and Lotfizadeh, H. (2014). Numerical analysis of the effects of changeable transverse and longitudinal pitches and porous media inserts on heat transfer from an elliptic tube bundle, Journal of Theoretical and Applied Mechanics, Vol. 52 nr 3. [Online]. Available: https://yadda.icm.edu.pl/baztech/element/bwmeta1.element.baztech-f94cf59a-7087-451e-870a-ccd81ae53e56

[29] Yeşilyurt, M. K., Experimental Investigation of the Effects of Conical Springs on In-Pipe Heat Transfer and Flow Instability in Two-Phase Flows. Master Thesis, Atatürk University, 2015.

[30] Sheikholeslami, M. and Ganji, D. D. (2016). Heat transfer enhancement in an air to water heat exchanger with discontinuous helical turbulators; experimental and numerical studies, Energy, 116, 341–352, doi: 10.1016/j.energy.2016.09.120.

[31] Li, P., Liu, P., Liu, Z., and Liu, W. (2017). Experimental and numerical study on the heat transfer and flow performance for the circular tube fitted with drainage inserts, Internatıonal Journal of Heat and Mass Transfer, 107, 686–696, doi: 10.1016/j.ijheatmasstransfer.2016.11.094.

[32] Karuppasamy, M., Saravanan, R., Chandrasekaran, M., and Muthuraman, V. (2020). Numerical exploration of heat transfer in a heat exchanger tube with cone shape inserts and Al2O3 and CuO nanofluids, Materials Today: Proceedings, 21, 940–947, doi: 10.1016/j.matpr.2019.08.242.

[33] Yadav, S. and Sahu, S. K. (2019). Heat transfer augmentation in double pipe water to air counter flow heat exchanger with helical surface disc turbulators, Chemical Engineering and Processing - Process Intensification, 135, 120–132, doi: 10.1016/j.cep.2018.11.018.

[34] Jiang, G., Gao, J., and Shi, X. (2019). Flow and heat transfer characteristics of mist/steam two-phase flow in the U-shaped cooling passage with 60 deg. ribs, International Communications in Heat and Mass Transfer, 105, 73–83, doi: 10.1016/j.icheatmasstransfer.2019.02.023.

[35] Sheikholeslami, M., Abohamzeh, E., Jafaryar, M., Shafee, A., and Babazadeh, H. (2020). CuO nanomaterial two-phase simulation within a tube with enhanced turbulator, Powder Technology, 373, 1–13, doi: 10.1016/j.powtec.2020.06.017.

[36] Jiang, G., Gao, J., Shi, X., Li, F., and Xu, L. (2020). Reprint of: Flow and Heat Transfer Characteristics of the Mist/Steam Two-Phase Flow Cooling the Rectangular Channel with Column-Row-Ribs, Internatıonal Journal of Heat and Mass Transfer, 161, 120236, doi: 10.1016/j.ijheatmasstransfer.2020.120236.

[37] Khetib, Y., Sedraoui, K., Melaibari, A. A., and Alsulami, R. (2021). The numerical investigation of spherical grooves on thermal–hydraulic behavior and exergy efficiency of two-phase hybrid MWCNT-Al2O3/water nanofluid in a parabolic solar collector, Sustainable Energy Technologies and Assessments, 47, 101530, doi: 10.1016/j.seta.2021.101530.

[38] Xiong, Q., Izadi, M., Shokri rad, M., Shehzad, S. A., and Mohammed, H. A. (2021). 3D Numerical Study of Conical and Fusiform Turbulators for Heat Transfer Improvement in a

Double-Pipe Heat Exchanger, Internatıonal Journal of Heat and Mass Transfer, 170, 120995, doi: 10.1016/j.ijheatmasstransfer.2021.120995.

[39] Bashtani, I., Esfahani, J. A., and Kim, K. C. (2021). Effects of water-aluminum oxide nanofluid on double pipe heat exchanger with gear disc turbulators: A numerical investigation, Journal of the Taiwan Institute of Chemical Engineers, 124, 63–74, doi: 10.1016/j.jtice.2021.05.001.

[40] Ajarostaghi, S. S. M., Aghanezhad, M., Davudi, H., and Amiri, M. M. (2021). Numerical evaluation of the heat transfer enhancement in a tube with a curved conical turbulator insert, International Journal of Ambient Energy, 1–14, doi: 10.1080/01430750.2021.1945490.

Kütahya Dumlupınar University
Institute of Graduate Studies

Journal of Scientific
Reports-A
E-ISSN: 2687-6167
Number 53, June 2023

RESEARCH ARTICLE

THEORETICAL INVESTIGATION OF PERFORMANCE OF VAPOR COMPRESSION COOLING CYCLE FOR DME, R125, R134A, R143A, R152A, AND R32 REFRIGERANTS AND THEIR MIXTURES

Oğuz Ozan YOLCAN[1,*]

[1] Kütahya Dumlupinar University, Faculty of Engineering, Department of Mechanical Engineering, Kütahya, oguzozan.yolcan@dpu.edu.tr, ORCID: 0000-0002-6664-5675

Receive Date:28.12.2022 *Accepted Date: 04.05.2023*

ABSTRACT

In this study, the performances of refrigerant mixtures in ideal vapor compression refrigeration cycles were investigated theoretically. By choosing six different refrigerants as dimethyl ether (DME), R125, R134a, R143a, R152a, and R32, eleven different refrigerant mixtures were handled. Each mixture's vapor compression refrigeration cycle performances were evaluated according to three different condenser outlet temperatures and nine different mass fractions (90%/10% to 10%/90%). To examine the thermodynamic performance of refrigerant mixtures, constant evaporator outlet temperature (-10 ^{o}C) and different constant condenser outlet temperatures (20 ^{o}C, 25 ^{o}C, and 30 ^{o}C) were determined. According to the evaluated refrigerant mixtures, the COP_R values of the refrigerant mixtures containing DME were calculated as the highest among all the mixtures. In the mixtures containing DME, it was observed that the COP_R values decreased as the mass percentage of DME decreased. The COP_R values are calculated in the range of 3.66-5.70 for the R134a/R32 mixture, 3.82-5.81 for the R134a/R143a mixture, 3.97-5.99 for the R143a/R32 mixture, 3.83-5.83 for the R125/R143a mixture, 3.86-5.98 for the R125/R32 mixture, 4.34-6.24 for R134a/R152a mixture, 3.78-5.81 for R143a/R152a mixture, 3.57-5.55 for R152a/R32 mixture, 3.40-6.28 for DME/R125 mixture, 4.34-6.27 for DME/R134a mixture and 3.59-5.82 for the DME/R32 mixture.
When the pure forms and mixtures of the refrigerants discussed in the study are compared, it is seen that the pure DME and R32 gases are slightly more performant than the gas mixtures examined. The R125 gas mixture shows a higher performance than the pure R125 gas, and the R134a and R143a mixtures show slightly higher performance than the pure gas forms. Finally, the specific energies of pure refrigerants and refrigerant mixtures were calculated within the scope of the study. DME has the highest specific energy among pure refrigerants, while DME/R32 mixture has the highest specific energy among refrigerant mixtures.

Keywords: *Refrigerant mixture, Dimethyl Ether, R125, R134a, R143a, R152a, R32, COP_R.*

JSR A
Journal of Scientific Reports

1. INTRODUCTION

Heat pumps and refrigeration machines work according to the vapor compression refrigeration cycle, and refrigerants are used in these cycles. Different refrigerants perform differently in vapor compression refrigeration cycles with the same pressure ranges. In this study, eleven different refrigerant mixtures were created by choosing six different refrigerants. The performance (COP_R) of the refrigerant mixtures in the ideal vapor compression refrigeration cycle has been investigated theoretically. This study aims to compare the refrigerant mixture performances with the pure refrigerant performances.

Dalkılıç theoretically investigated the performance of various refrigerants/refrigerant mixtures in a cascade refrigeration cycle in his study. Mixtures of mixed refrigerants consisting of HFC-134a, HFC-152a, HC-600a, and HC-290 were investigated. Theoretical calculations were made according to different evaporator and condenser temperatures. It has been stated that azeotrope mixtures have higher performance than zeotrope mixtures [1]. Hasan and Chitheer investigated the performance of various pure refrigerants and binary or triple refrigerant mixtures in the refrigeration cycle [2]. Kılıç and İpek investigated the thermodynamic performance of R410A gas, which is a mixture of R125 and R32 gases. COP values of the cycle were calculated according to different evaporator and condenser temperatures [3]. Taylor et al. compared the thermodynamic performances of binary alkane mixtures and pure alkanes. COP values and exergy efficiencies of the mixtures were calculated [4]. Wu et al. investigated the thermodynamic performance of zeotropic mixtures of refrigerants. In addition, expressions giving residual enthalpy and entropy values are created [5]. Zühlsdorf et al. investigated the thermodynamic performance of 14 different refrigerants by simulating their mixtures with each other [6]. Khordad and Mirhosseini theoretically investigated the thermal conductivity of refrigerant mixtures and studied the relationship of thermal conductivity with temperature [7]. Baskaran and Mathews investigated the thermodynamic performance of DME and R152a mixtures. According to the results, it was determined that the mixture was more performant than the pure R152a fluid [8]. Saleh et al. investigated the thermodynamic performances of pure refrigerants and refrigerant mixtures in ideal and cascade refrigeration cycles [9]. Sawjanya and Rao examined the mixtures of 27 different refrigerants according to 3 different mixing methods and compared the Vapor-Liquid Equilibrium of the theoretical data with the experimental data [10]. Bolaji and Huan investigated the thermodynamic performance of R290 and R600a refrigerant mixtures in different mass fractions. According to the results obtained, it was stated that the mixtures showed more cooling effect than the R134a refrigerant, and the COP values were close to each other [11]. Arcaklıoğlu and Erişen investigated the thermodynamic performances of binary/triple/quadruple mixtures of R12, R125, R134a, R143a, R152a, R22, R290, R32, R502, and R600a refrigerants. It was stated that the COPR values of all mixtures ranged from 3.7 to 6.7. Fixed evaporator and condenser temperatures are considered in theoretical calculations [12]. Ranjan Panda and Behera experimentally investigated the performances of R290/R600a, R290/R600, LPG (R290/R600/R600a) and LPG/R134a refrigerant blends. Theoretical calculations depended on the different condenser and evaporator temperatures [13]. This study investigated and evaluated the ideal vapor-compression refrigerant cycle performances of DME, R125, R134a, R143a, R152a, and R32 refrigerants at different condenser outlet temperatures. Energy efficiency can be achieved by putting the studies on the ideal cycle into practice.

JSR A
Journal of Scientific Reports

2. MATERIAL and METHOD

2.1. Selected Refrigerants

This study evaluated the thermodynamic performance of DME refrigerant and R125, R134a, R143a, R152a, and R32 refrigerants. Although DME is a highly flammable substance, it has recently found reuse as a working fluid in cooling and heating systems due to its minimal GWP and zero ODP [14,15]. Ozone Depletion Potential (ODP) and Global Warming Potential (GWP) values and ASHRAE Safety Groups of the selected refrigerants are shared in Table 1. All selected refrigerants have ODP values of 0, while R125 and R143a refrigerants have high GWP values. DME fluid has a low GWP. In the selection of refrigerants, attention was paid to the low ODP value, fire safety, cost-effectiveness, and accessibility of the thermophysical properties of the refrigerants for theoretical calculations. Thermophysical properties of all refrigerants whose thermodynamic performances were examined were obtained from NIST databases [16]. Theoretical calculations of the refrigerant mixture performances were made under ideal vapor compression refrigeration cycle conditions. Evaporator and condenser outlet temperatures were determined to suit all mixing ratios' ideal vapor compression refrigeration cycle conditions. The mass fractions of the mixtures were evaluated for primary and secondary gas; 90%/10%, 80%/20%, 70%/30%, 60%/40%, 50%/50%, 40%/60%, 30%/70%, 20%/80%, and 10%/90% respectively.

Table 1. ODP and GWP values of selected refrigerants.

Refrigerant	ODP	GWP (100 years)	Safety Group [17]	Reference
Dimethyl ether (DME)	0	0.3	A3	[14,18]
R125	0	2800	A1	[19]
R134a	0	1300	A1	
R143a	0	3800	A2	
R152a	0	140	A2	
R32	0	650	A2	

2.2. Ideal Vapor Compression Cooling Cycle

The performances of the refrigerant mixtures were evaluated in the ideal vapor compression refrigeration cycle. To examine the thermodynamic performance of refrigerant mixtures, constant evaporator outlet temperature (-10 ^{o}C) and three different constant condenser outlet temperatures (20 ^{o}C, 25 ^{o}C, and 30 ^{o}C) were determined. The specific pressure-enthalpy and temperature-entropy diagrams of the ideal vapor compression refrigeration cycle are shown in Figure 1 [20].

JSR A
Journal of Scientific Reports

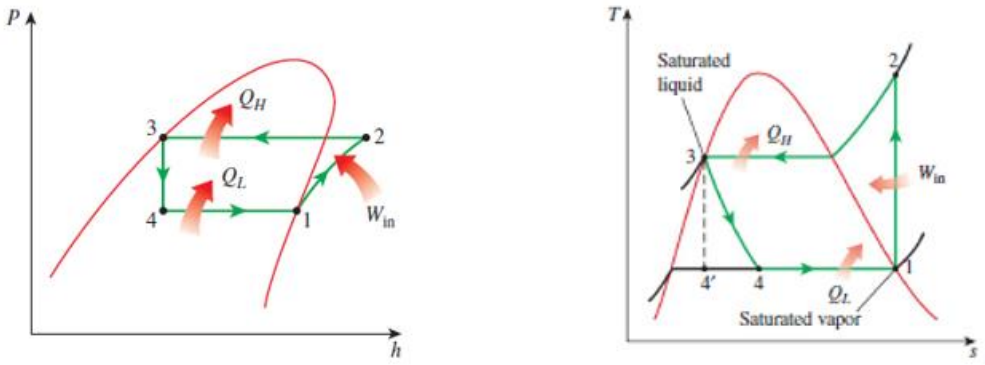

Figure 1. P-h and T-s diagrams of the ideal vapor compression refrigeration cycle [20].

The COP_R value of the ideal vapor compression refrigeration cycle is calculated by Eq. 1.

$$COP_R = \frac{h_1 - h_4}{h_2 - h_1} \quad (1)$$

Depending on the isentropic efficiency of the compressor, the enthalpy of point 2 is calculated by Eq. 2.

$$h_2 = \frac{(h_{2s} - h_1)}{\eta_c} + h_1 (kJ/kg) \quad (2)$$

The assumptions made in the calculations are given below.

Assumptions

- Steady-state flow.
- The cycle is accepted as the ideal vapor compression refrigeration cycle.
- In the calculations, the pressure drops in the cycle components, heat losses from the cycle to the environment, and heat gains from the environment to the cycle are neglected.
- The evaporator outlet temperature (T_1) was accepted as -10 ^oC, condenser outlet temperature (T_3) was accepted as 20 ^oC, 25 ^oC, and 30 ^oC.
- Compressor isentropic efficiency is accepted as 80%.
- Mixing ratios are given as mass fractions.

JSR A
Journal of Scientific Reports

3. RESULTS

3.1. Thermodynamic Performance of Refrigerant Mixtures

The COP_R charts of the refrigerant mixtures, according to their mass fractions and condenser outlet temperatures, are given below.

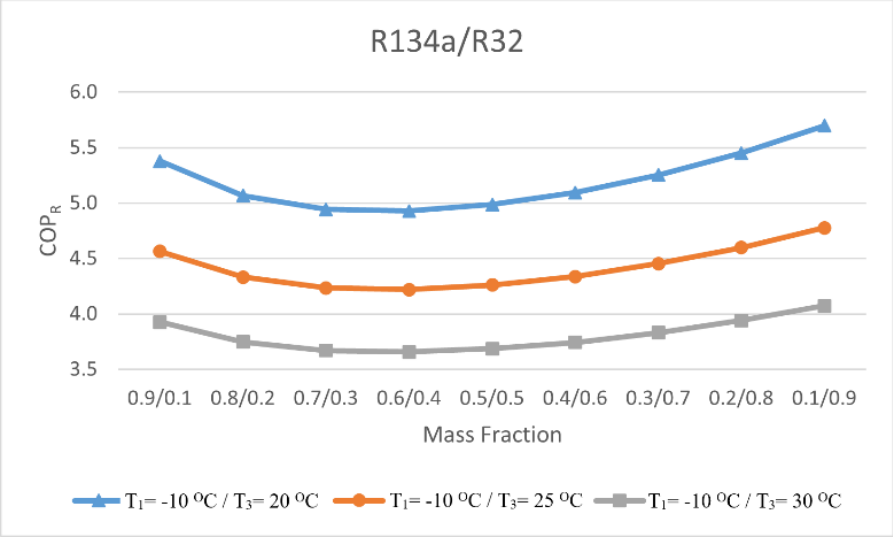

Figure 2. Thermodynamic performance of R134a/R32 mixture.

Figure 2 shows the COP_R values of the R134a/R32 mixture according to different condenser outlet temperatures and mass fractions. While it was observed that the COP_R value increased as the R32 mass ratio in the mixture increased, the highest COP_R values were calculated for the condenser outlet temperature of 20 ^oC. COP_R values are in the range of 3.66-5.70, in line with the acceptances.

Figure 3 shows the COP_R values of the R134a/R143a mixture according to different condenser outlet temperatures and mass fractions. While the mass ratio of R134a is high in the mixture, it is seen that the COP_R values are higher. The highest COP_R values were calculated for the condenser outlet temperature of 20 ^oC. COP_R values are in the range of 3.82-5.81, in line with the acceptances.

JSR A
Journal of Scientific Reports

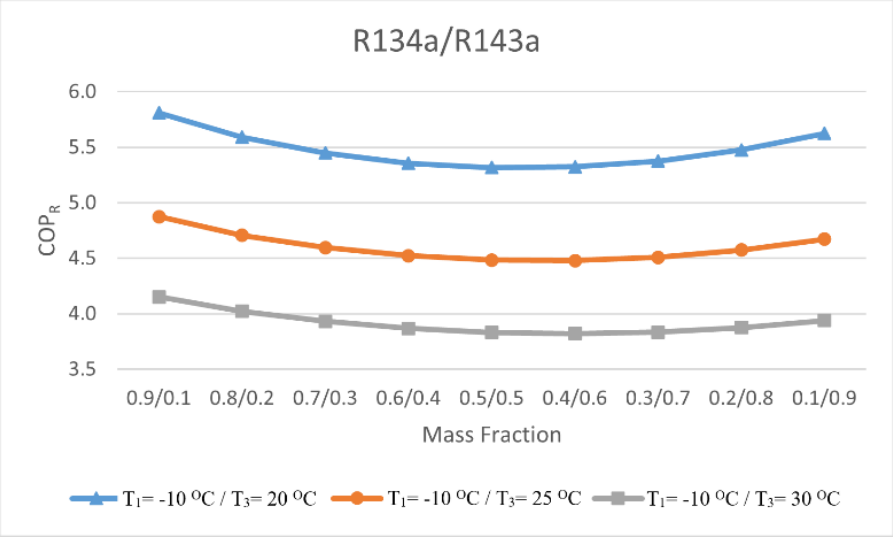

Figure 3. Thermodynamic performance of R134a/R143a mixture.

Figure 4 shows the COP_R values of the R143a/R32 mixture according to different condenser outlet temperatures and mass fractions. It is seen that the COP_R value of the mixture increases as the R32 mass ratio increases in the mixture. The highest COP_R values were calculated for the condenser outlet temperature of 20 ^oC. COP_R values are in the range of 3.97-5.99, in line with the acceptances.

Figure 5 shows the COP_R values of the R125/R143a mixture according to different condenser outlet temperatures and mass fractions. It is seen that the COP_R value of the mixture increases as the R143a mass ratio increases in the mixture. The highest COP_R values were calculated for the condenser outlet temperature of 20 ^oC. COP_R values are in the range of 3.83-5.83, in line with the acceptances.

Figure 6 shows the COP_R values of the R125/R32 mixture according to different condenser outlet temperatures and mass fractions. It is seen that the COP_R value of the mixture increases as the R32 mass ratio increases in the mixture. The highest COP_R values were calculated for the condenser outlet temperature of 20 ^oC. COP_R values are in the range of 3.86-5.98, in line with the acceptances.

JSR A
Journal of Scientific Reports

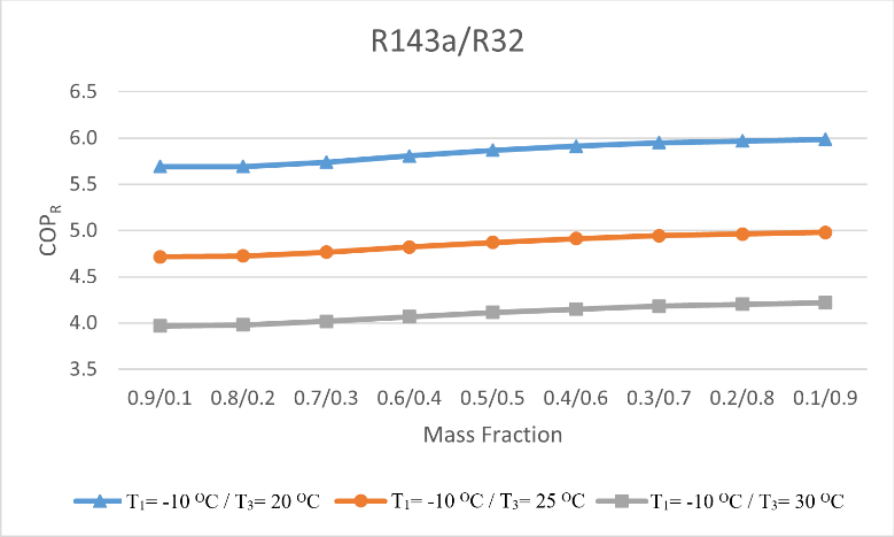

Figure 4. Thermodynamic performance of R143a/R32 mixture.

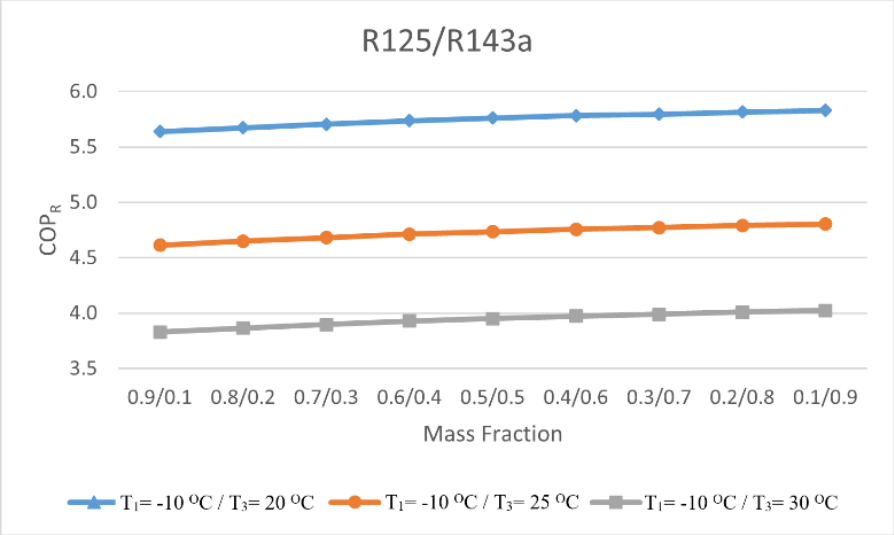

Figure 5. Thermodynamic performance of R1125/R143a mixture.

Figure 7 shows the COP_R values of the R134a/R152a mixture according to different condenser outlet temperatures and mass fractions. Although the COP_R values are constant according to the mass fractions, the COP_R values increase slightly as the ratio of R152a increases in the mixture. The highest

JSR A
Journal of Scientific Reports

COP_R values were calculated for the condenser outlet temperature of 20 ^oC. COP_R values are in the range of 4.34-6.24, in line with the acceptances.

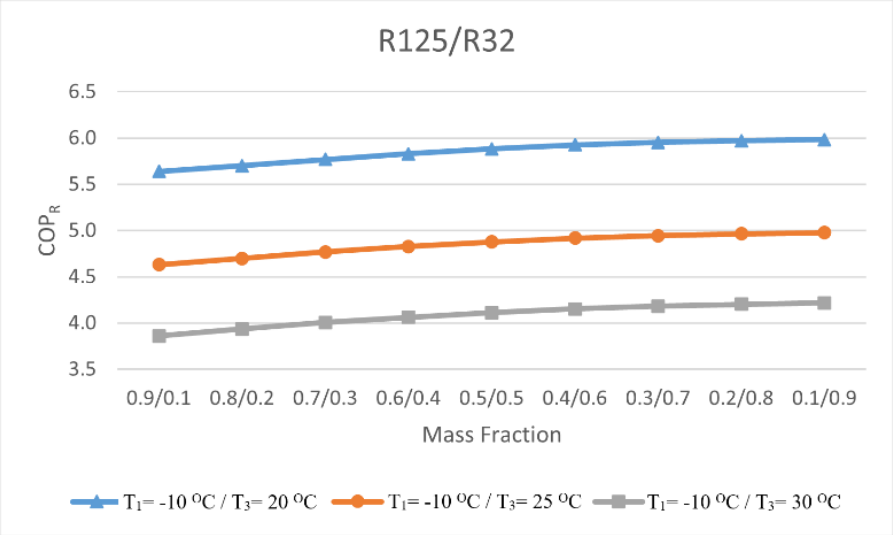

Figure 6. Thermodynamic performance of R125/R32 mixture.

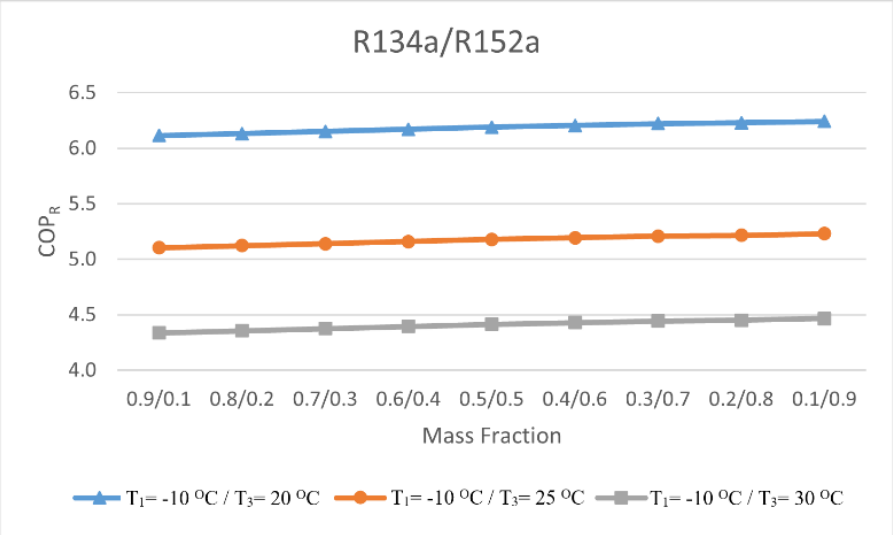

Figure 7. Thermodynamic performance of R134a/R152a mixture.

JSR A
Journal of Scientific Reports

Figure 8 shows the COP_R values of the R143a/R152a mixture according to different condenser outlet temperatures and mass fractions. While it was observed that the COP_R value increased as the R152a mass ratio in the mixture increased, the highest COP_R values were calculated for the condenser outlet temperature of 20 ^oC. COP_R values are in the range of 3.78-5.81, in line with the acceptances.

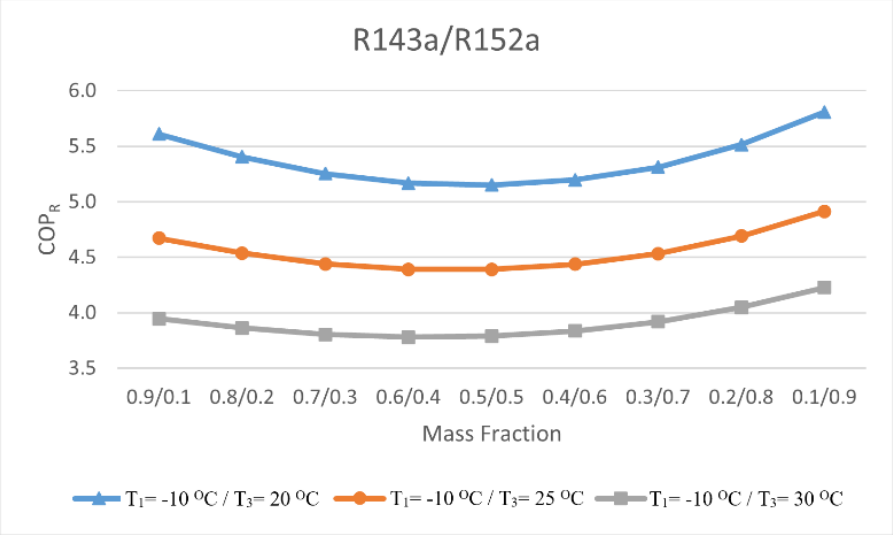

Figure 8. Thermodynamic performance of R143a/R152a mixture.

Figure 9 shows the COP_R values of the R152a/R32 mixture according to different condenser outlet temperatures and mass fractions. While it was observed that the COP_R value increased as the R152a mass ratio in the mixture increased, the highest COP_R values were calculated for the condenser outlet temperature of 20 ^oC. COP_R values are in the range of 3.57-5.55, in line with the acceptances.

JSR A
Journal of Scientific Reports

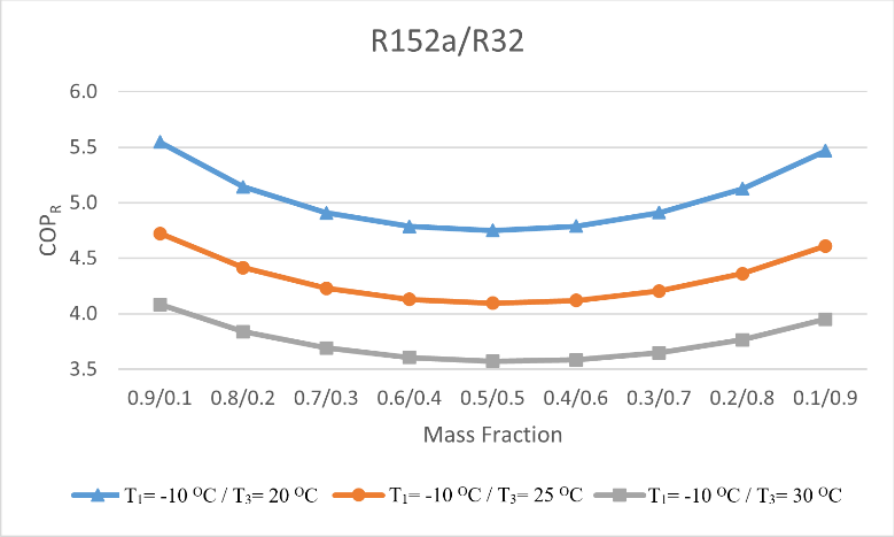

Figure 9. Thermodynamic performance of R152a/R32 mixture.

Figure 10 shows the COP_R values of the DME/R125 mixture according to different condenser outlet temperatures and mass fractions. As the mass ratio of R125 increases in the mixture, there is a sharp decrease in the COP_R values. The highest COP_R values were calculated for the condenser outlet temperature of 20 °C. COP_R values are in the range of 3.40-6.28, in line with the acceptances.

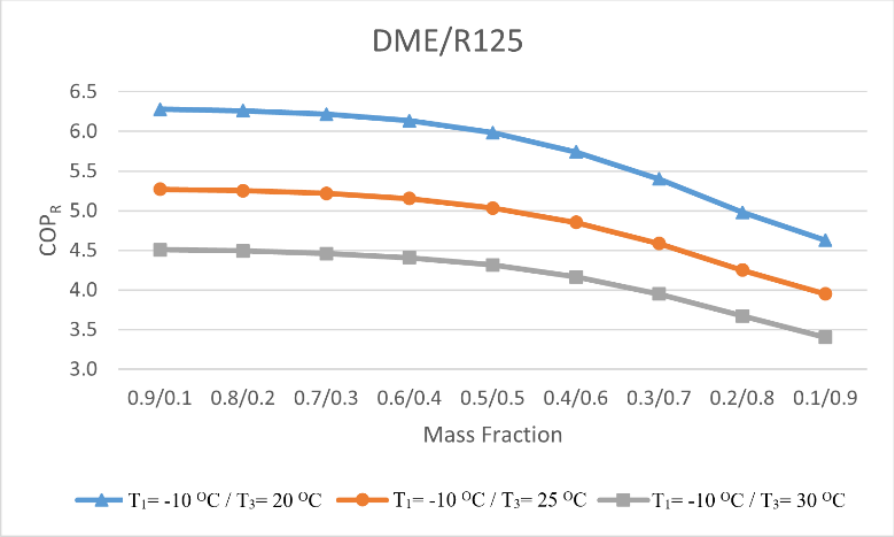

Figure 10. Thermodynamic performance of DME/R125 mixture.

JSR A
Journal of Scientific Reports

Figure 11 shows the COP_R values of the DME/R134a mixture according to different condenser outlet temperatures and mass fractions. Although the COP_R values are constant according to the mass fractions, the COP_R values increase slightly as the ratio of DME increases in the mixture. The highest COP_R values were calculated for the condenser outlet temperature of 20 ^oC. COP_R values are in the range of 4.34-6.27, in line with the acceptances.

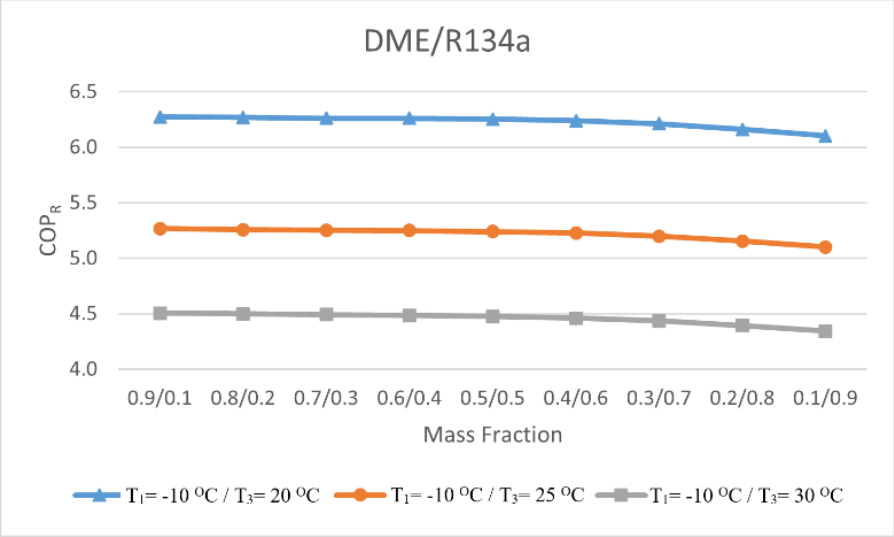

Figure 11. Thermodynamic performance of DME-R134a mixture.

Figure 12 shows the COP_R values of the DME/R32 mixture according to different condenser outlet temperatures and mass fractions. As the mass ratio of DME increases in the mixture, there is a sharp decrease in the COP_R values. The highest COP_R values were calculated for the condenser outlet temperature of 20 ^oC. COP_R values are in the range of 3.59-5.82, in line with the acceptances.

JSR A
Journal of Scientific Reports

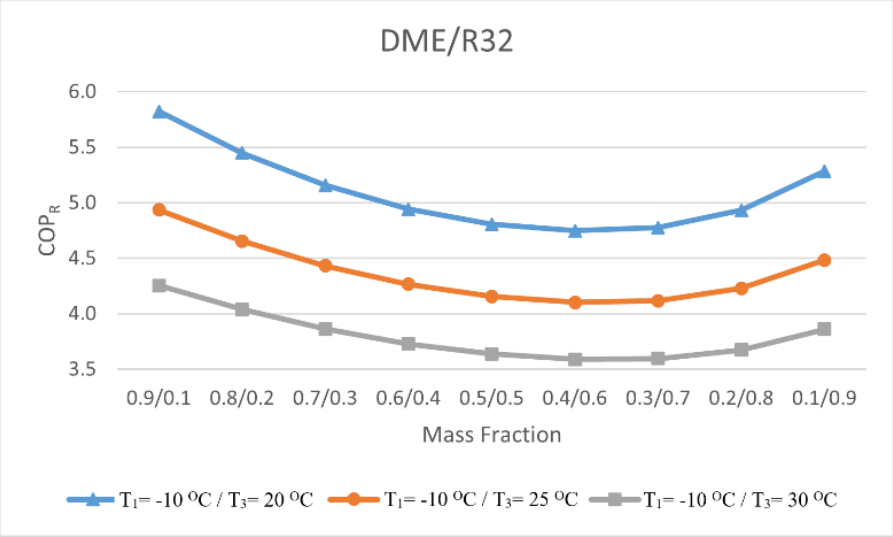

Figure 12. Thermodynamic performance of DME/R132 mixture.

The COP_R values of the refrigerant mixtures according to the condenser outlet temperatures and mass fractions are given in Table 2.

Table 2. COP_R values of the refrigerant mixtures according to the condenser outlet temperatures and mass fractions.

Mixture	Mass Fraction	T_1 (°C)	T_3 (°C)	COP_R	Mixture	Mass Fraction	T_1 (°C)	T_3 (°C)	COP_R
R134a/R32	0.9/0.1	-10	20	5.38	R134a/R143a	0.9/0.1	-10	20	5.81
	0.8/0.2			5.07		0.8/0.2			5.59
	0.7/0.3			4.94		0.7/0.3			5.45
	0.6/0.4			4.93		0.6/0.4			5.36
	0.5/0.5			4.99		0.5/0.5			5.32
	0.4/0.6			5.09		0.4/0.6			5.32
	0.3/0.7			5.25		0.3/0.7			5.37
	0.2/0.8			5.45		0.2/0.8			5.48
	0.1/0.9			5.70		0.1/0.9			5.63
	0.9/0.1		25	4.56		0.9/0.1		25	4.87
	0.8/0.2			4.33		0.8/0.2			4.71
	0.7/0.3			4.23		0.7/0.3			4.60
	0.6/0.4			4.22		0.6/0.4			4.52
	0.5/0.5			4.26		0.5/0.5			4.48
	0.4/0.6			4.34		0.4/0.6			4.48

JSR A
Journal of Scientific Reports

	0.3/0.7			4.45		0.3/0.7			4.51
	0.2/0.8			4.60		0.2/0.8			4.57
	0.1/0.9			4.78		0.1/0.9			4.67
	0.9/0.1			3.93		0.9/0.1			4.15
	0.8/0.2			3.75		0.8/0.2			4.02
	0.7/0.3			3.67		0.7/0.3			3.93
	0.6/0.4			3.66		0.6/0.4			3.87
	0.5/0.5		30	3.69		0.5/0.5		30	3.83
	0.4/0.6			3.74		0.4/0.6			3.82
	0.3/0.7			3.83		0.3/0.7			3.83
	0.2/0.8			3.94		0.2/0.8			3.88
	0.1/0.9			4.07		0.1/0.9			3.94

Table 2. COP_R values of the refrigerant mixtures according to the condenser outlet temperatures and mass fractions (continued).

Mixture	Mass Fraction	T_1 (^oC)	T_3 (^oC)	COP_R	Mixture	Mass Fraction	T_1 (^oC)	T_3 (^oC)	COP_R
	0.9/0.1			5.69		0.9/0.1			5.64
	0.8/0.2			5.69		0.8/0.2			5.67
	0.7/0.3			5.74		0.7/0.3			5.71
	0.6/0.4			5.81		0.6/0.4			5.74
	0.5/0.5		20	5.87		0.5/0.5		20	5.76
	0.4/0.6			5.91		0.4/0.6			5.78
	0.3/0.7			5.95		0.3/0.7			5.80
	0.2/0.8			5.97		0.2/0.8			5.82
	0.1/0.9			5.99		0.1/0.9			5.83
	0.9/0.1			4.72		0.9/0.1			4.61
	0.8/0.2			4.72		0.8/0.2			4.65
	0.7/0.3			4.77		0.7/0.3			4.68
R143a/R32	0.6/0.4	-10		4.82	R125/R143a	0.6/0.4	-10		4.71
	0.5/0.5		25	4.87		0.5/0.5		25	4.74
	0.4/0.6			4.91		0.4/0.6			4.76
	0.3/0.7			4.94		0.3/0.7			4.77
	0.2/0.8			4.96		0.2/0.8			4.79
	0.1/0.9			4.98		0.1/0.9			4.80
	0.9/0.1			3.97		0.9/0.1			3.83
	0.8/0.2			3.98		0.8/0.2			3.87
	0.7/0.3			4.02		0.7/0.3			3.90
	0.6/0.4		30	4.07		0.6/0.4		30	3.93
	0.5/0.5			4.12		0.5/0.5			3.95
	0.4/0.6			4.15		0.4/0.6			3.97
	0.3/0.7			4.18		0.3/0.7			3.99

JSR A
Journal of Scientific Reports

	0.2/0.8			4.20		0.2/0.8			4.01
	0.1/0.9			4.22		0.1/0.9			4.02

Table 2. COP_R values of the refrigerant mixtures according to the condenser outlet temperatures and mass fractions (continued).

Mixture	Mass Fraction	T_1 (^oC)	T_3 (^oC)	COP_R	Mixture	Mass Fraction	T_1 (^oC)	T_3 (^oC)	COP_R
R125/R32	0.9/0.1	-10	20	5.64	R134a/R152a	0.9/0.1	-10	20	6.12
	0.8/0.2			5.70		0.8/0.2			6.13
	0.7/0.3			5.77		0.7/0.3			6.15
	0.6/0.4			5.83		0.6/0.4			6.17
	0.5/0.5			5.88		0.5/0.5			6.19
	0.4/0.6			5.93		0.4/0.6			6.21
	0.3/0.7			5.95		0.3/0.7			6.22
	0.2/0.8			5.97		0.2/0.8			6.23
	0.1/0.9			5.98		0.1/0.9			6.24
	0.9/0.1		25	4.63		0.9/0.1		25	5.10
	0.8/0.2			4.70		0.8/0.2			5.12
	0.7/0.3			4.77		0.7/0.3			5.14
	0.6/0.4			4.83		0.6/0.4			5.16
	0.5/0.5			4.88		0.5/0.5			5.18
	0.4/0.6			4.92		0.4/0.6			5.19
	0.3/0.7			4.95		0.3/0.7			5.21
	0.2/0.8			4.96		0.2/0.8			5.22
	0.1/0.9			4.98		0.1/0.9			5.23
	0.9/0.1		30	3.86		0.9/0.1		30	4.34
	0.8/0.2			3.94		0.8/0.2			4.36
	0.7/0.3			4.00		0.7/0.3			4.38
	0.6/0.4			4.06		0.6/0.4			4.39
	0.5/0.5			4.11		0.5/0.5			4.41
	0.4/0.6			4.15		0.4/0.6			4.43
	0.3/0.7			4.18		0.3/0.7			4.44
	0.2/0.8			4.20		0.2/0.8			4.45
	0.1/0.9			4.22		0.1/0.9			4.46

JSR A
Journal of Scientific Reports

Table 2. COP_R values of the refrigerant mixtures according to the condenser outlet temperatures and mass fractions (continued).

Mixture	Mass Fraction	T_1 (°C)	T_3 (°C)	COP_R	Mixture	Mass Fraction	T_1 (°C)	T_3 (°C)	COP_R
R143a/R152a	0.9/0.1	-10	20	5.61	R152a/R32	0.9/0.1	-10	20	5.55
	0.8/0.2			5.40		0.8/0.2			5.14
	0.7/0.3			5.25		0.7/0.3			4.91
	0.6/0.4			5.17		0.6/0.4			4.79
	0.5/0.5			5.15		0.5/0.5			4.75
	0.4/0.6			5.20		0.4/0.6			4.79
	0.3/0.7			5.31		0.3/0.7			4.91
	0.2/0.8			5.51		0.2/0.8			5.13
	0.1/0.9			5.81		0.1/0.9			5.47
	0.9/0.1		25	4.67		0.9/0.1		25	4.72
	0.8/0.2			4.54		0.8/0.2			4.41
	0.7/0.3			4.44		0.7/0.3			4.23
	0.6/0.4			4.39		0.6/0.4			4.13
	0.5/0.5			4.39		0.5/0.5			4.10
	0.4/0.6			4.44		0.4/0.6			4.12
	0.3/0.7			4.53		0.3/0.7			4.20
	0.2/0.8			4.69		0.2/0.8			4.36
	0.1/0.9			4.91		0.1/0.9			4.61
	0.9/0.1		30	3.95		0.9/0.1		30	4.08
	0.8/0.2			3.86		0.8/0.2			3.84
	0.7/0.3			3.80		0.7/0.3			3.69
	0.6/0.4			3.78		0.6/0.4			3.61
	0.5/0.5			3.79		0.5/0.5			3.57
	0.4/0.6			3.84		0.4/0.6			3.59
	0.3/0.7			3.92		0.3/0.7			3.65
	0.2/0.8			4.05		0.2/0.8			3.76
	0.1/0.9			4.23		0.1/0.9			3.95

Table 2. COP_R values of the refrigerant mixtures according to the condenser outlet temperatures and mass fractions (continued).

Mixture	Mass Fraction	T_1 (°C)	T_3 (°C)	COP_R	Mixture	Mass Fraction	T_1 (°C)	T_3 (°C)	COP_R
DME/R125	0.9/0.1	-10	20	6.28	DME/R134a	0.9/0.1	-10	20	6.27
	0.8/0.2			6.26		0.8/0.2			6.27
	0.7/0.3			6.22		0.7/0.3			6.26
	0.6/0.4			6.13		0.6/0.4			6.26
	0.5/0.5			5.98		0.5/0.5			6.25

JSR A
Journal of Scientific Reports

	0.4/0.6			5.74		0.4/0.6			6.24
	0.3/0.7			5.40		0.3/0.7			6.21
	0.2/0.8			4.98		0.2/0.8			6.16
	0.1/0.9			4.63		0.1/0.9			6.10
	0.9/0.1		25	5.27		0.9/0.1		25	5.27
	0.8/0.2			5.25		0.8/0.2			5.26
	0.7/0.3			5.22		0.7/0.3			5.25
	0.6/0.4			5.15		0.6/0.4			5.25
	0.5/0.5			5.04		0.5/0.5			5.24
	0.4/0.6			4.85		0.4/0.6			5.23
	0.3/0.7			4.59		0.3/0.7			5.20
	0.2/0.8			4.25		0.2/0.8			5.16
	0.1/0.9			3.95		0.1/0.9			5.10
	0.9/0.1		30	4.51		0.9/0.1		30	4.51
	0.8/0.2			4.49		0.8/0.2			4.50
	0.7/0.3			4.46		0.7/0.3			4.49
	0.6/0.4			4.41		0.6/0.4			4.49
	0.5/0.5			4.31		0.5/0.5			4.48
	0.4/0.6			4.17		0.4/0.6			4.46
	0.3/0.7			3.95		0.3/0.7			4.44
	0.2/0.8			3.67		0.2/0.8			4.39
	0.1/0.9			3.40		0.1/0.9			4.34

Table 2. COP_R values of the refrigerant mixtures according to the condenser outlet temperatures and mass fractions (continued).

Mixture	Mass Fraction	T_1 (^oC)	T_3 (^oC)	COP_R
DME/R32	0.9/0.1	-10	20	5.82
	0.8/0.2			5.45
	0.7/0.3			5.16
	0.6/0.4			4.94
	0.5/0.5			4.81
	0.4/0.6			4.75
	0.3/0.7			4.78
	0.2/0.8			4.93
	0.1/0.9			5.28
	0.9/0.1		25	4.93
	0.8/0.2			4.66
	0.7/0.3			4.43
	0.6/0.4			4.27
	0.5/0.5			4.16
	0.4/0.6			4.10
	0.3/0.7			4.12

JSR A
Journal of Scientific Reports

	0.2/0.8			4.23
	0.1/0.9			4.48
	0.9/0.1			4.25
	0.8/0.2			4.04
	0.7/0.3			3.86
	0.6/0.4			3.73
	0.5/0.5		30	3.64
	0.4/0.6			3.59
	0.3/0.7			3.60
	0.2/0.8			3.67
	0.1/0.9			3.86

3.2. Comparison of Thermodynamic Performances of Pure and Mixed Refrigerants

In this part of the study, the pure thermodynamic performances of six different refrigerants whose thermodynamic performances were examined in the mixed state were evaluated. The conditions and assumptions applied in the thermodynamic performances discussed in the mixed form are also valid for pure refrigerants.

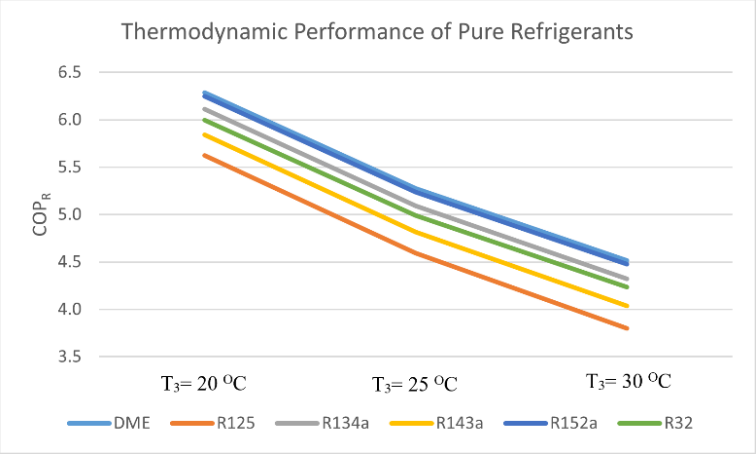

Figure 13. Thermodynamic performance of pure refrigerants.

The ideal vapor compression refrigeration cycle performances of pure refrigerants at evaporator outlet temperatures -10 °C and three different condenser outlet temperatures (20 °C, 25 °C, and 30 °C) are shown in Figure 13. According to the calculations, for the specified evaporator and condenser outlet temperatures, the COP_R values calculated; for DME gas are 6.3, 5.3, and 4.5; the COP_R values of R125 gas are 5.6, 4.6, and 3.8, and the COP_R values of R134a gas are 6.1, 5.1 and 4.3, COP_R values of R143a gas 5.8, 4.8 and 4.0, COP_R values of R152a gas 6.2, 5.2 and 4.5, COP_R values of R32 gas 6.0, 5.0 and 4.2, respectively.

JSR A
Journal of Scientific Reports

Table 3 compares the refrigerants' pure state performances with the mixing performances. In Table 3, the COPR values of the pure refrigerants according to the condenser outlet temperatures and the highest and lowest COPR values of the evaluated refrigerants in the mixture (IM) are given. Mixture details are given in the table description (MF=mass fraction).

Table 3. Comparison of pure and mixed refrigerants (a=DME/R125, T_3= 20 ^{O}C, MF=0.9/0.1, b=DME/R125, T_3= 30 ^{O}C, MF=0.1/0.9, c=DME/R134a, T_3= 20 ^{O}C, MF=0.9/0.1, d=R134a/R32, T_3= 30 ^{O}C, MF=0.6/0.4, e=R143a/R32, T_3= 20 ^{O}C, MF=0.1/0.9, f=R134a/R32, T_3= 30 ^{O}C, MF=0.6/0.4, g=R134a/R152a, T_3= 20 ^{O}C, MF=0.1/0.9, h=R152a/R32, T_3= 30 ^{O}C, MF=0.5/0.5).

	T_3= 20 ^{o}C	T_3= 25 ^{o}C	T_3= 30 ^{o}C	Highest COP_R IM	Lowest COP_R IM
DME	6.3	5.3	4.5	6.28 (a)	3.40 (b)
R125	5.6	4.6	3.8	6.28 (a)	3.40 (b)
R134a	6.1	5.1	4.3	6.27 (c)	3.66 (d)
R143a	5.8	4.8	4.0	5.99 (e)	3.78 (f)
R152a	6.2	5.2	4.5	6.24 (g)	3.57 (h)
R32	6.0	5.0	4.2	5.99 (e)	3.57 (h)

When Table 3 is examined, it is seen that pure DME and R32 gases are slightly more performant than the gas mixtures examined. The R125 gas mixture performs better than the pure R125 gas, and the R134a and R143a mixtures show slightly higher performance than the pure gas forms.

The specific energies (SE) of pure refrigerants and refrigerant mixtures are also calculated. While calculating the specific energies, the evaporator cooling load is considered in the ideal cycle. The specific cooling energy is calculated by Eq. 3.

$$SE = h_1 - h_4(kJ/kg) \quad (3)$$

Table 4. Specific energies of pure refrigerants according to different condenser outlet temperatures (kJ/kg).

Refrigerant	T_3=-20 ^{o}C	T_3=-25 ^{o}C	T_3=-30 ^{o}C
DME	377.16	365.02	352.74
R125	102.22	95.37	88.33
R134a	165.19	158.11	150.94
R143a	151.52	143.35	134.98
R152a	265.38	256.42	247.35
R32	276.9	267.42	257.7

The specific energies of pure refrigerants are shown in Table 4. Accordingly, the highest specific energy was calculated for DME fluid in the ideal vapor compression cycle, and the lowest specific energy was calculated for R125 fluid. As the constant condenser outlet temperature increases, the specific energy decreases.

JSR A
Journal of Scientific Reports

The specific energies of the refrigerant mixtures according to different mass fractions and condenser outlet temperatures are shown in Table 5. The DME/R32 mixture had the highest specific energy, while the lowest was in the R125/R143a mixture. As the constant condenser outlet temperature increases, the specific energy decreases. In mixtures containing DME, it is seen that the mass fraction of DME and the specific energy are directly proportional.

Table 5. Specific energies of refrigerant mixtures according to different mass fractions and condenser outlet temperatures (kJ/kg).

T_3 (^oC)	MF	R134a / R32	R134a / R143a	R143a / R32	R125 / R143a	R125 / R32	R134a/ R152a
20	0.9/0.1	176.41	164.17	160.93	107.81	119.04	176.06
	0.8/0.2	187.68	163.08	171.25	113.19	135.64	186.67
	0.7/0.3	198.97	161.94	182.38	118.39	152.31	197.05
	0.6/0.4	210.28	160.72	194.26	123.44	169.21	207.24
	0.5/0.5	221.56	159.43	206.8	128.36	186.43	217.26
	0.4/0.6	232.79	158.07	219.92	133.17	203.96	227.12
	0.3/0.7	243.96	156.61	233.57	137.87	221.79	236.85
	0.2/0.8	255.05	155.04	247.64	142.5	239.91	246.46
	0.1/0.9	266.05	153.36	262.11	147.04	258.28	255.97
25	0.9/0.1	169.1	157	152.58	100.82	111.84	168.75
	0.8/0.2	180.14	155.8	162.74	106.07	128.13	179.15
	0.7/0.3	191.19	154.56	173.73	111.13	144.51	189.32
	0.6/0.4	202.26	153.24	185.46	116.05	161.15	199.32
	0.5/0.5	213.3	151.85	197.88	120.84	178.11	209.14
	0.4/0.6	224.29	150.37	210.88	125.52	195.39	218.83
	0.3/0.7	235.22	148.8	224.41	130.09	212.99	228.38
	0.2/0.8	246.07	147.12	238.38	134.59	230.88	237.82
	0.1/0.9	256.81	145.32	252.74	139	249.02	247.17
30	0.9/0.1	161.68	149.71	144.02	93.65	104.46	161.35
	0.8/0.2	172.47	148.41	154.01	98.77	120.42	171.53
	0.7/0.3	183.28	147.06	164.83	103.69	136.51	181.5
	0.6/0.4	194.1	145.63	176.43	108.48	152.87	191.29
	0.5/0.5	204.88	144.12	188.71	113.13	169.56	200.93
	0.4/0.6	215.62	142.53	201.59	117.68	186.6	210.43
	0.3/0.7	226.29	140.84	215.01	122.12	203.96	219.81
	0.2/0.8	236.88	139.03	228.87	126.48	221.61	229.08
	0.1/0.9	247.36	137.09	243.13	130.77	239.53	238.26

JSR A
Journal of Scientific Reports

Table 5. Specific energies of refrigerant mixtures according to different mass fractions and condenser outlet temperatures (kJ/kg) (continued).

T_3 (^oC)	MF	R143a / R152a	R152a / R32	DME / R125	DME / R134a	DME / R32
20	0.9/0.1	162.32	266.77	353.34	357.12	370.7
	0.8/0.2	173.33	268.23	329.24	336.96	363.73
	0.7/0.3	184.46	269.74	304.79	316.67	356.18
	0.6/0.4	195.7	271.25	279.89	296.21	348.01
	0.5/0.5	207.04	272.73	254.41	275.53	339.1
	0.4/0.6	218.48	274.09	228.14	254.57	329.37
	0.3/0.7	230.02	275.32	200.79	233.25	318.65
	0.2/0.8	241.68	276.28	171.82	211.43	306.68
	0.1/0.9	253.46	276.88	140.23	188.87	293.01
25	0.9/0.1	154.11	257.79	341.78	345.49	358.89
	0.8/0.2	165.06	259.22	318.26	325.85	352.24
	0.7/0.3	176.12	260.69	294.38	306.07	345.02
	0.6/0.4	187.29	262.16	270.05	286.12	337.15
	0.5/0.5	198.55	263.59	245.13	265.96	328.54
	0.4/0.6	209.9	264.9	219.43	245.51	319.09
	0.3/0.7	221.35	266.06	192.63	224.7	308.63
	0.2/0.8	232.92	266.96	164.19	203.37	296.88
	0.1/0.9	244.61	267.48	133.08	181.31	283.41
30	0.9/0.1	145.7	248.68	330.09	333.74	346.94
	0.8/0.2	156.61	250.08	307.15	314.62	340.63
	0.7/0.3	167.62	251.5	283.85	295.36	333.71
	0.6/0.4	178.72	252.92	260.09	275.93	326.16
	0.5/0.5	189.91	254.29	235.75	256.28	317.84
	0.4/0.6	201.18	255.54	210.62	236.34	308.66
	0.3/0.7	212.55	256.63	184.36	216.04	298.44
	0.2/0.8	224.03	257.44	156.45	195.22	286.91
	0.1/0.9	235.63	257.87	125.8	173.66	273.6

4. EVALUATIONS

In this study, by choosing six different refrigerants as dimethyl ether (DME), R125, R134a, R143a, R152a, and R32, 11 different refrigerant mixtures were handled, and vapor compression refrigeration cycle performances of each mixture were evaluated according to three different condenser outlet temperatures and nine different mass fractions.

According to the evaluated refrigerant mixtures, the COP_R values of the refrigerant mixtures containing DME were calculated as the highest among all the mixtures. The COP_R value of the DME&R125 mixture with 90% DME - 10% R125 mass fraction was calculated as 7.85 for -10 ^oC

evaporator outlet temperature and 20 ^{o}C condenser outlet temperature. The COP_R value of the DME&R134a mixture with 90% DME - 10% R134a mass fraction was calculated as 7.84 for -10 ^{o}C evaporator outlet temperature and 20 ^{o}C condenser outlet temperature.

When the pure forms and mixtures of the refrigerants discussed in the study are compared, it is seen that the pure DME and R32 gases are slightly more performant than the gas mixtures examined. The R125 gas mixture shows a higher performance than the pure R125 gas, and the R134a and R143a mixtures show a slightly higher performance than the pure gas forms.
In this study, the vapor compression refrigeration cycle performances of six different pure refrigerants were determined, and the vapor compression refrigeration cycle performances of eleven different refrigerant mixtures formed by these pure refrigerants were theoretically investigated under the accepted conditions. In future studies, the performance of refrigerant mixtures under real conditions can be evaluated by considering an example system. At the same time, exergy analyses of refrigerant mixtures will be evaluated in future studies.

ACKNOWLEDGMENT

There is no conflict of interest with any person/institution in the paper.

REFERENCES

[1] Dalkılıç, A.S. (2012). Theoretical analysis on the prediction of performance coefficient of two-stage cascade refrigeration system using various alternative refrigerants. Journal of Thermal Science and Technology, 32 (1), 67–79.

[2] Ismael Hasan, M. and Mohsin Chitheer, J. (2021). Theoretical analysis of vapour refrigeration cycle with hybrid refrigerant of different types and mixing ratios. University of Thi-Qar Journal for Engineering Sciences, 111 (2), 24–32.

[3] Kılıç, B. and İpek, O. (2021). Performance analysis of vapor compression refrigeration system using mixed refrigerant R410a. International Journal of Energy Applications and Technologies, 8 (2), 60–64.

[4] Taylor, J.J., Carson, J.K., Hoang, D.K., Walmsley, T.G., Chen, Q. and Cleland, D.J. (2022). Use of refrigerant blends to improve thermal efficiency of heat pump cycles. Chemical Engineering Transactions, 94 (1), 1189–1194.

[5] Wu, Y., Zhang, H., Zhang, Q., Qiu, J. and Rui, S. (2017). The study of thermodynamic properties of zeotropic mixtures of R600a/R23/R14. Advances in Mechanical Engineering, 9 (3), 168781401769121.

[6] Zühlsdorf, B., Jensen, J.K., Cignitti, S., Madsen, C. and Elmegaard, B. (2017). Improving efficiency of heat pumps by use of zeotropic mixtures for different temperature glides.

Proceedings of ECOS 2017: 30th International Conference on Efficiency, Cost, Optimization, Simulation and Environmental Impact of Energy Systems, San Diego, California, USA, 2-6 July 2017.

[7] Khordad, R. and Mirhosseini, B. (2015). Transport Properties of refrigerant mixtures: thermal conductivity. Iranian Journal of Chemistry and Chemical Engineering, 34 (1), 75–85.

[8] Baskaran, A. and Mathews, K. (2015). Thermodynamic analysis of R152a and Dimethylether refrigerant mixtures in refrigeration system. Jordan Journal of Mechanical and Industrial Engineering, 9 (4), 289–296.

[9] Saleh, B., Aly, A.A., Alsehli, M., Elfasakhany, A. and Bassuoni, M.M. (2020). Performance analysis and working fluid selection for single and two stages vapor compression refrigeration cycles. Processes, 8 (9), 1017.

[10] Sawjanya, Y. and Rao, Y.C. (2007). Prediction of VLE data for alternative refrigerant mixtures. Korean Journal of Chemical Engineering, 24 (1), 106–112.

[11] Bolaji, B.O. and Huan, Z. (2013). Thermodynamic analysis of the performance of a vapour compression refrigeration system, working with R290 and R600a mixtures. Scientia Iranica B, 20 (6), 1720–1728.

[12] Arcaklioğlu, E. and Erişen, A. (2003). Soğutucu akışkan karışımlarının buhar sıkıştırmalı soğutma sisteminde termodinamik analizi. Pamukkale Üniversitesi Mühendislik Bilimleri Dergisi, 9 (2), 153–162.

[13] Ranjan Panda, S. and Behera, P. (2019). Experimental research on the performance of environmental friendly refrigerant mixtures in a vapour compression refrigeration system. Proceedings of International Conference on Artificial Intelligence in Manufacturing & Renewable Energy (ICAIMRE), Bhubaneswar, India, 25-26 October 2019.

[14] Gil, B., Fievez, A. and Zajaczkowski, B. (2021). Pool boiling heat transfer coefficient of dimethyl ether and its azeotropic ternary mixtures. International Journal of Heat and Mass Transfer, 171 (1), 121063.

[15] Gil, B. and Fijałkowska, B. (2019). Experimental study of nucleate boiling of flammable, environmentally friendly refrigerants. Energies, 13 (1), 160.

[16] NIST. (2020). NIST chemistry webbook, SRD 69, thermophysical properties of fluid systems. National Institute of Standards and Technology, USA.

[17] ASHRAE. (2008). ASHRAE standard designation and safety classification of refrigerants.

[18] Good, D.A., Francisco, J.S., Jain, A.K. and Wuebbles, D.J. (1998). Lifetimes and global warming potentials for dimethyl ether and for fluorinated ethers: CH_3 OCF_3 (E143a), CHF_2 $OCHF_2$ (E134), CHF_2 OCF_3 (E125). Journal of Geophysical Research: Atmospheres, 103 (D21), 28181–28186.

[19] Roy, Z. and Halder, G. (2020). Replacement of halogenated refrigerants towards sustainable cooling system: a review. Chemical Engineering Journal Advances, 3 (1), 100027.

[20] Cengel, Y.A. and Boles, M.A. (2015). Thermodynamics: an engineering approach. 8th Edition McGraw-Hill.

Kütahya Dumlupınar University
Institute of Graduate Studies

Journal of Scientific
Reports-A
E-ISSN: 2687-6167
Number 53, June 2023

REVIEW ARTICLE

THE APPLICATION OF HIGH HYDROSTATIC PRESSURE IN MEAT AND MEAT PRODUCTS: A REVIEW

Berna CAPAN[1*], Aytunga BAĞDATLI[2]

[1]Ege University, Faculty of Engineering, Food Engineering, Izmir, bernacapan@hotmail.com, ORCID: 0000-0002-6285-0081
[2]Manisa Celal Bayar University, Faculty of Engineering, Food Engineering, Manisa, aytunga.bagdatli@cbu.edu.tr, ORCID: 0000-0002-6080-7901

Receive Date:22.08.2022 *Accepted Date: 03.05.2023*

ABSTRACT

Heat treatment processes are widely used because they inactivate microorganisms and enzymes. However, thermal applications lead to changes in the physical and chemical structure of foods, as well as to deterioration of their sensory properties and natural components. For this reason, studies have been conducted on non-thermal technologies for food preservation. This technology extends the shelf life of foods and provides microbiologically safe, higher quality products. From the studies, it has good potential for the meat industry. The aim of this review was to compile the current state of research in this field and provide information on the characteristics, applications, advantages and disadvantages of non-thermal high hydrostatic pressure technology in meat and meat products.

Keywords: *High hydrostatic pressure, Meat quality, Meat products, Sensory, Texture profile*

1. INTRODUCTION

Numerous thermal and non-thermal processes have been developed in the meat industry to meet consumer demand for less processed products. Among all these non-thermal processes, the use of high hydrostatic pressure (HHP) is perhaps the most widely used [1]. High hydrostatic pressure is now used in the meat industry in many countries [2]. As a result, both food scientists and industry are increasingly interested in HHP processing [3]. Since this technology is applied at normal temperatures, which is one of the outstanding methods within the alternative processes, is one of the preservation methods that minimizes the negative effects that can be caused by high temperatures [4].

High hydrostatic pressure process is widely used not only for meat and meat products, but also for seafood, fruits and vegetables [5]. HHP is a physical process in which food is subjected to uniform pressure treatment from all directions [6]. It is a process in which solid and liquid foods are subjected to pressures of 100-1000 MPa with or without packaging [7; 8; 9; 10; 11; 12; 13]. Commercially, pressure application times range from milliseconds (by agitator pumps) to over 1200 seconds [14]. Sterilization of packaged foods by high hydrostatic pressure allows lower energy consumption and

reduction of chemical additives and preservatives [15]. The main principle is the compression of water by the surrounding material [7; 9; 11, 16]. However, it is also extremely important that the product is placed in a flexible container before the food is subjected to this process [17]. The packaging material should be able to form a strong barrier (about 15% deformation at 600 MPa for vacuum packed meat) and not migrate into the product [18].

The effects of HHP application on microorganisms and proteins/enzymes are similar to the effects of high temperatures. HHP is considered as "light technology" [19]. Thanks to low temperature, the natural properties of food such as smell, taste texture, and nutritional values are better preserved [20]. High pressure affects the morphological structures of microorganisms. The cell structure is very sensitive to pressure [21]. A pressure of several tens of MPa can reduce the growth rate, while a pressure of several hundreds of MPa can reduce the viability of bacterial cells [22]. Increasing the pressure and time applied to the food accelerates microbial inactivation [23].

High hydrostatic pressure does not break the covalent bonds [4]. During the preservation process, vitamins, flavors, and color molecules are preserved without degrading [24]. High hydrostatic pressure has the most application in meat technology [25]. In addition, HHP of meat products is a fast-growing industry as shown by the large number of patents granted in recent years [26]. This application has been developed and put into practice in many countries to obtain soft meat and improve its quality [27]. Food treated with high hydrostatic pressure is now commercially produced in developed countries [28].

A high hydrostatic pressure system consists of four main parts [29]:
- Pressure vessel
- Pressure generation system
- Material conveying system
- Temperature control device

The pressure chamber is loaded, closed, and degassed, and the pressure is transferred to the food via a liquid using a pump. HHP accelerates reactions involving volume change at the molecular level [18]. Special hydraulic oils, hydrocarbons, or water are used as pressurized fluids to transfer the pressure applied in the high-pressure hydrostatic system to the food. However, in practice, water is most commonly used because it reduces volume and is cheaper than gasses [30].
The main applications of high hydrostatic pressure are shown in Figure 1 [8, 16].

JSR A
Journal of Scientific Reports

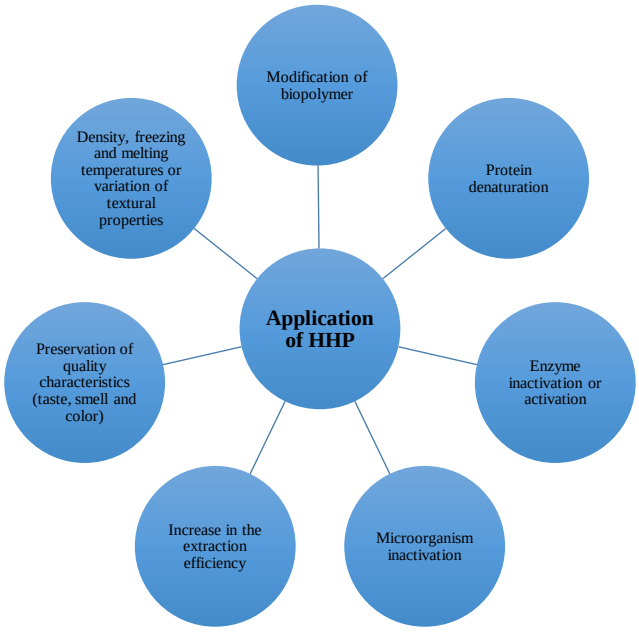

Figure 1. The main applications of HHP.

The advantages of using HHP

- Environmentally friendly method, as it consumes only electrical energy and does not generate waste [19].
- Since the pressure is evenly distributed on the food, it ensures homogeneous preservation of the food [8]
- Short processing times (compared to traditional methods) [11]
- The pressure to be applied does not depend on the shape and size of the food. Therefore, separate process parameters for each food are not required [31]
- HHP can be used to reduce the salt amount of emulsion-type meat products [8].

The disadvantages of using HHP [31]

- HHP requires the use of specially designed packaging.
- Some enzymes are resistant to high pressure processing, which affects food quality.
- High investment cost.

2. HISTORY of HHP

The first application of HHP in the food industry was carried out by Hite in 1899 for pasteurization of milk and fruit products [26]. It was found that the shelf life of milk could be extended by 4 days by

JSR A
Journal of Scientific Reports

subjecting raw milk to 600 MPa pressure at room temperature for one hour. Between 1970 and 1980, there were positive developments in the ceramic and metal industries. In the 1990s, various commercial food products entered the Japanese market. Japan is now a world leader in jam, marmalade, juice, yogurt, salad dressing, and fruit sauces [7, 8].

3. EFFECTS ofF HHP on MEAT QUALITY

HHP increases meat crispness, microbiological inactivation, pasteurization, prevention of overcooking, extension of storage time in the refrigerator, binding and gelatinization of sausage and salami meat with the help of pressure. It has been found to have many beneficial effects, such as increasing the capabilities of the meat, less dissolution losses at low temperatures, and faster dissolution of the meat [32].

This technology is a practical method for inactivating microorganisms in prepared foods, the shelf life of which is highly dependent on good hygiene and manufacturing practices. Therefore, many studies are concerned with the use of high hydrostatic pressure applications to extend the shelf life of raw hams, specialty sausages, etc. [26].

Additionally, to the microbiological quality of meat and meat products, physicochemical properties are also important for consumer preferences. The color of meat products, which is one of the most important quality characteristics, is an important criterion for consumer selection and purchase of the product [33]. It can also be used for the tenderness of meat [34]. HHP treatment of fresh meat products can result in a cooked appearance. Sometimes this application cause rubbery texture [35]. In addition, it has very important effects on lipid oxidation, color, and phase change of meat. It has also been reported that the salt content of emulsion meat products can be decreased [34].

In addition, the using of HHP reduces the heat required for the dissolution process and does not effect the appearance, shape, and size of the products because the pressure is uniform in the samples. Due to these advantages, freezing and thawing methods have been the focus of interest for many researchers in recent years [36]. The studies on HHP technology for meat and meat products are listed in Table 1.

Table 1. Studies of HHP technology in meat and meat products.

PRODUCT	PROCESS CONDITIONS	BASIC EFFECT	REFERANCE
Biceps femoris veal patties	High Hydrostatic Pressure (350, 475, or 600 MPa) for 5, 10, or 15 minutes) and sous vide cooking technique (55, 60, 65°C) combination	• Significant changes in color and texture parameters were reported in the HHP and sous vide combination. • Combinations of 350 MPa for 10 minutes and sous-vide cooking at 55°C reduced hardness and cooking loss.	[37]
Iberian	600 MPa for 8	• Microbial counts decreased.	[38]

"*salchichón*"	minutes	• *L** and *a** values decreased during storage at 20 °C. • *b** values increased. • Color changes were reported in the sensory evaluation. • Lipid and protein oxidation values increased.	
Yellowfin Tuna Meat -individual histamine-forming bacteria inoculated (*Morganella morganii* & *Photobacterium phosphoreum*)	250, 350, 450 and 550 MPa, 5 minutes	• The number of Histamine-forming bacteria decreased significantly as the high hydrostatic pressure increased. • Histamine-forming bacteria were not found in samples treated at 450 and 550 MPa.	[39]
Raw and smoked trout	200 MPa, 15 minutes, liquid smoke (0.50%, v/v) and freezing (−80 °C, overnight)	• HHP, liquid smoke, and freezing were found to have a significant synergistic effect, resulting in a 5.48 or 1.93 log CFU/g reduction when smoked or raw trout were used, respectively.	[40]
Red Claw Crayfish *Cherax quadricarinatus*	200 MPa, 400 MPa, and 600 MPa	• A statistically significant decrease in the moisture value. • Except for the crude lipid content, no statistically significant differences in ash, crude protein, or crude lipid content were found between the 200 MPa and 600 MPa treatments.	[41]
New Zealand lamb meat	200–600 MPa	• The total free amino acid composition increased significantly at all applied HHP when compared to the control. • It has been reported that 400 and 600 MPa pressure application resulted in higher levels of TBARS.	[42]
Fresh beef	300, 600 MPa	• The combination of treatments provided acceptable color and microbiological stability during 4 and 6 weeks of storage at 4°C.	[43]
Chicken breast	600 MPa, 2 minutes, 20 °C	• HHP treatment of cooked chicken resulted in a <3.3 log reduction	[44]

		of *Listeria monocytogenes*. • A combination of 2% Na lactate and high pressure maintained *Listeria monocytogenes* numbers below 50 CFU/g during storage.	
Inegol meatballs	100-200-400-600 MPa, 10 minutes, 4℃.	• Pressure application increased the gel strength and improved its elastic properties. • The microbial load decreased with the increase in the pressure level. • High pressure had negative effects on the color parameters of uncooked meatball samples. However, it was reported that after firing, the color difference disappeared. • The panelists stated that the consistency, flexibility and flavor of the patties, which were pressurized especially at 200-400 MPa, were better.	[45]
Sausages (mechanically separated poultry and minced pork)	500 MPa, 50-60-70-75 °C, 30 minutes or cooked at 75 °C, 30 minutes	• More flexible and firm but with a more cohesive sausage structure. • High pressure can impart an acceptable texture to cooked sausages produced with mechanically separated poultry meat.	[46]
Tilapia fillets	220MPa, 10 minutes	• *L** values of the HHP and UV+HHP applied groups were found to be higher than the control and only UV-treated samples.	[47]
Tan Mutton	100, 200, 300, 400 MPa 15 minutes 25 ± 1°C	• The tenderness value of lamb leg meat increased when 200 MPa pressure was applied.	[48]
Beef mince meat (frozen, unfrozen, vacuum-packed)	350 MPa, 10 minutes, 10 ◦C	• Freezing and high hydrostatic pressure caused increase pH value and decrease TBA value.	[49]
Rendered pork fat	800MPa, 19°C, 20 minutes	• The pressure treated samples have a higher peroxide value compared to the control group samples. This effect became more pronounced as the pressure increased. • The extent of lipid oxidation at	[50]

JSR A
Journal of Scientific Reports

		800 MPa for 20 minutes was increased by increasing the treatment temperature.	
Beef	100- 600 MPa, 260 seconds at 10 °C	• While the myofibrils of the control group of beef, on which they did not apply pressure, showed thin and thick filament ultrastructure and a normal sarcomere arrangement, there was no difference in the using of 130 MPa pressure for 260 seconds at 10°C compared to the control. • 325 MPa pressure did not cause a change in myofibril structure, but 520 MPa pressure caused a complete change in myofibril structure.	[51]
Cured ham and fillet	200 MPa (15-30 minutes) 300 MPa (15-30 minutes)	• Protein oxidation increased with increasing pressure and time.	[52]
Peccary meat (Tayassu tajacu)	100 - 400 MPa	• As pressure increased, shear force decreased and meat tenderness increased above 200 MPa. • HHP was effective in tenderizing the meat and having potential positive effects on color.	[53]
Asian hard clam (*Meretrix lusoria*)	200, 300, 400, 500, and 600 MPa for 3 minutes	• Clam meat became brighter and more transparent when the pressure was increased. • High pressure also significantly reduces the loads of aerobic plate count, psychotropic bacteria, coliforms, and *V. parahaemolyticus*.	[54]
Beef gels	200 MPa, 10 minutes, room temperature	• The total free amino acid content of beef gels was increased to 200 MPa. • 200 MPa was effective in producing beef gels while providing high quality textural and sensory properties.	[55]
Spanish chorizo sausage	349–600 MPa, 18°C	• Pathogen reductions increased with the pressure and duration of high hydrostatic pressure however pressures below 400 MPa did not lead to significant pathogen reductions.	[56]
Red abalone	200, 300, 400, and	• High hydrostatic pressure	[57]

muscle	500 MPa, 5 minutes	application improved abalone muscle protein digestibility. • The smallest changes in secondary protein structure were reported at 500 MPa.	

4. CONCLUSION

In recent years, with the increasing demand for ready-to-eat, easy-to-prepare, and minimally processed foods, new food quality and safety issues have emerged. To address these issues, approaches such as HHP through non-thermal processes are being investigated. High hydrostatic pressure can have both positive and negative effects depending on the type of product, the pressure conditions used (time, temperature, pressure level), and the other processing technologies with which it is used. This process extends the shelf life of food and provides microbiologically safe, higher quality products.
It is possible to largely avoid quality losses in terms of texture and sensory properties when microorganisms are inactivated using new technologies as an alternative to heat treatment. This is because heat treatment causes vitamins and antioxidants to degrade, which results in nutritional losses. Their importance is increasing day by day and they can meet the demands of consumers in recent years.

ACKNOWLEDGEMENT

The authors thank the reviewers for their valuable comments and suggestions, which improved the clarity and scope of the article.

REFERENCES

[1] Alpas, H., Pilavtepe, M., and Bozoğlu, F. (2009). Mechanism of inactivation microorganisms by pulsed high hydrostatic pressure. Tübitak Proje No: 107O309, ODTÜ Ankara.

[2] Ramaswamy, R., Balasubramaniam, V.M., and Kaletunç, G. (2009). High Pressure Processing Fact Sheet for Food Processors. Fact sheet extension OSU.

[3] Ramaswamy, H. S., and Chen, C. R. (2002). Maximising the quality of thermally processed fruits and vegetables. Fruit and vegetable processing, 188.

[4] Sayın, L., and Tamer, C. E. (2014). Yüksek Hidrostatik Basınç ve Ultrasonun Gıda Koruma Yöntemi Olarak Kullanımı. Uludağ Üniversitesi Ziraat Fakültesi Dergisi, 28(1), 83-93.

[5] Campus, M. (2010). High Pressure Processing of Meat, Meat Products and Seafood. Food Engineering Reviews, 2, 256–273.

JSR A
Journal of Scientific Reports

[6] Liu, H., Xu, Y., Zu, S., Wu, X., Shi, A., Zhang, J., Wang, Q., and He, N. (2021). Effects of High Hydrostatic Pressure on the Conformational Structure and Gel Properties of Myofibrillar Protein and Meat Quality: A Review. Foods, 10(8), 1872.

[7] Topdaş, E. F., and Ertugay, M. F. (2012). Yüksek Hidrostatik Basınç ve Vurgulu Elektriksel Alan İşlemlerinin Maillard Reaksiyonu Üzerine Etkisi. Gıda Teknolojisi Derneği, 37 (4), 235-242.

[8] Oğuzhan, P. (2013). Yüksek Hidrostatik Basınç Teknolojisinin Gıda Endüstrisinde Kullanımı. Erzincan Üniversitesi Fen Bilimleri Enstitüsü Dergisi, 6(2), 205- 219.

[9] Yangılar, F., and Kabil, E. (2013). Süt ve Süt Ürünlerinde Bazı Isıl Olmayan Mikrobiyal İnaktivasyon Yöntemleri. Uludağ Üniversitesi Ziraat Fakültesi Dergisi, 27(1), 97-108.

[10] Song, X., Zhou, C., Fu, F., Chen, Z., and Wu, Q. (2013). Effect of high-pressure homogenization on particle size and film properties of soy protein isolate. Industrial Crops and Products, 43, 538-544.

[11] Akkara, M., and Kayaardı, S. (2014). İleri Muhafaza Tekniklerinin Et Kalitesi Üzerine Etkisi. Akademik Gıda, 12(4), 79-85.

[12] Açu, M., Yerlikaya, O., and Kınık, Ö. (2014). Gıdalarda Isıl Olmayan Yeni Teknikler ve Mikroorganizmalar Üzerine Etkileri. Gıda ve Yem Bilimi Teknolojisi Dergisi, 14, 23-35.

[13] Kolomeytseva, M. (2014). Synergistic Effect of High-Pressure Processing and *Pediococcus acidilactici* in inactivation of *Listeria innocua* in Ready-to-Eat sausages. (Master Thesis), Universidade Católica Portuguesa.

[14] Arıcı, M. (2006). Gıda Muhafazasında Yüksek Hidrostatik Basıncın Mikroorganizmalar Üzerine Etkisi. Tekirdağ Ziraat Fakültesi Dergisi, 3(1), 41-49.

[15] Özkan, G., Subaşı, B. G., Beştepe, S. K., and Güven, E. Ç. (2022). Sürdürülebilir Gıda ve Tarımsal Atık Yönetimi. Çevre İklim ve Sürdürülebilirlik, 23(2), 145-160.

[16] Özcan, T., and Kurtuldu, O. (2011). Sütün Raf Ömrünün Uzatılmasında Alternatif Yöntemler. Uludağ Üniversitesi Ziraat Fakültesi Dergisi, 25(1), 119-129.

[17] Kınık, Ö., Kavas, G., Uysal, H., and Kesenkaş, H. (2004). Yüksek hidrostatik basınç tekniğinin süt endüstrisindeki uygulamaları. Gıda, 29(1), 95-102.

[18] Barbut, S. (2004). Other poultry preservation techniques. Poultry meat processing and quality, 207-210.

[19] Şen, D. B., Kılıç, B., Demir, E., and Kılıç, G. B. (2019). Et ve Et Ürünlerinde Mikrobiyal Dekontaminasyon İçin Bazı Isıl Olmayan Teknolojilerin Kullanımı. Gıda, 44(2), 202-215.

[20] Yıldız Agopyan, N., and Ekşi, A. (2021). Gıdalarda Proses Bulaşanları Oluşumu ve Azaltılması, Gıda Alerjenleri, Bulaşanları ve Halk Sağlığı Açısından Önemi. 49-60.

[21] Tülek, Y., and Filizay, G. (2011). Gıda Endüstrisinde Yüksek Hidrostatik Basınç Uygulamaları. Pamukkale Üniversitesi Mühendislik Bilimleri Dergisi, 12(3), 369-377.

[22] Suzuki, A., Kim, K., Tanji, H., Nishiumi, T., and Ikeuchi, Y. (2006). Application of high hydrostatic pressure to meat and meat processing. Food Science and Technology-New York-Marcel Dekker-, 158, 193.

[23] Gönen, K. (2021). Gıda ve Gıda İşletmelerinde Listerıa Monocytogenes ve Biyofilmine Karşı Kullanılan Bazı Modern Teknikler. Akademik Et ve Süt Kurumu Dergisi, (1), 19-26.

[24] Koutchma, T., Popović, V., Ros-Polski, V., and Popielarz, A. (2016). Effects of ultraviolet light and high-pressure processing on quality and health-related constituents of fresh juice products. Comprehensive Reviews in Food Science and Food Safety, 15(5), 844-867.

[25] Candoğan, K., and Özdemir, G. (2021). Sürdürülebilir Et Üretimi için Yenilikçi Yaklaşımlar. Gıda, 46(2), 408-427.

[26] Sarıçoban, C., Mahmood, M. S., and Al-Murjan, R. K. B. (2020). Yüksek Basınç Uygulamasının Et ve Et Ürünlerinin Güvenliği ve Raf Ömrü Açısından Rolü. Bilecik Şeyh Edebali Üniversitesi Fen Bilimleri Dergisi, 7(2), 1182-1195.

[27] Özdemir, V., and Yanar, M. (2021). Kırmızı Etin Gevrekleştirilmesinde Kuru ve Yaş Olgunlaştırma Yöntemleri. Journal of the Institute of Science and Technology, 11(1), 795-806.

[28] Karakaya, M., Caner, C., and Sarıçoban, C. (2004). Et Teknolojisinde Yüksek Hidrostatik Basınç Kullanımı. GIDA, 29(6), 465-470.

[29] Ludikhuyze, L., Loey, A. V., and Hendrickx, M. (2002). High pressure processing of fruit and vegetables. Fruit and vegetable processing: Improving quality, 346-362.

[30] Uçak, İ. (2018). Su Ürünleri İşleme ve Muhafazasında Yüksek Hidrostatik Basınç Kullanımı. Journal of Limnology and Freshwater Fisheries Research, 4(1), 47-57.

[31] Muntean, M-V., Marian, O., Barbieru, V., Câtunescu, G. M., Ranta, O., Drocas, I,. and Terhes, S. (2016). High Pressure Processing in Food Industry-Characteristics and Applications. Agriculture and Agricultural Science Procedia, 10, 377-383.

[32] Ensoy, Ü., and Coşar, B. (2006). Yüksek basınç uygulamalarının et ve et ürünlerinin duyusal, fiziksel ve biyokimyasal özellikleri üzerine etkileri. Gaziosmanpaşa Üniversitesi Ziraat Fakültesi Dergisi, 23(2),1-7.

JSR A
Journal of Scientific Reports

[33] Kara, R., Acaröz, U., Gürler, Z., and Soylu, A. (2021). Bazı Et Ürünlerinin Fizikokimyasal Özelliklerinin Araştırılması. Akademik Et ve Süt Kurumu Dergisi, (2), 5-12.

[34] Zorba, Ö., and Kurt, Ş. (2005). Yüksek Basınç Uygulamalarının Et ve Et Ürünleri Kalitesi Üzerine Etkisi. Yüzüncü Yıl Üniversitesi Veteriner Fakültesi Dergisi, 16(1), 71-76.

[35] Hugas, M., Garriga, M., and Monfort, J. M. (2002). New mild technologies in meat processing: high pressure as a model technology. Meat Science, 62(3), 359-371.

[36] Bozkır, H., Baysal, T., and Ergün, A. R. (2014). Gıda endüstrisinde uygulanan yeni çözündürme teknikleri. Akademik Gıda, 12(3), 38-44.

[37] Janardhanan, R., Virseda, P., Huerta-Leidenz, N., and Beriain, M. J. (2022). Effect of high–hydrostatic pressure processing and sous-vide cooking on physicochemical traits of *Biceps femoris* veal patties. Meat Science, 108772.

[38] Ramírez, R., Trejo, A., Delgado-Adámez, J., Martín-Mateos, M. J., and García-Parra, J. (2022). Effect of High-Hydrostatic-Pressure Processing and Storage Temperature on Sliced Iberian Dry-Cured Sausage ("Salchichón") from Pigs Reared in Montanera System. Foods, 11(9), 1338.

[39] J Huang, C. H., Hsieh, C. Y., Lee, Y. C., Ou, T. Y., Chang, T. H., Lee, S. H., Tseng, C. H., and Tsai, Y. H. (2022). Inhibitory Effects of High-Hydrostatic-Pressure Processing on Growth and Histamine Formation of Histamine-Forming Bacteria in Yellowfin Tuna Meat during Storage. Biology, 11(5), 702.

[40] Ekonomou, S. I., Bulut, S., Karatzas, K. A. G., and Boziaris, I. S. (2020). Inactivation of *Listeria monocytogenes* in raw and hot smoked trout fillets by high hydrostatic pressure processing combined with liquid smoke and freezing. Innovative Food Science & Emerging Technologies, 64, 102427.

[41] Lin, X., Liu, C., Cai, L., Yang, J., Zhou, J., Jiang, H., Shi, Y., and Gu, Z. (2021). Effect of High Hydrostatic Pressure Processing on Biochemical Characteristics, Bacterial Counts, and Color of the Red Claw Crayfish Cherax quadricarinatus. Journal of Shellfish Research, 40(1), 177-184.

[42] Kantono, K., Hamid, N., Oey, I., Wu, Y. C., Ma, Q., Farouk, M., and Chadha, D. (2020). Effect of High Hydrostatic Pressure Processing on the Chemical Characteristics of Different Lamb Cuts. Foods, 9(10), 1444.

[43] Giménez, B., Graiver, N., Califano, A., and Zaritzky, N. (2015). Physicochemical characteristics and quality parameters of a beef product subjected to chemical preservatives and high hydrostatic pressure. Meat science, 100, 179-188.

[44] Patterson, M. F., Mackle, A., and Linton, M. (2011). Effect of high pressure, in combination with antilisterial agents, on the growth of *Listeria monocytogenes* during extended storage of cooked chicken. Food Microbiology, 28(8), 1505–1508.

JSR A
Journal of Scientific Reports

[45] Okur, G. (2020). Yüksek Basınç Uygulamasının Geleneksel Bir Türk Köftesinin Bazı Kalite Özellikleri Üzerideki Etkisinin İncelenmesi, Yüksek Lisans Tezi, Ege Üniversitesi Fen Bilimleri Enstitüsü, İzmir, 212s.

[46] Yuste, J., Mor-Mur, M., Capellas, M., Guamis, B., and Pla, R. (1999). Mechanically Recovered Poultry Meat Sausages Manufactured with High Hydrostatic Pressure. Poultry Science, 78, 914-921.

[47] Monteiro, M. LG, Marsico, E.T, Rosenthal, A., and Conte-Junior, C.A. (2019). Synergistic effect of ultraviolet radiation and high hydrostatic pressure on texture, color, and oxidative stability of refrigerated tilapia fillets. Journal of the Science of Food and Agriculture, 99, 4474-4481.

[48] Xu, H., Zhang, X.K., Wang, X., and Liu, D.H. (2019). The effects of high pressure on the myofibrillar structure and meat quality of marinating Tan mutton. Journal of Food Process Engineering, 42, 13138–13152.

[49] Şayin Sert, T., and Coşkun, F. (2022). The Effects of High-Pressure Processing on pH, Thiobarbituric Acid Value, Color and Texture Properties of Frozen and Unfrozen Beef Mince. Molecules, 27(13), 3974.

[50] Indrawati, A., and Hendrickx, M. (2002). High pressure processing. The nutrition handbook for food processors, 433-461.

[51] Jung, S., de Lamballerie-Anton, M., and Ghoul, M. (2000). Modifications of Ultrastructure and Myofibrillar Proteins of Post-rigor Beef Treated by High Pressure. LWT-Food Science and Technology, 33(4), 313-319.

[52] Cava, R., Ladero, L., González, S., Carrasco, A., and Ramírez, M.R. (2009). Effect of pressure and holding time on colour, protein and lipit oxidation of sliced dry-cured Iberian ham and loin during refrigerated storage. Innovative Food Science and Emerging Technologies, 10, 76-81.

[53] Fernandes, H. R., Deliza, R., Neto, O. C., Silva, C. M., de Albuquerque, N. I., Martins, T. R., and Rosenthal, A. (2022). Effect of high hydrostatic pressure on the meat of collared peccaries (Tayassu tajacu) with different ages. African Journal of Food Science, 16(9), 215-225.

[54] Lin, C. S., Lee, Y. C., Kung, H. F., Cheng, Q. L., Ou, T. Y., Chang, S. K., and Tsai, Y. H. (2022). Inactivation of microbial loads and retardation of quality loss in Asian hard clam (Meretrix lusoria) using high-hydrostatic-pressure processing during refrigerated storage. Food Control, 133, 108583.

[55] Maksimenko, A., Kikuchi, R., Tsutsuura, S., and Nishiumi, T. (2020). Effect of high hydrostatic pressure in combination with low salt content for the improvement of texture and palatability of meat gels. In IOP Conference Series: Earth and Environmental Science, 548(2), 022078.

[56] Rubio, B., Possas, A., Rincón, F., García-Gímeno, R. M., and Martínez, B. (2018). Model for *Listeria monocytogenes* inactivation by high hydrostatic pressure processing in Spanish chorizo sausage. Food microbiology, 69, 18-24.

[57] Cepero-Betancourt, Y., Opazo-Navarrete, M., Janssen, A. E., Tabilo-Munizaga, G., and Pérez-Won, M. (2020). Effects of high hydrostatic pressure (HHP) on protein structure and digestibility of red abalone (Haliotis rufescens) muscle. Innovative Food Science & Emerging Technologies, 60, 102282.